

Dissertation

submitted to the
Combined Faculties of Natural Sciences and Mathematics of
the Ruperto-Carola University of Heidelberg, Germany
for the degree of
Doctor of Natural Sciences

Put forward by

M.Sc. Laura Olivera Nieto

born in Coria, Cáceres, Spain

Oral examination: February 7th, 2023

University of Heidelberg

Department of Physics and Astronomy

Resolving particle acceleration
and transport in the jets of the
microquasar SS 433 with H.E.S.S.
and HAWC

Referee **Prof. Dr. Jim Hinton**
Max Planck Institute for Nuclear Physics

Referee **Prof. Dr. Stefan Wagner**
ZAH, Landessternwarte
University of Heidelberg

Supervisors Prof. Dr. Jim Hinton, Dr. Brian Reville

Laura Olivera Nieto

Resolving particle acceleration and transport in the jets of SS 433 with H.E.S.S. and HAWC.

PhD Thesis, 7th February, 2023

Reviewers: Prof. Dr. Jim Hinton and Prof. Dr. Stefan Wagner

Supervisors: Prof Dr. Jim Hinton and Dr. Brian Reville

University of Heidelberg

Non-thermal astrophysics, div. Hinton

Max Planck Institute for Nuclear Physics

Department of Physics and Astronomy

Saupfercheckweg 1

69117 and Heidelberg

“Feminism and science share vital characteristics today. Both are filled with urgency and conviction, both are observing intently, both are concentrated on demystifying the self and the environment, recovering the truths of the life within. Women in science – both separately and collectively – stir the contemporary imagination. In their hyphenated identity are captured the pain and excitement of a culture struggling to mature.”

Vivian Gornick, *Women in Science* (2009)

Abstract

The microquasar SS 433 offers a unique laboratory to study the physics of mildly relativistic jets and the associated non-thermal processes. It hosts a compact binary system, from which a pair of counter-propagating jets is observed to emanate. The jets are resolved by observations out to distances of ~ 0.1 pc from the central source, but further out, they remain dark until they abruptly reappear at ~ 25 pc as bright X-ray sources. These outer jets were recently reported to be sources of TeV gamma-rays by the High Altitude Water Cherenkov (HAWC) observatory. This thesis presents a complete picture of the TeV emission from the jets of SS 433 including new data from the High Energy Stereoscopic System (H.E.S.S.) and the HAWC observatory.

To fully exploit the capabilities of the H.E.S.S. observations, a new approach to background rejection is presented. It is based on the detection of Cherenkov light from muons by large Imaging Atmospheric Cherenkov Telescopes (IACTs), such as the telescope located at the center of the H.E.S.S. array. The application of this technique leads to a factor four reduction in background above several tens of TeV in the H.E.S.S. stereoscopic analysis.

This thesis presents the detection of the SS 433 outer jets for the first time with an IACT array using H.E.S.S.. The superior angular and energy resolution of H.E.S.S. compared to HAWC allow for a detailed study of the emission from the jets, including a measurement of the physical extension of the emission and of the spectra out to tens of TeV. These observations also reveal the presence of striking energy-dependent morphology, ruling out a hadronic origin for the bulk of the gamma-ray emission. Photons above 10 TeV are observed only close to the base of the outer jets, implying efficient particle acceleration to very-high energies at that location. Evidence suggests that the acceleration is due to a shock, thus providing a clue to the long-standing question of the reappearance of the jets.

The observed energy-dependent morphology is modeled as a consequence of the particle cooling times and the advection flow of the jet, which constrains the jet dynamics and, in particular, results in an estimate of the velocity of the outer jets at their base. This solves several issues concerning the non-thermal processes occurring in the jets and their dynamics, but also opens up new questions that highlight our incomplete understanding of the SS 433 system.

A joint analysis of the H.E.S.S. and HAWC data would provide insights on the system across the entire range of TeV energies. To make this possible, a tool capable of reading and analyzing the data from both instruments is required. This thesis presents the extension and validation of an existing data format and analysis tool shared among IACTs to the data from particle detector arrays such as the HAWC observatory. This framework is then used to revisit the HAWC observations of the SS 433 region with the inclusion of additional data taken since the first detection was reported. The existence of this framework enables for the first time the joint analysis of the H.E.S.S. and HAWC data, the preliminary results of which are presented.

Zusammenfassung

Der Mikroquasar SS 433 stellt eine einzigartige Versuchsanordnung dar, um die Physik leicht relativistischer Jets und die assoziierten nichtthermischen Prozesse zu untersuchen. Das System besteht aus einem kompakten Doppelsternsystem und einem dort entstehenden Jet-Paar, welches sich entgegengesetzt zueinander ausbreitet. Diese Jets können durch Observationen bis zu Distanzen von ~ 0.1 pc von der zentralen Quelle aufgelöst werden. Weiter außerhalb jedoch bleiben sie unentdeckt, bis sie ab ~ 25 pc plötzlich wieder als helle Röntgenquellen sichtbar werden. Diese äußeren Jets wurden vor Kurzem auch als Quellen von TeV-Gammastrahlung durch das High Altitude Water Cherenkov (HAWC) Observatorium identifiziert. Diese Doktorarbeit präsentiert ein vollständiges Bild der TeV-Emission der SS 433-Jets mit Hilfe neuer Daten der Teleskope des High Energy Stereoscopic System (H.E.S.S.) und des HAWC Observatoriums.

Um die Sensitivität der H.E.S.S. Observationen vollständig auszunutzen, wird ein neuer Ansatz zur Hintergrundminimierung beschrieben. Dieser basiert auf der Detektion von Tscherenkowlicht von Myonen durch große Abbildende Tscherenkow Teleskope (IACTs), wie zum Beispiel das zentrale Teleskop des H.E.S.S. Systems. Die Anwendung dieser Methode führt zu einer Verminderung von Hintergrund oberhalb von Energien von einigen zehn TeV um einem Faktor von 4 in der stereoskopischen Analyse von H.E.S.S..

Diese Doktorarbeit präsentiert die erstmalige Entdeckung der äußeren Jets von SS 433 durch ein IACT System mit Hilfe von H.E.S.S. Die bessere Richtungs- und Energieauflösung von H.E.S.S. verglichen mit HAWC ermöglicht eine detaillierte Untersuchung der Jetemission, welche auch eine Messung der physikalischen Ausdehnung der Emission und der Spektren bis zu Energien von einigen zehn TeV beinhaltet. Die Beobachtungen legen auch eine eindeutige Änderung der Morphologie in Abhängigkeit der Energie offen, was wiederum einen hadronischen Ursprung eines Großteils der Gammaemission ausschließt. Photonen mit mehr als 10 TeV werden nur nahe an der Basis des äußeren Jets beobachtet, was eine effiziente Beschleunigung von Teilchen bis zu sehr hohen Energien dort andeutet. Die Belege legen nahe, dass die Beschleunigung durch einen Schock verursacht wird, was wiederum einen Hinweis auf die Antwort der lang bestehenden Frage des Wiederauftauchens von Jets geben kann.

Die beobachtete energieabhängige Morphologie wird als Folge der Abkühldauer von Teilchen und des Advektionsflusses des Jets modelliert. Dies wiederum beschränkt die Jetdynamik und führt vor allem zu einer Abschätzung der Geschwindigkeit der äußeren Jets an ihrem Ursprung. Dadurch werden einige offene Fragen bezüglich der nonthermalen Prozesse in Jets und ihrer Dynamik beantwortet, jedoch wiederum neue Fragen aufgeworfen, welche unser inkomplettes Bild von SS 433 zur Schau stellen.

Eine kombinierte Analyse der HAWC und H.E.S.S. Daten kann Einblicke in das System über den gesamten TeV-Energiebereich gewähren. Dafür ist ein Werkzeug benötigt, welches die Daten beider Instrumente lesen und gemeinsam analysieren kann. In dieser Doktorarbeit wird die Erweiterung und Validierung eines bereits existierenden Datenformats und Analysewerkzeugs, welches bisher für IACTs genutzt wurde, beschrieben, um die Analyse von Daten von Teilchendetektoren wie HAWC zu ermöglichen. Damit werden dann die HAWC Daten der SS 433 Region inklusive zusätzlicher Daten, welche seit der Bekanntgabe der Detektion genommen wurden, neu betrachtet. Durch das so erweiterte Analysewerkzeug können dann die H.E.S.S. und HAWC Daten gemeinsam analysiert werden und die vorläufigen Resultate werden in dieser Arbeit präsentiert.

Acknowledgements

The work presented in this thesis was the result of a little over three years of work, a time during which I was supported, both professionally and personally by a number of people who I will try to –probably unsuccessfully– do justice here.

First and foremost I want to thank my supervisor Prof. Dr. Jim Hinton for being a constant source of inspiration, interesting ideas and support. I feel very lucky to have had the chance to choose him as my PhD supervisor, a decision which I have not once felt the need to question over the course of these years. I would like to thank Dr. Brian Reville, for his utmost patience when explaining the same things to me for the n -th time, for the constant encouragement, the brilliant ideas and for very carefully proof-reading multiple chapters of this thesis. I would also like to thank Prof. Dr. Stefan Wagner who agreed to referee this thesis and Prof. Dr. Stephanie Hansmann-Menzemer for agreeing to be a part of my examination committee. I would like to thank Prof. Dr. Christian Fendt for organizing the IMPRS program and for kindly agreeing to be a member of both my thesis and my examination committee.

I would like to thank the H.E.S.S. Collaboration for making big parts of the work presented in this thesis possible by running and maintaining the telescopes, and in particular to Garret Cotter and Emma de Oña Wilhelmi, for their unwavering support to the SS 433 project within the Jets and Stellar working groups respectively. I would also like to thank Dr. Michelle Tsirou for her work with the SS 433 cross-check and for all of her help, and to Dr. Armelle Jardin-Blicq for kick-starting the SS 433 observations that became central to my thesis work.

I would also like to thank the HAWC and SWGO Collaborations, for all the discussions and support. In particular, to the HAWC members for making parts of the work presented in this thesis possible by running and maintaining the experiment.

I would like to thank the *Gammapy* developers team, and in particular Dr. Axel Donath for welcoming me in and providing a space for me to develop my coding skills and my understanding of gamma-ray data analysis hands-on, as well as for their work in creating and maintaining a remarkable tool that has been used repeatedly through this thesis.

I would like to thank all the members of the non-thermal astrophysics division at MPIK for the fantastic atmosphere, in which collaboration and interaction come naturally and fruitfully. In particular, I would like to thank the members of the H.E.S.S. and HAWC groups at MPIK for patiently looking at all of my intermediate results, even when the plots were ugly. I would like to thank Dr. Harm Schoorlemmer, who helped me understand how HAWC works and whose departure forced me to become more independent, which I needed. A special mention is for Dr. Vincent Marandon, who has taught me virtually everything I know about gamma-ray data analysis while pretending not to, who has walked down the hill with me innumerable times in the dark and who has carefully read multiple chapters of this thesis.

I would like to thank the PhD cohort at the division for all of the good times and distractions. In particular, I would like to thank Simon Steinmassl for being an unbelievably German partner in crime, for the constant support and mockery, occasional snack, unforgettable trips and for carefully proof-reading the most striking parts of this thesis and translating the abstract. I would also like to thank Hazal Göksu for always being exactly the friend I needed, for all the conversations, for watching hilarious and pretentious movies with me, for allowing me to join her along in her adventures and for proof-reading parts of this thesis.

Outside of MPIK, I would like to thank Emily Hunt and Loke Lönnblad Ohlin for being so patient when I talked about climbing constantly, for all the nice evenings and for their empathy and company. I wish you both the best of luck with your theses and can't wait to see you on the other side of this.

Besides the office and my home, the place that I've spent the most time at during my PhD has been by far the climbing gym. I would like to thank the whole climbing crew for all the fun times, the beers and the silliness. In particular to Prof. Dr. Jim Hinton for teaching me almost as much about climbing as he has about science, including the importance of using one's knees. To Dr. Rich White for setting a standard of climbing ability for all of us to aspire to and for proof-reading the abstract of this thesis. To Dr. Brian Reville for not being angry (or mad) at me after that time I talked to him through a (clean!) sock puppet. To Sophia Schmitt for her support, her unbelievable cakes and for kindly taking me to the emergency room after I unsuccessfully and recklessly tried to kill a fly. Finally, I would like to thank Dr.(?) Konstantin Beyer for being such an encouraging belaying partner that his credibility is brought up to question, for always being up for cooking food of different degrees of edibility with me and for proof-reading what was probably the worst chapter of this thesis at the time.

Outside of Heidelberg, I would like to thank my remote support system, who were always available even despite the distance. In particular, I would like to thank my best friend Rosana Hinojosa for being a constant source of encouragement, understanding, silliness and hope. Dr. Guillem Martí-Devesa for always proof-reading anything I sent him, for his constant support and friendship and for all the fun we had in Barcelona. Maryam Hami for allowing me to brag about having a friend who works for the JWST and for every single one of the dog pictures. Júlia Silva for building with me the playlists that have literally been the soundtrack of this thesis.

My deepest gratitude goes to Philippe Weitz, for being such a central part of my life without which I would never have become the person I am today. I owe you much more than I can fit into this section.

Finally, I would like to thank my parents Chema Olivera Mateos and Lola Nieto Clemente, who have made all of the good things in my life possible with their support. Muchas gracias papichus (y Elmo).

Contents

Abstract	vii
Zusammenfassung	ix
Acknowledgements	xi
Preface	1
1 Very-High-Energy Emission from Astrophysical jets	5
1.1 Astrophysical Jets	5
1.1.1 Jetted Sources in the Galaxy	7
1.2 Evidence of Particle Acceleration	9
1.3 Particle Acceleration	12
1.3.1 General Considerations	12
1.3.2 Particle Acceleration Mechanisms	13
1.4 Particle Acceleration in Shocks	15
1.4.1 Acceleration Timescale	18
1.4.2 Diffusion	18
1.5 Energy Losses	19
1.5.1 Radiative Losses	19
1.5.2 Adiabatic Losses	24
1.6 Summary and Outlook	24
2 The Microquasar SS 433	27
2.1 First Detection and Identification	27
2.2 Overview of the SS 433 System	27
2.3 Observations of the SS 433 Region	30
2.3.1 Radio	30
2.3.2 Infrared	34
2.3.3 Optical	34
2.3.4 Ultraviolet	36
2.3.5 X-ray	36
2.3.6 Gamma-Ray	38
2.4 Attempts at Modeling SS 433	43
2.4.1 Numerical Simulations of the Jets	43
2.4.2 Gamma-Ray Emission Models	45

2.5	Summary and Outlook	46
3	Detection of Very-High-Energy Gamma-Rays	49
3.1	Ground-Based Gamma-Ray Astronomy	49
3.1.1	Extensive Air Showers	49
3.1.2	Cherenkov Radiation	53
3.2	Imaging Atmospheric Cherenkov Telescopes	54
3.2.1	The H.E.S.S. Array	56
3.2.2	The Cherenkov Telescope Array	57
3.3	H.E.S.S. Data Reduction	57
3.3.1	Data Acquisition System	57
3.3.2	Calibration and Image Cleaning	58
3.3.3	Event Reconstruction and IMPACT Templates	59
3.3.4	Event Selection and Gamma-Hadron Separation	60
3.3.5	Instrument Response Functions	63
3.3.6	Background Modeling and Estimation	66
3.4	Particle Detector Arrays	68
3.4.1	The HAWC Observatory	68
3.4.2	The Southern Gamma-ray Wide-field Observatory	72
3.5	Gamma-Ray High-Level Analysis	73
3.5.1	<i>Gammapy</i>	73
3.5.2	Significance of the Observation	74
3.5.3	Model Fitting	75
3.5.4	Spectral "1D" Analysis	77
3.5.5	Spectro-Morphological "3D" Analysis	77
3.5.6	Flux Points and Upper Limits	79
3.6	Summary and Outlook	79
4	Improving Background Rejection at Very High Energies with IACTs	83
5	Towards a Common Data Format in VHE Gamma-Ray Astronomy	105
6	The H.E.S.S. view of SS 433	119
6.1	H.E.S.S. Observations	119
6.2	Analysis Configuration and Data Reduction	120
6.3	Modeling MGRO J1908+06	122
6.4	Detection of SS 433	124
6.5	Morphology of the Jets	125
6.6	Energy-Dependent Morphology	127
6.6.1	Verification of the PSF at High Zeniths and Offsets	128
6.6.2	3D Fits in Energy Bands	130
6.6.3	Flux Profiles	132
6.7	Spectra of the Jets	133

6.8	Search for Periodic Variability	134
6.9	The Central Source	134
6.10	Systematic Uncertainties	135
6.10.1	Systematic uncertainties introduced by the background estimation	135
6.10.2	Systematic Uncertainties in Model Parameters	136
6.11	Summary and Outlook	137
7	Acceleration Sites and Dynamics in the SS 433 Jets	139
7.1	Acceleration Sites in the SS 433 Jets	139
7.2	Multi-Wavelength SED	140
7.2.1	Radio Data	140
7.2.2	X-ray Data	140
7.2.3	GeV Data	142
7.3	Broadband Model	142
7.3.1	Age of the Jets	144
7.4	SS 433 as a Cosmic-Ray Source	145
7.5	Particle Transport in the Jets of SS 433	145
7.5.1	A Model for Particle Transport and Cooling	145
7.5.2	Application to SS 433	146
7.6	Revealing the Jet Dynamics	148
7.6.1	Favoring Deceleration	150
7.6.2	Estimate of the Jet Velocity Assuming Deceleration	151
7.6.3	Impact of the Injected Spectrum on the Jet Velocity.	153
7.7	Summary and Outlook	154
8	Joint Analysis of SS 433 using H.E.S.S. and HAWC Data	157
8.1	Revisiting SS 433 with HAWC	157
8.1.1	Data Reduction	158
8.1.2	Modeling MGRO J1908+06	158
8.1.3	The SS 433 Region	160
8.2	Joint Analysis using H.E.S.S. and HAWC Data	164
8.2.1	Modeling MGRO J1908+06	164
8.2.2	The SS 433 Region	165
8.3	Summary and Outlook	168
	Conclusions and Outlook	171
	Bibliography	173
	Bibliography of L. Olivera-Nieto	187
	List of Figures	189

List of Tables	201
Acronyms	203

Preface

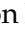






This thesis is organized in the following order:


- ✧ Chapter 1 introduces the phenomenon of astrophysical jets, with a special focus on Galactic jets. It briefly describes the particle acceleration mechanisms thought to be capable of accelerating particles to energies high enough to produce radiation at TeV energies.
- ✧ Chapter 2 introduces the Galactic microquasar SS 433. A summary of the observations and theoretical studies concerning this system since its detection 50 years ago is presented, with a focus on the non-thermal and high energy emission.
- ✧ Chapter 3 introduces the field of ground-based TeV astronomy by describing the basic physical processes and experimental techniques that make it possible to study TeV sources. Two particular experiments are highlighted, the High Energy Stereoscopic System (H.E.S.S.) array of telescopes and the High Altitude Water Cherenkov (HAWC) observatory. The process of high-level gamma-ray data analysis is also described.
- ✧ Chapter 4 proposes a new method to improve the background rejection performance of Imaging Atmospheric Cherenkov Telescopes based on the detection of Cherenkov light from muons. This method is used in the analysis presented in Chapter 6.
- ✧ Chapter 5 presents the validation of open-source data formats and tools for their use with data from particle detecting arrays such as the HAWC observatory. The work presented here makes it possible to do joint analyses using data from H.E.S.S. and HAWC, such as that presented in Chapter 8.
- ✧ Chapter 6 presents the results of dedicated observations of the SS 433 system by the H.E.S.S. array of telescopes, which result in the first ever detection of the system by such an experiment. A detailed analysis of the data is presented, which includes the discovery of energy-dependent morphology.
- ✧ Chapter 7 puts the findings described in the previous chapter into the larger context of our understanding of the dynamics and particle acceleration processes taking place in the jets of SS 433. Thanks to the H.E.S.S. observations, the site of efficient particle acceleration can be identified.









- ⊗ Chapter 8 presents a joint analysis of the SS 433 region using H.E.S.S. and HAWC data.

The work presented in Chapter 4 has been published in Olivera-Nieto et al. (2021) and Olivera-Nieto et al. (2022). The work presented in Chapter 5 has been published in Albert et al. (2022b) (corresponding author L. Olivera-Nieto). The work described in Chapters 6 and 7 will be published as a H.E.S.S. Collaboration paper which is in preparation (with corresponding author L. Olivera-Nieto). Large parts of the work presented in this thesis make use of the *Gammapy* analysis package, which I have contributed to as a part of the regular developer team. A publication about *Gammapy* is in preparation, with me as one of the authors.

Throughout this thesis I will use "we" in the text for simplicity. My individual contributions to the work presented in this thesis are outlined below:

- ⊗ **Chapter 3:** I optimized and validated the *hard* gamma-hadron separation thresholds described in Section 3.3.4. This process included the production of instrument response functions (IRFs) for the resulting values of the analysis cuts. The optimization and IRF production was done by adapting existing scripts developed by members the H.E.S.S. Collaboration.
- ⊗ **Chapter 4, Olivera-Nieto et al. (2021):** I participated in discussions with the rest of the co-authors to develop the idea and structure of the paper. I implemented and tested the "Simplified Muon Model", and used simulations provided by co-authors Konrad Bernlöhr  and Alison M. W. Mitchell  to study the properties of muons in showers and calculated the expected number of detectable muons for different types of telescopes. I led the paper text writing (>90% of text) and revision.
- ⊗ **Chapter 4, Olivera-Nieto et al. (2022):** With input from co-authors Jim Hinton  and Alison M. W. Mitchell  I led the design of the Algorithm for Background Rejection using Image Residuals (ABRIR), which I also then implemented and tested. I performed the validation analysis using real H.E.S.S. Crab data. I produced the H.E.S.S. performance plots shown in the appendix with the exception of the "hybrid" case which was done by co-author Helena X. Ren . I led the paper text writing (>90% of text) and revision.
- ⊗ **Chapter 5, Albert et al. (2022b):** I developed and tested the scripts to export the HAWC data and instrument response functions to the DL3 format. I exported the *Pass4* full-sky HAWC data set and IRFs to this format. Together with co-author Harm Schoorlemmer , we developed the idea behind the background model construction, which I then implemented and tested. With the guidance of co-author Axel Donath , I implemented the necessary changes to the *Gammapy* code that made HAWC analysis possible. I designed the structure of the validation section and carried out all three analyses shown in it, with the only exception of the values indicated as "From map" in the text, which were

obtained by co-author Vikas Joshi . I performed the joint Crab fit and prepared the public data release. I led the paper text writing (>90% of text) and revision.

- ⊗ **Chapter 6:** I carried out the whole analysis presented using *Gammapy*. The proposal for observation of SS 433 by H.E.S.S. in 2019, which resulted in ~25 hours of data, was led by Armelle Jardin-Blicq . I led the observation proposals in 2020 and 2021, which resulted in ~150 hours of data. I also lead the proposal to observe the Crab Nebula under different zenith and offset angles to verify the angular resolution of the analysis. The calibration of the H.E.S.S. data was done by Vincent Marandon . I reconstructed the data using existing scripts developed by members of the H.E.S.S. Collaboration. The reconstructed data was exported to the DL3 format using scripts provided by Lars Mohrmann . I ran ABRIR on the exported data, and produced background models using scripts provided by Lars Mohrmann . The main results of the analysis were reproduced by Michelle Tsirou  using a different H.E.S.S. pipeline as is required within the H.E.S.S. Collaboration.
- ⊗ **Chapter 7:** Together with Jim Hinton  and Brian Reville , we developed the physical interpretation of the H.E.S.S. observations. I collected the publicly-available multi-wavelength data with the exception of the X-ray range, for which Naomi Tsuji  performed the analysis. I implemented the broadband model using GAMERA and developed scripts using *Gammapy* to fit it to the flux points. Together with Jim Hinton, we designed the structure of the Monte Carlo simulation, which I then implemented and tested.
- ⊗ **Chapter 8:** I exported the HAWC event lists and instrument response functions from the *Pass5* reconstruction to the DL3 format, which I then used to construct a background model using the algorithms developed for Chapter 5. I performed the HAWC and joint analyses using *Gammapy*.

Chapter 1

Very-High-Energy Emission from Astrophysical jets

This chapter presents a short overview of astrophysical jets, with a particular focus on their non-thermal emission. First, some of the observational properties of astrophysical jets are presented, with a special mention of jetted sources in the Galaxy as it is pertinent to the rest of this thesis. Then, the evidence for the occurrence of particle acceleration in astrophysical settings is described and some of the most commonly considered mechanisms are introduced, with a special focus on acceleration by shocks. Finally, the most relevant the energy loss mechanisms that lead these particles to lose some of their gained energy but also to produce radiation at TeV energies are described.

1.1 Astrophysical Jets

The first observational evidence of astrophysical jets dates to more than a century ago, when optical observations of the M87 galaxy revealed a "*curious straight ray (...) apparently connected with the nucleus but a thin line of matter*" (Curtis, 1918). The advent of radio astronomy in the 1930s (Jansky, 1933) led to the discovery of many more such objects. A particularly relevant breakthrough came in 1953, when Cygnus A, a bright radio source associated with a nearby galaxy (a phenomenon referred to as *radio galaxy*), was resolved into two different jet lobes (Jennison and Das Gupta, 1953). A more recent Very Large Array (VLA) image of the Cygnus A jets can be seen in Figure 1.1. In the following decades, the number of sources in which jet phenomena were thought to occur increased rapidly (see Blandford et al., 2019, for a review). One such example is the discovery in 1963 of so-called "quasi-stellar radio sources" or *quasars*, which are also known now to host a jet, with the observation of the jet in 3C 273 (Schmidt, 1963; Hazard et al., 1963).

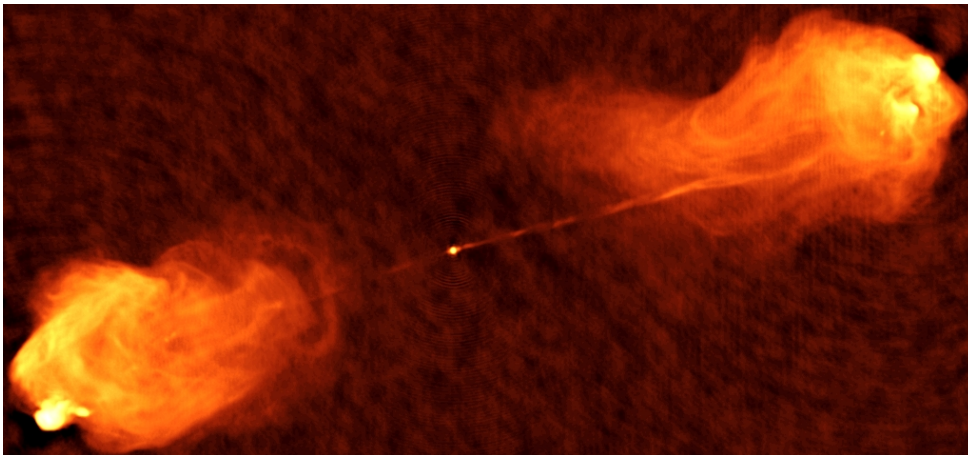


FIGURE 1.1: **The jets of Cygnus A.** 5 GHz frequency image of the jets of Cygnus A made with data from the VLA. The jets extend out to kpc distances from the core. Figure from Carilli and Barthel (1996).

The presence of polarization in the radio emission in the jet of M87 (Baade and Minkowski, 1954) led to the correct conclusion that the mechanism responsible for it was synchrotron radiation (see Section 1.5.1). Astrophysical jets are now understood to be highly collimated plasma streams moving at high velocities. The observation of apparent superluminal motions in the jets of 3C 273 (Cohen et al., 1971) led to the understanding of the fact that the jet velocities are in fact relativistic, that is, close to the speed of light c (Rees, 1966, 1967). The observed flux from a blob of plasma moving at relativistic speeds $\beta = v/c$ and the intrinsic one are related by the relativistic Doppler factor,

$$\delta_D = \frac{1}{\gamma(1 - \beta \cos \theta)}, \quad (1.1)$$

where γ is the Lorentz factor $\gamma = \frac{1}{\sqrt{1-\beta^2}}$ and θ the observation angle.

The dependence on observation angle of the Doppler factor means that the observed properties of relativistic jets will be very different depending on the angle with respect to the jet motion and the line of sight. This initially led to the proposal of multiple source classes to explain the range of observations connected to the central regions of some galaxies, a phenomenon now referred to as Active Galactic Nuclei (AGN, Padovani, 2017; Padovani et al., 2017). A unified model (Urry and Padovani, 1995) was then proposed to identify the underlying AGN type that gives rise to different observed classes through different orientations. In this framework, a classification can be made based on the observation angle with respect to the jet axis, which leads to the distinction between blazars ($\theta < 10^\circ$) and radio galaxies ($\theta > 10^\circ$).

Jets observed in the center of galaxies were quickly linked to supermassive ($M > 10^6 M_\odot$) black holes (SMBH) thought to be hosted by these galaxies (Salpeter, 1964; Zel'dovich and Novikov, 1965). SMBH are surrounded by orbiting gas, which is being accreted onto them. Conservation of the angular momentum of this accreting matter leads to the formation of a disk around the black hole (Frank et al., 2002; Shakura and Sunyaev, 1973). It is in the innermost parts of this disk that jets are

thought to be launched. Due to its complexity, the exact process by which the accretion of matter into the black hole is turned into an outflow is not fully understood. However, observational evidence points to the fact that jets originate from sources in which such a disk is present, meaning that the accretion disk must play an important role in jet formation. Note, however, that not all sources with an accretion disk result in jets, such as the case of cataclysmic variables (see e.g. Robinson, 1976).

It is also understood that magnetic fields must play an important role in jet formation. The current models generally assume that the jets are accelerated and collimated via magnetohydrodynamical processes. There are a number of mechanisms proposed to explain the exact manner in which jets form (see e.g. Blandford and Znajek, 1977; Blandford and Payne, 1982; Pudritz and Norman, 1986, 1983, ...), a review of which is outside the scope of this thesis. More information on astrophysical jets and the physical processes associated to them can be found in e.g. Hughes (1991) and Young (2002).

Some of the uncertainty related to how jets are launched arises from the fact that it is extremely challenging for observations to resolve the very small regions around SMBH in which jets are thought to arise. The recent imaging of the region around the M87 black hole by the Event Horizon Telescope (E.H.T. Collaboration et al., 2019) thus marks a very important step in the progress to understand the details of jet formation and collimation mechanisms.

Due to the observational challenges, our current understanding of jet physics relies heavily on numerical simulations, in particular those that solve the magnetohydrodynamic equations for the special relativistic (Camenzind, 1986, 1987) or general relativistic case (see Porth et al., 2019, for a recent code comparison). Due to the complexity and the different scales involved, the issue of jet formation and propagation is usually split into separate problems (see e.g. Fendt, 2002), such as how to generate the necessary magnetic fields (see e.g. Sikora and Begelman, 2013; Liska et al., 2020), how to collimate and accelerate the accretion disk wind into a jet (see e.g. Fendt and Elstner, 1999; Fendt and Elstner, 2000) and the stability of the jet propagation (see e.g. Falle, 1991; Massaglia et al., 2016). A review of the status of numerical simulations of jets can be found in e.g. Komissarov and Porth (2021).

1.1.1 Jetted Sources in the Galaxy

Note that all of the jets mentioned above are associated to extragalactic sources, in particular, to the center of galaxies. The discovery that jets can also be produced on much smaller scales by Galactic objects took place much later than their extragalactic counterparts. The first source in which jets were observed was SS 433, the object which this thesis will focus on and which is described in detail in Chapter 2. Evidence for the presence of jets in SS 433 was discovered in 1979 (Margon et al., 1979b). The reason why these relatively local jets were only discovered so much later than the much more distant jets of AGN is that the accretion disks around SMBH

are colder than those around less massive black holes. This means that their emission peaks in the optical and UV ranges. Accretion disks around smaller compact objects are instead usually identified via their X-ray emission, and X-ray astronomy is comparatively younger.

While jets with terminal velocities in the order of a few hundred to a few thousand km/s can be found in a variety of stellar systems, such as Herbig-Haro objects (Schwartz, 1983), planetary nebulae (Lopez, 1997) or novae (Chomiuk et al., 2021), Galactic jets moving at relativistic velocities are almost exclusively found in compact binary systems. Such systems, also referred to as X-ray binaries (Verbunt, 1993), are composed of a compact object, such as a stellar-mass black hole or a neutron star, which is orbiting another body, usually a star (Fender, 2006). When a jet is present in such a binary system, it is referred to as a *microquasar*, as they mimic, on a smaller scale, some of the phenomena seen in quasars. This analogy is not only morphological, as it has been suggested that simple scaling laws related to the mass of the black hole govern the physics of the flows around them (Sams et al., 1996; Rees, 1998; Mirabel and Rodríguez, 1999).

The black holes in microquasars have masses of a few solar masses, millions of times smaller than the SMBH responsible for quasars. Because of this, the sizes and timescales associated with the jet emission are much smaller in microquasars. This, together with their relative proximity to Earth, makes observations of microquasars a much more accessible laboratory for the study of jet physics.

A few tens of microquasars are known to date¹. The majority of them are associated to a black hole, although there are some such systems where the compact object is a neutron star (e.g. KS 1731-260, see Barret et al., 1998; Massi, 2007). A further distinction can be made depending on if the jet is observed only during relatively short-lived flares, such as the case of Cygnus X-3 (Koljonen et al., 2018) or if it seems to be a persistent feature of the system, like in SS 433. Note that the first observations of a microquasar are only a few decades old, so the description of jets as persistent can only refer to such timescales.

Much like their extragalactic counterparts, microquasars are observed under a wide range of angles with respect to the jet axis. Some, like SS 433, have jets that are almost orthogonal to the line of sight, a situation analogous to that of radio galaxies. Other objects, such as the microquasar V4641 Sgr are thought to have a jet roughly aligned with the line of sight (Gallo et al., 2014), a phenomenon referred to as *microblazar*.

The jet velocities observed in microquasars range between a few percent of the speed of light to almost 90% of it for the case of V4641 Sgr (Hjellming et al., 2000). Similarly to AGN jets, superluminal motions have been observed in a number of microquasars, such as in GRS 1915+105 (Mirabel and Rodríguez, 1994) or V4641 Sgr (Hjellming et al., 2000). It was in fact the observation of superluminal

¹<http://www.aim.univ-paris7.fr/CHATY/Microquasars/microquasars.html>

motions in these nearby, Galactic sources that led to a breakthrough in the understanding of such motions for jets in general (Mirabel and Rodríguez, 1994, 1999). In extragalactic jets, only the approaching ejecta is usually imaged due to strong Doppler suppression of the receding jet. It was thus unclear whether the superluminal motions were due to the propagation of waves through a slowly moving jet, or were in fact associated to the bulk motion of the plasma emitting the observed radiation. It was through the observation of microquasars that the latter became apparent as the answer. This highlights the way in which, the understanding of nearby systems hosting jets can be extrapolated to interpret the observed phenomena in their much larger extragalactic counterparts.

A comprehensive review of the general properties of Galactic sources with jets can be found in Mirabel and Rodríguez (1999). The focus of this thesis is the observation of highly energetic gamma-ray radiation from microquasar jets, which has long been predicted (Aharonian and Atoyan, 1998). The only microquasar confirmed to be a source of TeV gamma-rays, and the focus of this thesis is the SS 433 system, a detailed overview of which is presented in Chapter 2.

1.2 Evidence of Particle Acceleration

The radiation produced by the thermal motions of particles in matter is referred to as *thermal* radiation. If the radiating body and its surface are in thermodynamic equilibrium, the spectral radiance of the emission at frequency ν is given by the black-body formula,

$$B_\nu(T) = \frac{2\nu^2}{c^2} \frac{h\nu}{e^{h\nu/kT} - 1} \quad (1.2)$$

where T is the temperature of the body and c , h and k the speed of light, Planck constant and Boltzmann constants respectively.

If the characteristics of the emitted radiation do not depend on the temperature of the source, the radiation is known as *non-thermal* radiation. Non-thermal radiation processes result in emission over the entire electromagnetic (EM) spectrum. However, certain frequency ranges are of particular importance when studying non-thermal radiation due to the fact that either only non-thermal processes can reach them - as the temperatures needed for the radiation to be thermal would be too high - or that the spectral signatures clearly distinguish them from thermal processes. That is the case for example of the radio regime, in which the observation of power-law spectra (that is, flux densities $F_\nu \propto \nu^{-\alpha}$ where $\alpha \approx 0 - 1$) in astrophysical jets reveals the presence of non-thermal physical processes, in particular synchrotron emission from relativistic electrons (see Section 1.5.1).

There are a number of processes that result in non-thermal emission. The ones that are most relevant for this thesis are those arising from particles such as electrons (or positrons, hereafter included in the term electron) or protons moving at relativistic speeds, which will be described in detail in Section 1.5.1. These processes require

the presence of particles with very high velocities, close to the speed of light. The fact that non-thermal radiation is observed in a variety of astrophysical sources (see e.g. Aharonian, 2004; Longair, 2011), and is in particular a common feature of astrophysical jets (e.g. Blandford et al., 2019; Matthews et al., 2020), requires the existence of a process capable of accelerating particles to these very high velocities.

Another crucial piece of evidence for the occurrence of particle acceleration in astrophysical sources is the measurement of the cosmic ray spectrum. The fact that there is a flux of charged energetic particles with extraterrestrial origin is known since 1912, when Victor Hess measured an increase in ionizing radiation as a function of altitude from the ground (Hess, 1912). Successive experiments (see Hörandel, 2013; Walter and Wolfendale, 2012, for summaries in English) were able to confirm the extraterrestrial origin of this radiation, correctly identify its nature as charged particles, and study their absorption by the atmosphere. These milestones, together with the development of new technology, marked the beginning of cosmic ray astronomy, a field which has seen already several generations of experiments, both ground-based (Castellina, 2017) and air or space borne (Marrocchesi, 2017).

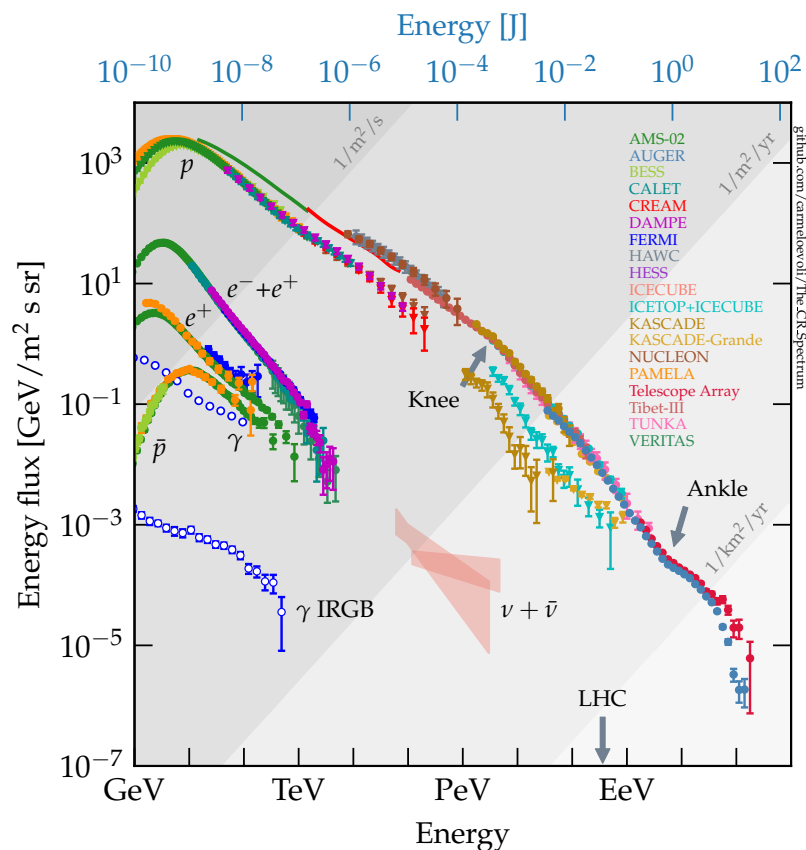


FIGURE 1.2: **The cosmic ray energy spectrum measured by several experiments.** The measured fluxes of electrons, gamma-rays and neutrinos are also shown. The spectral features described in the text are marked, as well as the particle rates expected for different level of flux. Figure by Carmelo Evoli, <https://doi.org/10.5281/zenodo.4396125>.

Note that the term cosmic rays is usually invoked to refer to hadronic charged particles, such as proton or higher mass atomic nuclei. However, there is also an astrophysical flux of electrons and positrons (see, e.g. Aharonian et al., 2008), usually referred to explicitly as cosmic ray electrons.

The cosmic ray spectrum spans more than twelve orders of magnitude in energy, which means that different instruments and experimental techniques are needed to cover the entirety of it. Figure 1.2 shows the cosmic-ray spectrum measured by a number of such experiments. The spectrum is remarkably smooth over many orders of magnitude, although not completely. Several spectral features are observed, which are interpreted as a result of differences in the production processes or astrophysical source classes involved, as well as a result of their propagation through space.

Low energy ($<10^9$ eV) cosmic rays are modulated by the Solar cycle, as the Sun's magnetic field shields the Solar system. At higher energies of around 10^{15} eV a spectral break, usually referred to as the *knee* can be seen. Below this energy, there are convincing physical arguments to suggest that particles are predominantly accelerated in supernova remnants (SNRs, see e.g. Bell et al., 2013; Vieu and Reville, 2022), though this theory currently lacks clear observational confirmation. At higher energies ($>5 \cdot 10^{18}$ eV), another spectral break, referred to as the *ankle* is observed. This is usually thought as marking the transition between Galactic and extragalactic origin of the cosmic rays (see, for example Drury, 2012 or Bell, 2013). For energies higher than this value, cosmic rays cannot be confined by a region the size of a galaxy for a reasonable magnetic field strength (see Equation 1.8), and thus are able to escape. At the highest energies, around 10^{20} eV, the flux finally tapers off. This could be the result of both an intrinsic cutoff in the spectra of cosmic ray sources, or the result of interaction of the cosmic rays with the Cosmic Microwave Background (CMB), an effect known as the Greisen–Zatsepin–Kuzmin cutoff (Greisen, 1966; Zatsepin and Kuz'min, 1966).

The existence of an astrophysical flux of charged particles spanning such a wide range of energies requires the existence of a physical process able to transfer large amounts of energy to the particles in an efficient manner. The remarkable smoothness of the cosmic ray spectrum over such a wide range of energies, which in turn translate into a wide range of physical sizes, could be a coincidence, or the result of relatively universal features in the particle acceleration over such scales. Note that the highest energies measured in cosmic rays, at around 10^{20} eV, are many orders of magnitude larger than those achieved in particle accelerating experiments built on Earth. It is thus only through the study of astrophysical objects that the processes responsible for such high energy particles can be studied.

1.3 Particle Acceleration

Particle acceleration mechanisms in astrophysical systems are an active area of research. In general terms, the proposed mechanisms can be divided into three classes (Longair, 2011):

- **Dynamic:** particles acquire energy through collisions with e.g. molecular clouds.
- **Hydrodynamic:** e.g. entire sheets of plasma are accelerated to high velocities.
- **Electromagnetic:** particles gain energy through interactions with electromagnetic fields such as in e.g. shocks.

Note that very often, these effects cannot be neatly disentangled and more than one would occur at the same time. For example, when considering charged particles, which will be the case through this section, the effects of electromagnetic fields usually need to be taken into account.

The movement of a particle with charge q , mass m and Lorentz factor γ moving with velocity \vec{v} in an electric (\vec{E}) and magnetic (\vec{B}) field can be written as

$$\frac{d}{dt}\gamma m\vec{v} = q(\vec{E} + \frac{\vec{v}}{c} \wedge \vec{B}). \quad (1.3)$$

Most astrophysical environments are made up of ionized gases, in which the very high electrical conductivity makes it hard to sustain static electric fields. Therefore, the electric field \vec{E} is usually simply $-\frac{\vec{u}}{c} \wedge \vec{B}$, where \vec{u} is the bulk velocity of the plasma.

1.3.1 General Considerations

For a particle being accelerated by an electric field, the change in kinetic energy $E_k = (\gamma - 1)mc^2$ is given by

$$\frac{dE_k}{dt} = \frac{d}{dt}(\gamma - 1)mc^2 = q\vec{v} \cdot \vec{E}, \quad (1.4)$$

which can be solved for E_k as

$$E_k = E_{k,0} + q \int \vec{E} \cdot d\vec{l}, \quad (1.5)$$

where $d\vec{l} = \vec{v}dt$. Taking $\vec{E} = -\frac{\vec{u}}{c} \wedge \vec{B}$, it follows that

$$E_k < q \frac{|\vec{u}|}{c} |\vec{B}| R = E_H, \quad (1.6)$$

where R is the size of the acceleration region. This limit on the maximum energy, E_H , achievable by a particle being accelerated in a region of size R with a magnetic field \vec{B} is usually referred to as the *Hillas condition* (Hillas, 1984).

In a uniform magnetic field, the $\vec{v} \wedge \vec{B}$ term in Equation 1.3 leads to circular motion, with the acceleration perpendicular to both the velocity of the particle and the direction of the magnetic field. This gyration has an angular frequency given by the Larmor frequency,

$$\omega_L = \frac{q|\vec{B}|}{\gamma mc} \quad (1.7)$$

and a gyroradius (or Larmor radius) of

$$r_g = \frac{|\vec{v}_\perp|}{\omega_L} = \frac{|\vec{v}| \sin \theta}{\omega_L} = \frac{\gamma mc |\vec{v}| \sin \theta}{q|\vec{B}|} \simeq \frac{|\vec{p}|c}{q|\vec{B}|} \quad (1.8)$$

where θ is the angle between \vec{v} and the direction of the magnetic field, taken here for simplicity to be 90° and $|\vec{p}| = \gamma m |\vec{v}|$ is the momentum of the particle.

Note that if $u = c$, then Equation 1.6 becomes equivalent to $r_g < R$, as the acceleration region must be larger than the gyroradius for the particle to be confined to it. However, this distinction is relevant, since for most of the acceleration processes discussed here, $u < c$.

The application of the Hillas condition to possible acceleration sites for different values of $\beta = \frac{u}{c}$ can be summarized with a so-called *Hillas plot*, such as the one shown in Figure 1.3.

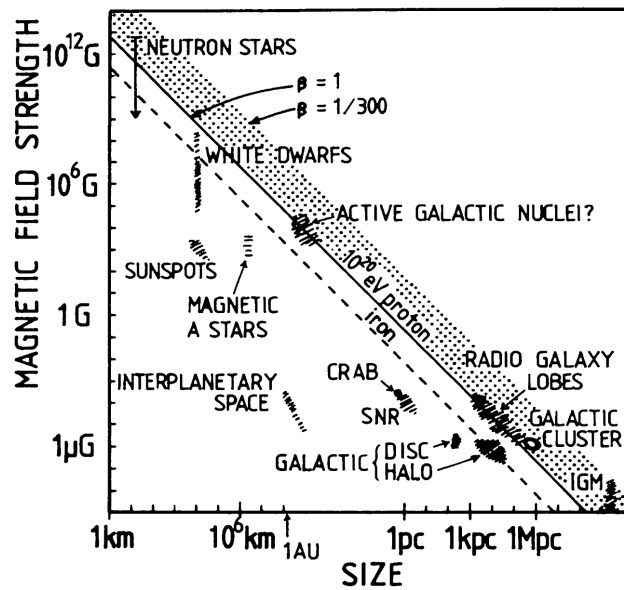


FIGURE 1.3: **The Hillas condition.** Size and magnetic field strength of possible sites of particle acceleration. The diagonal represents the boundary below which objects can't accelerate protons to 10^{20} eV. Figure from Hillas (1984).

1.3.2 Particle Acceleration Mechanisms

An early attempt to explain the power-law spectral shape of the cosmic ray spectrum (see Figure 1.2) was made by Fermi (Fermi, 1949), who proposed a mechanism in

which particles gain energy in collisions with magnetized high-velocity clouds moving with velocities V . In each of these collisions, the particles gain or lose a fraction proportional to $\pm V/c$ of their energy. In general, there is a net energy gain due to the fact that head-on collisions are more likely. This process can be understood as the particles trying to come to thermal equilibrium with the clouds. Given the considerably larger masses of the clouds, even if their motions are not very fast, there is a large amount of energy for the particles to tap into by interacting with them.

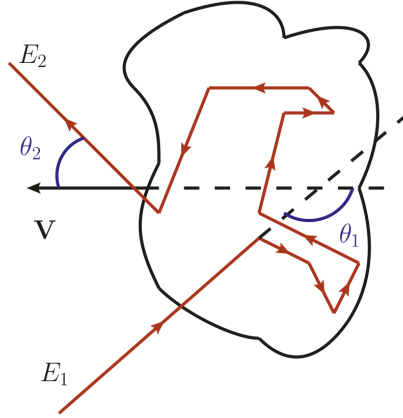


FIGURE 1.4: **Schematic depiction of second-order Fermi acceleration.** A particle with energy E_1 enters a magnetized cloud, which results in it undergoing several scatterings until it leaves, with a new trajectory θ_2 and energy E_2 . Figure by Cosimo Nigro (Nigro, 2019).

The energy gain averaged over many collisions can be derived through a series of reference frame transformations (e.g. Longair, 2011) and is written as

$$\left\langle \frac{\Delta E}{E} \right\rangle = \frac{8}{3} \left(\frac{V}{c} \right)^2. \quad (1.9)$$

The Fermi acceleration mechanism attracted early attention due to the fact that it can, in certain situations, result in a power-law energy spectrum. This is obtained by solving the diffusion-loss equation governing the evolution of a particle population $N(E)$:

$$\frac{dN}{dt} = D\nabla^2 N + \frac{\partial}{\partial E} (b(E)N(E)) + Q(E), \quad (1.10)$$

where $b(E) = -\frac{dE}{dt}$ is the energy gain term, which we write as $b(E) = -\alpha E$ (see Equation 1.9) and the source term $Q(E)$ is taken to be null far from injection energies. For a single-zone model, we can replace the spatial diffusion by $D\nabla^2 N = -\frac{N}{\tau_{esc}}$, where τ_{esc} is the timescale in which the particles escape the acceleration region. The steady-state ($\frac{dN}{dt} = 0$) version of Equation 1.10 is then given by

$$\frac{dN(E)}{dE} = - \left(1 + \frac{1}{\alpha\tau_{esc}} \right) \frac{N(E)}{E}, \quad (1.11)$$

which has as solution $N(E) \propto E^{-x}$ with $x = 1 + 1/(\alpha\tau_{esc})$. This expression results

in a power-law if both the loss and escape terms have the same dependence on the particle energy.

There are a number of problems with this mechanism, one of them being that the velocities of clouds in the Galaxy are actually rather small compared to the speed of light. Additionally, these collisions are not very frequent, in the order of a few per year, meaning the acceleration is slow (see Equation 1.19). That is why, subsequent proposals considered instead scattering off of magnetic waves (e.g. Melrose, 1980)s, in which case u_c would be replaced by the Alfvén speed $v_A = B/\sqrt{4\pi\rho}$. Finally, there is no a priori reason why the power-law exponent x should be between 2-3 as required by observations. In order to achieve a similar cosmic ray spectrum in different sources, one would need the escape time to be finely tuned to the energy gain rate, including their respective dependence on particle energy. This contrasts with other mechanisms such as particle acceleration in shocks, detailed in Section 1.4, which naturally gives rise to $x \approx 2$ (Bell, 1978a).

Another mechanism that has recently gained a lot of attention, particularly in jets, is magnetic reconnection. The basic idea behind it is that the locations where magnetic field lines of opposing polarity approach each other and meet could result in the transfer of magnetic energy to particles. Reviews on the topic can be found in e.g. Hoshino and Lyubarsky (2012) and Kagan et al. (2015).

Shear acceleration is another mechanism proposed to occur in jets in which particles scatter across a shear layer such as that at the edge of a jet (e.g. Rieger and Duffy, 2004). Magnetic kink instabilities can also result in particle distributions that follow a power-law (Alves et al., 2018). More details on the acceleration of particles in astrophysical jets can be found in Matthews et al. (2020) and references therein.

1.4 Particle Acceleration in Shocks

We will cover the acceleration of particles in astrophysical shocks with some more detail due to its relevance to further topics in the thesis (see Chapter 7). A shock wave or shock is a propagating discontinuity in the pressure, temperature, velocity and density of a medium which moves faster than the speed of sound. There are several mechanisms proposed for how particles could be accelerated in shocks, see Marcowith et al. (2016) for a review. Here we will focus on diffusive shock acceleration (DSA, Axford et al., 1977; Krymskii, 1977; Blandford and Ostriker, 1978; Bell, 1978a,b), in which particles gain energy by diffusing across the shock multiple times. There are several excellent reviews on the topic of particle acceleration in shocks (e.g. Drury, 1983; Blandford and Eichler, 1987; Bell, 2013, 2014...). In this section we will describe some of the basic aspects of particle acceleration in shocks and refer to the literature for further details. The discussion presented here largely follows that of Longair (2011), Bell (1978a) and Drury (1983).

Let us formulate the Fermi acceleration mechanism described in Section 1.3.2 in a slightly different way. Given a population of N_0 particles in an acceleration region,

we write the energy of a particle with initial energy E_0 after one cycle as βE_0 and define the probability of said particle to remain in the acceleration region after the collision as P . The fractional energy gain is related to β as $\beta = \frac{\Delta E}{E} + 1$. Then, after a number k of cycles, the number of particles inside the acceleration region is $N = N_0 P^k$, and their energies $E = E_0 \beta^k$. We can combine these two expressions into

$$\frac{N}{N_0} = \left(\frac{E}{E_0} \right)^{\ln P / \ln \beta}. \quad (1.12)$$

And thus we can write

$$\frac{dN}{dE} dE \propto E^{(\ln P / \ln \beta) - 1} dE. \quad (1.13)$$

Evidently, the term $(\ln P / \ln \beta)$ in Equation 1.13 is equivalent to the quantity $-(\alpha \tau_{esc})^{-1}$ introduced in Section 1.3.2, with P being related to the escape timescale and β to the energy gain α .

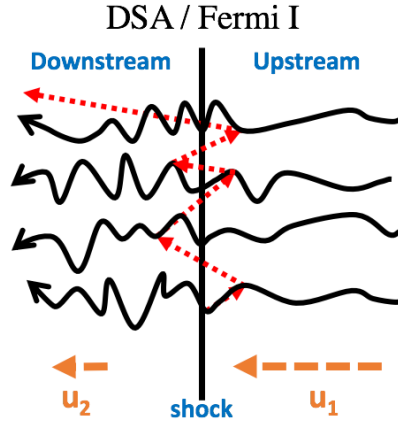


FIGURE 1.5: **Schematic depiction of shock acceleration.** Bulk velocities in the rest frame of the shock are shown with orange dashed lines, particle trajectories in red dashed lines and magnetic field lines as black arrows. Figure from Matthews et al. (2020).

Let us now consider a non-relativistic parallel shock moving with velocity \vec{u}_s along the magnetic field lines (see Figure 1.5). The shock velocity is supersonic, meaning $|\vec{u}_s| \gg c_s$ where c_s is the speed of sound in the ambient medium. We will restrict the discussion to those particles (either electrons or protons) whose energy is already high enough for their gyroradius (see Equation 1.8) to be larger than the shock thickness, and thus are capable to freely move between the upstream and downstream regions. In the upstream region there is turbulence in the form of Alfvén waves excited by the particles themselves. These waves scatter the particles, leading to them being overtaken by the shock. As a result particles are capable of crossing the shock many times and thus increase their energy more than once.

It is often useful to consider the frame of reference in which the shock is at rest. In this frame, the upstream gas is flowing into the shock with a velocity $u_1 = u_s$

and leaving the shock with a velocity u_2 . These two velocities are connected via the continuity equation

$$\rho_1 u_1 = \rho_1 u_s = \rho_2 u_2, \quad (1.14)$$

where ρ_1 and ρ_2 are the densities of the upstream and downstream regions respectively. For a strong shock the ratio of densities is given by the *compression ratio* $\chi = \rho_2/\rho_1 = (\Gamma + 1)/(\Gamma - 1)$ where Γ is the heat capacity ratio or adiabatic index of the gas. For the case of a monoatomic or fully ionized gas, $\Gamma = 5/3$, which means $u_1 = 4u_2$.

The particles ahead of the shock are approximately isotropic in the frame of reference of the ambient gas due to scattering on magnetic fluctuations. The shock advances through this medium with velocity u_s , and when a particle crosses the shock front, it increases its energy by $\Delta E/E \sim u_s/c$. After crossing the shock, particles are again scattered so that their velocity distribution is once more isotropic with respect to the flow, and so when they cross the shock again they encounter the upstream gas moving towards the shock, again with the same velocity, leading to the same increase in energy. This means that every time a particle crosses the shock, it gains energy, unlike in the cloud collision scenario (see Section 1.3.2) in which some collisions lead to an energy loss. The energy gain after a cycle of a particle moving with velocity $v \approx c$ can be derived (see e.g. Bell, 1978a; Drury, 1983) and is

$$\beta - 1 = \frac{\Delta E}{E} = \frac{4}{3} \frac{u_1 - u_2}{c}. \quad (1.15)$$

The probability of a particle completing a cycle is given by

$$P = 1 - \frac{4u_2}{c}. \quad (1.16)$$

And thus, following Equation 1.13, the resulting differential energy spectrum is

$$\frac{dN}{dE} dE \propto E^{-\mu} dE, \quad (1.17)$$

where

$$\mu = \frac{2u_2 + u_1}{u_1 - u_2}. \quad (1.18)$$

For a strong shock with Mach number $M = \frac{u_s}{c_s} \gg 1$ and $\chi = 4$, the power-law exponent is $\mu = 2$. This result arises naturally from the properties of shock acceleration and does not require any fine-tuning, as was the case with the Fermi acceleration mechanism described in Section 1.3.2.

Since the proposal of shock acceleration in the 1970s, there have been numerous improvements to the theory that expand it beyond the relatively simple description presented above. Such examples include non-linear effects (see e.g. Malkov and Drury, 2001) or the effect of relativistic shock velocities (see e.g. Kirk et al., 2000). These expansions are outside of the scope of this thesis..

1.4.1 Acceleration Timescale

The acceleration timescale is a combination of the *cycle* time intrinsic to the acceleration process such as the time between collisions, or crossing time for shock acceleration, and the energy gain per cycle. This is written as

$$t_{\text{acc}} = \frac{E}{\Delta E} t_{\text{cycle}}. \quad (1.19)$$

The acceleration timescale needs to be fast enough to compete with energy losses (see Section 1.5) in order to result in net particle acceleration. In the case of shock acceleration, the mean time it takes for a relativistic particle to complete one cycle of entering the downstream region, returning upstream and then returning to the downstream region is given by (Drury, 1983)

$$t_{\text{cycle}} = \frac{4}{c} \left(\frac{D_1}{u_1} + \frac{D_2}{u_2} \right), \quad (1.20)$$

where D_1 and D_2 are the diffusion coefficients in the upstream and downstream regions respectively. It follows from Equation 1.19 that the acceleration timescale for DSA is thus

$$t_{\text{acc}} = \frac{3}{u_1 - u_2} \left(\frac{D_1}{u_1} + \frac{D_2}{u_2} \right). \quad (1.21)$$

Note that the diffusion coefficients depend on particle energy, and so does the acceleration timescale.

1.4.2 Diffusion

The diffusion coefficients in the upstream and downstream media are generally subject to high uncertainty in most applications to astrophysical sources. It is thus often useful to parameterize the diffusion coefficient in terms of the Bohm diffusion coefficient $D_B(E)$ (e.g. Lagage and Cesarsky, 1983; Aharonian, 2004), which represents a lower limit for the diffusion coefficient for magnetized particles, i.e. particles moving in helical trajectories. In the Bohm diffusion scenario, the particle mean free path λ is assumed to be equal to the gyroradius (see Equation 1.8). The diffusion coefficient for particles moving at speeds close to the speed of light c can thus be written as

$$D(E) = \frac{1}{3} \lambda c = \frac{1}{3\eta} r_g c = \frac{D_B(E)}{\eta}, \quad (1.22)$$

where $\eta \leq 1$ parameterizes how far the diffusion occurs from the Bohm regime. If $\eta = 1$, the diffusion coefficient is the smallest possible for magnetized transport and thus the acceleration time is the shortest possible.

1.5 Energy Losses

Acceleration processes that increase the energy of particles are competing with a number of mechanisms that reduce their energy. In order to determine the net energy gain of a particle it is thus necessary to compare their effects. Additionally, some of these processes result in the emission of non-thermal emission, which can in turn be used to infer the properties of the emitting particle population. Which mechanisms dominate the energy loss depends on both particle energy and the properties of the medium. In this section we will cover some aspects of the energy loss mechanisms that are most relevant to the work presented in this thesis, neglecting those that only contribute a negligible amount to the physical scenarios considered. A general overview of energy losses for high energy particles can be found in e.g. Longair (2011).

In order to characterize the energy loss, and also to compare the effect of acceleration to the losses, a useful quantity to define is the loss timescale,

$$t_{\text{loss}} = \frac{E}{|dE/dt|} \quad (1.23)$$

defined as the ratio of the particle energy to the energy loss rate.

1.5.1 Radiative Losses

Some energy loss mechanisms result in the emission of non-thermal radiation. These processes are relevant not only as a competing mechanism to the acceleration, but also because this radiation becomes an observable that can be used to investigate the presence and properties of the accelerated particles. We will focus on the two processes that will be of most relevance to the rest of this thesis, synchrotron emission and inverse Compton scattering, with a brief mention of the emission processes associated with particles of hadronic nature.

Synchrotron Radiation

A relativistic charged particle that is accelerated by the Lorentz force (see Equation 1.3) will produce synchrotron radiation (Blumenthal and Gould, 1970). The properties of synchrotron radiation can be derived using the expression of the power emitted by a relativistic particle with Lorentz factor γ and charge q moving with an acceleration a , typically referred to as Larmor's formula. A derivation of this expression can be found in, e.g. Longair (2011).

$$P = \left(\frac{dE}{dt} \right) = \frac{2}{3} \frac{q^2 \gamma^4}{c^3} (a_{\perp}^2 + \gamma^2 a_{\parallel}^2) \quad (1.24)$$

Note that the parallel (a_{\parallel}) and perpendicular (a_{\perp}) components of the acceleration are defined with respect to the direction of motion.

A charged particle in the presence of a regular magnetic field describes a rotating motion describing a spiral path with a pitch angle θ , governed by the expressions introduced in Section 1.3. For gyrating motion $a_{\parallel} = 0$ and $a_{\perp} = w_L v_{\perp}$ where $v_{\perp} = v \sin \theta$ and w_L is the Larmor frequency defined in Equation 1.7. Inserting these into the equation above results in

$$P_{\text{synch}} = \frac{2}{3} \frac{q^2 \gamma^4}{c} \frac{v_{\perp}^2 q^2 B^2}{\gamma^2 m^2 c^2} = \frac{2}{3} \frac{\beta^2 q^4 B^2}{m^2 c^3} \gamma^2 \sin^2 \theta, \quad (1.25)$$

where $\beta = v/c$.

Assuming an isotropic distribution for the pitch angle we can derive its average as

$$\langle \sin^2 \theta \rangle = \frac{1}{4\pi} \int_0^{4\pi} \sin^2 \theta d\Omega = \frac{2}{3}, \quad (1.26)$$

where $d\Omega$ is the solid angle differential. Now, recalling the definition of the Thomson cross-section $\sigma_T = \frac{8\pi}{3} \left(\frac{q^2}{m_e c^2} \right)^2$ and defining the magnetic energy density $u_B = \frac{B^2}{8\pi}$ we can write the expression for the average synchrotron power emitted by a single particle as

$$\langle P_{\text{synch}} \rangle = \frac{4}{3} \gamma^2 c \sigma_T \left(\frac{m_e}{m} \right)^2 u_b. \quad (1.27)$$

The term $\left(\frac{m_e}{m} \right)^2$ heavily suppresses the radiation of particles with larger mass than electrons, such as protons.

The synchrotron cooling timescale can now be derived using Equation 1.23 as

$$t_{\text{synch}} = \frac{E}{|\langle P_{\text{synch}} \rangle|} = \frac{\gamma m c^2}{\frac{4}{3} \gamma^2 c \sigma_T \left(\frac{m_e}{m} \right)^2 u_b} \propto \frac{1}{\gamma B^2}, \quad (1.28)$$

which implies that high magnetic field intensities lead to faster synchrotron cooling, and that higher energy particles cool faster than low energy ones.

The radiation spectrum of a single particle emitting synchrotron radiation peaks around a critical frequency $\nu_c = \frac{3}{4\pi} \gamma^2 \frac{qB}{mc} \sin \theta$ (e.g. Blumenthal and Gould, 1970). From the spectra of a single particle, that of a population can be obtained by integrating over the entire electron distribution. Following the discussion in Section 1.2, we expect the spectral distribution of accelerated electrons to follow a power-law. The synchrotron radiation emitted by electrons distributed as $\frac{dN_e}{dE_e} \propto E_e^{-\alpha}$ is also a power-law, the index of which can be derived as

$$E_{\gamma} \frac{dN_{\gamma}}{dE_{\gamma} dt} = \frac{dN_e}{dE_e} \frac{dE_e}{dE_{\gamma}} \frac{dE_{\gamma}}{dt} \propto E_e^{-\alpha} \cdot \frac{1}{E_e} \cdot E_e^2 \propto E_e^{1-\alpha}, \quad (1.29)$$

where we have used the fact that $E_{\gamma} = h\nu_c \propto E_e^2$ and Equation 1.27. Therefore, the photon spectrum has a shape

$$\frac{dN_{\gamma}}{dE_{\gamma} dt} \propto E_{\gamma}^{-(\alpha+1)/2}. \quad (1.30)$$

Note that this derivation is an approximation, but it agrees with the result of the full calculation (see e.g. Blumenthal and Gould, 1970).

Figure 1.6 shows the synchrotron spectrum radiated by a population of electrons with power-law index $\alpha = 2$. The radiation spectrum has been computed using the GAMERA package (Hahn, 2015; Hahn et al., 2022) for different magnetic field intensities. GAMERA can calculate the spectral evolution of a particle population in the presence of time-dependent or constant injection, energy losses and particle escape. It can also derive the radiation spectrum from a parent particle population. As expected, the resulting photon spectrum follows a power-law with index $(\alpha + 1)/2 = 1.5$.

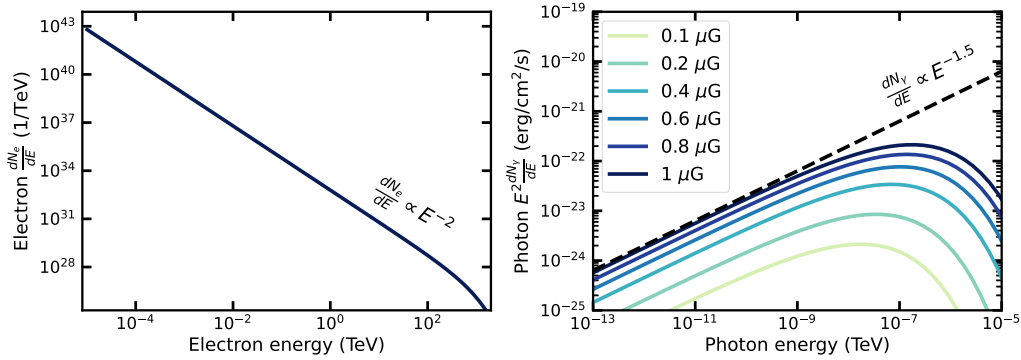


FIGURE 1.6: **Synchrotron radiation from electrons.** **Left:** Spectrum of the electrons producing the radiation. The normalization is such that the total energy above 10 MeV is 10^{33} erg. **Right:** Resulting synchrotron radiation spectrum for different intensities of the magnetic field. Note that the quantity depicted is $E^2 \frac{dN}{dE}$.

Inverse Compton Scattering

When relativistic electrons encounter and scatter comparatively low energy ambient photons, they lose part of their energy and increase that of the photons (Jones, 1968; Blumenthal and Gould, 1970). This is referred to as inverse Compton (IC) because, unlike in the classical Compton scattering case, it is the electron which loses energy and not the photon. Depending on the energy of the target photons ($h\nu$), two regimes are distinguished:

- Thomson scattering ($h\nu \ll m_e c^2$): the scattering is almost elastic, meaning that the change in electron energy is not very large. This process is described by the Thomson cross-section defined in Section 1.5.1.
- Klein-Nishina scattering ($h\nu > m_e c^2$): in this case the scattering is inelastic, meaning that the transfer of energy is large. The Thomson cross-section no longer applies, and the correct one needs to be derived using quantum electrodynamics (Klein and Nishina, 1929).

In the Thomson regime and in the electron rest frame (indicated with a prime symbol), the total power emitted by an electron exposed to some photon field is

given by (e.g. Longair, 2011):

$$\left(\frac{dE}{dt}\right)'_{tot} = \sigma_T c u'_{rad}, \quad (1.31)$$

where u'_{rad} is the ambient radiation energy density in the electron rest frame.

Now using the fact that the emitted power is an invariant quantity, $\left(\frac{dE}{dt}\right)' = \left(\frac{dE}{dt}\right)$ and that for an isotropic radiation field

$$u'_{rad} = \gamma^2 \left(1 + \frac{\beta^2}{3}\right) u_{rad}, \quad (1.32)$$

where γ and β are the Lorentz factor and velocity of the electrons. We can derive the angle-averaged scattered power in the interaction as

$$\frac{dE}{dt}_{tot} = \sigma_T c \gamma^2 \left(1 + \frac{\beta^2}{3}\right) u_{rad}. \quad (1.33)$$

Now, in order to derive the energy loss rate of the electron, we need to subtract the initial energy of the low-energy photons $\sigma_T c u_{rad}$ which results in

$$\langle P_{IC} \rangle = \frac{dE}{dt} = -\frac{4}{3} \gamma^2 \beta^2 \sigma_T c u_{rad}. \quad (1.34)$$

This expression is only valid in the Thomson regime. For the Klein-Nishina case, the cross-section needs to be modified (see e.g. Blumenthal and Gould, 1970).

We can now derive the cooling timescale for IC in the Thomson regime using Equation 1.23 as

$$t_{IC} = \frac{E}{|\langle P_{IC} \rangle|} = \frac{E}{\frac{4}{3} \gamma^2 \beta^2 \sigma_T c u_{rad}} \propto \frac{1}{\gamma u_{rad}}, \quad (1.35)$$

which implies that, analogously to the synchrotron case, high target radiation densities lead to faster cooling, and that higher energy particles lose their energy faster than low energy ones.

In order to illustrate the IC spectrum, we again use the GAMERA code, which includes the full Klein-Nishina calculation, to calculate the IC emission from electrons distributed as $\propto E^{-2}$. We consider as target photon fields a thermal black-body spectrum (see Equation 1.2) for different values of the temperature. The resulting photon spectra can be seen in Figure 1.7.

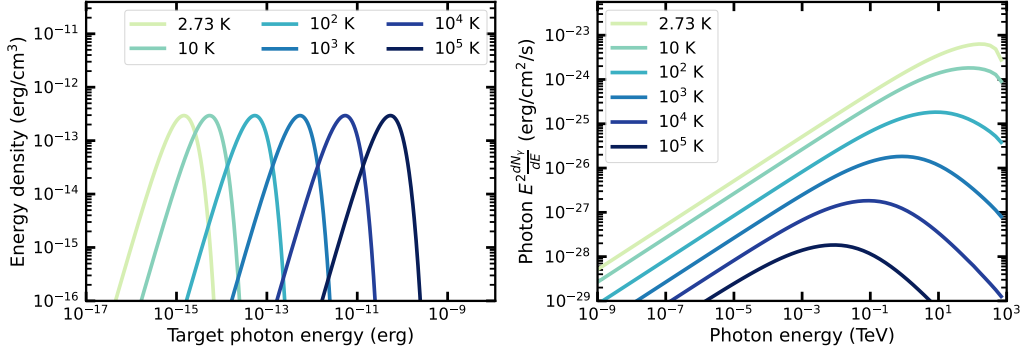


FIGURE 1.7: **IC radiation from electrons.** **Left:** Energy density of the target blackbody photons for different temperatures. **Right:** Resulting IC radiation spectrum for the different target fields. The electron spectrum is the same as shown in Figure 1.6.

Hadronic Processes

Although the IC scattering and synchrotron emission of protons are inefficient due to their higher mass compared to electrons, very high energy protons can interact with both radiation fields and ambient matter through hadronic processes. Inelastic interactions of protons with radiation fields ($p\gamma$ interactions) have a relatively low cross-section but can be important in situations where the ambient mass density is very low, such as for example AGN jets (see e.g. Mannheim and Biermann, 1989; Mücke et al., 2000).

Interactions of protons with target matter (pp interactions, Aharonian, 2004) also result in the production of pions, which decay to produce gamma-rays, electron-positron pairs and neutrinos. gamma-rays are emitted with energies $\approx 1/6$ times that of the parent protons. The total gamma-ray emission rate is proportional to the ambient density (see e.g. Kelner et al., 2006; Kafexhiu et al., 2014), which means that relatively dense targets are required in order to produce significant photon emission. Additionally, the spatial distribution of the emission will then follow that of the targets, which are *illuminated* by their interaction with the protons (see e.g. Abdo et al., 2009, 2010). Note that the energy dependence of the pp cross-section is logarithmic, and so the cooling time of protons via pp interaction has a weak dependence of energy, which can be approximated as constant over relatively small energy ranges. In particular, for very high proton energies, the pp cooling timescale in units of years can be approximated by

$$t_{pp} \approx \frac{5.3 \cdot 10^7}{n}, \quad (1.36)$$

where n is the target number density in units of cm^{-3} (Aharonian, 2004). More details on hadronic processes can be found in e.g. Aharonian (2004).

1.5.2 Adiabatic Losses

Besides by emitting radiation, particles can also lose their energy if they are confined within an expanding volume. The energy loss rate due to adiabatic expansion is related to the velocity of said expansion, \vec{v}_{exp} . For a relativistic gas we have (e.g. Longair, 2011):

$$\frac{dE}{dt} = -\frac{1}{3}(\nabla \cdot \vec{v}_{\text{exp}})E. \quad (1.37)$$

The $\nabla \cdot \vec{v}_{\text{exp}}$ term can be connected to the density of the expanding gas via the continuity equation

$$\frac{\partial \rho}{\partial t} + \nabla \cdot (\rho \vec{v}_{\text{exp}}) = 0, \quad (1.38)$$

which expands into

$$\frac{\partial \rho}{\partial t} + \vec{v}_{\text{exp}} \cdot \nabla \rho = -\rho(\nabla \cdot \vec{v}_{\text{exp}}). \quad (1.39)$$

Recalling the definition of the convective derivative $\frac{d}{dt} = \frac{\partial}{\partial t} + v \cdot \nabla$, we can write,

$$\frac{1}{\rho} \frac{d\rho}{dt} = -(\nabla \cdot \vec{v}_{\text{exp}}). \quad (1.40)$$

And so the adiabatic loss rate can be written as a function of the fluid density,

$$\frac{dE}{dt} = -\frac{1}{3} \left(\frac{1}{\rho} \frac{d\rho}{dt} \right) E. \quad (1.41)$$

In the case of a ballistic jet, $\rho \propto z^{-2}$ where z is the coordinate along the jet axis. Defining the jet velocity along the axis as $v_{\text{jet}}(z) = \frac{dz}{dt}$ we can write

$$\frac{1}{\rho} \frac{d\rho}{dt} = -2 \frac{v_{\text{jet}}(z)}{z}, \quad (1.42)$$

and so the energy loss rate is simply

$$\frac{dE}{dt} = -\frac{2}{3} \frac{v_{\text{jet}}(z)}{z} E. \quad (1.43)$$

The cooling timescale for adiabatic losses in an expanding jet is thus

$$t_{\text{ad}} = \frac{E}{|dE/dt|} = \frac{E}{\frac{1}{3}(\nabla \cdot \vec{v}_{\text{exp}})E} = \frac{3}{\nabla \cdot \vec{v}_{\text{exp}}(z)} = -\frac{3}{2} \frac{z}{v_{\text{jet}}}, \quad (1.44)$$

which is independent of the particle energy.

1.6 Summary and Outlook

This chapter presented a brief overview of the non-thermal processes most relevant to this thesis, as well as an introduction to the phenomenon of astrophysical jets. The topic of the following chapter is one of the most studied jetted sources in the

Galaxy, the microquasar SS 433. The discovery of non-thermal X-ray and gamma-ray emission from its jets (see Section 2.3) indicates that particle acceleration is taking place somewhere in the system. The dedicated gamma-ray band observations of the SS 433 region presented in Chapter 6 of this thesis will allow for a characterization of the acceleration sites and non-thermal radiative processes in the jets of SS 433, the details of which will be discussed in Chapter 7.

Chapter 2

The Microquasar SS 433

The microquasar system SS 433 provides a unique opportunity to study collimated mildly relativistic jets in our own Galaxy. While much is known about the nature of the precessing inner jets, the dynamics at large distances from the central binary system are poorly constrained. This chapter summarizes the existing observational data across the EM spectrum, as well as some of the theoretical models which have been proposed to explain the dynamics and emission mechanisms in SS 433. As it is the focus of this thesis, special attention is given to the non-thermal emission of the outer jets. More general descriptions of the system, such as a detailed review of early observations of SS 433 or a thorough examination of the properties of the jets and accretion disk of SS 433 can be found in Margon (1984) and Fabrika (2004) respectively.

2.1 First Detection and Identification

The detection of the microquasar SS 433 was first reported in 1977 by Stephenson and Sanduleak in their catalog of stars with bright H α line emission (Stephenson and Sanduleak, 1977). Soon after, a bright variable X-ray source was reported at a consistent location (Clark and Murdin, 1978; Marshall et al., 1978), suggesting a more unusual nature for the source. Measurements of the optical spectra revealed variable lines, which were identified by Margon et al. (1979b) as the spectra of Hydrogen and Helium shifted by positive and negative velocities of thousands of km/s. These puzzling features were quickly identified as arising from the observation of two precessing, oppositely directed jets of gas moving at speeds of around 25% of the speed of light (Abell and Margon, 1979; Fabian and Rees, 1979; Milgrom, 1979; Margon et al., 1979a). This paradigm is usually referred to as the "kinematic model" for SS 433.

2.2 Overview of the SS 433 System

SS 433 is a binary stellar system composed of a compact object, likely a black hole (Seifina and Titarchuk, 2010; Cherepashchuk et al., 2019, 2021), and a type A supergiant star (Gies et al., 2002; Hillwig and Gies, 2008). These systems are usually characterized by X-ray emission produced by accretion from the donor star into the compact

object, and so are referred to as X-ray binaries (see Section 1.1.1). SS 433 stands out among other X-ray binaries because the accretion onto the compact object occurs with a very large ($10^{-3} - 10^{-4} M_{\odot}/\text{yr}$) mass transfer rate, as opposed to the much lower values ($< 10^{-8} M_{\odot}/\text{yr}$) usually found in other systems (Shkrovskii, 1981; Heuvel, 1981). This high accretion rate seems to be maintained continuously for as long as the system has been observed, unlike in other systems, which have been observed to reach high mass transfer rates but only during short-lived flares (Fabrika, 2004).

As a consequence of the accretion, two symmetric jets are launched from the central engine, oriented almost perpendicular at $\sim 80^{\circ}$ (Roberts et al., 2010) with respect to the line of sight, making the SS 433 system a microquasar (see Section 1.1.1). The jets are launched with a velocity usually taken to be $0.26c$, although speeds in the range between 0.24 - $0.32c$ have been observed (Blundell and Bowler, 2004; Blundell et al., 2007), with the highest speeds connected to episodic flares (Jeffrey et al., 2016). The jets describe a precession motion with an half-opening angle of 20° with a period of 162 days (Fabian and Rees, 1979; Milgrom, 1979; Margon et al., 1979b; Hjellming and Johnston, 1981; Fabrika, 2004). The jet kinetic power is estimated to be $\sim 10^{39} \text{erg/s}$ (e.g. Margon, 1982).

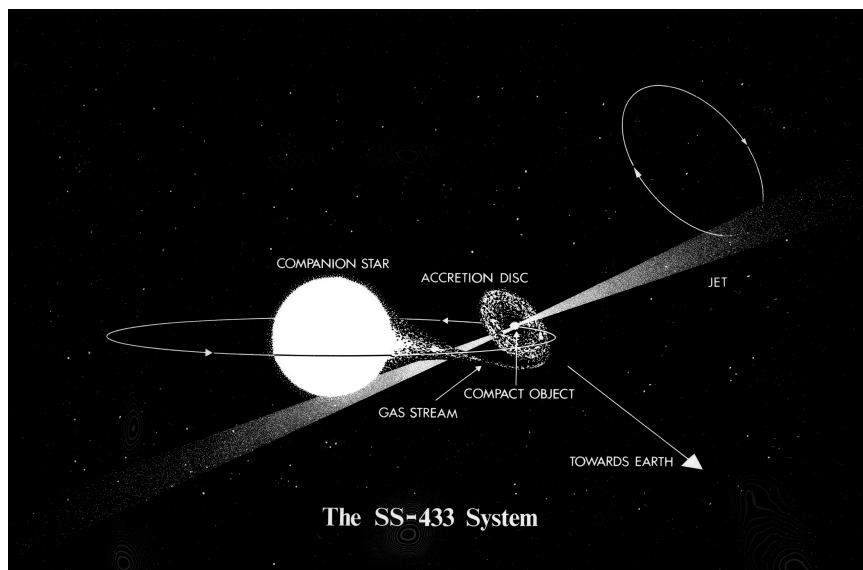


FIGURE 2.1: **The SS 433 system.** Schematic diagram showing the main components of the SS 433 system. Image credit: European Southern Observatory (ESO).

The distance to SS 433 is usually accepted to be 5.5 kpc (Blundell and Bowler, 2004), although smaller estimates such as 4.7 kpc (Rosado et al., 2021) exist. The lowest existing estimate comes from the analysis of astrometric data, which suggests a distance of 3.8 kpc (Arnason et al., 2021). However, note that this estimate is considered less reliable because of the binary orbital motion in SS 433.

Assuming a distance of 5.5 kpc, as we will through this thesis, optical and radio observations see these precessing jets extend only out to distances of $\sim 10^{-3}$ (Davidson and McCray, 1980) and ~ 0.1 pc (Spencer, 1979; Blundell and Bowler, 2004) from

the core respectively. Further out, no emission from the jet is detected until distances of around 25 pc from the compact object, where X-ray observations reveal comparatively large-scale outer jets (see Figure 2.2) which, in contrast to the inner jets, are bright non-thermal X-ray emitters (Brinkmann et al., 1996; Safi-Harb and Ögelman, 1997; Safi-Harb et al., 2022; Kayama et al., 2022). The outer jets are usually distinguished by referring to the one extending towards increasing values of the right ascension coordinate as the *eastern* jet, whereas the one extending towards decreasing values is referred to as the *western* jet (see Figure 2.2). For reasons that are unknown, the opening angle of these jets is significantly smaller than the precession angle described by the jets when they launch. This demands either different jet episodes or jet recollimation occurring between those two stages of the jet (see, e.g. Bowler and Keppens, 2018).

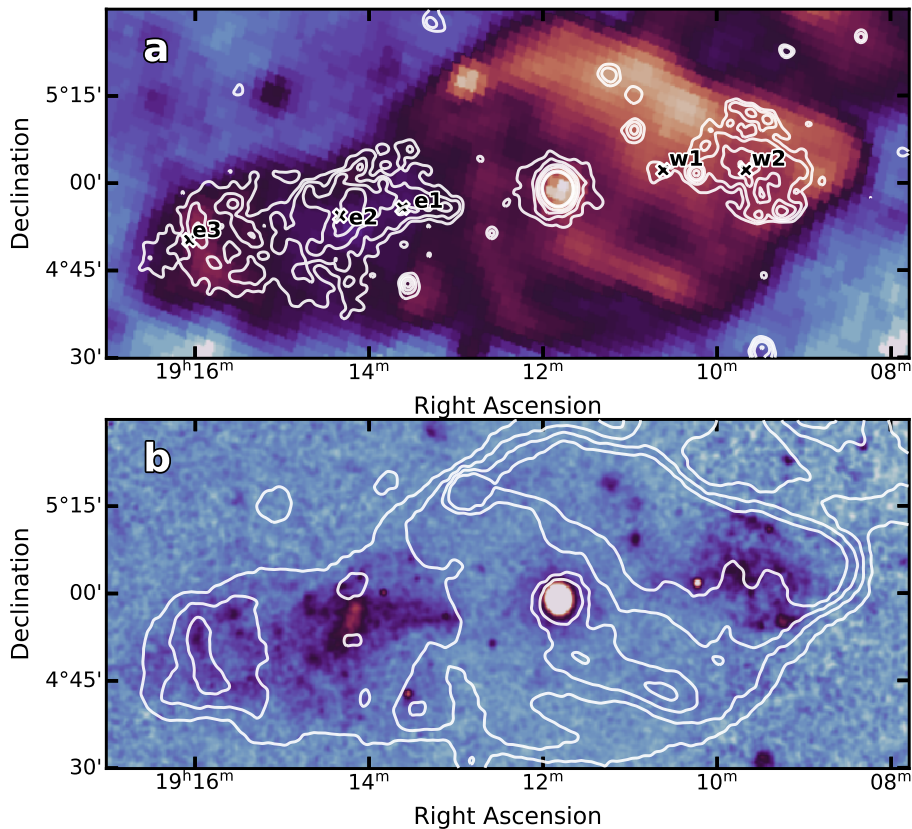


FIGURE 2.2: **Interaction of the SS 433 jets with W50.** **a:** Radio image of W50 at 11 cm by the Effelsberg radio telescope (Reich et al., 1984, 1990; Furst et al., 1990) with X-ray contours overlaid in white. The X-ray regions defined by Safi-Harb and Ögelman (1997) are marked with crosses. The ones in the eastern jet have an *e* in their name, whereas the ones in the western jet have a *w*. **b:** X-ray image of SS 433 and the outer jets by the ROSAT satellite (Brinkmann et al., 1996; Safi-Harb and Ögelman, 1997) with radio contours overlaid in white. Figure adapted from Goodall et al. (2011a) using publicly available data.

The outer jets are sources of TeV gamma-rays (Abeysekara et al., 2018), making SS 433 the only microquasar firmly identified in that energy range. The study of

the TeV emission from the outer jets of SS 433 is the central topic of this thesis (see Chapters 6, 7 and 8), which is why through this chapter, we will pay special attention to the properties of the outer jets and, in particular, to their non-thermal emission.

The jets terminate after nearly 100 pc into the surrounding W50 nebula, a bright radio structure that is typically thought to be a supernova remnant (SNR) associated with the compact object in SS 433 (Elston and Baum, 1987), although other explanations for its origin and relation to the jets exist (see e.g Ohmura et al., 2021). The morphology of W50 presents two distinct elongated deformations, sometimes referred to as *ears*, aligned with the SS 433 jet axis which are thought to be the result of the interaction of the jet with the shell. Figure 2.2 shows the interplay of the jets with the nebula through radio and X-ray observations.

2.3 Observations of the SS 433 Region

Since its detection, the SS 433 system has been observed in virtually every wavelength range over the course of almost half a century. A complete list of these observations and the conclusions drawn from them is thus virtually an unfeasible task. In this section we will attempt instead to build an incomplete but informative description of a selection of observational campaigns with a focus on the outer jets and the observational implications for non-thermal emission sites in the system.

2.3.1 Radio

Observations in the radio band probe the presence of relativistic electrons via synchrotron emission (see Section 1.5.1) and molecular gas via molecular line emission (Rybicki and Lightman, 1986), which in turn can be a target for interaction with relativistic protons (see Section 1.5.1). It is thus a critically important regime to the study of non-thermal processes (see Section 1.2).

Radio observations of synchrotron emission from the inner jets of SS 433 allowed for an early description of their proper motions (Spencer, 1979), which was followed up by the first images of their precession motion with the VLA (Hjellming and Johnston, 1981). A later imaging campaign with the VLA (Blundell and Bowler, 2004) revealed iconic images of the corkscrew pattern described by the jet motion (see Figure 2.3). From these images it could be elucidated that the jets are symmetric, launched with speeds ranging between 0.24 to 0.28 c and at a distance of 5.5 kpc from Earth (Blundell and Bowler, 2004). The same findings were corroborated later by Blundell et al. (2007), extending the measured jet speeds to values as high as 0.32 c during flares, which are observed both in the region near the central engine and in the inner jets (Vermeulen et al., 1993a,b).

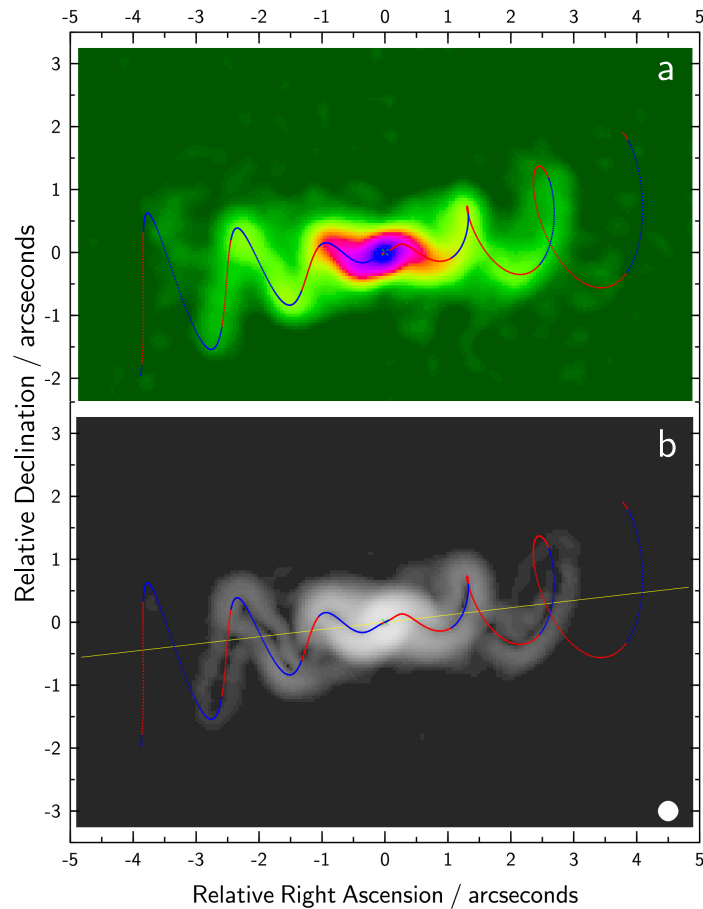


FIGURE 2.3: **Radio images of the precessing jets.** **a:** Total intensity image at 4.85 GHz observed with the VLA. Overlaid is the projection on the sky of two oppositely directed jets with the inferred SS 433 parameters. **b:** Sobel-filtered version of the image shown in **a**. Figure from Blundell and Bowler (2004).

A series of deep dedicated campaigns (Roberts et al., 2008, 2010; Bell et al., 2011) with the VLA revealed that both the eastern and western jet are remarkably symmetric. The jet power experiences temporal variations of order at least 5 (Bell et al., 2011), and the velocity in the order of 10% (Roberts et al., 2008), but these differences are always matched in both jets. The absence of deceleration between the scales imaged by optical (10^{-3} pc) and radio (0.1 pc) observations indicate that the jets are denser than their surroundings to a factor of at least 300:1.

As the jets propagate, they expand. Millimeter wavelength observations with the Atacama Large Millimeter Array (ALMA) reveal that the energy loss of the radiating electrons in the inner jets is dominated by adiabatic expansion (see Section 1.5.2) and not of synchrotron losses (Martí et al., 2018).

The inner jets are not the only outflow in SS 433 that has been observed in the radio band. Simultaneous imaging using the Very Long Baseline Array (VLBA), MERLIN and the VLA revealed the presence of an wind-like equatorial outflow perpendicular to the axis of the jets moving with speeds estimated around 300 km/s (Blundell et al., 2001). Figure 2.4 shows an image of this outflow.

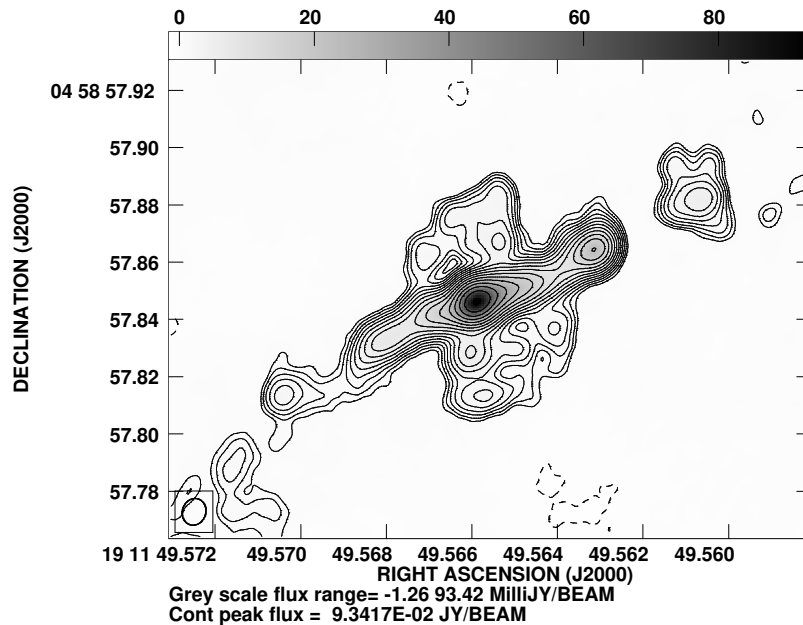


FIGURE 2.4: **Equatorial outflow from SS 433.** Total intensity image at 4.99 GHz of SS 433 on March 7th 1998, combining VLBA, MERLIN, and VLA data. Figure from Blundell et al. (2001).

The first component of the SS 433 system to be imaged in the radio was W50 (Velusamy and Kundu, 1974), which is a bright radio source (see Figure 2.2). Since then it has been imaged repeatedly in a variety of continuum wavelengths (e.g. Geldzahler et al., 1980; Elston and Baum, 1987; Dubner et al., 1998; Reich et al., 1984; Furst et al., 1990; Reich et al., 1990). The existence of high-resolution observations of W50 over several decades allows to study the proper motions of the radio filaments in the nebula. Figure 2.5 shows two images of W50 separated by over a decade in which such filaments are highlighted. In particular, the filaments located in the ears where the SS 433 jet terminates do not move distances greater than the instrumental resolution over the observation time, a fact which can be used to derive an upper limit on the jet velocity at termination. Goodall et al. (2011b) used this to derive an upper limit of $0.0405c$, which was later updated by Sakemi et al. (2021) to $0.023c$. This means the jet must have considerably decelerated by the time it reaches the edge of W50.

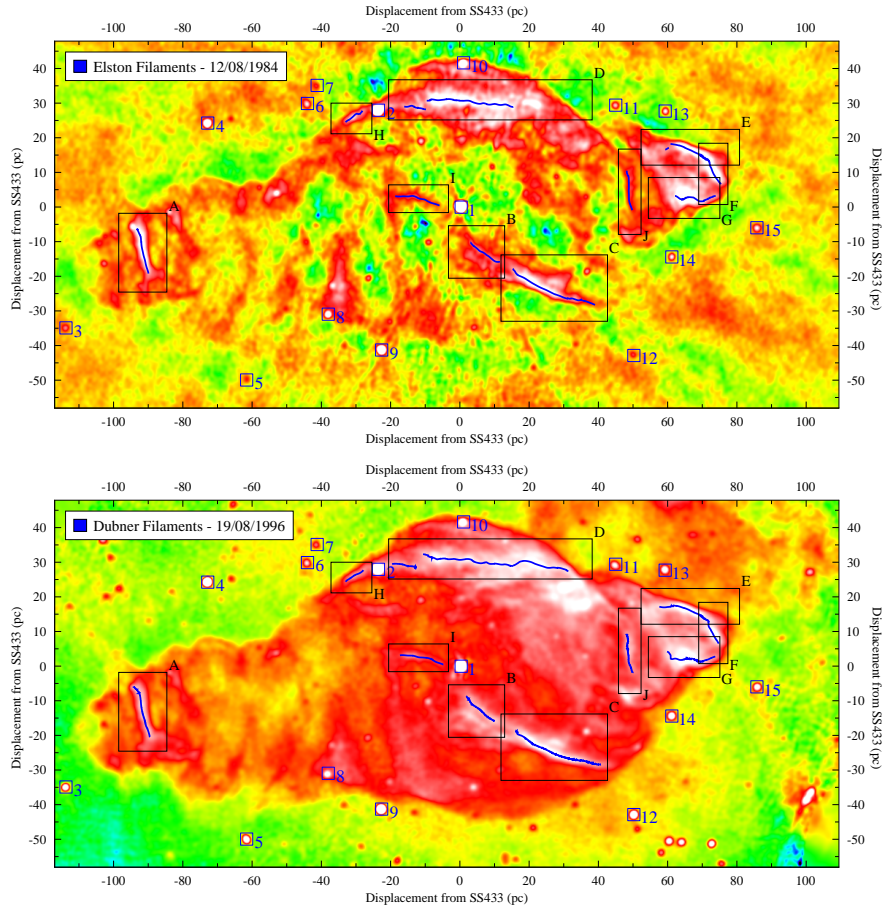


FIGURE 2.5: **Time evolution of the radio filaments.** . Radio observations of W50 in 1984 (Elston and Baum, 1987) and 1996 (Dubner et al., 1998) with the radio filaments selected for the study of their proper motions highlighted. Figure adapted from Goodall et al. (2011b).

Wide-field polarization observations of the SS 433/W50 complex with the Australia Telescope Compact Array (Farnes et al., 2017) reveal that the large-scale magnetic structure of W50 is consistent with the hypothesis of its SNR nature. A Faraday rotation measure (RM) gradient is measured across the central region of W50, with an axis perpendicular to the jet axis, indicating a connection between the evolution of the jets and the W50 shell. The eastern jet termination region also presents a RM gradient, interpreted as a result of the interaction of the jet with the ISM.

Observations of molecular line emission, such as CO or HI reveal a number of molecular clouds in the vicinity of the system (Band and Gordon, 1989), some of them aligned with the SS 433 jet axis (Su et al., 2018), in particular in the western tip of W50 (Liu et al., 2020; Yamamoto et al., 2022). Their kinematic characteristics indicate a possible connection with SS 433. However, there are no distance estimates to these clouds, meaning that their actual position with respect to the jets is unclear.

The outer jets have not been detected in the radio band.

2.3.2 Infrared

Observations in the infrared band probe the thermal emission from the central engine, which is a weak but detectable infrared source at 12μ and 25μ (Band, 1987). High-resolution spectra of the central source in the infrared H and K bands reveal that the spectrum is dominated by hydrogen and helium emission lines, the temporal behavior of which confirms the kinematic model.

2.3.3 Optical

The brightest optical lines radiated in the SS433 jets are hydrogen lines emanating from the jets, namely the $H\alpha$ line. Higher order Balmer lines are not as well studied due to the fact that SS 433 is weaker in the blue range and also this region of the spectrum is more complex, leading to increased difficulties in identifying the lines. As mentioned above, the first detection of the peculiar shifted lines of SS 433 was reported by Margon et al. (1979b). Many spectroscopic observations of the inner jets have been performed since, such as e.g. Vermeulen et al. (1993c), in which changes to the positions of the lines can be observed in the timescale of days (see Figure 2.6.)

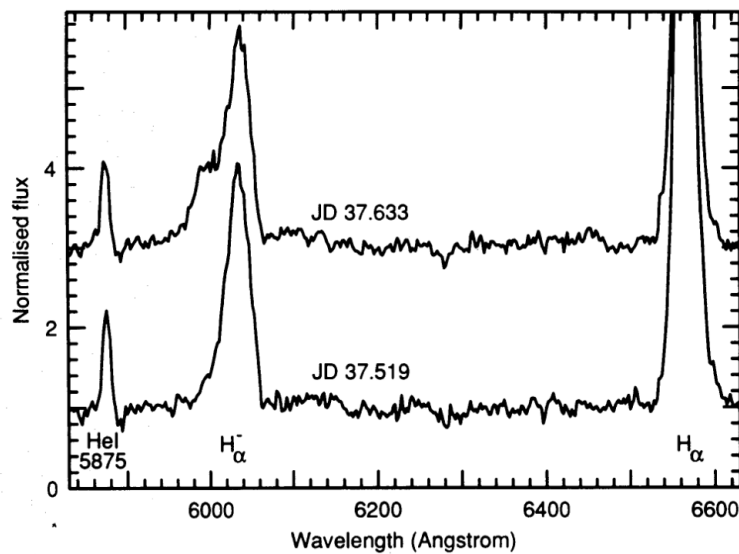


FIGURE 2.6: $H\alpha$ spectra of SS 433 in two consecutive days.. Fragments of two spectra of SS 433. Figure from Vermeulen et al. (1993c).

The optical lines have been used to repeatedly test the kinematic model invoking the Doppler boosting of emitting material in the jets over the years (Ciatti et al., 1981; Anderson et al., 1983; Margon and Anderson, 1989). Most recently, Eikenberry et al. (2001) made use of observations of SS 433 over the course of 20 years to validate this interpretation of the observed emission (see Figure 2.7).

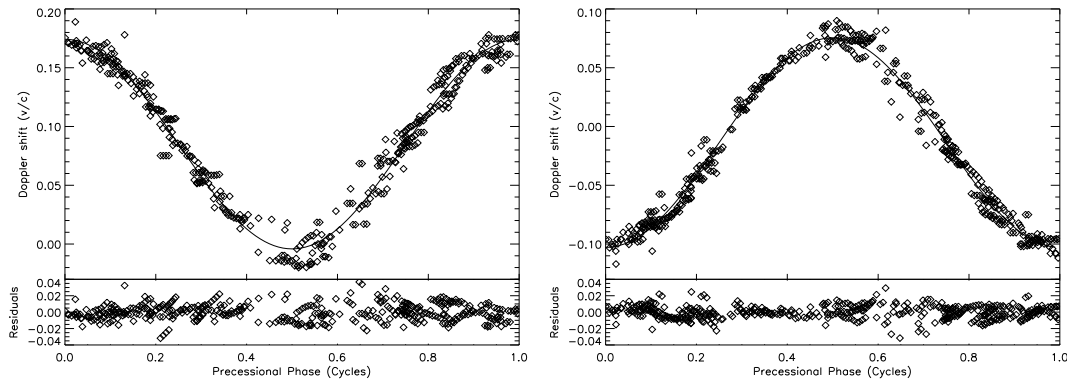


FIGURE 2.7: **Check of the kinematic model over twenty years.** Measured Doppler shifts, model prediction, and residuals as a function of precessional phase for the approaching (left panel) and receding (right panel) jets. Figures taken from Eikenberry et al. (2001).

Optical observations also provide information on the binary system at the core of SS 433. Measurements of the spectra of the donor star have identified it as a type A supergiant with a mass ranging between $\sim 8 - 15 M_{\odot}$ (Gies et al., 2002; Hillwig and Gies, 2008). The observation of temporal variations in the optical magnitude of the central region result in an estimate of the total mass of the binary system and its orbital parameters. Putting these together, an estimate of the mass of the compact object can be obtained. The values found are consistent with the compact object being a black hole of around $10 M_{\odot}$ (Blundell et al., 2008; Kubota et al., 2010; Cherepashchuk et al., 2019, 2021).

Interferometry measurements are able to spatially resolve the optical jets. These observations reveal the presence of discrete ejecta or *bullets* and find evidence of different ejection episodes in the relative expansion of the different bullets (Waisberg et al., 2019a). Further observations of the inner jets confirmed the presence of equatorial outflows and a wind connected to the accretion disk (Waisberg et al., 2019b; Picchi et al., 2020).

Additionally to spectroscopic measurements, optical imaging can reveal the presence of target material, in the form of optical filaments, which would interact with relativistic protons (see Section 1.5.1). Wide-field $H\alpha$ observations of the W50/SS 433 complex (Boumis et al., 2007) reveal the presence of optical filaments that correlate with the radio shell of W50 (see Figure 2.8). No dense filaments are observed to correlate with the outer jets.

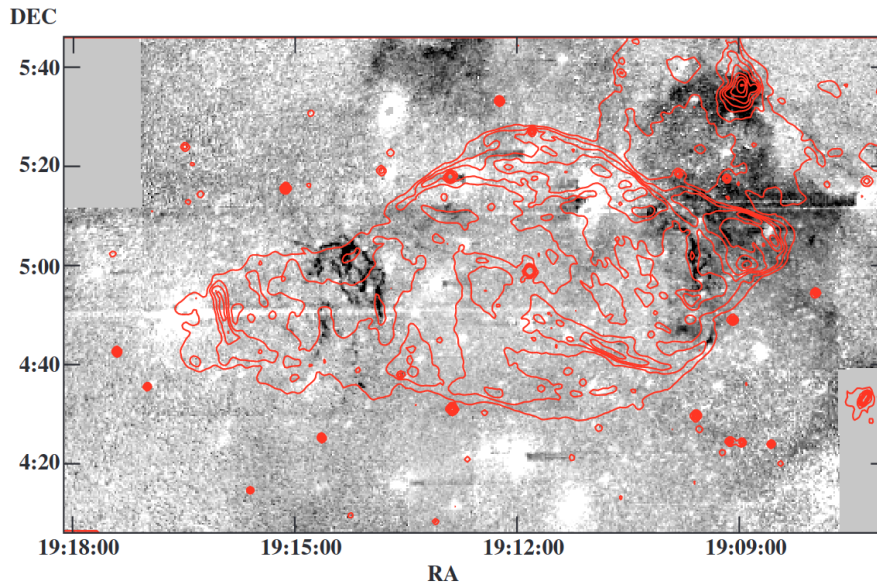


FIGURE 2.8: **Optical-radio correlation of the W50 filaments** Combined image of the negative continuum-subtracted mosaic of W50 in the light of $H\alpha+[N II]$ and the radio emission at 1465 MHz (solid lines). The 1465 MHz (Dubner et al., 1998) radio contours scale linearly. Figure taken from Boumis et al. (2007).

2.3.4 Ultraviolet

Hubble observations of the central source in SS 433 (Dolan et al., 1997) reveal that the emission in this region is of thermal nature, consistent with a black-body (see Equation 1.2) of the same temperature as in the optical range.

2.3.5 X-ray

The X-ray regime covers photon energies in which the emission can either be of thermal origin due to thermal bremsstrahlung (see e.g. Longair, 2011), or non-thermal origin due to synchrotron emission from relativistic electrons (see Section 1.5.1). The distinction between them is often done on the basis of the value of the temperature required to explain the emission as thermal.

Early observations of SS 433 identified it as an X-ray source (Clark and Murdin, 1978; Marshall et al., 1978). Follow-up measurements of the spectral lines from the core region with the EXOSAT satellite revealed that the X-ray lines are also Doppler shifted in agreement with the kinematic model (Watson et al., 1986), resulting in a coherent picture of the jet motion between the radio, optical and X-ray bands. High-resolution spectra of the inner jets reveal the presence of iron lines (Brinkmann et al., 1991; Migliari et al., 2002), indicating that the jets of SS 433 are so-called "heavy jets", that is, composed of baryonic matter. The inner jets are also observed to flare (Band, 1989) in the X-ray band at times correlated with the active and quiescent radio states. The base of the jets displays very bright X-ray emission consistent with thermally radiating matter at X-ray temperatures (Brinkmann et al., 1988).

The outer jets were first imaged by the Einstein telescope (Seward et al., 1980; Watson et al., 1983), revealing the two-sided degree-scale jets appearing at distances of roughly 25 pc from the central engine (see Figure 2.2). Follow-up observations of the entire system with the ROSAT satellite (Brinkmann et al., 1996; Safi-Harb and Ögelman, 1997) confirm the thermal nature of the emission from SS 433 itself but find a number of non-thermal X-ray emission sites along the outer jets. The jets have a very non-uniform surface brightness, with bright X-ray knots in both sides, at approximately the distance of the presumed original location of the shell of W50. A thermal emission fit to these knots would require extremely high temperatures, and so the radiation is very likely non-thermal. Detailed observations of the eastern jet with the XMM-Newton satellite (Brinkmann et al., 2007) confirm this picture.

If X-ray radiation is due to relativistic electrons, X-ray observations are, together with radio data, crucial to determine the value of the magnetic field (see e.g. Equation 1.27), as well as the spectral index of the electron distribution responsible for the emission (see Equation 1.30).

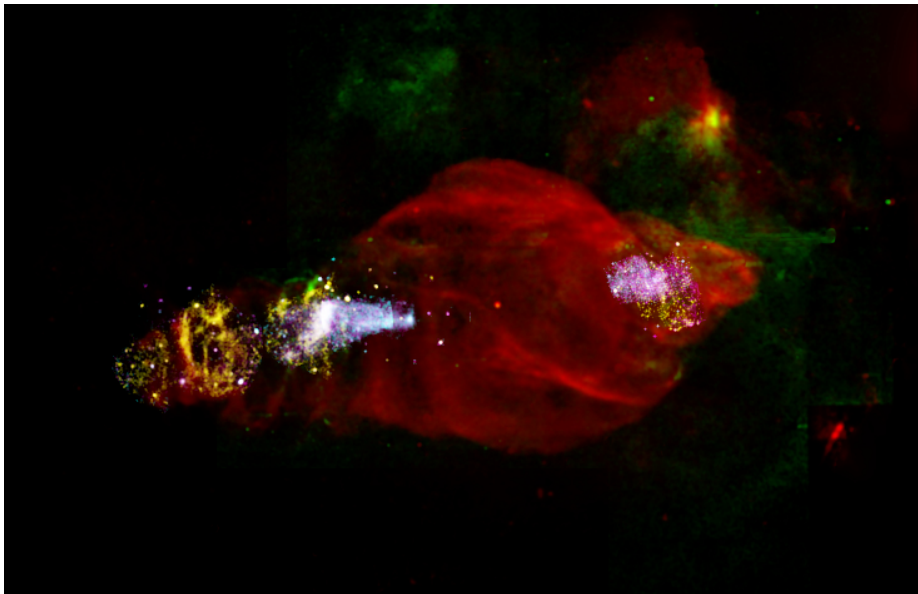


FIGURE 2.9: **Composite color image of the SS 433/W50 complex.** Multi-wavelength image of the W50 nebula. Red: radio (Dubner et al., 1998); green: optical (Boumis et al., 2007); yellow: soft X-rays (0.5-1 keV); magenta: medium energy X-rays (1-2 keV); cyan: hard X-ray emission (2-12 keV). Figure from Safi-Harb et al. (2022).

Most recently Safi-Harb et al. (2022) used NuSTAR, XMM-Newton, and Chandra data (see Figure 2.9) of the eastern jet to reveal the presence of very hard spectral index (1.58 ± 0.05 in the 0.5-30 keV band) X-ray emission at the base of the jet. The spectral index gradually steepens eastward out to the radio "ear" where thermal soft X-ray emission dominates. Kayama et al. (2022) report the presence of very hard emission with a compatible index (1.42 ± 0.10 in the 1-7 keV band) at the equivalent location in the western jet.

2.3.6 Gamma-Ray

The gamma-ray range of the spectrum is dominated by non-thermal emission originated by relativistic particles, such as electrons via IC (see Section 1.5.1) or protons via pp interactions (see Section 1.5.1). This range is usually split into two ranges: *high-energy* (few MeV to hundreds of GeV) and *very-high-energy* (above hundreds of GeV) gamma-rays. A detailed overview of gamma-ray astronomy with a focus in the very-high-energy regime is presented in Chapter 3.

High-Energy Gamma-Rays

There have been a number of works presenting evidence for GeV emission from the SS 433/W50 complex based on data from the *Fermi* Large Area Telescope (*Fermi*-LAT, Atwood et al., 2009). Analysis of data from this region presents a number of challenges, the main one being contamination from a nearby pulsar, PSR J1907+0602, as well as source confusion in the crowded Galactic plane and uncertainty in the diffuse emission. For this reason, different analyses of the region have yielded significantly inconsistent results, even when analyzing the same range of observation times.

Bordas et al. (2015) reported the detection of very extended emission of more than 5° across, partially coincident with SS 433/W50. A later analysis with more data reduced the size of the emission to almost entirely overlap with the SS 433/W50 region (Bordas et al., 2017). No variability is detected.

Rasul et al. (2019) uses only 2 more years of observations but reports the detection of variability in the GeV emission with both the orbital phase of the binary and the precession phase of the jets. This finding is not confirmed by Xing et al. (2019) which uses the same data set, and which additionally finds an entirely different morphology, with only the western side of the outer jets as a significant source. Sun et al. (2019) also uses the same data set, reports no variability and a morphology consistent with Bordas et al. (2017) but almost an order of magnitude less flux.

A more careful treatment of the contamination by the nearby pulsar is employed by Li et al. (2020), which report no large-scale emission but only a sub-threshold excess partially coincident with the western jet (see Figure 2.10). This excess shows no signs of temporal variability. This data set was then used by Fang et al. (2020) to perform a joint analysis with data from the High Altitude Water Cherenkov (HAWC) observatory (see Section 2.3.6).

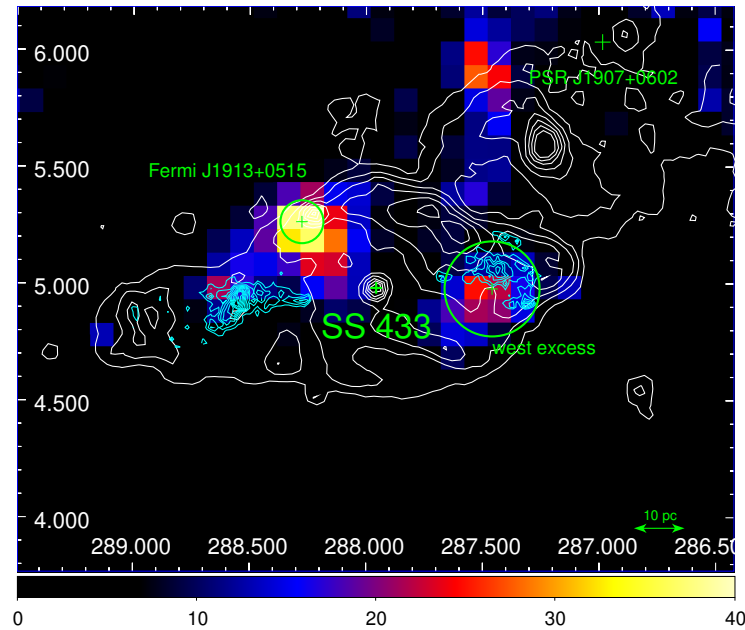


FIGURE 2.10: **The *Fermi*-LAT view of SS 433.** *Fermi*-LAT map of the SS 433 region in the 0.1-300 GeV range during the off-peak phase of PSR J1907+0602. Background sources have been modeled and subtracted. The color scale shows the test statistic (TS) value, the square root of which gives an approximate detection significance. The X-ray and radio emission from the system is represented with blue and white contours respectively. Figure from Li et al. (2020), see also Fang et al. (2020).

Most intriguingly Li et al. (2020) reports the detection of a new source, Fermi J1913+0515, coincident with the W50 shell in the direction orthogonal to the jets but observed to pulsate with the jet precession period. The distance between the central engine and the location of this excess, assuming both are located at 5.5 kpc from Earth is estimated to be of around 40 pc. If the detected variability is real and related to the jets, its origin is very difficult to explain. Fermi J1913+0515 lies outside of the SS 433 jet cone, meaning that it cannot be directly illuminated by the jets. Scenarios where protons are accelerated near the jet base and diffuse outwards, to then create gamma-ray when they find a target cannot explain the periodicity of the signal. Even the presence of a relativistic equatorial outflow could not naturally explain the observed signal, as the distance between the central engine and Fermi J1913+0515 is still too large to maintain the coherence of the pulsations. Figure 2.11 shows the *Fermi*-LAT significance maps for the off and on phase, as well as the light-curve of Fermi J1913+0515.

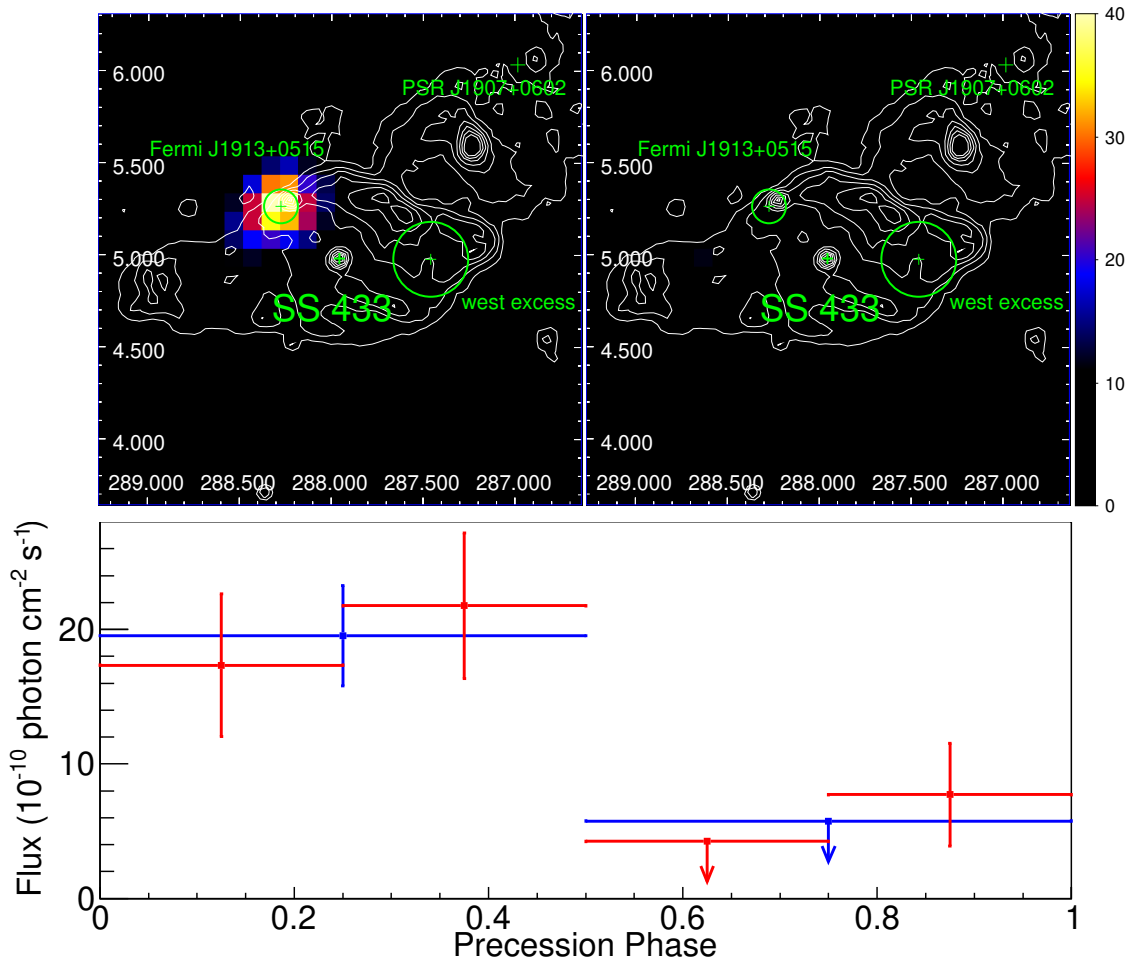


FIGURE 2.11: **The pulsating excess Fermi J1913+0515.** **Top:** TS maps (see Section 3.5.2) of the SS 433 region in the 1-300 GeV band for the precessional phases 0.0-0.5 (left) and 0.5-1.0 (right). **Bottom:** Precessional phase light curve of Fermi J1913+0515 in the 1-300 GeV band for bin sizes of 0.5 (blue) and 0.25 (red). Figure from Li et al. (2020).

Very-High-Energy Gamma-Rays

The SS 433 region was first observed by the HEGRA array of telescopes, which did not result in the detection of any parts of the system (Aharonian et al., 2005). Later follow-ups, by the Very Energetic Radiation Imaging Telescope Array System (VERITAS) array (Kar and Collaboration, 2017) and a combined analysis of H.E.S.S. and Major Atmospheric Gamma-ray Imaging Cherenkov (MAGIC) data (MAGIC and H.E.S.S. Collaborations et al., 2018) also lead to a non-detection, with updated upper limits for the central engine and the jets.

In 2018, the HAWC Collaboration reported the detection of TeV gamma-rays from the outer jets of SS 433 (Abeysekara et al., 2018). Figure 2.12 shows the significance map including two hotspots consistent with the position of the X-ray emission in the jets. The HAWC angular resolution combined with the relatively low statistics did not allow for a measurement of the extent of the gamma-ray emission, which is

consistent with a point-like source. This places upper limits on the physical size of the hotspots at 24 pc and 34 pc for the east and west respectively.

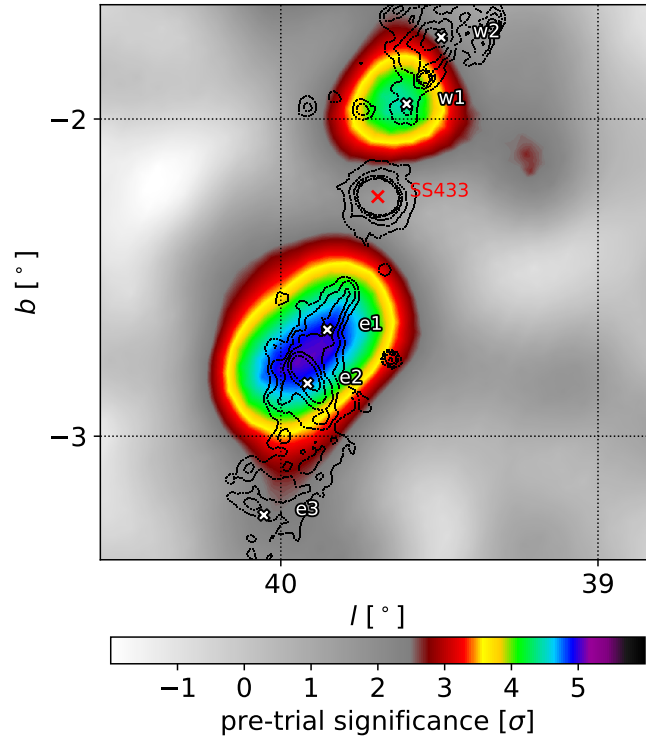


FIGURE 2.12: **Detection of TeV emission from the outer jets.** HAWC significance map of the SS 433 region showing the two significant hotspots. This map is computed after the fitting and subtraction of emission from the spatially extended source MGRO J1908+06. The jet regions e1, e2, e3, w1 and w2 defined using the X-ray data are indicated, as well as the location of the central binary. From Abeysekara et al. (2018).

A difficulty for the HAWC analysis of this region is the presence of a very extended nearby source MGRO J1908+06. The relatively poor angular resolution of HAWC means that the emission from this source and that of the western jet to almost fully overlap. Thus careful modeling and subtraction of the TeV emission from MGRO J1908+06 are needed in order to disentangle it from the emission from the jets. Figure 2.13 shows the HAWC significance maps of the entire field of view (FoV) before and after modeling and subtracting MGRO J1908+06.

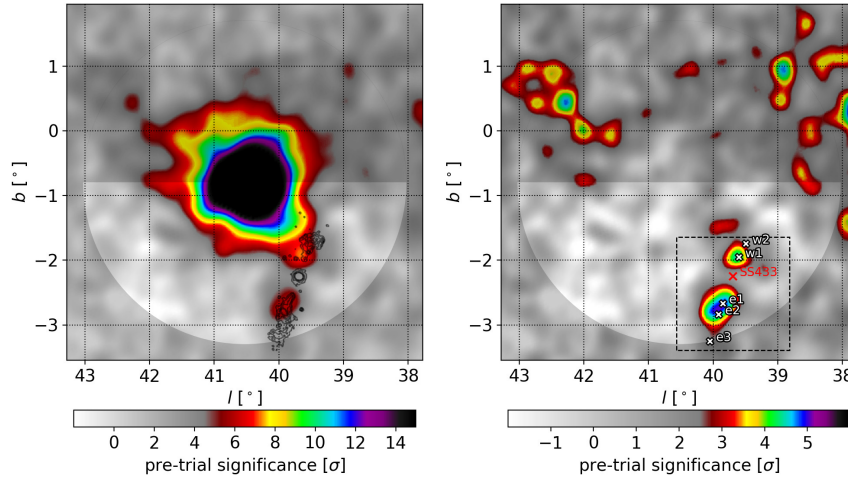


FIGURE 2.13: **Modeling the nearby extended source MGRO J1908+06.** HAWC significance map of the entire SS 433 FoV including the region of MGRO J1908+06. The left panel shows the significance map without any modeling, whereas the right panel shows the residual from subtracting the best-fit model of MGRO J1908+06. The dashed square corresponds to the sky portion shown in Figure 2.12. From Abeysekera et al. (2018).

Despite the lack of clear association due to poor angular resolution, the emission from the jets was interpreted to be connected to the bright X-ray knots located at the e1, e2 and w1 positions because of the likely non-thermal nature of their X-ray emission. The energy resolution of the analysis did not allow for a characterization of the spectral shape, but only to measure the flux at 20 TeV for each of the jet. The measured flux from the eastern side was combined with the X-ray and radio fluxes from a similar region to build a multi-wavelength spectral energy distribution (SED) of the eastern hotspot, shown in Figure 2.14. These data can be explained by a model that invokes a single population of electrons producing radio to X-ray photons through synchrotron emission in a magnetic field and TeV gamma-rays through inverse Compton scattering of the CMB (see Section 1.5.1). The power required to match the gamma-ray flux imply that only a small fraction of the total emission can be due to hadronic processes associated to accelerated protons.

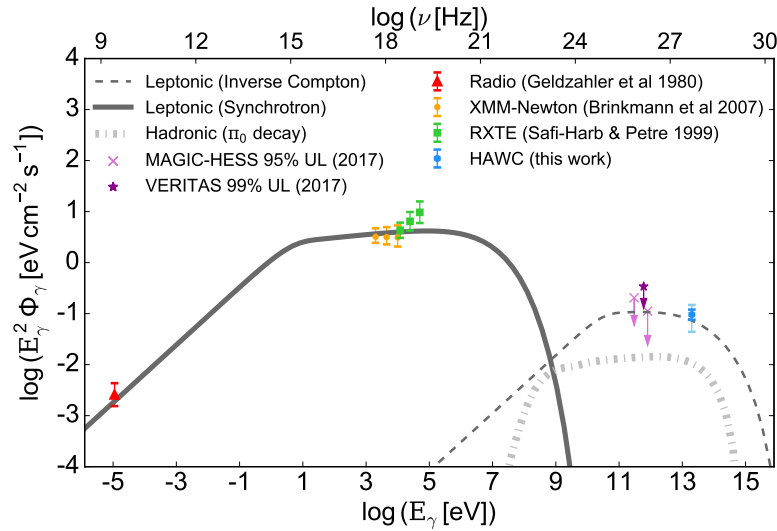


FIGURE 2.14: **Multi-wavelength SED of the eastern jet.** The data include radio, soft X-ray, hard X-ray and TeV gamma-ray upper limits, and HAWC measurements of e1. Figure from Abeysekara et al. (2018).

2.4 Attempts at Modeling SS 433

There have been numerous attempts at explaining the variety of observations of SS 433 via modeling. The best example and also perhaps the most supported by evidence is the so-called kinematic model which explains the observations of the inner jets via their precessing motion. The picture of the outer jets is however much less clear. In this section we describe briefly some of these attempts with a focus on the dynamics of the outer jets and their gamma-ray emission.

2.4.1 Numerical Simulations of the Jets

Early two-dimensional simulations of the precessing jets of SS 433 were able to achieve jet recollimation on large scales (Eichler, 1983; Peter and Eichler, 1993). This relied on an assumption of a small angular spread in the jets, which would then be able to propagate and focus downstream due to ambient pressure.

Later, more complex simulations of the W50/SS 433 complex were able to explain the peculiar morphology of W50 as a result of the interaction of the jets with a SNR shell (Velázquez and Raga, 2000; Zavala et al., 2008). This scenario was thoroughly explored by Goodall et al. (2011a), which concluded that the elongated morphology of W50 and the observed change in jet opening angle in the outer jets require of at least three distinct jet episodes, with different combinations of jet geometries (conical, cylindrical) and precession characteristics. This is exemplified by the two realizations of the combined jet and SNR simulations shown in Figure 2.15, where a collimated jet results in a morphology close to the observed one for W50 but a jet with a 20° opening angle fails to reproduce the observations. Goodall et al. (2011a) are also able to explain the asymmetry between the eastern and western side of the

outer jets and W50 (see Figure 2.2) as a consequence of the ambient density gradient towards the Galactic plane, as can be seen in Figure 2.15.

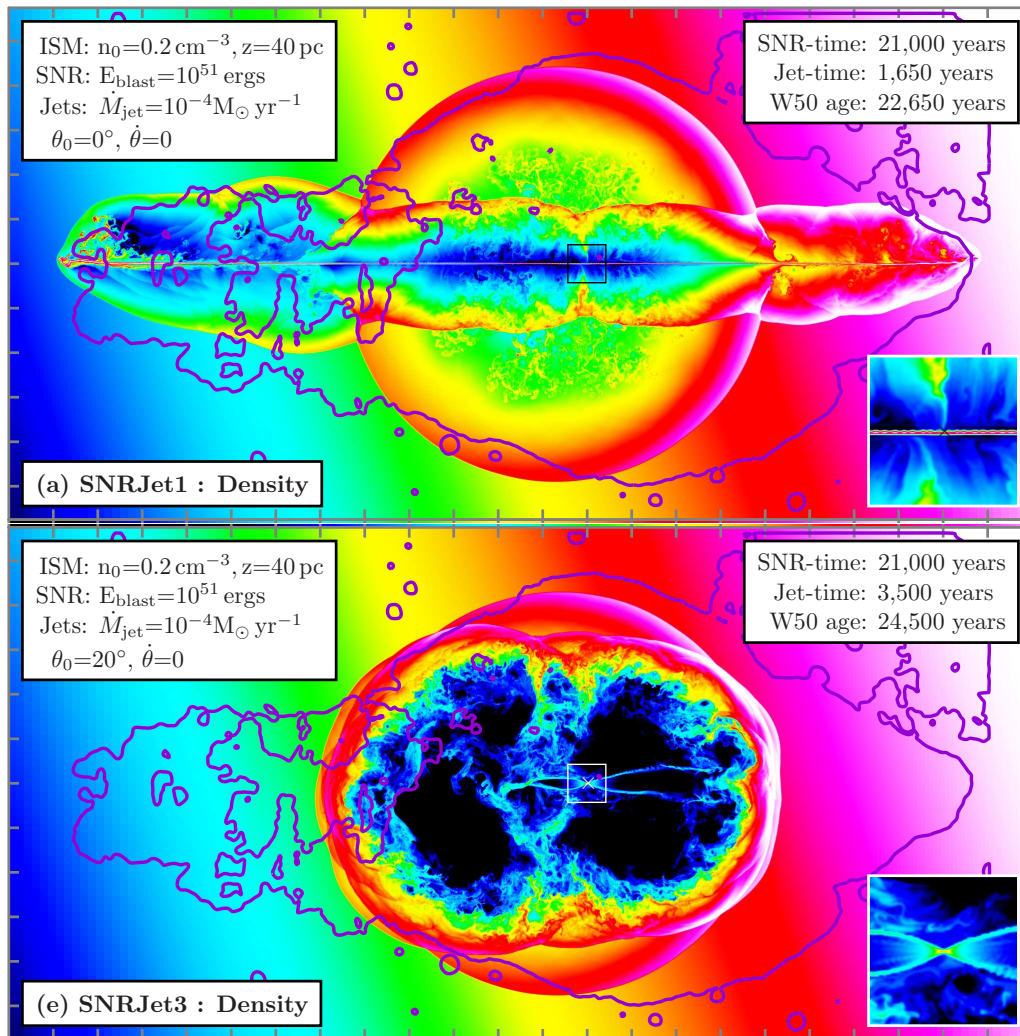


FIGURE 2.15: **Simulations of the interaction between a jet and a SNR shell.** The top panel shows the interaction of a non-precessing jet with a SNR shell, which results in a morphology consistent with the observed shape of W50 (purple outline). The bottom panel shows the interaction of a jet with the observed precession angle observed in the inner jets of SS 433 today and a SNR shell. As can be seen, the elongated shape of W50 is not reproduced. Figures adapted from Goodall et al. (2011a).

On the other hand, Monceau-Baroux et al. (2015) achieve the transition from a precessing jet to a continuous hollow non-precessing jet with a smaller opening angle in a single jet episode. In their simulations, successive windings of the jet undergo gradual deceleration due to interaction with the ISM, to ultimately merge in a hollow straight jet at distances of about 0.068 pc from the source. This distance is explained as that where the ram pressure of individual jet elements match the ISM pressure. Unfortunately, this explanation made use of an incorrect value of the jet density (Monceau-Baroux et al., 2017) which when adjusted results in a mismatch

between the observed distance in the simulation and the one obtained analytically.

Bowler and Keppens (2018) addressed this issue by deriving analytical scaling relations relating the distance to collimation with the pressure of the ambient medium. They conclude that the precessing jets could be responsible for the observed characteristics of W50. For reasonable values of ambient pressure and temperature, collimation is achieved within ~ 10 pc. This process would considerably decrease the velocity of the jet head to values of around $\sim 0.003c$.

Panferov (2017) employ analytical calculations to describe the viscous interaction of the jet, via turbulence, with the ambient medium. They find that the nature of W50 is consistent with a SNR originated 100,000 years ago, and predict a jet deceleration of 60% by distances of 40 pc, when the jet reaches the outer shell of W50.

Ohmura et al. (2021) explore, via two-dimensional simulations, the possibility that W50 is in fact not a SNR but instead a structure created by the jets themselves. They achieve a similar morphology to W50 without the need to invoke an existing circular structure that the jets collide into, but by making the jets less dense than the ambient medium. Such explanations for the nature of W50 as other than a SNR are not new. Another interesting example is Konigl (1983), which proposed that the expansion of W50 is driven by a strong stellar wind from the binary companion of SS 433, rather than a SNR. In this picture, SS 433 would be surrounded by a three-phase interstellar medium, with an additional phase in between the W50 shell and SS 433 due to the wind. However, and despite these alternative possibilities, W50 is still widely assumed to be a SNR.

2.4.2 Gamma-Ray Emission Models

Due to the presence of non-thermal X-ray emission in the jets of SS 433, the existence of gamma-ray emission was also predicted (e.g. Aharonian, 2004). Following the discovery of TeV emission sites along the jets by the HAWC Collaboration, a number of models invoking accelerated electrons were put forward to explain this emission.

Sudoh et al. (2020) proposes the bright X-ray knots along the outer jets as the particle acceleration sites, in particular of electrons. Their model accounts for the multi-wavelength data except for the GeV data, suggesting that the GeV emission is a consequence of a different mechanism or originates in a different region. In order to explain the gamma-ray flux, efficient acceleration is needed, which, if protons are accelerated at the same efficiency as electrons, implies that SS 433 can accelerate protons to energies beyond a PeV.

A very similar model is proposed by Kimura et al. (2020), which also assume that electrons are accelerated in the X-ray knots. Additionally, they also propose the existence of hadronic emission connected to the observed optical filaments (see Figure 2.8). They find that both the hadronic and leptonic models can account for the observational data, including the GeV range.

Fang et al. (2020) perform a joint fit of the HAWC emission with the GeV emission sites (see Figure 2.10) and find that the observed gamma-ray emission is consistent

with inverse Compton emission by an electron population that is accelerated at some location along the jets. However, in order to explain both the HAWC and *Fermi*-LAT measurements, the electrons need to have a soft intrinsic energy spectrum, or cool very rapidly. Fang et al. (2020) also propose the existence of a Poynting-dominated EM jet on-axis, additionally to the observed precessing inner jet, in order to explain the outer jets and their observed opening angle.

2.5 Summary and Outlook

Despite the fact that the SS 433 system has been extensively studied in virtually all wavelengths, there are still many open questions surrounding it. While the dynamics of the precessing inner jets are relatively well understood, little is known about the outer jets and their interplay with the W50 nebula. Below we present a summary of some of the unresolved issues with this system that have been highlighted by the observations described in this chapter, with a special focus on the outer jets and non-thermal emission as it is pertinent to the content of this thesis.

- **Jet collimation.** The outer jets are much narrower than the precession cone of the jets observed at launch. This implies the existence of either distinct jet episodes with very different properties, or the occurrence of jet collimation at some point before the reappearance of the outer jets. Many mechanisms have been proposed, each with different implications for the dynamics of the outer jets.
- **The outer jets.** The reason why the jets suddenly become bright X-ray emitters at distances of around 25 pc from the core is not known. There is no reason, other than the jet reappearance, to attach any physical significance to this location, as the shell of W50 has a much larger radius, of around 50 pc. Both jets reappear at approximately the same distance from the core, a symmetry which indicates that the origin of this surface is connected to the system as a whole, and it is not due to, for example, one of the jets hitting some external target coincidentally located at that distance.
- **Nature of the X-ray knots in the outer jets.** X-ray observations of the outer jets reveal an inhomogeneous surface brightness, with two particularly bright spots (or knots) located approximately at the radius of W50. These locations have been suggested to be the sites of particle acceleration to the highest energies, as a result of the dissipation of the jet energy as it collides with W50.
- **Dynamics of the outer jets.** From long baseline radio observations, it is inferred that the jets must have significantly slowed down by the time they reach the tip of W50. However, the dynamical evolution of the jets from launch to this point is completely unknown, and ties to other issues mentioned above such as the occurrence of collimation or the possible presence of different jet episodes.

- **The pulsating GeV source.** The detection of a GeV excess perpendicular to the jet axis which appears to be pulsating with the jet precession period is a challenge to existing models of the SS 433 complex.
- **Nature of W50 and age.** W50 is usually assumed to be a SNR associated with the birth of the compact object in SS 433. However competing explanations for its origin exist, such as it being the result of a combination of the jets themselves and the accretion wind. Such wind is also invoked in some of the possible explanations for the presence of the pulsating excess mentioned above. The age of SS 433 is usually estimated to be $\sim 10^5$ yr by assuming that W50 is a SNR, the time evolution of which is well understood. However, if that were not the case, the age of the system would also be largely unconstrained.

Many attempts have been made to interpret the non-thermal aspects and internal dynamics of the system using X-ray observations (see Section 2.3.5). Whilst these results are intriguing, they cannot alone resolve the distribution of accelerated particles due to the ambiguity of the observed synchrotron emission with the unknown magnetic field strength and morphology (see Section 1.5.1). Measurements by the HAWC observatory (see Section 2.3.6) reveal that the same energetic electrons responsible for the X-ray emission also produce gamma-rays by inverse Compton scattering. Given the close to uniform large-scale radiation fields of the region, inverse Compton emission can, in contrast, directly trace the distribution of accelerated electrons. However, the angular resolution of the HAWC observatory is insufficient to resolve the emission regions and firmly identify the source of the energetic electrons.

In Chapter 6, dedicated observations of SS 433 with the H.E.S.S. array of telescopes (see Section 3.2.1) are presented. The improved energy and angular resolution of H.E.S.S. with respect to that of HAWC allow for a more detailed study of the TeV emission sites and their properties. The effect of the contamination by the nearby extended source MGRO J1908+06 into the jet emission is also reduced due to the better angular resolution, which decreases the impact of systematic effects due to imperfect modeling of the nearby source.

Chapter 3

Detection of Very-High-Energy Gamma-Rays

This chapter presents an overview of the physical processes and techniques that make it possible to detect very-high-energy (VHE) gamma-rays using ground-based instruments. Two specific observational approaches are discussed, Cherenkov telescope arrays and particle detector arrays, with a focus on one particular instrument of each class. Finally, an overview of the basic steps of high-level analysis of gamma-ray data is presented, illustrated using publicly available data.

3.1 Ground-Based Gamma-Ray Astronomy

The Earth's atmosphere is opaque to radiation in the gamma-ray range of the spectrum. In the range between a few MeV and hundreds of GeV, usually referred to as the high-energy (HE) gamma-ray range, this issue is circumvented by the deployment of satellite detectors outside of the atmosphere. Examples of such instruments are the *Fermi* Large Area Telescope (*Fermi*-LAT, Atwood et al., 2009) or the *AGILE* (Tavani et al., 2008) mission. For energies higher than a few hundreds of GeVs (the VHE gamma-ray range), the collection area of satellites is too small for the very low flux expected from astrophysical sources. This means that detectors have to be ground-based and need to exploit the signatures arising from the absorption of VHE photons by the Earth's atmosphere.

3.1.1 Extensive Air Showers

When a highly energetic photon or particle, such as a proton or electron, enters the Earth's atmosphere it interacts with the atoms in the air. This interaction triggers a cascade of further interactions leading to the development of "showers" of secondary particles which travel at relativistic speeds. These particle cascades are referred to as extensive air showers (EAS). Depending on the nature of the primary particle, the interactions are of EM or hadronic nature. This translates into differences in the shower structure and evolution, a fact which is exploited by the experiments in order to discriminate between gamma-rays and cosmic rays (see Section 3.3.4).

The processes responsible for the development of EAS are particle interaction and decay. The atmosphere target material is characterized by its mass density ρ (g cm^{-3}) and number density n (cm^{-3}), from which the interaction length λ (g cm^{-2}) of a process with cross-section σ is derived as

$$\lambda = \frac{\rho}{n\sigma}. \quad (3.1)$$

The depth of a particle inside the atmosphere is usually described by the so-called slant depth X (g cm^{-2}), which is measured from the top of the atmosphere downwards, so

$$X = \int_h^\infty \rho(z) dz. \quad (3.2)$$

The depth at which the shower development reaches its maximum number of particles is referred to as height of shower maximum, X_{max} .

Using these quantities, the development of a cascade of particles in the atmosphere can be described by a system of equations with an equation for each particle type i that interacts with particles of type j :

$$\frac{dN_i(E_i, X)}{dX} = -\frac{N_i(E_i, X)}{\lambda_i} - \frac{N_i(E_i, X)}{d_i} + \sum_{j=1}^J \int_E^\infty \frac{F_{ji}(E_i, E_j)}{E_i} \frac{N_j(E_j, X)}{\lambda_j} dE_j, \quad (3.3)$$

where $N_i(E_i, X)dE_i$ is the number of particles of type i at slant depth X with energies in the interval E to $E + dE$. The interaction with particles of type j is described by the function $F_{ji}(E_i, E_j)$ which is the dimensionless particle yield following from the cross-section of that interaction (see Gaisser et al., 2016, for details).

A comprehensive study of Equation 3.3 and its solution for the EM case can be found in Rossi and Greisen (1941), as well as in Gaisser et al. (2016). Here instead, we will simply focus on the differences between hadronic and EM showers using a simplistic model of the shower development, as these differences are critical to distinguish between signal and background in ground-based gamma-ray astronomy.

Electromagnetic Showers

The physical processes that dominate the development of an EM cascade are pair production and bremsstrahlung (Bethe and Heitler, 1934). After each interaction length, the number of particles is doubled, as a photon will become an electron-positron (e^\pm) pair, while an electron will emit photons via bremsstrahlung. The radiation lengths of these two processes are of similar order to each other ($\lambda_{\text{pair}} = 9/7\lambda_{\text{brem}}$). The growth of the shower stops when the energy of the electrons reaches a critical energy $E_e^c \approx 87$ MeV (Gaisser et al., 2016) at which ionization becomes the dominating energy loss mechanism.

The Heitler model (Heitler, 1954) is a very simple model that is useful to illustrate the general features of the shower development. It assumes that all interactions happen in fixed intervals of $d = \ln(2)\lambda_e$ where λ_e has a value of 36 g/cm^2 and 37 g/cm^2

for water and air respectively. After step k in the shower development, there are 2^k particles in the shower, and their energy is $E = E_0/2^k$ where E_0 is the energy of the primary particle. A sketch of this process is shown in Figure 3.1.

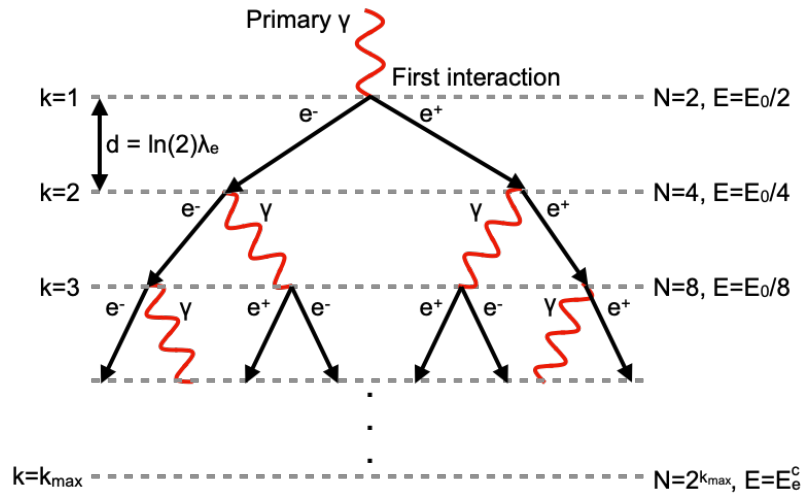



FIGURE 3.1: **EM shower.** Schematic illustration of the development of an EM shower in the Heitler model. In this sketch the primary particle is a gamma-ray of energy E_0 , which interacts with a nucleus in the atmosphere, after which a cascade develops. After each step of $d = \ln(2)\lambda_e$, the number of particles doubles, until the point where ionization losses become dominant. Image credit: Edna Ruiz Velasco  (Ruiz Velasco, 2021).

Hadronic Showers

The physical process that dominates the development of a hadronic cascade is the production of pions in strong interactions. Charged pions (π^\pm) decay into muons (μ^\pm) and muon neutrinos (ν_μ) and, with smaller probabilities, electrons and electron neutrinos (ν_e). Neutral pions (π^0) immediately decay into two photons which in turn originate two EM cascades. The shower can also contain fragments of the target atmospheric nucleus (N), neutrons (n) and protons (p). The Heitler model was extended to hadronic showers by Matthews (2005). The shower development stops when the energy of the pions in the shower reaches a critical energy below which the decay length is smaller than the atmosphere thickness. At that point, pions decay into muons and further pion production via strong interactions becomes impossible. The shower is then dominated by the muonic component which travels until it is absorbed by the ground. Figure 3.2 shows a sketch of these processes in a hadronic shower.

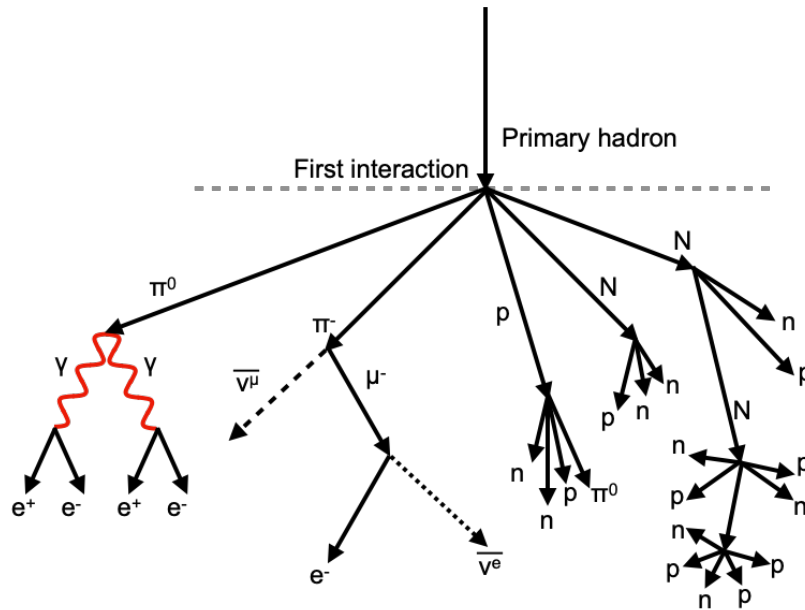


FIGURE 3.2: **Hadronic shower.** Schematic illustration of the development of an hadronic shower. The processes involved are more varied than in the EM case. Image credit: Edna Ruiz Velasco (Ruiz Velasco, 2021).

Observational Differences between Hadronic and EM showers

The different physical processes involved in the development of EM and hadronic showers translate to differences in the measurable properties of the EAS. These differences are then exploited to distinguish between both types of showers. The simple models described above are no longer used in the study of EAS development, and instead sophisticated simulation packages, such as CORSIKA (Heck et al., 1998) are employed. Figure 3.3 shows several simulated EM (top) and hadronic (bottom) showers. From the figure, several obvious differences between the two class of showers can be elucidated. Below we list some of the most relevant ones.

- **Muon content.** Muons are produced in very large numbers in hadronic EAS, primarily from the decay of charged pions. They are however very rare in EM showers. The potential to use these muons to discriminate between hadronic and EM cascades and hence do gamma-ray astronomy, has long been recognized (see for example Gaisser et al., 1991) and will be discussed in Chapter 5.
- **Sub-structure.** The decay of neutral pions produced in hadronic showers results in EM sub-showers, which lead to variability in the structure of hadronic showers. In contrast, EM showers are more homogeneous and present less variability from shower to shower.
- **Depth of first interaction.** In general, hadronic showers develop deeper into the atmosphere than EM ones due to the longer interaction length of hadronic interactions.

- **Lateral spread.** As can be clearly seen in Figure 3.3, the transverse momentum acquired by the particles in the EM showers is much smaller than in the hadronic showers. This results in narrow, compact showers in the EM case which contrast with the much larger lateral spread of hadronic showers.

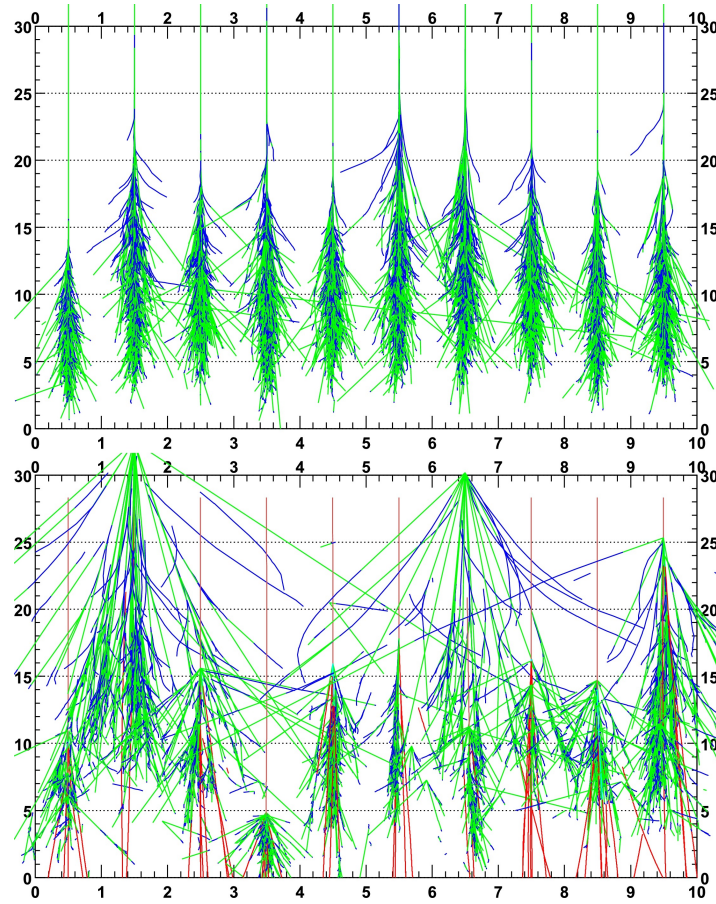


FIGURE 3.3: **Comparison between simulated EM and hadronic showers.** Green lines represent photon trajectories, blue represent electrons, light red muons and dark red protons. **Top:** Ten simulated showers initiated by a 300 GeV gamma-ray. **Bottom:** Ten simulated showers initiated by a proton of the same energy. Figure from De Naurois and Mazin (2015).

3.1.2 Cherenkov Radiation

A charged particle moving at high velocity v through a dielectric medium with refraction index n creates a polarization that is symmetrical in the azimuth direction but not along the axis of motion, resulting in a dipole field. Normally the radiation emitted by this dipole interferes destructively such that at some distant point from the particle track, the resulting field is zero. However, if the particle is moving at speeds greater than the phase velocity of light in the medium, c/n , then the resulting radiation will be in phase under a certain emission angle θ which is given by

$$\cos \theta = \frac{c}{vn}. \quad (3.4)$$

This results in the emission from each element of the particle track to propagate along a cone with semi-opening angle θ , as can be seen in the sketch in Figure 3.4.

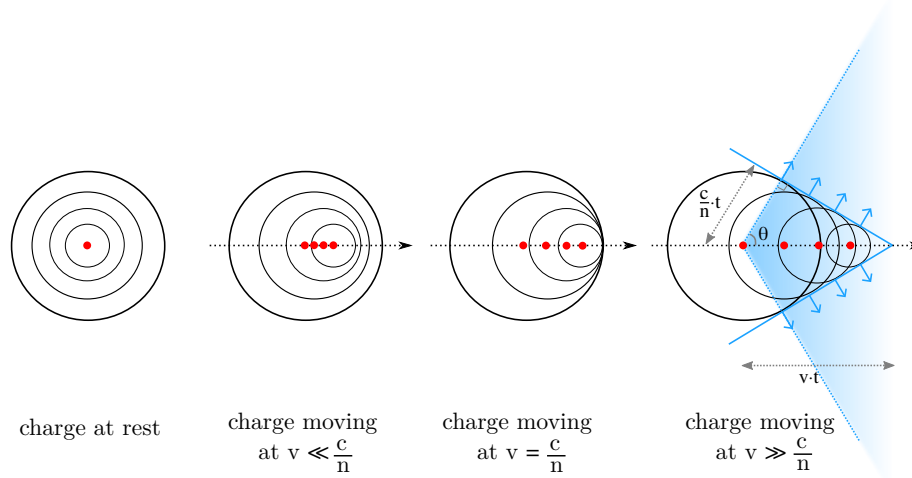



FIGURE 3.4: **Cherenkov radiation.** Sketch of the emission from a moving particle in a dielectric medium at different speeds. Image credit: Armelle Jardin-Blicq  (Jardin-Blicq, 2019).

As an EAS moves through the atmosphere, Cherenkov light is emitted when the charged particles in the showers move faster than the threshold velocity $\beta_{th} = v_{th}/c = 1/n$. In air at sea level, the refractive index is $n = 1.00029$. This translates to threshold energies of ~ 21 MeV and ~ 4.4 GeV for electrons and muons respectively. For water, $n = 1.33$, and the thresholds are then reduced to ~ 0.8 MeV and ~ 160 MeV respectively.

The number of Cherenkov photons N_γ produced by a particle of charge Z per path length dl between wavelengths λ_1 and λ_2 , is described by the Cherenkov yield,

$$\frac{dN_\gamma}{dl} = 2Z^2\pi\alpha \int_{\lambda_1}^{\lambda_2} (1 - (\beta n)^{-2}) \frac{d\lambda}{\lambda^2}, \quad (3.5)$$

where α is the fine-structure constant. Because of the wavelength dependence goes as $1/\lambda$, Cherenkov radiation is emitted mostly at short wavelengths, making it blue.

3.2 Imaging Atmospheric Cherenkov Telescopes

The central idea of the Imaging Atmospheric Cherenkov Telescope (IACT) technique is to image the nanosecond-long flashes of Cherenkov light produced by the EAS as they traverse the atmosphere. In this way, the atmosphere acts as a calorimeter in which the shower energy is deposited. This approach is able to achieve collection areas in the order of km^2 , required to detect the faint fluxes of astrophysical sources above a few TeV in a reasonable timescale.

As can be seen in the schematic picture in Figure 3.5, the telescopes located inside the Cherenkov light pool image the shower in their cameras. From this image,

the properties of the primary particle, such as its energy and direction can be reconstructed. When more than one telescope image the same shower, providing a stereoscopic view of it, the direction reconstruction becomes more accurate.

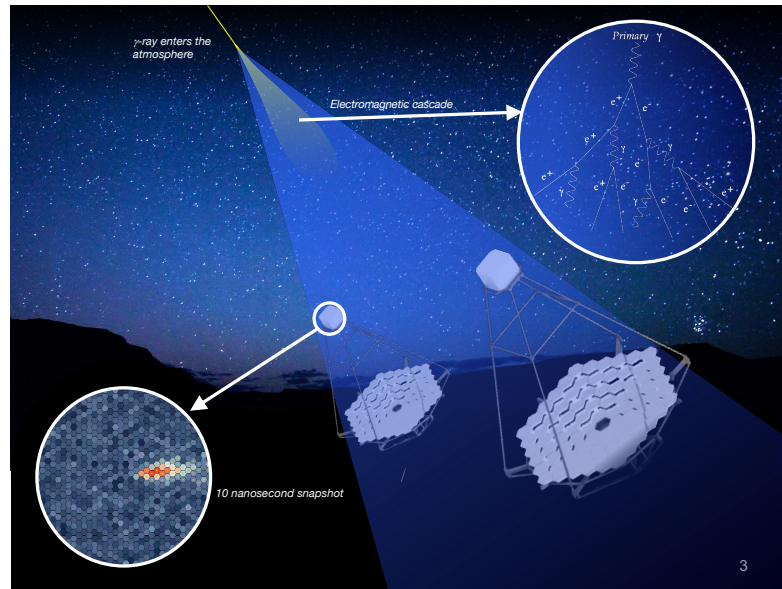



FIGURE 3.5: **The IACT technique.** Illustration showing the basics of the IACT technique. A gamma-ray enters the atmosphere and initiates an EAS, which in turn produces a cone of blue Cherenkov light. Telescopes inside this light pool detect the light and image the EAS. An example shower image in an IACT camera can be seen in the bottom left of the figure. Image credit: Richard White .

Because the Cherenkov light flashes are very faint blue optical light, IACTs can only operate during the night and are affected by bright moonlight and weather conditions, which limits their duty cycle to around a thousand hours of observations a year.

A detailed overview of the history of IACTs and the techniques that made their success possible can be found in Hillas (2013). Here we present a brief summary, with mentions of instruments that represented major steps in performance. The first generation of Cherenkov telescopes included the Fred Lawrence Whipple observatory, which in 1988 reported the detection of the Crab Nebula with a statistical significance of 9σ above 0.7 TeV (Weekes et al., 1989), making it the first ever VHE gamma-ray source. In that same year, the first VHE gamma-ray catalog was published (Weekes, 1988), including a total of 13 sources. The second generation of instruments was characterized by the use of the stereoscopic technique, that is, the presence of more than one telescope. The High Energy Gamma Ray Array (HEGRA) was made of five small IACTs, and it had improved angular resolution thanks to the stereoscopic observation mode. The following generation of IACTs is the current one, with instruments like the Major Atmospheric Gamma-ray Imaging Cherenkov (MAGIC) telescope, the VERITAS and the High Energy Stereoscopic System (H.E.S.S.), the later of which will be described with detail in the rest of this chapter. The future generation of IACT

arrays will be driven by the Cherenkov Telescope Array (CTA), see Section 3.2.2 for more details.

3.2.1 The H.E.S.S. Array

H.E.S.S. is an array of IACTs located in Namibia, at an altitude of 1,800 m. H.E.S.S. is sensitive to gamma-rays ranging from tens of GeV to tens of TeV. The array consists of five Cherenkov telescopes: four with mirror diameters of 12 m (referred to as CT1–CT4) placed in a square configuration and a single telescope at the center (CT5) with a mirror diameter of 28 m. A picture of H.E.S.S. can be seen in Figure 3.6. The small telescopes array is sensitive to gamma-rays of energies above hundreds of GeV (Aharonian et al., 2006), while the central, large telescope is able to detect fainter emission, which in turns translates to lower gamma-ray energies (Holler et al., 2015).

The CT1-4 telescopes have a Davies-Cotton configuration (Davies and Cotton, 1957) with a camera at the focal point. The mirror facets of CT5 are arranged in a parabolic shape. The cameras of the CT1-4 telescopes have 960 pixels, each equipped with a photomultiplier tube (PMT) resulting in a FoV of 5° . The current camera of the CT5 telescope has 1764 pixels and a FoV of 3.5° .

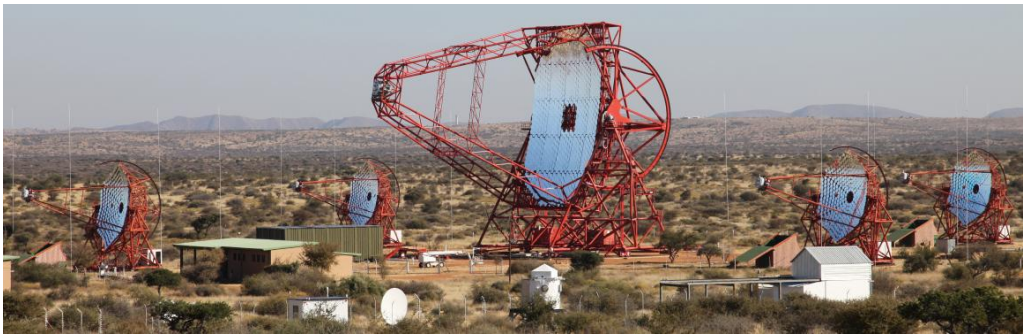


FIGURE 3.6: **H.E.S.S.**. Picture of the completed H.E.S.S. array in Namibia. Image credit: H.E.S.S. Collaboration.

H.E.S.S. started operations in 2003, when it was made up by only CT1-4. This era is referred to as the H.E.S.S. I phase. The cameras of these telescopes were later upgraded in 2016 (Ashton et al., 2020), starting the era referred as H.E.S.S. IU. The central telescope, CT5, was built in 2012, and the full array configuration is referred to as H.E.S.S. II. The CT5 camera was upgraded in 2019 (Bi et al., 2022). The array can be operated in three modes:

- **stereo mode:** only CT1-4 are considered. Only events that trigger two or more of the telescopes are recorded.
- **mono mode:** only CT5 is considered.
- **hybrid mode:** all five telescopes are considered. If CT5 is triggered, the event is recorded. If CT5 is not triggered, the remaining telescopes have the same requirement of two telescopes for the trigger as in the stereo mode.

H.E.S.S., like all IACTs, needs to be pointed to the target regions in the sky. This is done following an observation program that includes long-term monitoring of sources, target-of-opportunity observations and deep exposures on proposed regions. Observations are conducted in *runs* of 28 m duration.

3.2.2 The Cherenkov Telescope Array

The next generation of IACTs will be dominated by the CTA, the construction of which is already underway. It will be made up of two separate arrays, one in the Northern Hemisphere and one in the Southern one, in order to have full-sky coverage. Three different sizes of telescopes are planned:

- **Large-sized telescopes (LSTs):** A total of eight 23 m diameter telescopes will extend the energy range below 100 GeV.
- **Medium-sized telescopes (MSTs):** The core energy range of CTA (100 GeV to 10 TeV) will be covered by 40 12 m telescopes.
- **Small-sized telescopes (SSTs):** The highest energies above 10 TeV will be imaged with unprecedented resolution by 70 telescopes with 4 m mirror diameter.

More details on the organization, science goals and technical specifications of CTA can be found in CTA-Consortium (2019).

3.3 H.E.S.S. Data Reduction

In order to use the raw measurements of the Cherenkov flashes for the study of astrophysical sources, the data needs to be processed in a chain that includes multiple stages. In this section we will briefly describe the most important ones, with a special focus on gamma-hadron separation and instrument response functions, as they will be the topic of further chapters in this thesis.

3.3.1 Data Acquisition System

When a EAS is imaged by a telescope, that is, an individual camera is triggered, it sends a signal to the H.E.S.S. central trigger, which gathers the signals from the different cameras. The central trigger takes into account the time delays between the different signals and issues a decision on whether to accept or reject the event, based both on the time coincidence and the telescope multiplicity condition. If the event is accepted, the central trigger issues a confirmation of the cameras, which then send the image to the computer farm on site. A detailed description of the H.E.S.S. data acquisition system can be found in Balzer et al. (2014).

3.3.2 Calibration and Image Cleaning

In order to be able to reconstruct the physical properties of the EAS from the measured raw PMT data, the electronic response and the PMTs have to be accurately calibrated.

Each PMT i in the CT1-4 cameras records analog-to-digital converter (ADC) charge in two channels, a high-gain (HG) and a low-gain (LG) channel. From that quantity, the calibrated number of photoelectrons (p.e.) in each channel C_i is derived as

$$C_i^{HG} = \frac{ADC_i^{HG} - P_i^{HG}}{G_i^{HG}} \cdot FF_i \cdot B_i^{HG} \quad (3.6)$$

$$C_i^{LG} = \frac{ADC_i^{LG} - P_i^{LG}}{G_i^{HG}} \cdot (HG/LG)_i \cdot FF_i \cdot B_i^{LG}, \quad (3.7)$$

where P_i is the pedestal position, that is the mean ADC value recorded in the absence of any Cherenkov light. The flat-field coefficients (FF_i) take into account the relative efficiency of the different pixels. The broken-pixel flag B_i indicates whether that pixel has to be excluded. Reasons why pixels have to be excluded can be permanent malfunction but also temporary exclusion due to the presence of bright stars or satellites. The gain of the HG channel is denoted as G_i^{HG} , and the ratio between this value and the LG channel gain is $(HG/LG)_i$. Some of these calibration coefficients, such as the FF_i and G_i^{HG} values are derived from dedicated calibration runs, whereas others like the pedestal and $(HG/LG)_i$ ratio are directly derived from the data in each observation run.

The current camera installed in CT5 has only one gain channel which already provides the baseline-subtracted charge \tilde{C}_i , from which the calibrated number of photoelectrons is derived as

$$C_i = (\tilde{C}_i - P_i) \cdot FF_i \cdot B_i. \quad (3.8)$$

More details on the calibration of the CT1-4 H.E.S.S. cameras can be found in Aharonian et al. (2004).

The calibrated camera images are then cleaned to remove most of the noise, which in the case of H.E.S.S. is dominated by the Night Sky Background (NSB) noise. This is usually done using the so-called *tailcuts* cleaning method in which pixels in an image are required to be above a lower threshold $I_1 = 4$ p.e. and to have a neighbor above a higher one $I_2 = 7$ p.e. Thresholds of 5 p.e. and 10 p.e. are also used (Aharonian et al., 2006). Additionally to the tailcuts, a lower intensity threshold is also defined based on the width of distribution of pedestal values in each run, with only pixels that recorded 3 times more charge than the pedestal width being considered. Other cleaning methods that instead use the arrival time of the photoelectrons in order to distinguish the random NSB noise from the coherent Cherenkov signal are being developed.

3.3.3 Event Reconstruction and ImPACT Templates

From the calibrated and clean shower images, the properties of the EAS can be reconstructed. The most important quantities obtained in this step are the direction and the energy of the primary particle of the shower.

The simplest approach to reconstructing the direction of an incoming EAS is to use the Hillas parameters (Hillas, 1985), which approximate and parameterize the shower image as an ellipse. Figure 3.7 shows a schematic depiction of these parameters in the case of a stereoscopic observation. For the case of mono observations, the direction can still be reconstructed using the major axis of the ellipse, however this approach can be degenerate and is less precise.

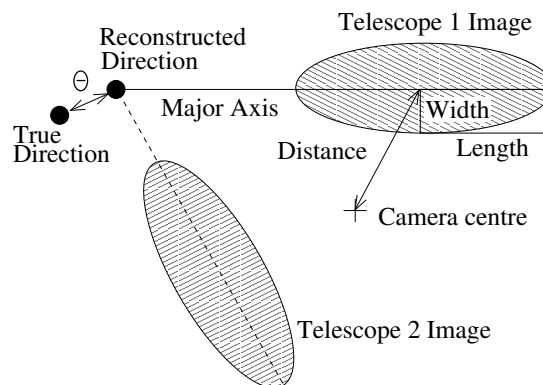


FIGURE 3.7: **Hillas parameters.** Sketch illustrating the Hillas parameterization of the shower images. The shape recorded by the camera is approximated as an ellipse, with a certain width and length. The major axis of this ellipse indicates the direction of the incoming shower, which can be reconstructed with higher accuracy if the same shower is imaged by more than one telescopes as shown in the diagram. Figure from Aharonian et al. (2006).

More energetic primary particles produce more secondary particles in the shower which in turn result in more Cherenkov light. The total charge recorded by the cameras then depends on the primary particle energy and the distance between the telescope and the ground impact point of the shower core, referred to as impact distance. The zenith angle direction of the incoming particle also plays a role, as the further away from zenith, the more atmosphere the particle traverses, thus affecting the shower development.

A more sophisticated approach which is widely used in the current generation of IACTs is the production of libraries of templates of simulated gamma-ray images. The Image Pixel-wise fit for Atmospheric Cherenkov Telescopes (ImPACT, Parsons and Hinton, 2014) algorithm is one of such methods developed for H.E.S.S.. The templates are built with a full Monte Carlo (MC) gamma-ray air shower simulation, followed by ray-tracing of the telescope optics and simulation of the instrument electronics. Using the result of the Hillas-based reconstruction as a seed, the recorded image is fitted against these templates using a maximum likelihood method. This

fit is computationally expensive, so it is only performed after a first round of background rejection is applied. For each event this process results in an image of what the most similar gamma-ray event would look like in each of the telescopes (see Chapter 5), and the reconstructed parameters of such event, including the direction and the energy. Figure 3.8 shows a comparison of the energy and angular resolution of the Hillas parameter approach and the ImPACT likelihood fit.

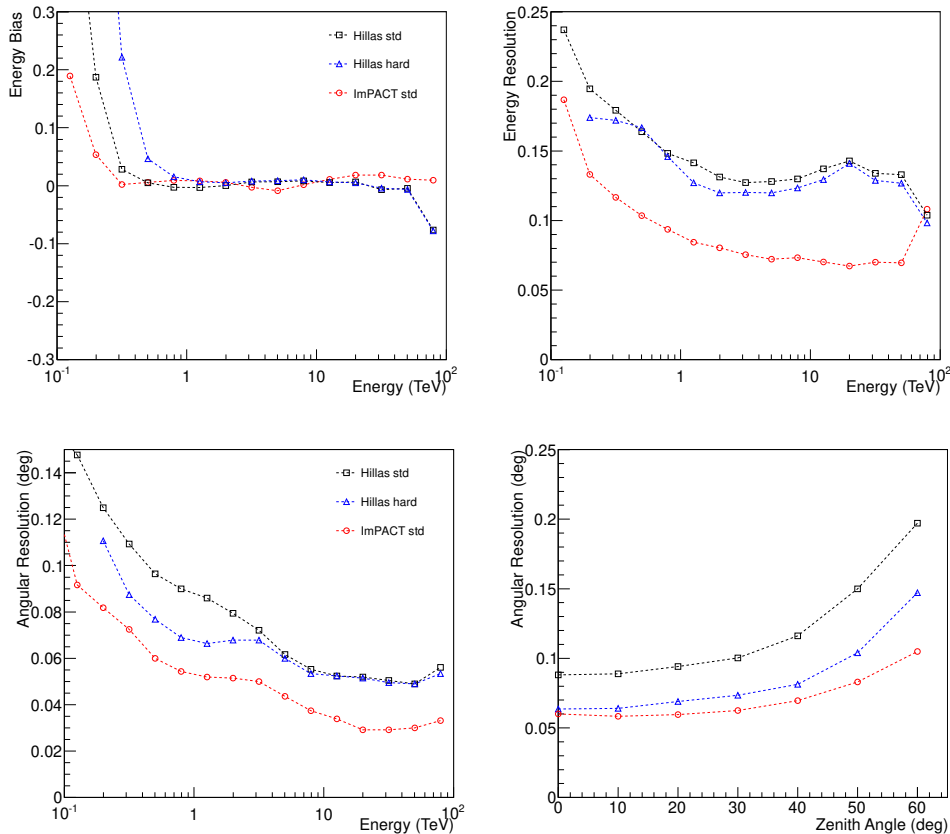


FIGURE 3.8: **Performance of the ImPACT reconstruction.** Comparison of the energy bias (top left), energy resolution (top right), and angular resolution as a function of both energy (bottom left) and observation zenith angle (bottom left) for the reconstruction using just the Hillas parameters (black and blue lines) and the one using the ImPACT method (red lines). The ImPACT reconstruction outperforms the simpler methods in all cases. Adapted from Parsons and Hinton (2014).

3.3.4 Event Selection and Gamma-Hadron Separation

Differences in shower structure have been exploited in order to distinguish gamma-rays and hadronic showers since the dawn of VHE gamma-ray astronomy. The Hillas parameters introduced in the previous section, mainly the width and length, have been the basis to most gamma-hadron discrimination methods employed in the existing Cherenkov telescopes.

The first generation telescopes employed simple *box-cuts*, that is, defining a threshold for each of the relevant parameters below or above which an event is considered gamma-ray like (Aharonian et al., 2000). Second generation instruments, like the H.E.S.S. telescopes have developed a more sophisticated approach, through the use of Boosted Decision Trees (BDTs, Ohm et al., 2009). BDTs are a class of Machine Learning algorithm that allows for the extension of simple cut-based analysis techniques described above to multivariate algorithms. They are made of a large number of nodes, each of which defining a binary criterion on one of the parameters. An event, described by a set of parameter values, is then ran through this structure until it ends up in a final node or *leaf*, where it is assigned a value of the BDT response variable, ζ . This value can then be used to classify the event as a signal or background event. In the application of this method to H.E.S.S. data, ζ is usually transformed to represent the gamma-ray efficiency associated with a threshold in the actual BDT response in order to easily select equivalent thresholds across the full energy range (see Section 4.2 of Ohm et al., 2009).

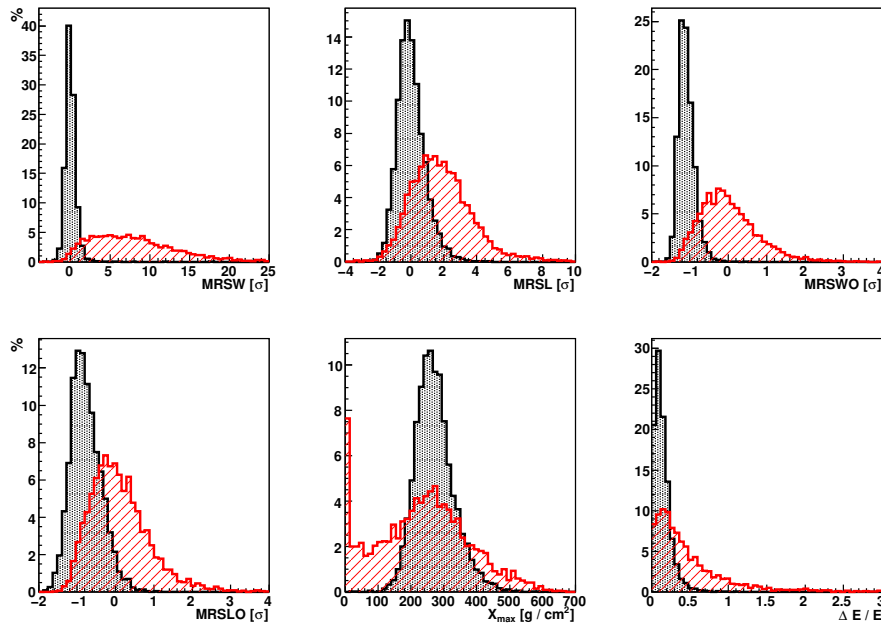


FIGURE 3.9: **Distributions of the input parameters to the BDTs.** The figure shows the distribution of each of the parameters considered by the multivariate approach for simulated gamma-rays (black) and background from off-runs (red). The parameters shown, from top to bottom and left to right are: the Hillas width and length derived from gamma-ray simulations and averaged over telescopes (MRSW, MRSL), the Hillas width and length derived from background data and averaged over telescopes (MRSWO, MRSLO), the height of shower maximum (X_{\max}) and the spread in energy reconstruction averaged over the telescopes. Figure from Ohm et al. (2009)

Based on this BDT classification, several sets of analysis cuts can be developed, optimized for the different expected spectral properties of gamma-ray sources (see

Section 4.2 of Ohm et al., 2009). Each set of analysis cuts is defined by an pre-selection total intensity threshold and a cut on ζ . Two of these cuts typically used for the analysis of Galactic sources are the *standard* cuts optimized for a source with a Crab Nebula-like spectral index of 2.6 and 10% of the Crab Nebula flux and the *hard* cuts, optimized for a faint source (1% of Crab flux) with spectral index 2. The specific values corresponding to each cut set are collected in Table 3.1. The values of the intensity cut are applied to the cleaned images, and per telescope. The higher minimum total intensity threshold of the *hard* cuts translates into a higher energy threshold but also higher quality events and more precise reconstructed parameters, such as core location or energy.

Configuration	Total intensity threshold (p.e.)	ζ threshold
<i>standard</i>	60	0.84
<i>hard</i>	200	0.8

TABLE 3.1: Selection cuts defining the *standard* and *hard* analysis cuts. Note that the total intensity cut is also to the input training data used to optimize the BDT algorithm weights used for the estimation of ζ .

The performance of background rejection algorithms is tested and optimized using simulated gamma-ray events and, when available, real data of the cosmic-ray background. For this purpose, what is referred to as *off-runs* are used, that is, observations in which the telescopes are pointed at fields without a known gamma-ray source. These off-runs are typically the result of dedicated observations of known empty fields, or also observations of extragalactic objects like dwarf spheroidal galaxies that did not yield a gamma-ray detection (Abramowski et al., 2014). These are not completely free of gamma-ray events, due to large-scale diffuse emission like the extragalactic gamma-ray background and also due to possible undetected faint gamma-ray sources. However, the relative fluxes of background cosmic-rays to these gamma-ray sources make it safe to neglect this contribution. It would also be possible to use simulations of proton-initiated showers in order to eliminate this contamination. However, due to uncertainties in the hadronic models used for high-energy particle interactions (Parsons and Schoorlemmer, 2019; Pastor-Gutiérrez et al., 2021), there are significant differences between the properties of measured background events and those that result from simulations. For this reason whenever it is possible, the background is characterized only using real data, as it is not dependent on the agreement between data and simulations.

At low energies - that is, below a few TeV - this method has shown to be very effective (Ohm et al., 2009). However, the background rejection power of this approach becomes limited above several tens of TeVs. In Chapter 4 we address this issue by proposing a novel approach to background rejection that uses the central telescope of H.E.S.S. as a muon veto.

3.3.5 Instrument Response Functions

The resulting product of the event reconstruction and gamma-hadron separation is a list of gamma-ray-like events. For each event the minimum information kept is the reconstructed sky coordinate, the event energy and the time of arrival. These events can then be binned into a map in sky coordinates to build a counts map. In order to extract meaningful physical quantities from the measured counts from a putative source, the instrument response to a given astrophysical flux has to be understood. This includes the level of cosmic-ray background that survive the gamma-hadron separation, the effective area of the detector, and the accuracy and precision of the energy and direction reconstruction. This information is stored in the instrument response functions (IRFs), which describe the combined detection abilities and precision of an instrument data-taking and reconstruction procedure.

In IACT data analysis, the IRFs are usually split into

- **Effective area (AEFF):** The effective area is the collection area of the detector, and it depends on the energy of the photons, the offset from the pointing position, the observation zenith angle and the optical efficiency of the telescopes. It is typically combined with the observation time or **exposure** (t_{live}), which does not depend on energy, to derive the so-called **effective exposure**. This quantity has units of $\text{cm}^2 \cdot \text{s}$ and given a flux from a source in units of $\text{photons}/\text{cm}^2/\text{s}$, the expected excess counts can then be derived by taking the ratio of those two quantities. Figure 3.10 shows an example effective area table for a H.E.S.S. observation at 45° zenith with the *hard cuts*.

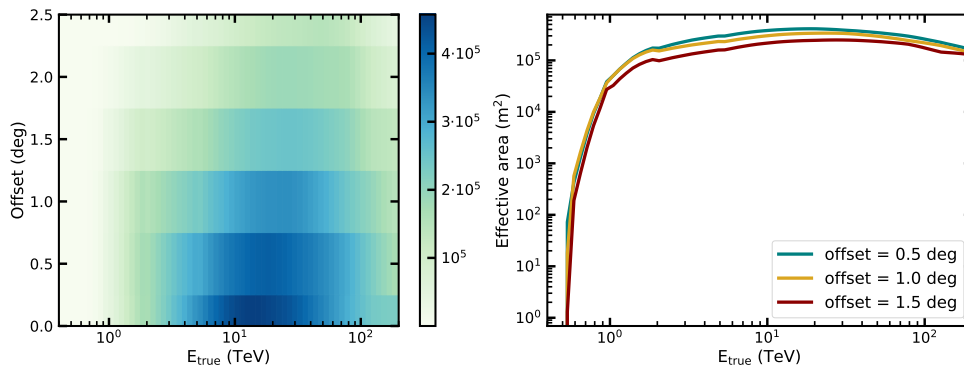


FIGURE 3.10: **Effective area.** *Left:* Example effective area table for a H.E.S.S. observation at 45° zenith. *Right:* Effective area curves as a function of energy for some selected offsets.

- **Energy dispersion matrix (EDISP):** Represents the probability that a gamma-ray with energy E_{true} will be reconstructed with energy E_{reco} . The left panel of Figure 3.11 shows an example matrix for a H.E.S.S. observation at 45° zenith with the *hard cuts*. A useful quantity derived from this matrix is the energy bias, and example of which is shown in the right panel of Figure 3.11.

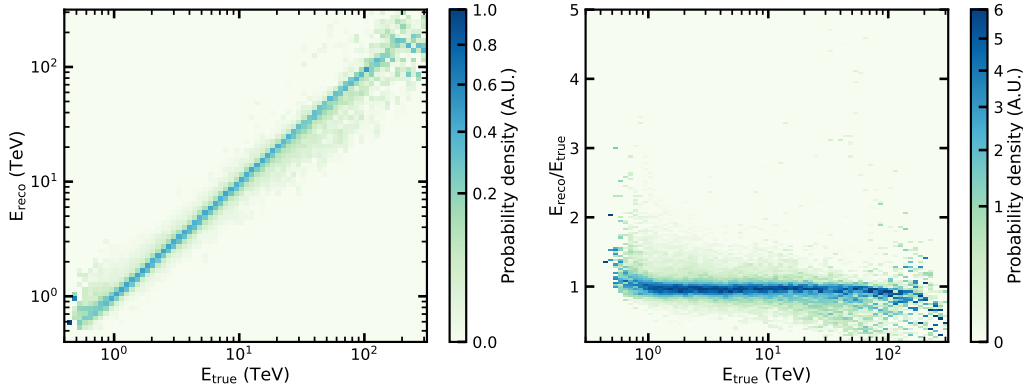


FIGURE 3.11: **Energy dispersion matrix.** *Left:* Example energy dispersion matrix for a H.E.S.S. observation at 45° zenith. *Right:* Energy bias derived from the energy dispersion matrix.

- **Point-spread function (PSF):** Represents the reconstruction accuracy in the direction of the incident gamma-ray. For IACTs, it depends on the true energy of the photons, the offset from the pointing position, the observation zenith angle and the optical efficiency of the telescopes. It is usually summarized by the containment radius, or angular distance to contain a certain fraction of the signal. Figure 3.12 shows an example PSF curve for a H.E.S.S. observation at 45° zenith with the *hard cuts* as well as the dependence of the 68% and 95% containment radius as a function of energy for offset 0.5° .

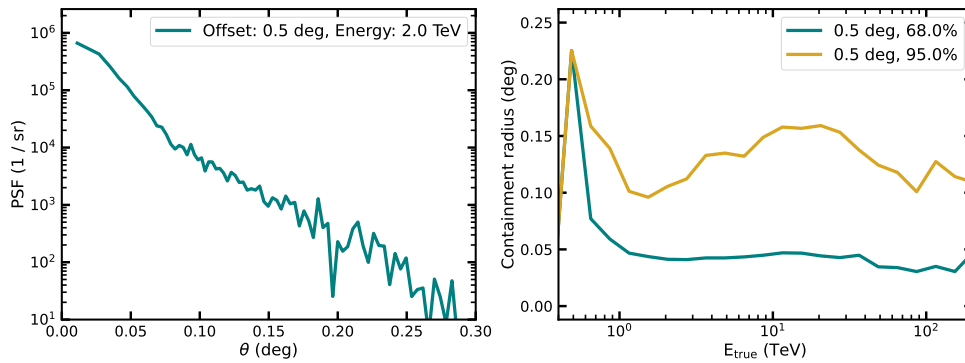


FIGURE 3.12: **Point-spread function.** *Left:* Example PSF at a given energy and offset for a H.E.S.S. observation at 45° zenith. *Right:* 68% and 95% containment radius as a function of energy for offset 0.5° .

- **Background model (BKG):** Represents the expected remaining hadronic background after gamma-hadron separation due to misclassified events. It depends on the reconstructed energy and the offset from the pointing position. Figure 3.13 shows an example background curve for a H.E.S.S. observation at 45° zenith with the *hard cuts*.

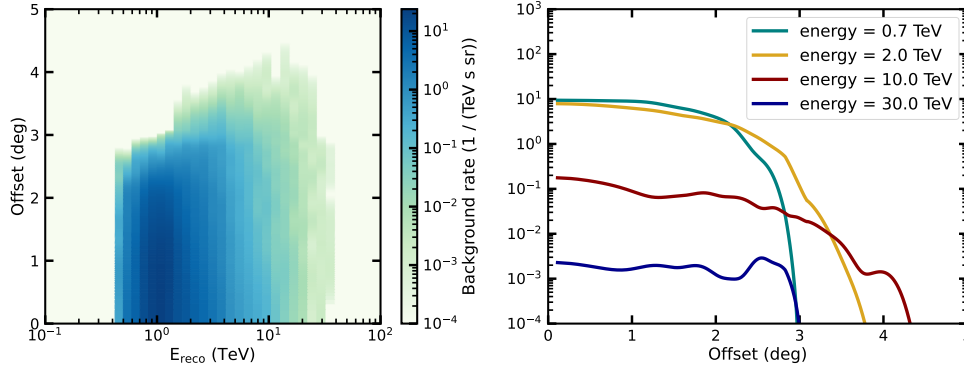


FIGURE 3.13: **Background model.** *Left:* Example background model table for a H.E.S.S. observation at 45° zenith. *Right:* Background rates as a function of offset from the pointing position for several values of the energy.

The IRFs are derived using gamma-ray simulations, with the exception of the background for which either off-runs or hadronic simulations are used. Good agreement between the data and the simulations is thus essential to avoid systematic errors. All the IRFs of IACTs depend on the offset from the pointing position. During data reduction, they are projected into the sky, often assuming radial symmetry. Deviations of this symmetry are sometimes considered, in particular for the background model (see Section 3.3.6).

With this factorization of the instrument response, the predicted excess counts from a source at the sky location \vec{x}_{true} and flux $\phi(\vec{x}_{\text{true}}, E_{\text{true}})$ can be derived as

$$N_{\text{pred}}(\vec{x}_{\text{reco}}, E_{\text{reco}}) = N_{\text{BKG}}(\vec{x}_{\text{reco}}, E_{\text{reco}}) + t_{\text{live}} \int_{\vec{x}_{\text{true}}} d\vec{x}_{\text{true}} \int_{E_{\text{true}}} dE_{\text{true}} R(\vec{x}_{\text{reco}}, E_{\text{reco}} | \vec{x}_{\text{true}}, E_{\text{true}}) \phi(\vec{x}_{\text{true}}, E_{\text{true}}) \quad (3.9)$$

where N_{BKG} is the predicted background counts derived from the background model (see Section 3.3.6) and the response $R(\vec{x}_{\text{reco}}, E_{\text{reco}} | \vec{x}_{\text{true}}, E_{\text{true}})$ is the combination of the remaining IRFs:

$$R(\vec{x}_{\text{reco}}, E_{\text{reco}} | \vec{x}_{\text{true}}, E_{\text{true}}) = \text{AEFF}(\vec{x}_{\text{true}}, E_{\text{true}}) \cdot \text{PSF}(\vec{x}_{\text{reco}} | \vec{x}_{\text{true}}, E_{\text{true}}) \cdot \text{EDISP}(E_{\text{reco}} | \vec{x}_{\text{true}}, E_{\text{true}}) \quad (3.10)$$

The IRFs are also used to select ranges of the reconstructed parameters, such as the energy or the offset from the pointing position, to be considered *safe* to use in the analysis of the data. This is typically done by imposing a maximum threshold on the energy bias, or a minimum fraction of the total effective area.

More information on the different IRFs and their constituents can be found in the documentation of the so-called *gamma-astro-data-format* (GADF¹, Nigro et al., 2021), an initiative that aimed to define a unified standard for the data and IRFs of gamma-ray instruments (see Chapter 5 for more details).

¹<https://gamma-astro-data-formats.readthedocs.io/en/latest/>

3.3.6 Background Modeling and Estimation

The correct characterization of the residual hadronic background is crucial to accurately determine the number of excess counts measured. In this section we will briefly describe the procedure to derive a background model from off-runs and some of the most common methods to obtain the predicted number of background counts from such a model.

Background Model Construction

The background model describes the response of the camera to events that are erroneously identified as gamma-rays by the gamma-hadron separation. It contains the expected background event rate as a function of reconstructed energy and camera coordinates. In the simplest case, the camera coordinate is the offset from the pointing position, and radial symmetry is assumed. This is referred to as a 2D background model. However, one can also build the background model using both radial and azimuthal camera coordinates, in the so-called 3D case. Deviations from the radial assumption are expected at relatively low energies.

To construct the background model, off-runs from the relevant instrumental eras are selected, and the events recorded in them after gamma-hadron separation are binned into a histogram of energy and camera coordinates, taking into account exclusion regions for possible gamma-ray sources. A full description of the procedure to make both 3D and 2D background models can be found in Mohrmann et al. (2019).

Background Estimation

The background model provides the shape of the expected hadronic background, as well as the average rate. However, run-to-run variation in the trigger rate due to, for example atmospheric conditions or the degradation of the hardware, mean that this average rate needs to be adjusted to the actual conditions of the observation run. This is done in general terms by ensuring that the number of counts in sky regions where no sources are expected matches the prediction of the background counts, or directly measuring the background level from said regions. Note that this assumes that the spatial properties of the expected background are not affected, which is not necessarily true for all situations. A detailed description and comparison of the different methods can be found in Berge et al. (2007). Here we will briefly describe the three most relevant to this thesis.

- **Ring background:** For each of the pixels in a sky-map, a ring around it is used to provide an estimate of the number of expected background counts, taking into account exclusion regions and the shape of the background model integrated in energy (see Figure 3.14). The radius of the ring can be fixed or adapt to the exclusion regions nearby each pixel, in order to ensure that enough pixels in the ring fall outside these regions. It is typically used for morphological

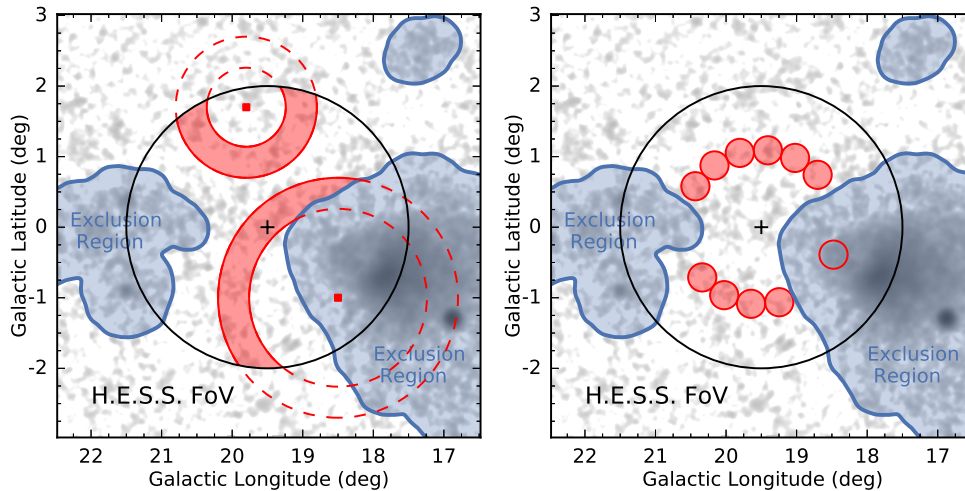


FIGURE 3.14: **Ring and reflected background.** *Left:* Illustration of the ring method. The red rings illustrate the regions in which the background is estimated for two positions in the FoV. The ring size in each case is adaptively enlarged to ensure an adequate background estimate. The black circle represents a 2° FoV around the pointing position (black cross). *Right:* Illustration of reflected region background estimation method. The empty red circle represents the ON region, whereas the filled ones represent the OFF regions from which the background level is measured. Adapted from H.E.S.S. Collaboration et al. (2018).

analysis without energy dependence. Only the spatial shape of the background model is considered.

- **Reflected regions background:** For each observation run, the background level inside of an ON region of a certain shape and size is estimated by measuring the number of counts in OFF regions of the same shape and size and offset from the pointing position as the ON region but outside of exclusion regions (see Figure 3.14). A background model is not required since this method assumes that the camera response is radially symmetric. However, it can generally only be used for spectral analysis, as the spatial dimension is lost when grouping the pixels inside of the ON region.
- **FoV background:** When performing combined spectro-morphological analysis (see Section 3.5.5), a third method is used. In this approach, the background model is projected into the sky in different energy bands, and in like the other methods, an exclusion mask is defined to cover known and expected sources. For each run, the counts predicted by the model outside of this exclusion mask are compared to the counts measured in the same region run-wise by fitting two parameters: a normalization and a tilt that varies the spectral shape, assuming a power-law energy dependence. This procedure corrects the background model for possible variations due to atmospheric conditions and instrumental degradation, as described in Mohrmann et al. (2019).

3.4 Particle Detector Arrays

A complementary approach to the detection of VHE gamma-rays are particle detector arrays. Instead of imaging the entire shower in the atmosphere, particle detector arrays capture the properties of the shower as it passes through the detectors, usually water volumes equipped with PMTs. Particle detector arrays are usually located at higher altitudes than IACTs, in order to be closer to the height of shower maximum. The advantage of this technique is that it does not require ambient darkness, as the relevant Cherenkov light is emitted inside light-tight tanks. This dramatically increases the duty-cycle from the $\sim 10\%$ of IACTs to almost 100%. The continuous observation allows an unbiased view of the sky, as a large fraction of it is observed all the time, without the need to a priori identify interesting pointing positions. Particle detector arrays also have a huge FoV, which makes them ideally suited for the study of fast transients and large-scale structures.

An overview of the history of the early particle detector array experiments can be found in Hillas (2013). The two largest currently operating instruments are the High Altitude Water Cherenkov (HAWC) observatory and the Large High Altitude Air Shower Observatory (LHAASO). The Southern Wide-field Gamma-ray Observatory (SWG0) is a planned array that is currently in the research and development phase. In the rest of this section, a brief description of the HAWC observatory and the SWGO is presented.

3.4.1 The HAWC Observatory

The HAWC observatory is a wide-field particle detector array situated on the flanks of the Sierra Negra in Mexico. It is made up by 300 water Cherenkov detectors (WCDs) of 4.5 m height and 7.3 m diameter. Each WCD is equipped with four PMTs which are submerged in 200 m³ of purified water. Three of the PMTs are 8 inch Hamamatsu PMTs arranged in a triangle, surrounding a central 10 inch Hamamatsu PMT. HAWC is sensitive to gamma-rays and cosmic rays in the energy range from a few hundreds of GeV to more than a hundred TeV with a wide FoV of almost 2 sr.

The HAWC observatory has been fully operating since 2015. In late 2018 a major upgrade was completed with the addition of a sparse outrigger array of 345 smaller WCDs surrounding the main array. This upgrade extended the instrumented area by a factor 4, dramatically improving the ability to reconstruct the properties of the highest energy showers, which are normally too large to be fully contained in the main array (Marandon et al., 2019).



FIGURE 3.15: **The HAWC observatory.** Picture of the completed HAWC array including the outrigger upgrade. Image credit: The HAWC Collaboration.

Data Acquisition System and Calibration

The HAWC data-taking and processing is entirely automatized, with a dedicated farm of computers and electronics installed at the site. When shower particles traverse the water tanks, they produce Cherenkov light which is recorded by the PMT. Each PMT outputs a pulse from which the times of arrival of the particles and the amount of charge in p.e. are calibrated. More details can be found in Abeysekara et al. (2017).

Event Reconstruction

After the data from individual PMTs has been calibrated, the shower parameters can be reconstructed from the combined shower slice image made up by all the PMTs in the array that were triggered by it. Only showers activating more than 6% of the total channels are collected for further reconstruction. The fraction of the array that is triggered by a shower has considerable implications on the accuracy of the resulting reconstructed parameters. Small showers have limited information and can be contaminated by other small showers arriving at the same time near the array. Higher energy showers, which trigger a large fraction of the detector, are better reconstructed as they dominate over the noise. At the highest energies however, showers can saturate the detector even when the core falls outside of the array, which makes the determination of their energy and direction difficult. For this reason, the data is divided into different bins depending on the fraction of the available PMTs triggered by the air shower, a quantity referred to as f_{Hit} . The different f_{Hit} bins are defined in Table 3.2.

Bin number	Low edge	High edge
1	0.067	0.105
2	0.105	0.162
3	0.162	0.247
4	0.247	0.356
5	0.356	0.485
6	0.485	0.618
7	0.618	0.740
8	0.740	0.840
9	0.840	1.00

TABLE 3.2: Event size (f_{Hit}) bins. Bins are defined from the fraction of PMTs triggered by each event.

Bin	Low edge (TeV)	High edge (TeV)
a	0.316	0.562
b	0.562	1.00
c	1.00	1.78
d	1.78	3.16
e	3.16	5.62
f	5.62	10.0
g	10.0	17.8
h	17.8	31.6
i	31.6	56.2
j	56.2	100
k	100	177
l	177	316

TABLE 3.3: The energy bins. Note that the first two bins are not used in the analysis as the estimate is highly biased.

The value of f_{Hit} is only weakly correlated with the energy of a shower (see Figure 3.16). In order to estimate the energy on an event-by-event basis, more advanced algorithms have been developed. The ground-parameter (GP) algorithm is based on the charge density deposited at the ground by the shower. The neural network (NN) algorithm estimates energies with an artificial neural network that takes as input several quantities computed during the event reconstruction. A detailed overview of both algorithms can be found in Abeysekara et al. (2019). Energy bins are typically defined beforehand in HAWC analysis and referred to with letter names, as described in Table 3.3. The combination of event sizes and energy bins leads to a 2-dimensional bin scheme, with 108 analysis bins resulting from the combination of each event size bin 1 to 9 with the 12 energy bins. However, only a subset of these bins are populated with enough event statistics, for example, low energy events are very unlikely to have large event sizes.

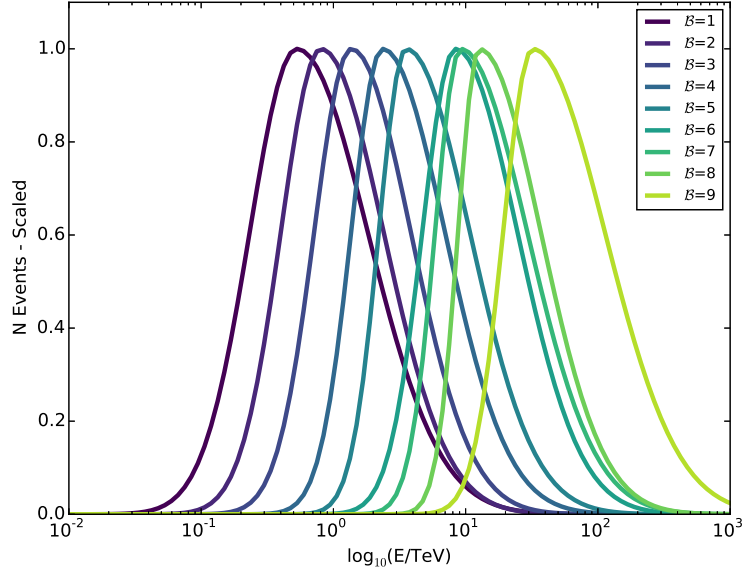


FIGURE 3.16: f_{Hit} bins and event energy. True energy distribution of photons from a simulated source with Crab Nebula-like spectrum and declination for the different f_{Hit} bins (indicated with \mathcal{B}), summed across a transit of the source. From Abeysekara et al. (2017).

The direction of the shower is reconstructed by making use of the gradient in arrival times of photons in the shower plane. To first order, the EAS particles arrive on a plane defined by the speed of light and direction of the primary particle. A number of effects lead to a deviation from this planar shape and the presence of curvature (see Abeysekara et al. (2017) for a detailed overview). A curvature correction derived from gamma-ray simulations is applied to account for this effect. The resulting shower plane is fit to the data, resulting in an estimate of the direction of the primary particle.

Gamma-Hadron Separation

In each of the 108 analysis bins, gamma-hadron cuts are optimized using a cut in two variables that separate the properties of hadronic and gamma-ray showers.

- **Compactness (\mathcal{C}):** The variable $CxPE40$ is the effective charge measured in the PMT with the largest effective charge outside a radius of 40 meters from the shower core. It reaches higher values for hadronic events than for gamma-ray events. With it, the compactness of the shower is defined as

$$\mathcal{C} = \frac{f_{\text{Hit}}}{C_{xPE40}}. \quad (3.11)$$

- **"Clumpiness" (\mathcal{P}):** This variable is defined using the lateral distribution of the shower. For each of the PMTs, the logarithm of the measured charge ζ_i is compared to the average measured charge in all the PMTs in an annulus centered in the core of the shower and containing the PMT with a width of 5 m ($\langle \zeta_i \rangle$).

The variable \mathcal{P} is then computed for the combined hits from a shower N as

$$\mathcal{P} = \frac{1}{N} \sum_{i=0}^N \frac{(\zeta_i - \langle \zeta_i \rangle)^2}{\sigma_{\zeta_i}^2}, \quad (3.12)$$

where the σ_{ζ_i} is determined from a study of very likely gamma-ray events arriving from the vicinity of the Crab Nebula sky location.

More details on the gamma-hadron separation employed by the HAWC observatory can be found in Abeysekara et al. (2017).

Background Estimation

Even with gamma-hadron separation, the HAWC data is still dominated by hadronic cosmic ray events, especially so in low f_{Hit} bins. The estimation of the level and shape of this background is typically done using the so-called direct integration method (Abdo et al., 2012). This method deals with the expected dipole cosmic-ray anisotropy by splitting the data into time intervals (usually 2h) and estimating the background in each of these intervals, which are then added up to build a sky map. Note that unlike IACTs, the wide-field of HAWC allows to continuously sample more than enough sky areas devoid of known gamma-ray sources, allowing a much more accurate characterization of the background rate. Additionally, water Cherenkov detectors are also less sensitive to the atmospheric condition and NSB than IACTs, which in turn translates to a more stable background.

3.4.2 The Southern Gamma-ray Wide-field Observatory

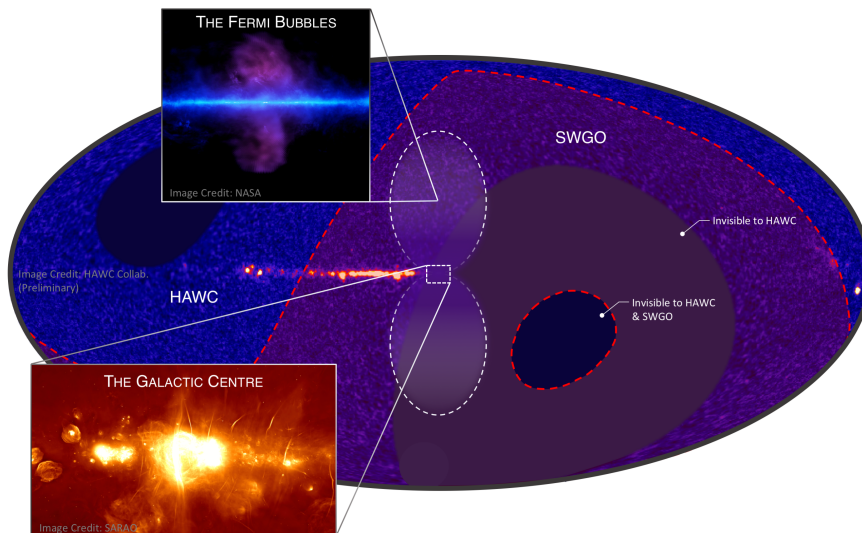



FIGURE 3.17: **The case for a wide-field observatory in the Southern Hemisphere.** The HAWC full-sky significance map is shown together with the expected FoV of SWGO. Image credit: Richard White .

Both HAWC and LHAASO are located in the Northern hemisphere, meaning that a large fraction of the sky, which includes the Galactic center (see Figure 3.17) is not accessible to them in the range where the instrument performance is best. For that reason, the SWGO has been proposed in order to cover the gap and complete the TeV coverage of the sky, complementary to the CTA. More details on the current status of the SWGO can be found in Hinton and SWGO Collaboration (2022).

3.5 Gamma-Ray High-Level Analysis

After event reconstruction and gamma-hadron separation have been performed, the data from gamma-ray observatories can be structured essentially in the same way, and the statistical procedures used in the analysis are generally independent on the type of instrument that took the data.

In this section we will summarize the different steps in the high-level analysis of gamma-ray data using the observation runs of the Crab Nebula region included in the H.E.S.S. public data release (H.E.S.S. Collaboration, 2018) and the *Gammapy* analysis software (Deil et al., 2017). The Crab Nebula is usually considered to be the *standard candle* of TeV astronomy, as it is the brightest steady point-like source in the sky. It is typically assumed to be a point-like source despite the fact that its extension at TeV energies has actually been measured (H.E.S.S. Collaboration, 2020), because its size is small enough to be below the sensitivity of most analyses. Observations of it are routinely used to validate the performance of the analysis chain, including the characterization of the IRFs.

3.5.1 *Gammapy*

Gammapy is a community-developed Python² package for gamma-ray astronomy. It builds upon the standard scientific Python packages: *numpy* (Harris et al., 2020), *scipy* (Virtanen et al., 2020), *matplotlib* (Hunter, 2007) and *astropy* (Astropy Collaboration et al., 2013). *Gammapy* will be used as the base package for the science tools of the future CTA. *Gammapy* is routinely used for the analysis of IACTs data (Mohrmann et al., 2019; Nigro et al., 2019) and in Chapter 5 its use will be extended and validated for the analysis of data from particle detector arrays.

The analysis workflow in *Gammapy* begins with a list of events selected for gamma-ray-likeness and the associated IRFs. The events are then binned into multidimensional sky maps, using pixelization schemes such as the World Coordinate System (WCS, Calabretta and Greisen, 2002) or HEALPix (Górski et al., 2005). In most cases, the maps have an additional energy axis. The IRFs are then projected

²<https://www.python.org/>

into the same geometry. The background is estimated using one of the methods described in Section 3.3.6. The resulting maps are bundled into a so-called `MapDataset`³, which is then the input to all the procedures described in the rest of the section.

3.5.2 Significance of the Observation

The first step to the high-level analysis of gamma-ray data is to determine whether there is a significant gamma-ray signal. In general this is done via hypothesis testing, where either a model or an excess of counts (\mathcal{H}_1) is tested against a null hypothesis (\mathcal{H}_0) in which no source is present. The difference in test statistic (TS), defined as,

$$TS = -2 \log \left(\frac{\mathcal{L}(\mathcal{H}_0)}{\mathcal{L}(\mathcal{H}_1)} \right) \quad (3.13)$$

where $\mathcal{L}(\mathcal{H})$ is the likelihood of hypothesis \mathcal{H} , is used as a means to assess the probability that the measurement is the product of a statistical fluctuation of the background instead of a real source. For situations where there is only one degree of freedom, the significance (σ) is calculated as $\sigma = \sqrt{TS}$. In case of a negative signal, that is, when a negative fluctuation of the background is measured, $\sigma = -\sqrt{TS}$ by convention. The threshold to claim that a measured excess is due to the detection of a gamma-ray source is typically taken to be 5σ . An excess with that significance has a probability of being produced by a background fluctuation of about one-in-a-million.

A typical example of this procedure is the computation of a significance map to determine whether any gamma-ray sources are present in a given sky region. This can be done in two different ways:

- **Based on a model:** For each pixel of the map, the measured excess counts are compared with the prediction of a model with the normalization set free. The resulting value of the significance would then depend on the choice of model, which includes both the morphology of the source (extended, point-like) and its spectral behavior.
- **Based on excess:** For each pixel of the map, the measured counts are compared with the expected or measured background in that pixel. The TS is computed using the expressions in Li and Ma (1983). The resulting value is not model-dependent, although when producing maps, pixels are grouped within a certain angular size, which in turn influences the spatial size of the structures that will arise in the significance map.

Figure 3.18 shows a counts map from the Crab Nebula region of the public H.E.S.S. data release, together with the expected background map derived using the FoV method and the resulting significance map derived from the excess. A top-hat smoothing is applied with correlation radius of 0.1° .

³<https://docs.gammapy.org/1.0/api/gammapy.datasets.MapDataset.html#gammapy.datasets.MapDataset>

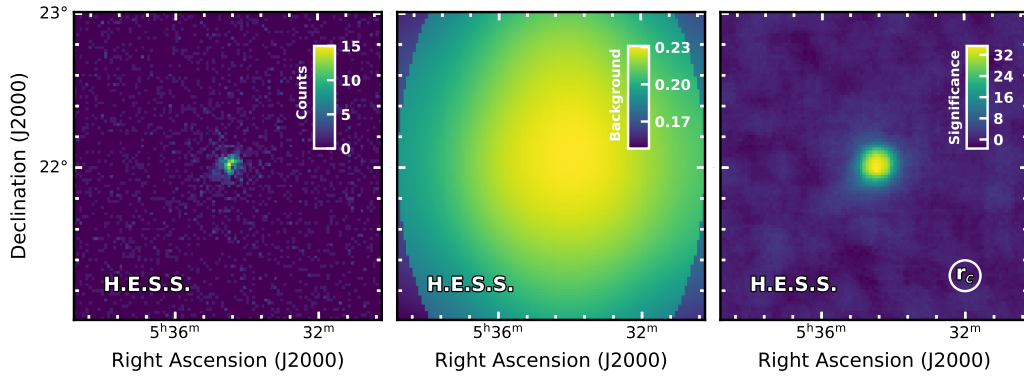


FIGURE 3.18: **Counts, background and significance maps.** *Left:* Counts sky-map of the Crab Nebula region. *Middle:* Expected background counts map. *Right:* Significance of the excess counts over the background of nearly isotropic cosmic rays. The top-hat filter with radius r_c used to smooth the counts and background maps is drawn in the image as a white circle.

The significance map can also be used to assess the impact of systematic uncertainties introduced by the background estimation, as the distribution of significance values in regions where no source is present should be a Gaussian function centered in 0 with width 1 as shown in Figure 3.19.

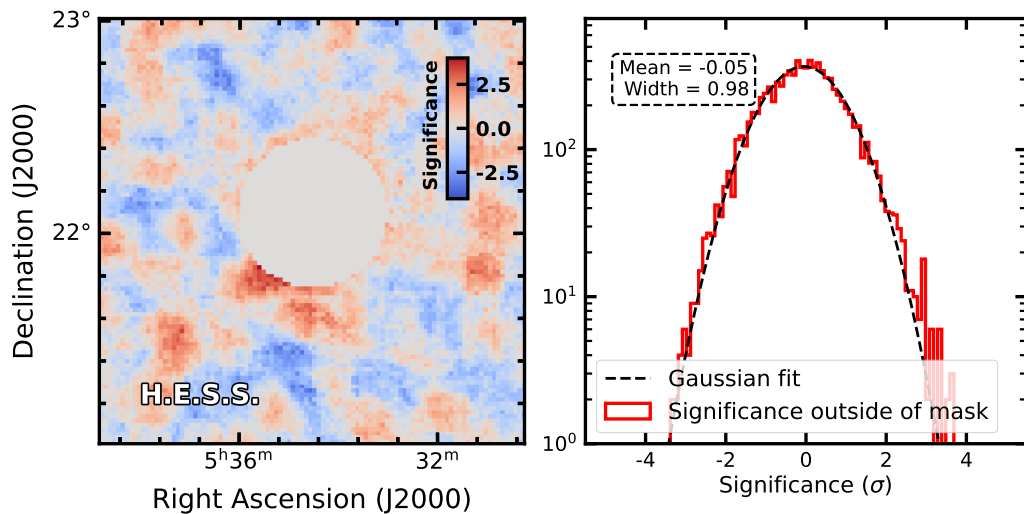


FIGURE 3.19: **Excluded significance map.** *Left:* Significance map with the source region masked. As expected, no regions above and below 5σ are seen. *Right:* Histogram of the significance values outside of the mask (red) and a Gaussian fit (black). As expected, the mean and width of the Gaussian are roughly 0 and 1. This means the background was correctly estimated.

3.5.3 Model Fitting

After the presence of a source in the region of interest is confirmed, the next step is to find a model that correctly describes it. This is done using a maximum-likelihood approach by assuming a model that describes the spectral and/or spatial properties

of the signal and finding the set of best-fit parameters that maximize the likelihood function (Cramér, 1946; Zacks, 1975; Sirca, 2016).

The simplest model to describe the differential number of photons dN emitted by a non-thermal source per energy interval dE (usually referred to as the source spectrum) is a power-law,

$$\frac{dN}{dE} = N_0 \left(\frac{E}{E_0} \right)^{-\Gamma} \quad (3.14)$$

with index Γ . This model can be made more complex by adding the presence of an exponential cutoff at energy E_c ,

$$\frac{dN}{dE} = N_0 \left(\frac{E}{E_0} \right)^{-\Gamma} \exp(-E/E_c) \quad (3.15)$$

or the presence of curvature β , a shape usually referred to as a "log-parabola",

$$\frac{dN}{dE} = N_0 \left(\frac{E}{E_0} \right)^{-\Gamma - \beta \log(\frac{E}{E_0})}. \quad (3.16)$$

The simplest spatial model to describe a source is a point,

$$\phi(\theta, \phi) = \delta(\theta - \theta_0, \phi - \phi_0), \quad (3.17)$$

where $\delta(\vec{x})$ is the Dirac delta function.

The gamma-ray emission from Galactic sources is however often extended, which requires more complex descriptions. A useful example is the generalized Gaussian distribution, which reduces to the usual Gaussian when the parameter $\chi = 0.5$,

$$\phi(\theta, \phi) = \phi(r) = \frac{1}{2\pi\sqrt{1 - e^2}r_0^2\chi\Gamma(2\chi)} \times \exp \left[- \left(\frac{r}{r_{\text{eff}}} \right)^{(1/\chi)} \right], \quad (3.18)$$

where $r_{\text{eff}}(\theta, \phi) = \sqrt{(r_M \sin(\Delta\phi))^2 + (r_m \cos(\Delta\phi))^2}$. The major (minor) semi-axis of the ellipse is given by r_M (r_m). $\Gamma(x)$ is the gamma function, $\Delta\phi$ is the difference between the position angle of the model, and the position angle of the evaluation point. If the eccentricity (e) is null r_{eff} reduces to r_0 .

Other, more complex distributions, both spatial and spectral, resulting from physical modeling of the non-thermal processes presumed to occur in the sources (see Section 1.5.1) can also be fitted. Two models can easily be compared by taking the difference of their TS values as long as they are nested. If that is not the case, other tests such as the Akaike Information Criterion (Akaike, 1973) can be used. For the special case of nested models where the difference in degrees of freedom is 1, the statistical significance of the description with one more parameter can be estimated as simply the square root of the increase in TS associated with it, as mentioned above.

3.5.4 Spectral "1D" Analysis

The simplest analysis case is when the morphology of the source is ignored and only the spectral behavior is measured. In this case, the number of excess events per energy bin falling inside of a region chosen to cover the majority of the source are compared with the prediction of a spectral model. Following the example with the H.E.S.S. public data release, we chose the same region used as an exclusion mask in Figure 3.19 and fitted the number of measured excess counts in it to a log-parabola spectral model. The choice of model was motivated by the fact that the Crab Nebula spectrum is known to be curved (see e.g Cao et al., 2021). The resulting best-fit model, as well as the comparison of its prediction with the measured excess can be seen in Figure 3.20. The spectra shown in the figure is represented in the $E^2 \frac{dN}{dE}$ form, usually referred to as spectral energy distribution (SED).

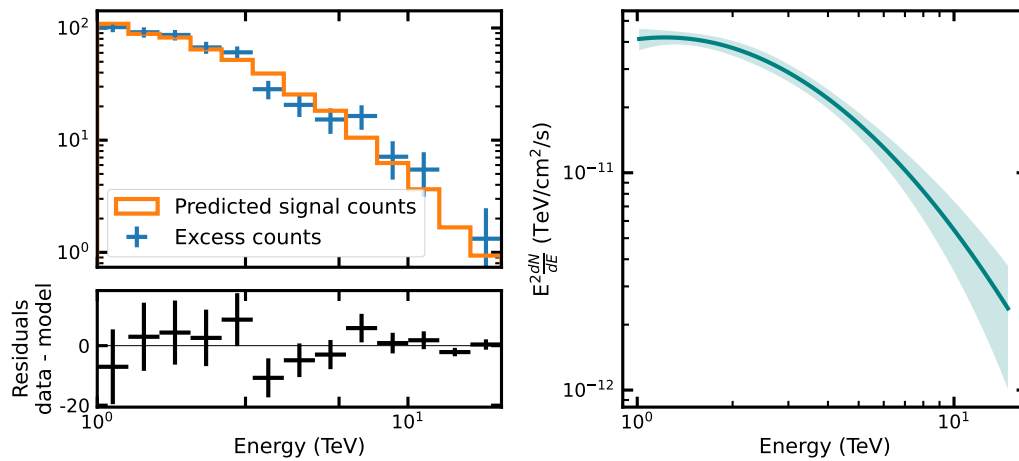


FIGURE 3.20: **1D spectral analysis.** *Left:* Measured excess counts in the extraction region (blue) compared to the predicted excess counts of the best fit model (orange). The residuals are shown in the bottom panel. *Right:* Best-fit power law model including statistical error bands.

3.5.5 Spectro-Morphological "3D" Analysis

The 1D analysis is a powerful and well-tested tool to measure the spectrum of an isolated source. However, the study of Galactic sources often presents more complicated situations that require a careful treatment. For example, in sky regions containing several overlapping sources, the 1D approach cannot disentangle the contribution of each source to the total flux in the chosen extraction region. Sources with extended or complex morphology can result in the measured flux being underestimated and heavily dependent on the size of the extraction region. Additionally, the 1D approach neglects the energy-dependence of the PSF.

For such situations a more complex approach is needed, the so-called 3D analysis. The three relevant dimensions are the two spatial angular coordinates and an energy axis. In this framework, a combined spatial and spectral model is fit to the data. More details on the 3D analysis approach can be found in Mohrmann et al. (2019).

Following the illustration with the H.E.S.S. public data release, we fit a combined point-source and log-parabola model to the Crab Nebula. The resulting model, as well as the significance map after subtracting it can be seen in Figure 3.21.

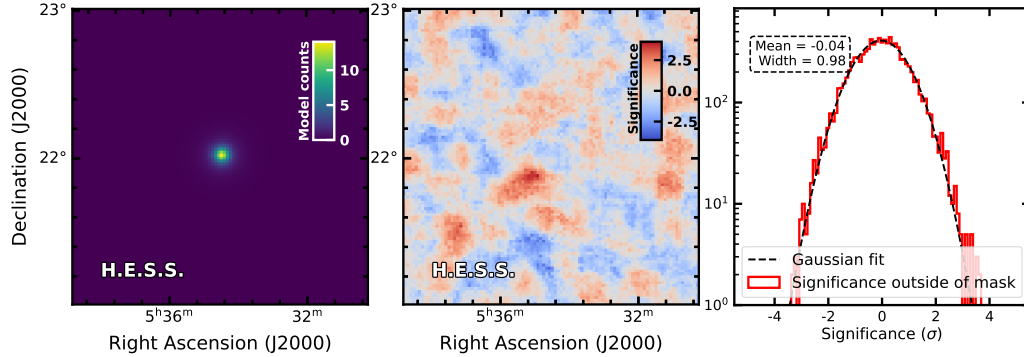


FIGURE 3.21: **Significance map after source subtraction.** *Left:* Predicted model counts over the entire energy range for the best-fit 3D model. *Middle:* Significance map after the best fit model has been subtracted. *Right:* Histogram of the significance values of the entire map (red) and a Gaussian fit (black). As expected, the mean and width of the Gaussian are roughly 0 and 1. This means the source was correctly modeled.

If the extraction region is large enough to contain the source, and the morphology of the source is reasonably regular, the spectral measurements obtained with the 1D and 3D methods should agree. This check can be easily performed by comparing the best-fit spectral model obtained using both methods, which are shown in Figure 3.22.

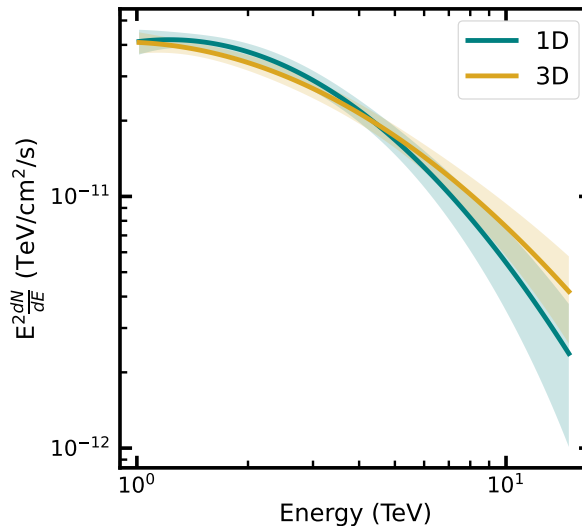


FIGURE 3.22: **Comparison of 3D and 1D spectra.** Best-fit spectral model including statistical error bands for the 1D (teal) and 3D (yellow) analysis.

3.5.6 Flux Points and Upper Limits

The spectral shapes being fit to the entire energy range are usually smooth and relatively featureless. In order to verify the spectral behavior in smaller energy scales, flux points are computed. For this, a number of energy bins is selected and in each of them, a normalization factor is fitted to the prediction of the best-fit model. Note that the result will depend on the shape of the assumed model. If not enough excess counts are measured in a bin, an upper limit is instead derived, indicating the maximum flux level that would result in such a non-detection given the instrument response. The flux points derived for the Crab Nebula using the H.E.S.S. public data release, including upper limits at the highest energies can be seen in Figure 3.23.

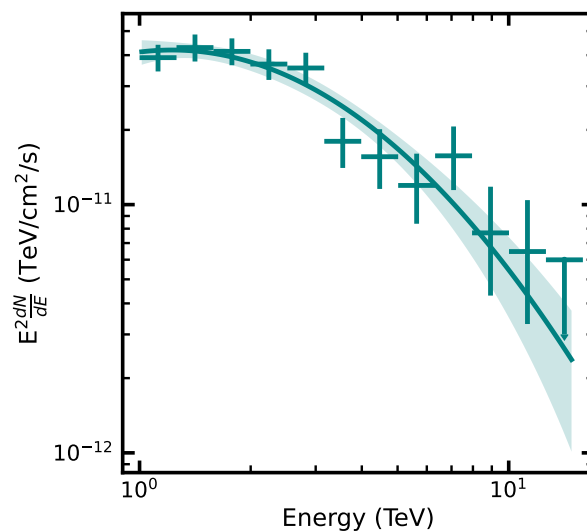


FIGURE 3.23: **Flux points and upper limits.** Flux points and upper limits from the Crab Nebula spectral measurement.

The same approach can be used to measure the flux in the spatial dimension, to build flux profiles, or as a function of time in light-curves.

3.6 Summary and Outlook

This chapter summarized the basic principles for the detection of VHE gamma-rays, focusing on two particular experiments: the H.E.S.S. array of IACTs and the HAWC particle detector array. The different strengths and weaknesses of the two techniques makes their view of the gamma-ray sky complementary. Due to its wide FoV and high duty cycle, the HAWC observatory has an unbiased view of the sky, which is advantageous for the discovery of the unexpected. This was for example the case with the HAWC discovery of TeV emission from the jets of the microquasar SS 433 (see Section 2.3.6). However, the relatively poor angular resolution of the HAWC observations (see Figure 3.24) did not allow for a detailed study of this emission. IACTs, on the other hand, need to be pointed at a target and have a much lower duty cycle. But their resolution, both spatial and spectral is significantly better. Following up

on the detection of a gamma-ray source by a particle detector array with dedicated IACT observations is thus a natural synergy between both instrument classes. This thesis presents an example of such a strategy, with the result of dedicated H.E.S.S. observations of the microquasar SS 433 following the HAWC detection being presented in Chapter 6. The superior angular and energy resolution of H.E.S.S. compared to HAWC allow for a detailed study of the emission from the jets.

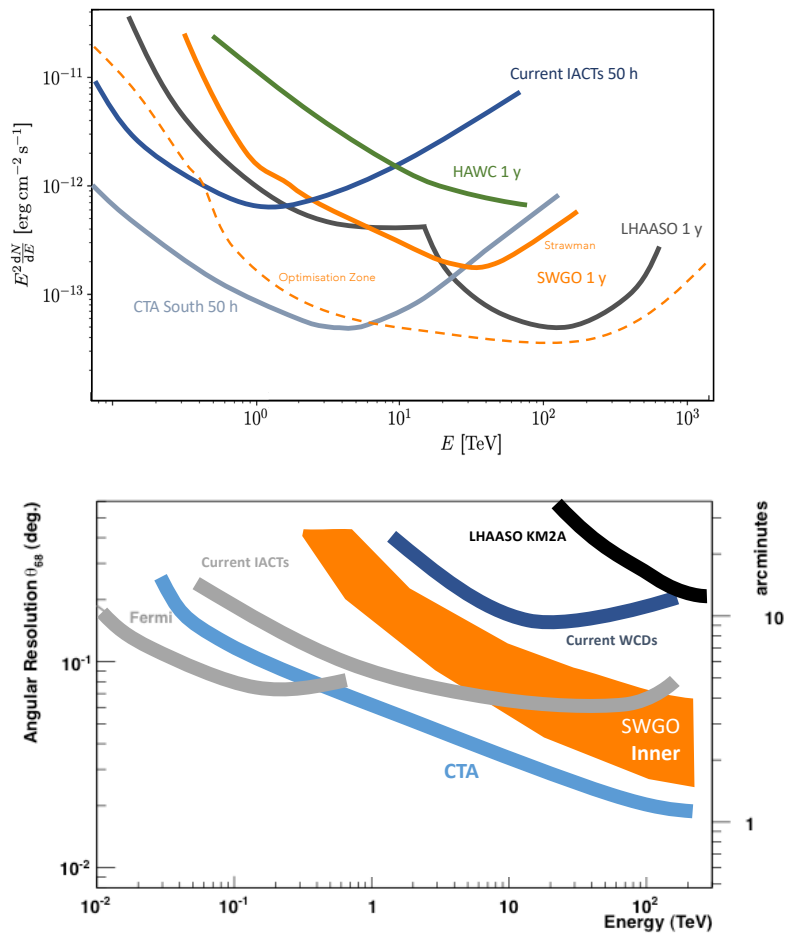



FIGURE 3.24: **Performance of current and future experiments.** *Top:* Estimated and projected sensitivity for current and future gamma-ray instruments. The dark blue curve represents the existing IACTs. The green and black lines show the sensitivity of HAWC and the LHAASO array respectively. The upcoming CTA south site is depicted by the light blue line, and the sensitivity of the SWGO is expected to lie between the solid and dashed orange lines. *Bottom:* Estimated and projected angular resolution for current and future gamma-ray instruments. The dark gray curve represents the existing IACTs, such as H.E.S.S.. The dark blue line shows the resolution of WCD arrays such as HAWC. The black line shows the angular resolution of the LHAASO. Values for the upcoming CTA are depicted by the light blue line, whereas the expected resolution of the SWGO is represented by the orange band. Figures by Jim Hinton .

The future of IACT astronomy will be dominated by the upcoming CTA observatory (see Section 3.2.2). Despite its improved sensitivity and sky coverage with

respect to the previous generation of IACTs, CTA will suffer from the same limited duty cycle as its predecessors. Hence, the synergy between CTA and the next generation of particle detector arrays, which includes the LHAASO and the SWGO will be especially important. Particle detector arrays will also be able to extend the coverage well beyond hundreds of TeV, as can be seen in the top panel of Figure 3.24. In order to facilitate the sharing of data and the existence of joint analyses between the different types of instruments, the existence of a common analysis framework is required. This includes the definition of a unified data format. These efforts will be discussed in Chapter 5, where an existing data format and analysis tool tailored for the CTA data will be extended and validated for their use by particle detector arrays, thus ensuring that the synergies between the two instrument types can be exploited fully.

Chapter 4

Improving Background Rejection at Very High Energies with IACTs

The main source of background for VHE gamma-ray astronomy are the hadronic cascades caused by charged cosmic ray primary particles (see Sections 3.1.1 and 3.3.4). In the energy window relevant to ground-based gamma-ray instruments, the cosmic ray flux is higher than that of most gamma-ray sources. This means that, in order to successfully do gamma-ray astronomy, it is crucial to separate the gamma-ray initiated showers from the cosmic-ray background. In this chapter we propose a new approach to the task of background rejection in IACT arrays based on the identification of light produced by muons. The fact that muons are produced in much higher numbers in hadronic showers compared to EM showers is routinely used by particle-detector arrays, such as LHAASOs, to perform background rejection. However, it has never been exploited for IACTs.

In the first part (Olivera-Nieto et al., 2021), we show, using simulations, that IACTs with large mirrors ($\gtrsim 23$ m) can detect a large fraction of muons in a hadronic shower. This means that effective muon identification in the shower images could lead to background rejection powers of up to 10^5 at tens of TeVs, which would mean an improvement of several orders of magnitude with respect to traditional approaches described in Section 3.3.4.

In a follow-up study (Olivera-Nieto et al., 2022), we show that a simplified approach in which muon light is not necessarily identified as such in the shower image by a large telescope but instead light other than the main shower is flagged already has the potential to improve background rejection by a factor 3-4 above 20 TeV. We apply this algorithm to data from the H.E.S.S. array, using the images from the central, 28 m diameter mirror telescope.

The background rejection techniques described in this chapter will be used for the analysis of H.E.S.S. data from the SS 433 region detailed in Chapter 6.



Muons as a tool for background rejection in imaging atmospheric Cherenkov telescope arrays

L. Olivera-Nieto^{1,a} , A. M. W. Mitchell^{2,3} , K. Bernlöhr¹ , J. A. Hinton¹ 

¹ Max-Planck-Institut für Kernphysik, P.O. Box 103980, 69029 Heidelberg, Germany

² Department of Physics, ETH Zurich, 8093 Zurich, Switzerland

³ Erlangen Centre for Astroparticle Physics, Friedrich-Alexander-Universität Erlangen-Nürnberg, 91058 Erlangen, Germany

Received: 28 June 2021 / Accepted: 23 November 2021 / Published online: 14 December 2021

© The Author(s) 2021

Abstract The presence of muons in air-showers initiated by cosmic ray protons and nuclei is well established as a powerful tool to separate such showers from those initiated by gamma rays. However, so far this approach has been fully exploited only for ground level particle detecting arrays. We explore the feasibility of using Cherenkov light from muons as a background rejection tool for imaging atmospheric Cherenkov telescope arrays at the highest energies. We adopt an analytical model of the Cherenkov light from individual muons to allow rapid simulation of a large number of showers in a hybrid mode. This allows us to explore the very high background rejection power regime at acceptable cost in terms of computing time. We show that for very large ($\gtrsim 20$ m mirror diameter) telescopes, efficient identification of muon light can potentially lead to background rejection levels up to 10^{-5} whilst retaining high efficiency for gamma rays. While many challenges remain in the effective exploitation of the muon Cherenkov light in the data analysis for imaging Cherenkov telescope arrays, our study indicates that for arrays containing at least one large telescope, this is a very worthwhile endeavor.

1 Introduction

The hadronic cascades associated to charged cosmic ray primary particles typically produce large numbers of muons, primarily from the decay of charged pions. The potential to use these muons to discriminate between hadronic and electromagnetic cascades and hence do gamma-ray astronomy, has long been recognised (see for example [1]).

The performance of the LHAASO array [2,3], demonstrates the power of this approach for very-high and ultra-high energy gamma-ray astronomy (from tens to hundreds of

TeV). An important factor contributing to the success of the LHAASO array is the very large total area of muon detectors, a factor of nearly 20 larger than the CASA-MIA [4] array, resulting in a more than hundredfold improvement in background rejection.

Ground level muons become a useful separation tool for showers above ~ 1 TeV at high altitude [5]. However, excellent hadron rejection power, that is, over a factor 10^4 reduction, is possible only at tens of TeV [3].

Imaging Atmospheric Cherenkov Telescope (IACT) arrays have superior rejection power to other ground-based arrays in the domain around 1 TeV, exploiting primarily the differences in shower width and substructure between electromagnetic and hadronic showers in this energy range [6–8]. However, IACTs have not so far demonstrated excellent rejection power at tens of TeV. Traditional separation approaches are limited by the fact that, beyond small impact distances, large events are typically not fully contained by the camera image, which significantly affects the estimation of the necessary shower parameters. The current background rejection power attained by the traditional separation methods at energies above a few tens of TeVs reaches levels between 10^{-2} and 10^{-3} [6,7,9]. This loss of performance at high energies can also be seen, albeit indirectly, in the expected background rate after background rejection cuts for CTA.¹ The surviving background rate falls by a factor 500 between 0.1 and 1 TeV but less than a factor of 10 between 10 TeV and a 100 TeV – while the proton flux falls by a factor of 50 per decade.

The ring-like images produced when ground-level muons pass through IACTs have long been used as a means of calibration [10], see [11] for a recent review. Recently, [12] suggested that the identification of a much higher fraction

^a e-mail: Laura.Olivera-Nieto@mpi-hd.mpg.de (corresponding author)

¹ <https://www.cta-observatory.org/science/cta-performance/#1472563453568-c1970a6e-2c0f>.

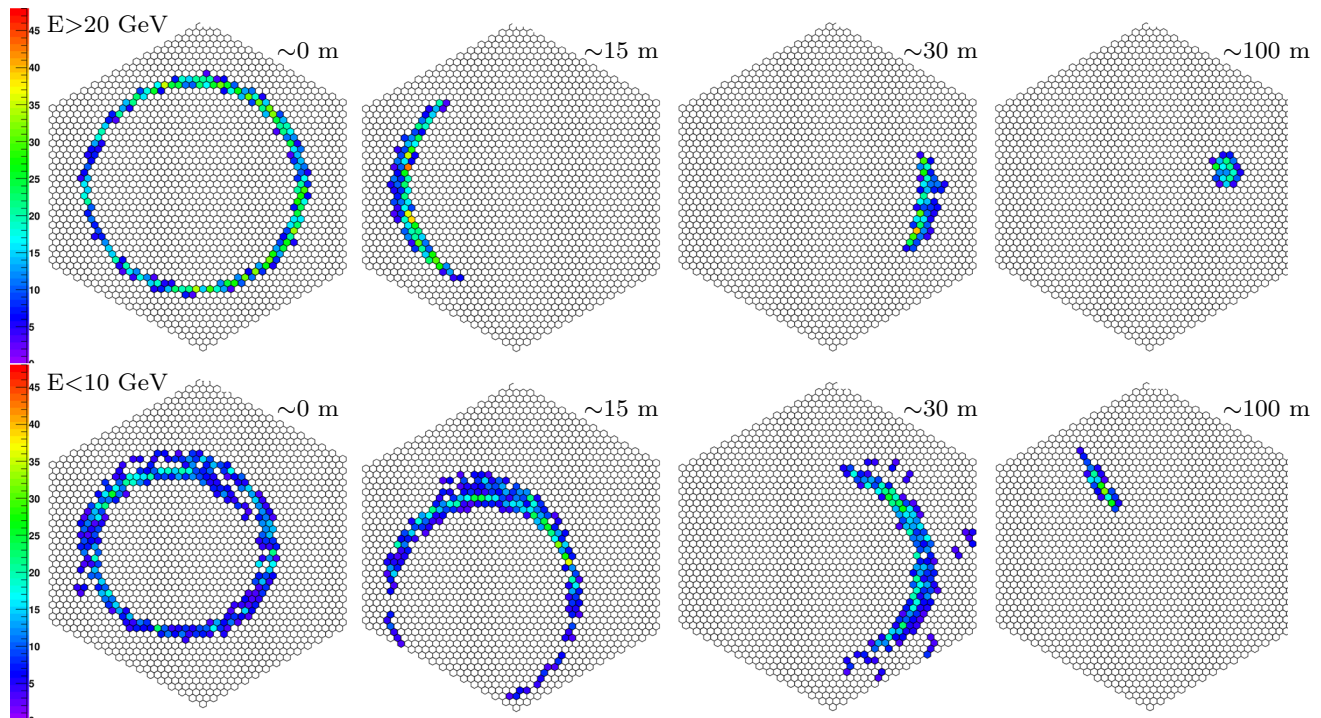


Fig. 1 Example simulated muon images in a 28 m telescope at different energies and impact distances. All simulated muons are produced at 11 km above sea level and are observed at 1835 m with a zenith angle of 20°

of muons produced in extensive air showers is possible with IACTs.

Large telescopes such as the central telescope of H.E.S.S. [13] and the Large-Sized Telescopes (LSTs) of CTA [14] enable the detection of individual muons out to large impact distance. This has traditionally been seen as a problem due to their apparent similarity to gamma-like events [15], but can also be seen as an opportunity for improvement of the background rejection power at the highest energies if characteristic differences of muons to gamma rays are identifiable.

In this paper we explore the potential for muon measurement with IACTs as a tool for background rejection by characterizing the number of muons that are detectable by a large Cherenkov telescope in proton- and gamma-initiated showers of different energies. In our simulations we adopt a hybrid approach to allow exploration of the very high background rejection power regime at acceptable cost in terms of computing time. This approach is introduced and motivated in Sect. 2. Section 3 discusses the muon content of showers from the perspective of air-Cherenkov detection and details the criteria used to label muons as detectable by a telescope. Section 4 presents the result of said criteria applied to showers initiated by both protons and gamma rays, both for large- and medium-dish telescopes. Finally, Sect. 5 discusses the implications and potential for muons as a means to improving IACT background rejection.

2 Cherenkov light from muons

The properties of the Cherenkov emission of a single atmospheric muon are very well determined and straight-forward to calculate in comparison to air-showers in general. The suppressed bremsstrahlung cross-section of muons with respect to electrons allows a majority of muons to reach ground-level with only ionisation losses. Similarly, the reduced multiple scattering of muons with respect to electrons means that the assumption of a linear trajectory is reasonable in most cases. For these reasons the simulation of muons in full detail may not be necessary to capture the essential characteristics of Cherenkov light from muons in showers. We implement a simplified muon model (SMM) which, starting from basic muon properties, approximates the Cherenkov light production and telescope simulation with an analytical treatment, described below. Table 1 compares the SMM approach to the combination of the CORSIKA [19] package for shower and Cherenkov light simulation and the *sim_telarray* [17] package for the telescope response and camera simulation. In order to verify the predictions of the SMM, we produced a small set of full CORSIKA+*sim_telarray* muon simulations with energies between 5 and 100 GeV for different starting heights. Note that the Cherenkov threshold for muons at 1835 m above sea level is slightly above 5 GeV.

The key parameters affecting the Cherenkov image properties of individual muons are the initial energy and produc-

Table 1 Comparison of muon treatment between the CORSIKA+*sim_telarray* approach and the simplified muon model

	CORSIKA + <i>sim_telarray</i>	Simplified muon model
Cherenkov light production	Ignoring wavelength dependence of refractive index ^a	
Atmospheric absorption	Wavelength-dependent tabulated atmospheric absorption [16]	
Atmosphere characterization	Tabulated atmospheric profiles at H.E.S.S. location [17]	
Muon scattering	Full treatment	Ignored
Muon bremsstrahlung	EGS4 [18]	Ignored
Ionization losses	Bethe–Bloch formula	2 MeV per g/cm ²
Telescope response	Full treatment	Full treatment
Ray-tracing	Full treatment	Simplified
Camera trigger	Patch of 9 neighboring pixels with total intensity above 68 p.e	
Pixel shape	Realistic, hexagonal	Simplified, square
Night sky background	Optional, ignored here	Ignored
Bending in geomagnetic field	Included	Ignored

^aNote that CORSIKA can generate photons according to a wavelength-dependent index of refraction but it is not used by default for reasons of computing efficiency.

tion height in the atmosphere. Muons that reach ground level and land close to, or intersect, a telescope dish, produce a ring-shaped image in the telescope camera, with a full circle for muons hitting the dish and reduced sections of arc as the impact distance becomes larger. The surface brightness of the images, however, remains mostly constant, which allows muons to trigger out to large impact distances, even when the ring section captured by the camera is small enough to no longer resemble an arc, but rather a small cluster of pixels. Figure 1 illustrates the evolution of muon image properties with impact distance, as imaged in the 28 m telescope of H.E.S.S., based on CORSIKA and *sim_telarray* simulations.

The first step to determine whether an incoming muon can be detected by a telescope located at a certain distance from its ground impact point, is to compute the amount of Cherenkov photons collected by the telescope camera as a function of said distance. This distribution is calculated assuming a straight trajectory of the muon through the atmosphere from the production height h_{prod} . The atmospheric density $\rho(h)$ and refractive index $n(h)$ profiles are described by the same model used by *sim_telarray* at the H.E.S.S. location [17]. The wavelength dependence of the refractive index is ignored. For a muon with incoming zenith angle θ_z , the actual path through the atmosphere is then described by $l = h / \cos \theta_z$ for $h \in [h_{\text{ground}}, h_{\text{prod}}]$, where h_{ground} is taken to be 1835 m above sea level. The emitted photons are subject to wavelength-dependent atmospheric absorption $A(\lambda, h)$, which is integrated along the photon path, assumed here for simplicity to be the same as the muon path starting at the point where the photon is produced. The photons produced at a height h then arrive at the ground at a distance

$R(h)$ from the point where the muon hits the ground

$$R(h) = (h - h_{\text{ground}}) \cdot \frac{\sin \theta_c}{\cos \theta_z}, \tag{1}$$

where $\theta_c = \arccos((n \cdot \beta)^{-1})$ is the Cherenkov angle of a muon traveling with velocity $\beta = v/c$ in a medium with refractive index n . Note that θ_c varies with height, because of energy losses and the refractive index profile.

The number of Cherenkov photons N_γ initially produced by the muon per path length dl between wavelengths λ_1 and λ_2 , is described by

$$\frac{dN_\gamma}{dl} = 2\pi\alpha \left(1 - (\beta n)^{-2}\right) \int_{\lambda_1}^{\lambda_2} \frac{d\lambda}{\lambda^2}, \tag{2}$$

where α is the fine-structure constant. This quantity needs to be convolved with the telescope response, which consists of many different elements. For this, we used the response of the telescopes in the H.E.S.S. array. The wavelength-dependent telescope response $W_T(\lambda)$ is the combination of the mirror reflectivity, quantum efficiency of the camera and plexiglas transmittance of the camera window. Additionally, there are wavelength-independent corrections for the telescope area projection and the camera and Winston cones shadowing, which combine to a factor $f \sim 0.6$ for a 28 m telescope. Combining the number of photons initially produced with the telescope response results in the number of Cherenkov photons produced by a muon per unit path length that are detected by the telescope:

$$\frac{dN_{\gamma,T}}{dl} = 2f\pi\alpha \left(1 - (\beta n)^{-2}\right) \int_{\lambda_1}^{\lambda_2} A(\lambda, h) W_T(\lambda) \frac{d\lambda}{\lambda^2}. \tag{3}$$

The photons distribute radially on the ground from the impact position of the muon, which defines the origin of the coordinate system. Using Eqs. 1 and 3 we can compute the

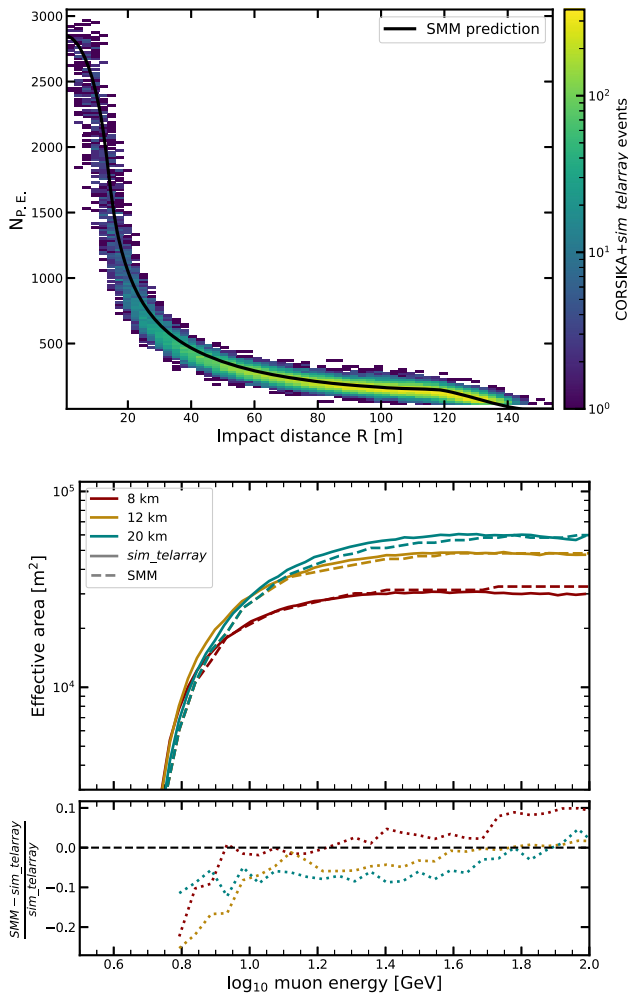


Fig. 2 Top: Comparison of the amount of photoelectrons predicted by the analytical model for a 28 m dish (black line) and the resulting distribution for simulated muon showers for energies above 20 GeV, scattering distance smaller than 5 m and starting height ~ 10 km. Bottom: Effective area comparison between the simulations and the simplified model for different starting heights. Includes all events, even those that undergo significant scattering and bremsstrahlung

ground density of detected photons

$$\rho_{\gamma,T}(R) = \frac{dN_{\gamma,T}}{dA} = \frac{dN_{\gamma,T}}{2\pi R dR} = \frac{dN_{\gamma,T}}{dl} \frac{dl}{2\pi R dR}, \quad (4)$$

where R is the distance to the muon impact position. Placing a test telescope with a circular mirror of diameter D_T in the ground at position $(x = 0, y = R)$, the amount of photoelectrons (P.E.) collected by the dish as a function of R is then given by

$$N_{P.E.}(R) = \int_{R-R_T}^{R+R_T} dx \int_{-\alpha}^{\alpha} dy \cdot \rho_{\gamma,T}(\sqrt{x^2+y^2}), \quad (5)$$

where $\alpha = \sqrt{R_T^2 - (x - R)^2}$.

The number of photoelectrons predicted by the SMM is compared in the top panel of Fig. 2 with that resulting

from the CORSIKA+*sim_telarray* simulations. Note that if a muon has undergone significant scattering while traveling through the atmosphere, the impact position on the ground is no longer a meaningful parameter to describe its trajectory. For this reason, the comparison shown in Fig. 2 is done with a subset of the full simulations with events selected for modest scattering. As expected, the agreement is very good. A further check utilizing the entire set of simulations is described below.

Once the properties of the photoelectrons produced by a muon and captured by the camera are known, the next step is to determine if they would activate the camera trigger. For this we base our trigger definition on the one used by Flash-Cam, the camera installed in the largest H.E.S.S. telescope since October 2019 [20]. The criterion is passed when an image has a group of nine neighboring pixels with a total of more than 68 photoelectrons. For each combination of muon starting height, initial energy and telescope distance from muon position, the corresponding muon image in the telescope is generated from the Cherenkov light distribution in the SMM and tested against this criterion. This allows for a trigger decision dependent on those three parameters only, which we will refer to as the simplified trigger criterion.

To verify that this is an accurate description of the real trigger conditions we once again use the small sample of CORSIKA+*sim_telarray* simulations. For this comparison, we include muon events undergoing significant scattering, a process which, together with bremsstrahlung, is ignored by the SMM (see Table 1). To do this, we compare, for different muon starting heights and as a function of energy and impact distance, the total number of muons arriving at the ground in the CORSIKA sample with the number of muons detected by the telescope after processing the sample with *sim_telarray*. Integrating the ratio of these numbers radially results in an effective area for a given energy and starting height. Similarly, for the same set of input CORSIKA events, we use their energy, production height and angular direction to compute our simplified trigger criterion. We then compute the muon effective area in the same way. These quantities are shown in the bottom panel of Fig. 2. This comparison includes muon events that undergo scattering and bremsstrahlung, confirming that the simplified trigger criterion is accurate to well within 10% across all energies.

The distribution of arrival times of the Cherenkov photons produced by the muon is straightforward to compute with the setup described above. Defining the instant in which a muon produced at height h_μ arrives at the ground as t_μ , we can compute the relative delay in arrival time of a photon produced by the muon at height h , $t_\gamma(h)$ as

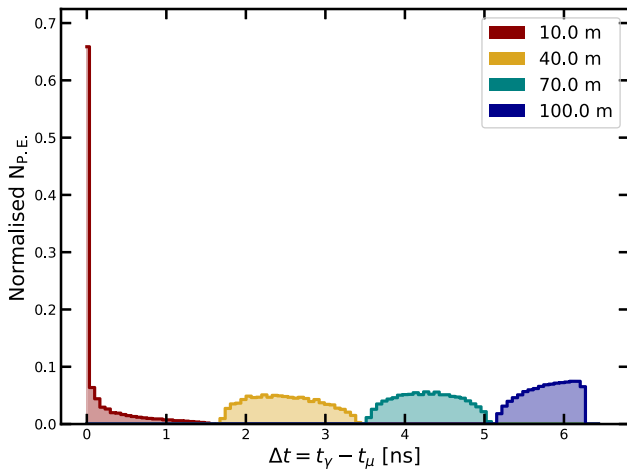


Fig. 3 Distribution of the arrival time of Cherenkov photons for a muon of energy 20 GeV and starting height 11 km as seen from several impact distances. The quantity in the y-axis is normalised for equal area at each impact distance

$$\Delta t(h) = t_\gamma(h) - t_\mu = \frac{h \cdot c}{\cos \theta_c(h)} - t_\mu, \tag{6}$$

where $\theta_c(h)$ is the Cherenkov angle. Using Eq. 1 we compute $\Delta t(R)$, that is, the relative photon arrival time as a function of the ground distance to the muon impact point.

Now, combining this quantity with Eq. 5 allows us to compute the number of photons that arrive to the dish of a telescope $N_{P,E}$ for each value of $\Delta t(R)$. An example of such distributions for a muon of energy 20 GeV can be seen in Fig. 3. Note that the distribution for each telescope location is normalised for equal area.

3 Detectable muons in showers

Considering shower development only down to the Cherenkov threshold for muons allows extremely rapid simulations with CORSIKA, even up to primary energies of many hundreds of TeV. For both gamma-ray- and proton-initiated showers, over 10^7 showers were produced with energies between 10^1 and $10^{2.5}$ TeV, distributed as $\propto E^{-1}$ to ensure enough events at the highest energies. For all showers, the primary particle initial direction was $\theta_z = 20^\circ$. From these showers, the production height, energy, ground level direction and impact point were extracted for all the muons present. Figure 4 summarises the basic properties of these muons.

The very high statistics allows us to probe the characteristics of the very rare most muon-poor proton showers, which form the irreducible background of the muon-tagging approach. We define a muon as *detectable* if they fulfill three separate conditions, with the first being the simplified trigger criterion described in Sect. 2. The remaining conditions

refer to the muon trajectory and are described below. We assume for simplicity that the telescope is always pointed towards the shower axis and located at the shower ground impact position. The second condition is then given by the fact that the angular distance between the muon trajectory and the axis must be smaller than half of the telescope field of view (FoV), taken here to be that of the central H.E.S.S. telescope, 3.5° .

Beyond simply being able to detect light from muons, in order to use their presence as a background rejection criterion, it is crucial to accurately identify them as such. Muon identification can be carried out via different techniques, which exploit the properties of the muon Cherenkov signal described in Sect. 2. A thorough study of the different muon identification techniques and their performance is beyond the scope of this paper (see [12,21,22] for some recent efforts). Current background rejection methods implemented in IACTs rely on the properties of the time-integrated Cherenkov light images. In this case, a complete overlap in the camera image between the main shower component and the light coming from muons makes this identification very difficult. In order to take this into account, and also to explore the effect of different muon identification efficiencies, we impose a third and final condition for detectability: a requirement on the minimum angular distance between the trajectories of the muon and the primary particle. We choose a reference value for this distance of 0.3° which corresponds to the survival of, as can be seen in Fig. 5 around half of the muons that pass the first and second detectability conditions described above.

Note that possible muon identification techniques that exploit the arriving times of Cherenkov photons would not be limited by image overlap. Additionally, even techniques that are based in the integrated image can also strongly be affected by the shape of the separable muon component rather than its size in pixels. Hence this requirement on the minimum angular distance is only a proxy of the fact that only a fraction of the detected muons will realistically be tagged as such. In any case, as we show later in Sect. 4, the background rejection power attainable with the muon tagging strategy would be competitive up to a muon identification efficiency of a few percent.

4 Results

Figure 6 shows the logarithmic distribution of the number of muons classified as detectable, $\log_{10} N_{\mu,\text{det}}$, for showers with both protons and gamma rays as the primary respectively. The energy of the primary particle energies ranges between 10 and 250 TeV. The differences between both distributions are striking, revealing that a large fraction of the initially high (see Fig. 4) number of muons in proton showers can

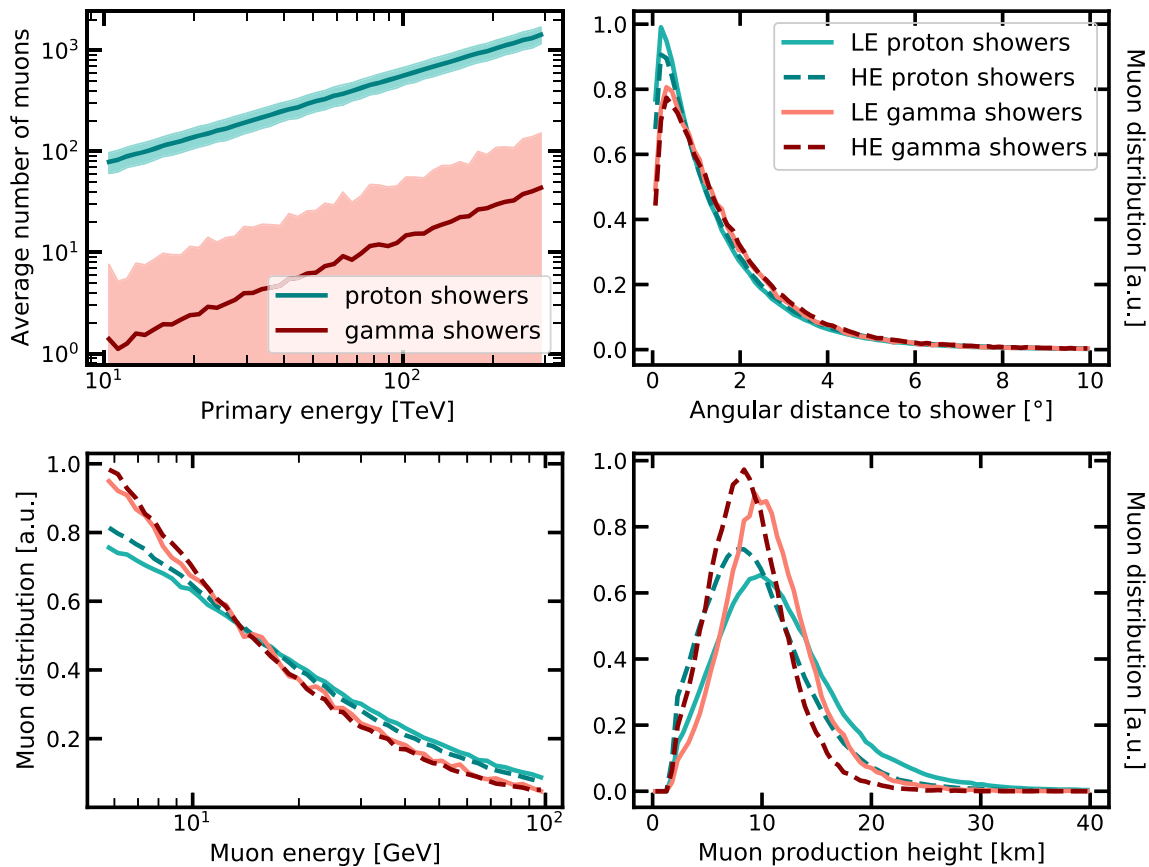


Fig. 4 Characteristics of muons produced in proton- and gamma-ray-initiated showers. The top left panel shows the average number of muons present as a function of primary energy, with the shaded area representing the standard deviation. The remaining panels show the distributions of angular distance to the shower, energy and production height for

muons produced by showers in two energy ranges, normalised for equal area. Solid lines correspond to “low-energy” (LE, 10–20 TeV) showers, while dashed lines represent muons in “high-energy” (HE, 100–120 TeV) showers

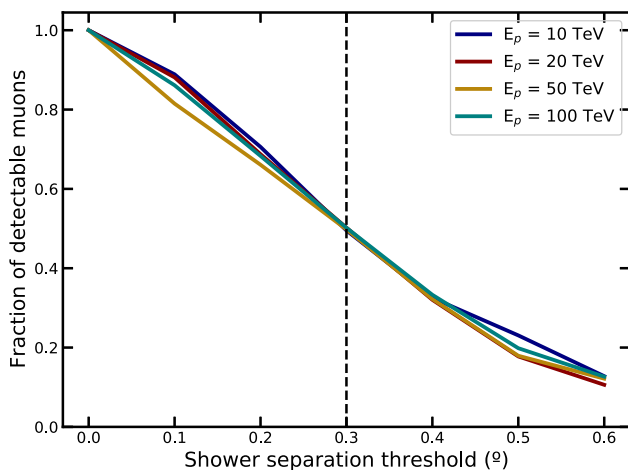


Fig. 5 Fraction of surviving muons as a function of the minimum shower separation threshold for several energies. Both the trigger and FoV criteria have already been applied. The dashed line indicates the chosen reference value of 0.3° which translates to roughly 50% survival due to this criterion

be in principle detectable by a large telescope. Conversely, for gamma-ray showers, the distribution is shifted towards a much lower number of detectable muons. The bottom panel of both figures shows the probability that a shower does not contain any detectable muons. Above 100 TeV this number is of the order of 10^{-5} for proton showers, a number which assumes a 50% muon identification efficiency as described in Sect. 3. This number represents the irreducible background of this approach, and is orders of magnitude below the current rejection power reached at those energies [6, 7, 23], even assuming a less effective muon identification strategy.

Let us refer to the probability distributions of detectable muons shown in Fig. 6 as $f(N_{\mu,\text{det}}|E_{\text{pri}})$, where E_{pri} is the energy of the primary particle. From this quantity, we can compute the fraction of showers expected to contain less than a certain number N of detectable muons as:

$$F(N_{\mu,\text{det}} < N|E_{\text{pri}}) = \int_0^N f(N_{\mu,\text{det}}|E_{\text{pri}}) dN_{\mu,\text{det}}. \quad (7)$$

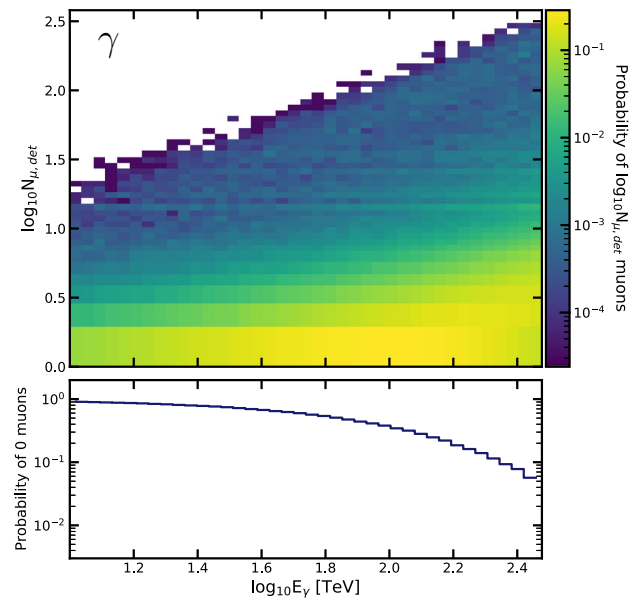
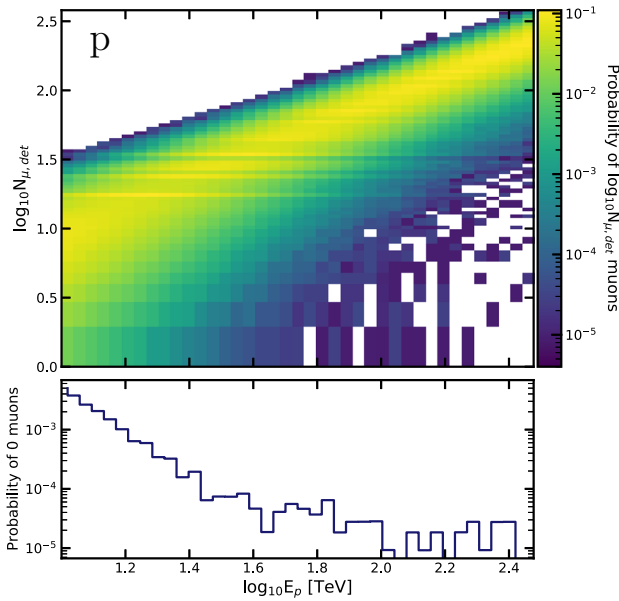


Fig. 6 Top panel: Logarithm of the number of detectable muons in showers vs primary energy. The distribution is normalised at each primary energy bin. The type of particle initiating the showers is indicated

on the top left corner. Bottom panel: Probability of 0 muons in a shower vs primary energy. Normalised together with the upper panel at each energy

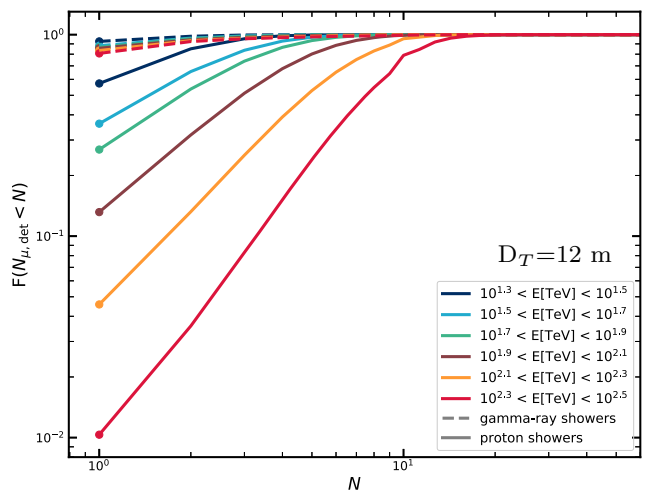
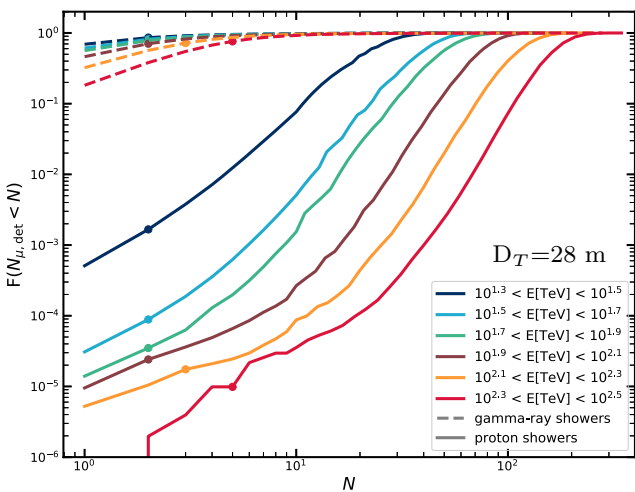


Fig. 7 Cumulative distribution of the number of detectable muons in proton-initiated showers (solid lines) and gamma-ray-initiated showers (dashed lines) for several primary energy ranges. A round marker is

placed at the x-position defined by a 70% signal efficiency. The corresponding telescope size is indicated with D_T in each panel

Note that this corresponds to an integral as a function of the y-axis of each panel in Fig. 6. We show this quantity corresponding to several ranges of primary particle energies for both gamma-ray and proton showers in the left panel of Fig. 7. Beyond 30 TeV substantial separation power would clearly result from effective identification of single muons within shower images. For energies higher than 80 TeV the separation power could reach 10^{-5} , well beyond that achieved so far for IACT arrays.

4.1 Smaller telescopes

The large collection area of the telescope is critical to the number of muons whose light is collected by the dish. The simplified model results shown in Fig. 6 and the left panel of Fig. 7 correspond to a telescope with a diameter of 28 m. Repeating the same process for a smaller telescope, with a diameter of 12 m yields very different results. As can be seen in the right panel of Fig. 7, the background rejection power achievable with the muon-tagging approach worsens

dramatically by several orders of magnitude. This is due to the fact that large dishes translate to a larger light collection area. Hence more light can be collected by the PMTs, allowing the detection of a higher number of muons, which are faint emitters compared to showers.

5 Discussion

It is clear from Fig. 7 that very significant potential exists for improving the background rejection of IACT arrays containing at least one large telescope at the highest energies provided that individual muon arcs can be identified with reasonable efficiency in the presence of bright shower images. A very large fraction of the muons initially present in the shower can in principle be detected by the telescope, thanks in part to the fact that the typical angular displacement from the shower is small enough to remain inside the FoV, as can be seen in Fig. 4. In order to exploit this potential, effective muon identification is required. There are several promising strategies, which use different characteristics of the muon Cherenkov light. As shown in Fig. 3, light produced by muons arrives to the telescope in short, concentrated bursts, unlike the shower photons, which span a range of tens of nanoseconds [24]. This difference could be exploited to identify muons if the time distribution of the photons, rather than only the time-integrated images, is available [25].

On the other hand, for time-integrated images, it has become very common and effective to employ template fitting approaches [26, 27] during the reconstruction. However, very energetic events produce very bright and large shower images, which are often not entirely contained in the camera field of view. The very bright pixels from the shower image likely dominate the fit and obscure the presence of dim, constant surface-brightness muon images. Simply masking out the main shower image and analyzing the residual emission will likely result in an increased rate of muon identification, provided that the image cleaning procedure is not excessively harsh. More sophisticated approaches, making use of pixel-based deep learning techniques have already shown some promising results [22]. The recent development of dedicated packages such as CTLearn [28] or GammaLearn [29] will likely facilitate the application of such techniques to the muon identification issue.

Large Cherenkov telescopes are widely seen as a useful asset for the low-energy range of the very-high energy spectrum due to their reduced threshold, but of limited use when considering the highest energies. However, as can be seen by comparing both panels of Fig. 7, this same reduced threshold is key when it comes to detecting the faint light coming from muons, which are overwhelmingly more common in proton-induced showers (see Fig. 4). Exploiting this potential of large telescopes through efficient muon identification

algorithms could provide significant improvements in background rejection above several tens of TeVs, and in turn, improve the instrument sensitivity at the highest energies.

Another option is, of course, to build ground level muon detectors. However, these are not planned for either the existing or upcoming IACT arrays. Additionally, an improved muon detection technique could be applied retroactively to the entire data archive from an observatory, in the case of existing IACT arrays. This would effectively, and without increased observation time or hardware improvements, increase the detection capability at higher energies.

The results in Sect. 4 were produced for showers arriving from a distance of 20° from zenith. We also produced smaller samples of showers from 0° and 40° to explore the effect of the zenith angle on the result. With increasing zenith angle, the number of detected muons goes up slightly, since the distance out to which muons are able to trigger goes up (see Eq. 1).

As can be seen in Fig. 6, muons are often produced, albeit in low numbers, by the highest energy gamma-ray showers. This is because at those energies, the number of interactions is so large that rare processes, such as muon pair production, become relevant. This indicates that perhaps the most useful separation parameter in terms of gamma-ray efficiency might not solely be the identification of individual muons, but rather a measure of the muonic content of an event.

The hadronic background is in fact not solely made up by protons, but also heavier nuclei [30]. The muon content in these showers is higher, which translates into a higher number of expected detectable muons. In a sense, the proton case is the worst-case scenario, being the hadronic background species most likely to initiate muon-poor showers. However, protons are most likely to masquerade as a gamma ray in traditional background rejection approaches [15], and therefore the room for improvement is greater.

Acknowledgements The authors would like to thank the H.E.S.S. Collaboration for allowing the use of H.E.S.S. simulations in this publication, as well as providing useful discussions and input to the paper. This work made use of `numpy` [31], `scipy` [32], `pandas` [33] and `matplotlib` [34].

Funding This research was supported by the Max Planck Society and ETH Zurich. AMWM is supported by the Deutsche Forschungsgemeinschaft (DFG, German Research Foundation) – Project Number 452934793, MI 2787/1-1.

Data Availability Statement Data sharing not applicable to this article as no datasets were generated or analysed during the current study.

Open Access This article is licensed under a Creative Commons Attribution 4.0 International License, which permits use, sharing, adaptation, distribution and reproduction in any medium or format, as long as you give appropriate credit to the original author(s) and the source, provide a link to the Creative Commons licence, and indicate if changes were made. The images or other third party material in this article are included in the article's Creative Commons licence, unless indicated otherwise in a credit line to the material. If material is not

included in the article's Creative Commons licence and your intended use is not permitted by statutory regulation or exceeds the permitted use, you will need to obtain permission directly from the copyright holder. To view a copy of this licence, visit <http://creativecommons.org/licenses/by/4.0/>.
Funded by SCOAP³.

References

1. T.K. Gaisser, T. Stanev, F. Halzen et al., Gamma-ray astronomy above 50 TeV with muon-poor showers. *Phys. Rev. D* **43**(2), 314 (1991). <https://doi.org/10.1103/PhysRevD.43.314>
2. Z. Cao, F.A. Aharonian, Q. An et al., Ultrahigh-energy photons up to 1.4 petaelectronvolts from 12 γ -ray Galactic sources. *Nature* (2021). ISSN:1476-4687. <https://doi.org/10.1038/s41586-021-03498-z>
3. F. Aharonian, Q. An, Axikegu et al., Observation of the Crab Nebula with LHAASO-KM2A—a performance study. *Chin. Phys. C* **45**(2), 025002 (2021). <https://doi.org/10.1088/1674-1137/abd01b>
4. A. Borione, C.E. Covault, J.W. Cronin et al., A large air shower array to search for astrophysical sources emitting γ -rays with energies $\geq 10^{14}$ eV. *Nucl. Instrum. Methods Phys. Res. A* **346**(1–2), 329 (1994). [https://doi.org/10.1016/0168-9002\(94\)90722-6](https://doi.org/10.1016/0168-9002(94)90722-6)
5. H. Schoorlemmer, J. Hinton, R. López-Coto, Characteristics of extensive air showers around the energy threshold for ground-particle-based γ -ray observatories. *Eur. Phys. J. C* **79**(5), 427 (2019). <https://doi.org/10.1140/epjc/s10052-019-6942-x>
6. R.D. Parsons, S. Ohm, Background rejection in atmospheric Cherenkov telescopes using recurrent convolutional neural networks. *Eur. Phys. J. C* **80**(5), 363 (2020). <https://doi.org/10.1140/epjc/s10052-020-7953-3>
7. S. Ohm, C. van Eldik, K. Egberts, γ /hadron separation in very-high-energy γ -ray astronomy using a multivariate analysis method. *Astropart. Phys.* **31**(5), 383 (2009). <https://doi.org/10.1016/j.astropartphys.2009.04.001>
8. J. Albert, E. Aliu, H. Anderhub et al., Implementation of the random forest method for the imaging atmospheric Cherenkov telescope MAGIC. *Nucl. Instrum. Methods Phys. Res. A* **588**(3), 424 (2008). <https://doi.org/10.1016/j.nima.2007.11.068>
9. D. Berge, S. Funk, J. Hinton, Background modelling in very-high-energy γ -ray astronomy. *Astron. Astrophys.* **466**(3), 1219 (2007). <https://doi.org/10.1051/0004-6361/20066674>
10. G. Vacanti, P. Fleury, Y. Jiang et al., Muon ring images with an atmospheric Čerenkov telescope. *Astropart. Phys.* **2**(1), 1 (1994). [https://doi.org/10.1016/0927-6505\(94\)90012-4](https://doi.org/10.1016/0927-6505(94)90012-4)
11. M. Gaug, S. Fegan, A.M.W. Mitchell et al., Using muon rings for the calibration of the Cherenkov telescope array: a systematic review of the method and its potential accuracy. *Astrophys. J. Suppl.* **243**(1), 11 (2019). <https://doi.org/10.3847/1538-4365/ab2123>
12. A.M.W. Mitchell, H.P. Dembinski, R.D. Parsons, Potential for measuring the longitudinal and lateral profile of muons in TeV air showers with IACTs. *Astropart. Phys.* **111**, 23 (2019). <https://doi.org/10.1016/j.astropartphys.2019.03.005>
13. M. de Naurois, H.E.S.S.-II—Gamma ray astronomy from 20 GeV to hundreds of TeV's, in *European Physical Journal Web of Conferences*, vol. 136 (2017), p. 03001. <https://doi.org/10.1051/epjconf/201713603001>
14. CTA-Consortium, *Science with the Cherenkov Telescope Array* (World Scientific, Singapore, 2019). <https://doi.org/10.1142/10986>
15. G. Maier, J. Knapp, Cosmic-ray events as background in imaging atmospheric Cherenkov telescopes. *Astropart. Phys.* **28**(1), 72 (2007). <https://doi.org/10.1016/j.astropartphys.2007.04.009>
16. K. Bernlöhr, Impact of atmospheric parameters on the atmospheric Cherenkov technique*. *Astropart. Phys.* **12**(4), 255 (2000). [https://doi.org/10.1016/S0927-6505\(99\)00093-6](https://doi.org/10.1016/S0927-6505(99)00093-6)
17. K. Bernlöhr, Simulation of imaging atmospheric Cherenkov telescopes with CORSIKA and sim_telarray. *Astropart. Phys.* **30**(3), 149 (2008). <https://doi.org/10.1016/j.astropartphys.2008.07.009>
18. W.R. Nelson, Y. Namito, The EGS4 code system: solution of gamma-ray and electron transport problems, in *Presented at the International Conference on Supercomputing in Nuclear Applications* (1990), pp. 12–16
19. D. Heck, J. Knapp, J.N. Capdevielle et al., *CORSIKA: a Monte Carlo Code to Simulate Extensive Air Showers* (Forschungszentrum Karlsruhe GmbH, Karlsruhe, 1998)
20. S. Sailer, F. Werner, G. Hermann et al., Trigger performance verification of the FlashCam prototype camera. *Nucl. Instrum. Methods Phys. Res. A* **936**, 392 (2019). <https://doi.org/10.1016/j.nima.2018.08.104>
21. J. Tyler, Muon identification with VERITAS using the Hough transform, in *International Cosmic Ray Conference*, vol. 33 (2013), p. 3096
22. Q. Feng, T.T.Y. Lin, The analysis of VERITAS muon images using convolutional neural networks. *Proc. Int. Astron. Union* **12**(S325), 173–179 (2016). <https://doi.org/10.1017/S1743921316012734>
23. R.D. Parsons, S. Ohm, Private Communication (2021)
24. P. Hazarika, U.D. Goswami, V.R. Chitnis et al., Lateral density and arrival time distributions of Cherenkov photons in extensive air showers: a simulation study. *Astropart. Phys.* **68**, 16 (2015). <https://doi.org/10.1016/j.astropartphys.2015.02.003>
25. R. Mirzoyan, D. Sobczynska, E. Lorenz et al., Tagging single muons and other long-flying relativistic charged particles by ultra-fast timing in air Cherenkov telescopes. *Astropart. Phys.* **25**(5), 342 (2006). <https://doi.org/10.1016/j.astropartphys.2006.03.006>
26. R. Parsons, J. Hinton, A Monte Carlo template based analysis for air-Cherenkov arrays. *Astropart. Phys.* **56**, 26 (2014). ISSN:0927-6505. <https://doi.org/10.1016/j.astropartphys.2014.03.002>
27. M. de Naurois, L. Rolland, A high performance likelihood reconstruction of γ -rays for imaging atmospheric Cherenkov telescopes. *Astropart. Phys.* **32**(5), 231 (2009). <https://doi.org/10.1016/j.astropartphys.2009.09.001>
28. A. Brill, B. Kim, D. Nieto et al., CTLearn: deep learning for imaging atmospheric Cherenkov telescopes event reconstruction (2021). <https://doi.org/10.5281/zenodo.4576196>
29. M. Jacquemont, T. Vuillaume, A. Benoit et al., GammaLearn: a deep learning framework for IACT data. *PoS ICRC2019*, 705 (2019). <https://doi.org/10.22323/1.358.0705>
30. K.-H. Kampert, M. Unger, Measurements of the cosmic ray composition with air shower experiments. *Astropart. Phys.* **35**(10), 660 (2012). <https://doi.org/10.1016/j.astropartphys.2012.02.004>
31. C.R. Harris, K.J. Millman, S.J. van der Walt et al., Array programming with NumPy. *Nature* **585**, 357–362 (2020). <https://doi.org/10.1038/s41586-020-2649-2>
32. P. Virtanen, R. Gommers, T.E. Oliphant et al., SciPy 1.0: fundamental algorithms for scientific computing in Python. *Nat. Methods* **17**, 261 (2020). <https://doi.org/10.1038/s41592-019-0686-2>
33. W. McKinney et al., Data structures for statistical computing in python, in *Proceedings of the 9th Python in Science Conference, Austin, TX*, vol. 445 (2010), pp. 51–56. <https://doi.org/10.25080/Majora-92bf1922-00a>
34. J.D. Hunter, Matplotlib: a 2D graphics environment. *Comput. Sci. Eng.* **9**(3), 90 (2007)



Background rejection using image residuals from large telescopes in imaging atmospheric Cherenkov telescope arrays

L. Olivera-Nieto^{1,a} , H. X. Ren¹ , A. M. W. Mitchell² , V. Marandon¹ , J. A. Hinton¹ 

¹ Max-Planck-Institut für Kernphysik, P.O. Box 103980, 69029 Heidelberg, Germany

² Friedrich-Alexander-Universität Erlangen-Nürnberg, Erlangen Centre for Astroparticle Physics, 91058 Erlangen, Germany

Received: 10 August 2022 / Accepted: 23 November 2022
© The Author(s) 2022

Abstract Identification of Cherenkov light generated by muons has been suggested as a promising way to dramatically improve the background rejection power of Imaging Atmospheric Cherenkov Telescope (IACT) arrays at high energies. However, muon identification remains a challenging task, for which efficient algorithms are still being developed. We present an approach in which, rather than identifying Cherenkov light from muons, we simply consider the presence of Cherenkov light other than the main shower image in IACTs with large mirror area. We show that in the case of the H.E.S.S. array of five telescopes this approach results in background rejection improvements at all energies above 1 TeV. In particular, the rejection power can be improved by a factor $\sim 3\text{--}4$ at energies above 20 TeV while keeping $\sim 90\%$ of the original gamma-ray efficiency.

1 Introduction

The Earth's atmosphere is opaque to very-high-energy (VHE) radiation. Incoming gamma-ray photons lose their energy by initiating electromagnetic particle cascades in the atmosphere. The particles in these cascades are highly relativistic and cause the production of Cherenkov light, which is in turn collected by the telescope dishes of Imaging Atmospheric Cherenkov Telescopes (IACTs). Given the huge rates of background cosmic-rays, a factor 10^4 greater than those of gamma-rays [1], differentiating between hadronic and electromagnetic cascades is a task critical to gamma-ray astronomy.

IACTs have superior rejection power to other ground-based arrays in the domain around 1 TeV, exploiting primarily the differences in shower width and substructure between electromagnetic and hadronic showers [2]. At higher ener-

gies, of around tens of TeVs the rejection power worsens. High-energy events are often not fully contained in the camera, which makes the determination of the image parameters difficult. Additionally, this parameterisation becomes dominated by the very bright central component of high-energy showers, with additional faint emission that would indicate a hadronic origin being overlooked.

Large numbers of muons, primarily resulting from the decay of charged pions, are usually produced in the hadronic cascades initiated by cosmic-rays. The potential of muons as a tool to separate between these two classes of showers has long been recognized (see, for example [3]). Recently, [4] showed that for very large ($\gtrsim 20$ m mirror diameter) telescopes efficient identification of muon light can potentially lead to background rejection levels up to 10^{-5} at energies above 10 TeV.

However, muon identification is not a trivial task. Muons that pass directly through the telescope dish produce a distinguishable ring-like image in the telescope camera. But once the ground impact distance increases beyond some tens of meters only a fraction of the ring arc is detected (see top panel of Fig. 1). Therefore muons which arrive far from the telescopes can easily be confused for low-energy shower images, or optical night-sky-background (NSB) noise. Alternative approaches, like making use of the signature of arrival time of muon light are promising, yet even then the task of muon identification remains a challenge [5].

Nevertheless, given the magnitude of the achievable background rejection power shown in [4], less-than efficient muon identification could still result in a significant improvement to the current background rejection power of IACTs. We present an approach in which, rather than being concerned with whether a recorded event contains muon light or not, we simply consider the presence of light other than the main shower image (see bottom panel of Fig. 1). This, of course, has the downside of being less precise in the sense that light

^a e-mail: Laura.Olivera-Nieto@mpi-hd.mpg.de (corresponding author)

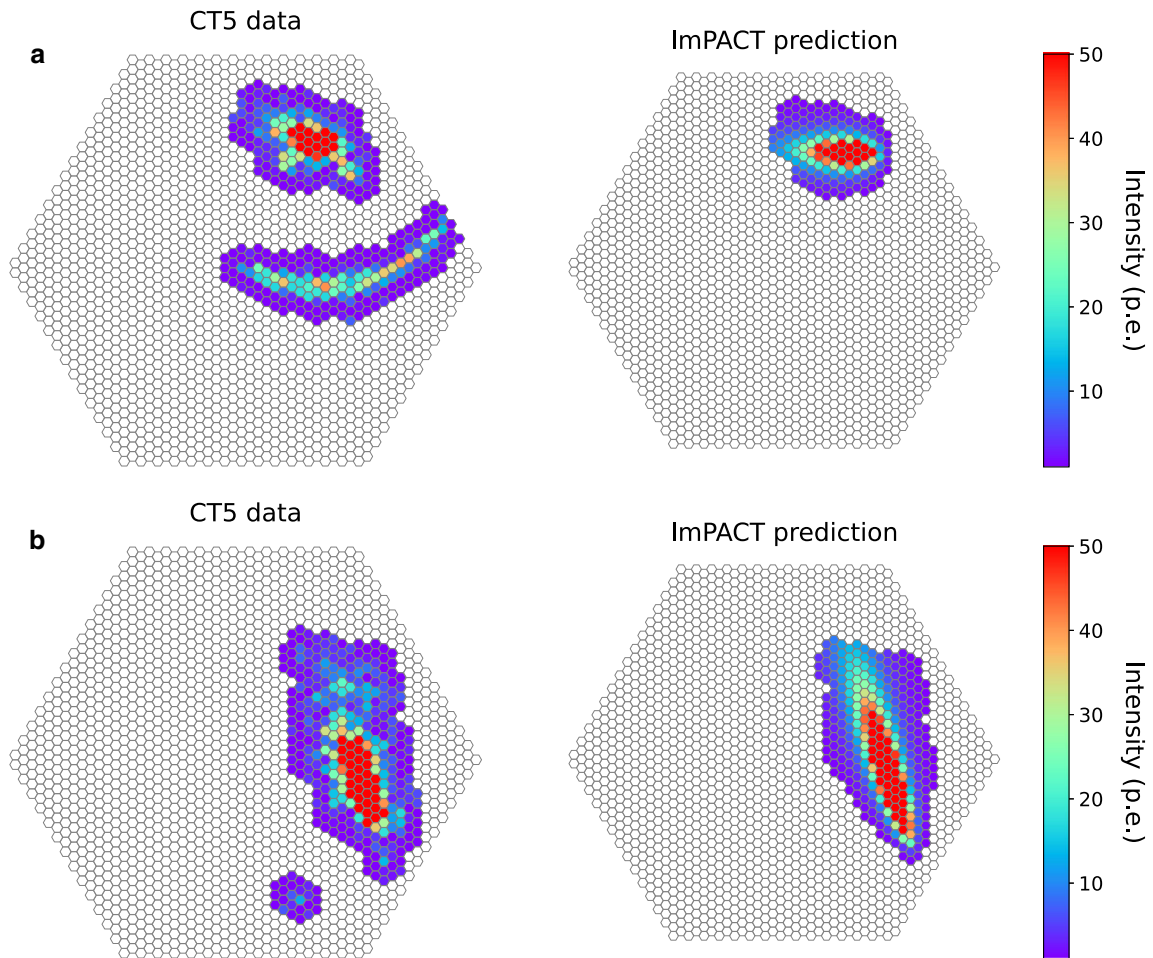


Fig. 1 Large telescope images of rejected events that would be labelled as gamma-ray candidates in the small telescope reconstruction. In both cases, the right panel shows the ImpACT prediction associated with that event, whereas the left panel shows the actual recorded event image. The event image shown in the panel labelled as “a” contains a clear muon

arc, whereas the additional feature in the image in panel “b” is much smaller and has a simpler shape. However, the maximum pixel intensity in this feature is more than double what is expected from NSB noise. Note that the colorbar has been restricted so that the fainter features are visible, since the main shower is much brighter in both cases

from particles other than muons – electrons, for example – may be used to reject events. Additionally, unusually high NSB noise could lead to an event being rejected. However, it results in a much simpler implementation which, as shown below, still leads to improved background rejection power.

For this task we used data and simulations from the telescopes in the High Energy Stereoscopic System (H.E.S.S.) [6]. The H.E.S.S. experiment is comprised of a total of five telescopes: four with a dish of 12 m diameter referred to as CT1-4 and a central one, CT5, with a dish of 28 m diameter. The event reconstruction is referred to as *stereo* when only the small CT1-4 telescopes are used, and *hybrid* when data from the entire array is used. In this work we present an alternative approach in which only the data of CT1-4 is used for the event reconstruction, that is, *stereo* mode, but the data of CT5 is used for an extra step of background rejection.

2 Background rejection with image residuals: ABRIR

ABRIR (*Algorithm for Background Rejection using Image Residuals*) is a background rejection algorithm which draws additional information from the event image taken by a large telescope, such as CT5 for the case of the H.E.S.S. array. This algorithm is applied after the usual H.E.S.S. *stereo* reconstruction, which includes an initial step of background rejection based on Boosted Decision Trees (BDTs) [2]. In particular, we use two sets of initial cuts: the H.E.S.S. *standard* selection cuts (see Section 4.2 of [2]), optimized for a Crab Nebula-like source and the so-called *hard* cuts, optimized for a faint hard source. The main difference between both sets of cuts is that while the *standard* cuts only require images to have a total intensity larger than 60 photoelectrons (p.e.), the *hard* cuts require a minimum of 200 p.e. This translates into a higher energy threshold but also higher quality events and

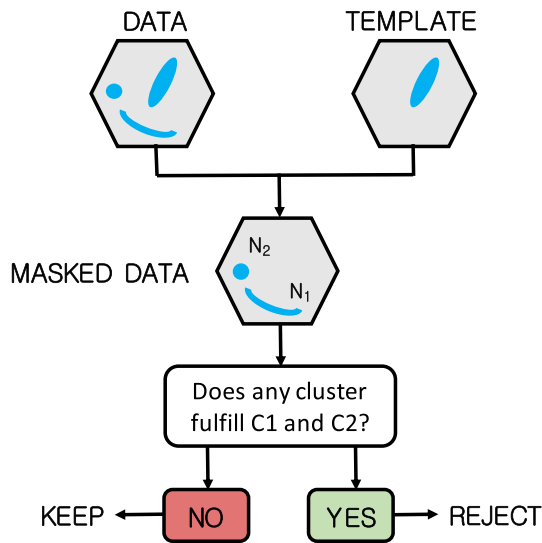


Fig. 2 Schematic diagram representing the algorithm structure

more precise reconstructed parameters, such as core location or energy. Additionally the threshold of the BDT parameter [2] is different, with 0.84 for the *standard* case and 0.8 for the *hard* cut. We will denote the gamma-ray and background efficiency of this first cut as $\eta_{BDT,\gamma}$ and $\eta_{BDT,B}$ respectively. We will apply ABRIR only to the events that survive this initial cut. Only at this step is the data from CT5 used, and it is exclusively CT5 images being considered by the algorithm due to the advantaged muon detection capabilities of large telescopes. Note that the total gamma-ray and background efficiency ($\eta_{tot,\gamma}$ and $\eta_{tot,B}$) needs to be computed as the product of that of the initial cut and that of ABRIR, so:

$$\eta_{tot,\gamma} = \eta_{\gamma} \cdot \eta_{BDT,\gamma}$$

$$\eta_{tot,B} = \eta_B \cdot \eta_{BDT,B}$$

where η_{γ} and η_B are the gamma-ray and background efficiency of ABRIR (see Sect. 3).

2.1 The ImPACT templates

In order to identify light as not a part of the main shower, we need to identify the main shower itself. We do this with the help of the *Image Pixel-wise fit for Atmospheric Cherenkov Telescopes* (ImPACT) algorithm [7], which is routinely used by the H.E.S.S. experiment. ImPACT is a gamma-ray event reconstruction algorithm that is based on the likelihood fitting of camera pixel amplitudes to an expected image template. These templates are built with a full Monte Carlo gamma-ray air shower simulation, followed by ray-tracing of the telescope optics and simulation of the instrument electronics [8,9]. This fit is computationally expensive, so it is only performed after a first round of background rejection is applied. For each event this process results in an image of what the

most similar gamma-ray event would look like in each of the telescopes. We use this prediction to mask the main component of CT5 image in order to better identify residual features. Note that the CT5 image is not used in this likelihood fit, with the CT5 template being derived only from the best-fit parameters of the CT1-4 fit.

2.2 The rejection criteria

After the main shower is masked, the remaining residual image is searched for clusters of pixels (N). A cluster is only considered if it is comprised of more than three neighboring pixels. For each of the clusters we compute the maximum intensity $I_{max,N}$, the total intensity $I_{tot,N}$ and the distance to the main shower d_N . In the next step, two conditions are checked against each of the clusters:

$$(C1) I_{tot,N} \cdot d_N^2 > I_{tot} \cdot d^2$$

$$(C2) I_{max,N} > I_{max}$$

where the threshold values used here for I_{max} and $I_{tot} \cdot d^2$ are 9 p.e. and 2 p.e. · pixel² respectively. These values were selected to maintain a gamma-ray efficiency of around 90%, which in turn results in the background rejection performance described in Sect. 3. A different requirement on the gamma-ray efficiency would naturally impact the background rejection power, with better rejection achievable if a higher fraction of gamma-rays is lost. Additionally, these values are specific to the current state of the central telescope in the H.E.S.S. array and should be adjusted as appropriate for application to other telescopes or cameras.

The first condition (C1) selects clusters by their total intensity with a penalization on proximity to the main shower. This is done to reject clusters created solely by a mismatch between the outer row of pixels of the main shower image and the predicted template. Such clusters might have a high total intensity, but they are also very close to the main shower, which means the product of intensity and distance will fall below the required threshold. Additionally, this cut is always survived by relatively bright clusters that are far from the shower, and thus have a high probability of not originating from a mismatch between the data and the template. The second condition (C2) aims to reject clusters resulting from uncleaned noise from the NSB. It does so by requiring the maximum pixel intensity of a given cluster to be above a threshold defined by the 5 σ level of the pedestal width of a typical run. Note that this specific value depends on the image cleaning method used, as well as on the camera performance and expected NSB level.

Events that fail either of the two conditions are kept, as well as events with too small or no clusters outside of the main image. A schematic view of the algorithm is shown in Fig. 2. Additionally, events for which no light in the large telescope

was predicted by the template, but something is seen are also marked as rejected, as well as the opposite case, events in which an shower image was predicted, but all pixels in the data are below a minimal threshold of 1 photoelectron.

3 Performance

We assess the performance of the algorithm by testing it on different types of events. Note that both the background rejection power and the gamma-ray efficiency presented in this section are a relative improvement on the value for the initial H.E.S.S. *standard* and *hard* selection cuts. Those curves are shown in Fig. 6.

3.1 Background rejection power

In order to test the performance of the algorithm on the cosmic-ray background, we use what is referred to as *off-runs*, that is, observations in which the telescopes are pointed at fields without a known gamma-ray source. These off-runs are typically the result of dedicated observations of known empty fields, or also observations of extragalactic objects like dwarf spheroidal galaxies that did not yield a gamma-ray detection [10]. These are not completely free of gamma-ray events, due to large-scale diffuse emission like the extragalactic gamma-ray background and also due to possible undetected faint gamma-ray sources. However, the relative fluxes of background cosmic-rays to these gamma-ray sources make it safe to neglect this contribution. It would also be possible to use simulations of proton-initiated showers in order to eliminate this contamination. However, due to uncertainties in the hadronic models used for high-energy particle interactions [11, 12], there are significant differences between the properties of measured background events and those that result from simulations. For this reason we decide to use real data only to characterize the background, as it is more realistic and not dependent on the agreement between data and simulations.

Figure 1 shows two example rejected events from one of these off runs which pass the *standard* H.E.S.S. cuts. The right panel shows the ImpACT prediction associated with each event, whereas the left panel shows the actual recorded event image. For both cases, the conditions C1 and C2 are fulfilled.

Figures 3 and 4 show the ABRIR cut efficiency for different samples as a function of the event reconstructed energy for several observation zenith angles. Figure 3 corresponds to the case where events surviving the H.E.S.S. *standard* cuts are given as input, whereas the input events for the curves in Fig. 4 survive the *hard* cuts. The efficiency shown in the figures is calculated simply as the ratio of the number of events before and after the application of ABRIR. As can be seen,

the cut rejects a significant fraction of off-run events in both cases (red line) at all energies. Background rate reductions of up to a factor 2.5 are obtained for energies above a few TeV for the *standard* cuts case, while when using only the higher quality events selected by the *hard* cut as input, this improvement goes up to factors of 3 and even 4 for energies above tens of TeV.

3.2 Gamma-ray efficiency

Besides rejecting a lot of suspected background events, it is important to keep a high fraction of the true gamma-ray events. Some gamma-ray events are expected to be flagged as rejected by the algorithm, and they belong to three different categories:

1. **Gamma-ray events that contain muon light.** As shown by [4], a small fraction of high-energy gamma-ray initiated showers will actually contain muons, which can be detected by the large telescope. These events make up an irreducible set of lost gamma-ray events associated with muon-tagging based rejection.
2. **Gamma-ray events with low-altitude electrons.** Since our approach does not identify muon light as such, the light from any other particle that would create a component in the image besides the gamma-ray shower could lead to an event being rejected. Camera images of gamma-ray showers can contain light from scattered electrons from the shower that emit close to the telescope dish. This can create additional image components separated from the main shower image. The likelihood of this effect drops rapidly as the shower core ground impact point moves away from the telescope position.
3. **Gamma-ray events with unusually high NSB noise.** A fraction of gamma-ray events will contain noise from the NSB that is brighter than the threshold set by condition C2 from Sect. 2.2. This can happen in the simulations due to fluctuations in the NSB level, but it is also important in real data, especially since the NSB is not the same for all regions of the sky. This fraction is thus heavily dependent on the NSB conditions that were assumed when the algorithm's parameters were chosen, and also on the type of cleaning that is used to remove the NSB contribution to the images.

We compute the gamma-ray efficiency of ABRIR by running it on simulated gamma-ray events, using the CORSIKA package [9] for shower and Cherenkov light simulation and the *sim-telarray* package [8] for the telescope response and camera simulation. In order to check the consistency of the result in real data, we also check with a sample of events which reconstructed direction falls within 0.2° of the Crab Nebula and PKS 2155-304, which are known bright gamma-

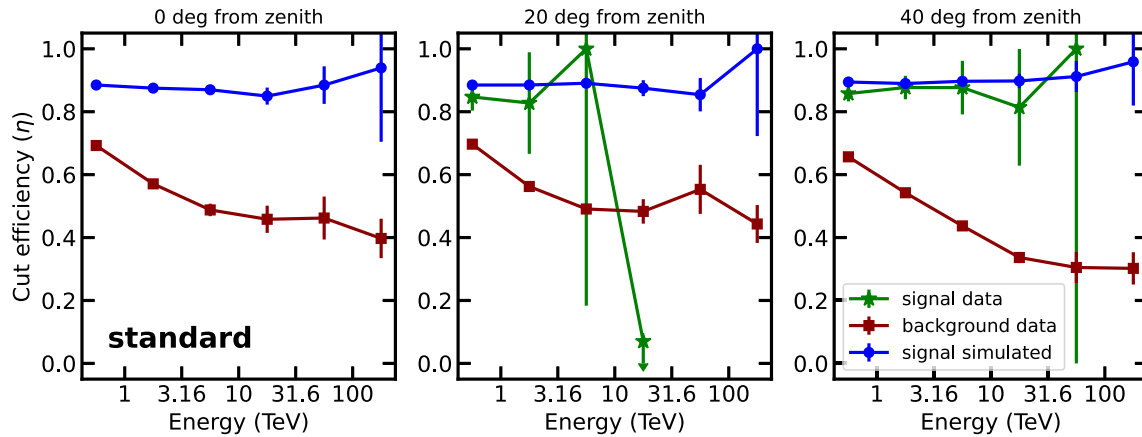


Fig. 3 Fraction of events kept by the ABRIR cut applied after the H.E.S.S. *standard* cuts for simulated gamma-rays (blue dots), background data from off-runs (red squares) and events taken from a radius of 0.2° from bright gamma-ray sources (green stars), in particular the blazar PKS 2155-304 at zenith angles of 20° and the Crab Nebula for

the 40° zenith range. Note that since PKS 2155-304 is an extragalactic source, no gamma-rays are expected to arrive from it above a few TeV due to absorption on the extragalactic background light. When zero events survive the cut, the 68% containment limit is drawn assuming Poissonian statistics

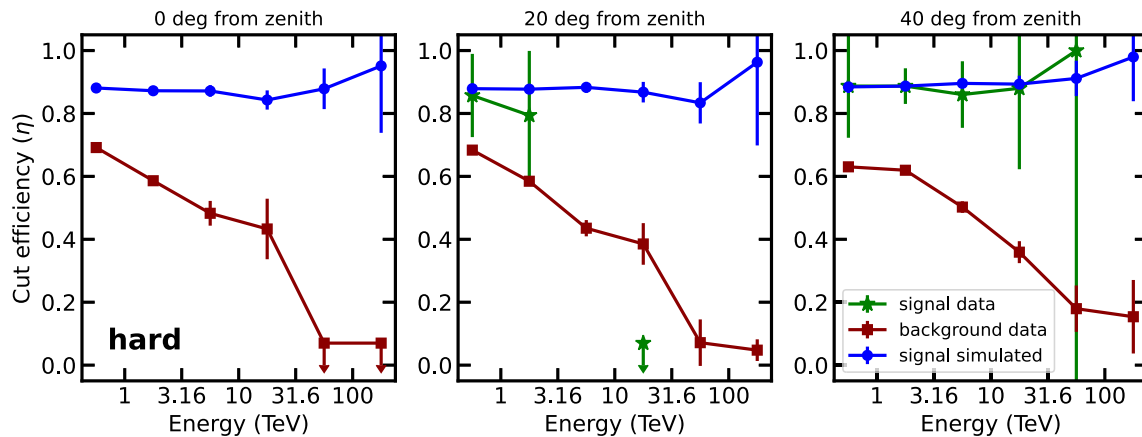


Fig. 4 Fraction of events kept by the ABRIR cut applied after the H.E.S.S. *hard* cuts. Meaning of different panels and colors is the same as in Fig. 3. When zero events survive the cut, the 68% containment limit is drawn assuming Poissonian statistics

ray sources. Note that this sample is expected to contain some small fraction of cosmic-ray background, as cosmic-ray events are distributed roughly uniformly on the sky. However, due to the relatively high gamma-ray flux of these sources, the majority of events in this sample will be true gamma-rays, and thus can be used to check the performance on real data events. Note that this comparison is restricted to the zenith angles in which these sources can be observed by the H.E.S.S. experiment and also by the energies reached by the sources themselves.

Figures 3 and 4 show the ABRIR cut efficiency for the simulated gamma-ray sample (blue lines) as well as the events selected around known gamma-ray sources (green line). Note that the gamma-ray efficiency is mostly flat as a function of energy. This indicates that the group dominating the rejected

gamma-rays are those with residual features caused by the NSB, since, unlike the expected number of muons, this does not depend on the event energy. The gamma-ray efficiency computed with real data is consistent with that found in simulations, which in turn confirms that the simulated NSB level is consistent with that encountered in a typical field.

3.3 Application to a gamma-ray source: the Crab Nebula

In order to verify the expected improved performance, we perform an analysis of the same dataset from a real gamma-ray source with and without the use of ABRIR and compare the results. For this, we use a total of 30 h of observations of the Crab Nebula by the full array of the H.E.S.S. telescopes. Note that since the goal of this paper is to demonstrate the

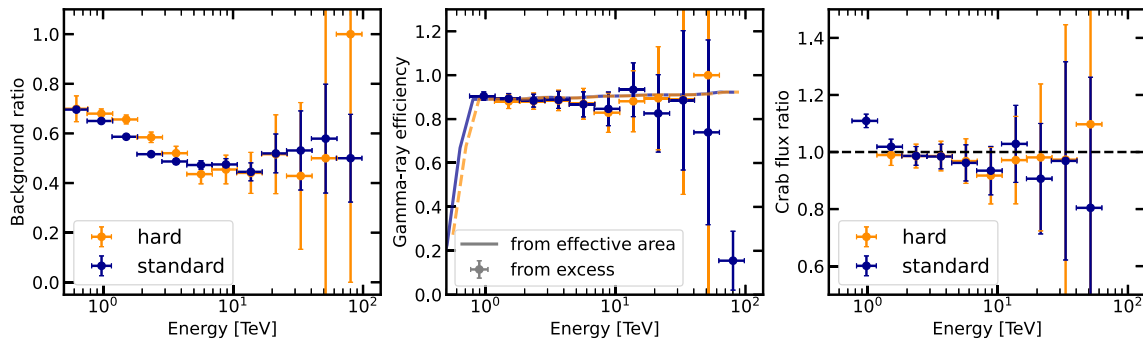


Fig. 5 Verification of the performance using data from the Crab Nebula. All ratios shown in this figure are computed as the quantity after applying the ABRIR cut divided by the same quantity before the cut. *Left*: Ratio of background counts with and without the use of ABRIR for both the *standard* (dark blue) and *hard* (orange) cuts. *Middle*: Gamma-ray efficiency computed as the ratio of the resulting effective area for

the datasets with and without ABRIR (solid lines) and as the ratio of the measured excess (data points), again for both sets of cuts using the same color scheme as in the left panel. *Right*: Ratio of the measured flux from the Crab Nebula as a function of energy with and without the use of ABRIR for both sets of initial cuts

relative performance of this analysis technique, only ratios of the relevant quantities will be shown.

In both cases, we first perform a *stereo* reconstruction of the data which excludes the large central telescope. This results in a list of events which, in the case without ABRIR are directly bundled with the relevant instrument response functions (IRFs) via the *Gammapy* [13] package, as described in [14]. When applying ABRIR, an extra step is performed in which the algorithm is applied, the flagged events are removed from the event list and the effective areas are corrected by the gamma-ray efficiency computed from simulations. The new event lists and IRFs are bundled in the same way as before.

Once both datasets are ready, we can extract and compare different quantities from them. First, we estimate the background level in a region of 0.3° radius around the Crab location using the so-called *reflected-region* background method (see [15] for a detailed description). This choice of region size is relatively large for a standard H.E.S.S. point-source analysis, but allows for increased statistics on the background measurement. The ratio of the measured background before and after applying ABRIR as a function of energy can be seen in the left panel of Fig. 5, for both sets of initial cuts. The resulting background efficiency is consistent with the one derived from the off runs shown in Figs. 3 and 4 within statistical errors. Using this measurement of the background, we can compute the excess counts in the source region, and compare it to the ratio of the effective areas. This is an additional verification that the performance on simulated gamma-rays is observed in real data. The result can be seen in the middle panel of Fig. 5. Finally we can compute the flux from the Crab nebula as a function of energy. The rightmost

panel of Fig. 5 shows the ratio of flux measured before and after applying ABRIR as a function of energy for both sets of cuts. As can be seen, they are consistent with a ratio of unity within statistical errors, with the exception of the lowest energy point in the *standard* result. This indicates a possible mischaracterization of the effective area at the lowest energies. Given that effective areas were not produced from scratch for the ABRIR dataset, but rather derived from existing ones using an energy-dependent correction, it is possible that the region near threshold, where the effective area raises rapidly, is less accurately characterized. Dedicated IRFs or an increased threshold would solve this issue.

3.4 Comparison to *hybrid* reconstruction

The background rejection powers achieved with the combination of the baseline *stereo* algorithms and ABRIR are superior than those obtained when data from the large telescope is included in the reconstruction from the beginning – i.e. *hybrid* reconstruction. This can be seen when comparing the combination of the ABRIR efficiencies shown in Figs. 3 and 4 and the baseline *stereo* efficiencies shown in Fig. 6 with those of the *hybrid* analysis shown in Fig. 7. The reason for this lack of performance is that combining information from different telescope sizes at the reconstruction level is a non-trivial task, especially for the algorithms that rely on image shape parameters. Ongoing improvements to the H.E.S.S. *hybrid* chain have shown promising results and may achieve a performance comparable to that of ABRIR in the low energy range. However, at high energies ABRIR will likely continue to provide improved performance beyond that achieved by a hybrid analysis based on the standard image parameters.

4 Discussion

We have presented an algorithm that makes use of large-dish telescopes in an IACT array as a veto step in order to improve the background rejection. Its use improves the background rejection power of the baseline H.E.S.S. *stereo* reconstruction by a factor ranging between 2 and 4, depending on energy and the specifics of the initial cut. The combined efficiency of this extra cut with the baseline rejection power of the *stereo* reconstruction can reach background rejection powers higher than 10^4 for high energies. Improved background rejection is crucial for the detection and characterization of extended and faint sources. Reducing the background rate also reduces the uncertainties associated with it, leading to improved precision at high energies. This improvement can be decisive in order to determine, for example, the presence of energy-dependent morphology.

The different performance at high energies depending on the chosen initial cut for the *stereo* reconstruction is due to their different image amplitude thresholds. The *standard* cuts keep events whose image has a total brightness of more than 60 p.e. in two of the four telescopes at least. The threshold for the *hard* cuts is 200 p.e. The image of an event can have low brightness either because the primary particle had relatively low energy, or because the location of the shower core is far from the array. This means that some events that are below the 200 p.e. threshold will be reconstructed with high energies but large core distances. At large core distances, the number of muons that are detectable by the telescope will be reduced [4], meaning that the power of the veto approach is reduced.

All results shown here are based on images for which the noise has been cleaned using the so-called *tail-cuts* cleaning method, which requires each pixel to have an intensity exceeding a threshold I_1 and a neighbour exceeding a threshold I_2 [16]. In particular we have used $I_1 = 7$ p.e. and $I_2 = 4$ p.e., as required for the ImPACT algorithm [7]. As mentioned in Sect. 3, remaining NSB noise seems to be the leading cause of loss of gamma-ray events when applying ABRIR. A different image cleaning approach, such as those based on the time information of the shower image [17] could improve these results.

The presence of broken or unusable pixels in the camera, that is regions of the camera which do not take data, could in principle impact the ability to identify the presence of additional charge away from the shower [16]. However, in the case of the HESS CT5 camera, the number of such pixels is usually very small. There are just 6 isolated permanently turned off pixels, and for certain sky regions, the presence of bright stars can result in one or two more pixels being turned off [18]. This leads to a very small effect given that the camera has 1764 pixels in total and muons are uniformly distributed across it.

We have shown here the performance of ABRIR when applied to the H.E.S.S. array, which is made up of four middle-sized telescopes and one large, central telescope. The future Cherenkov Telescope Array (CTA) will be made up of telescopes of three sizes, the largest of which is smaller than the central H.E.S.S. telescope yet still large enough to efficiently detect muons. The idea behind the algorithm will thus be applicable to the CTA array, although whether or not will it be a competitive technique will depend on the analysis approaches used for mixed-telescope types and sub-array selection of the observations. Large telescopes are typically seen as an asset only at the low energies due to their reduced threshold. However, as we show here, including large telescopes when observing targets for which the spectrum is expected to extend to high energies is worthwhile given the achievable improvements especially in background rejection.

Acknowledgements The authors would like to thank the H.E.S.S. Collaboration for allowing the use of H.E.S.S. data and simulations in this publication, as well as providing useful discussions and input to the paper. This work made use of `numpy` [19], `scipy` [20], `pandas` [21], `matplotlib` [22], `uproot` [23] and `ctapipe` [24].

Funding This research was supported by the Max Planck Society. AMWM is supported by the Deutsche Forschungsgemeinschaft (DFG, German Research Foundation) – Project Number 452934793.

Data Availability Statement This manuscript has no associated data or the data will not be deposited. [Authors' comment: The data and simulations used for this work are propriety of the H.E.S.S. Collaboration.]

Open Access This article is licensed under a Creative Commons Attribution 4.0 International License, which permits use, sharing, adaptation, distribution and reproduction in any medium or format, as long as you give appropriate credit to the original author(s) and the source, provide a link to the Creative Commons licence, and indicate if changes were made. The images or other third party material in this article are included in the article's Creative Commons licence, unless indicated otherwise in a credit line to the material. If material is not included in the article's Creative Commons licence and your intended use is not permitted by statutory regulation or exceeds the permitted use, you will need to obtain permission directly from the copyright holder. To view a copy of this licence, visit <http://creativecommons.org/licenses/by/4.0/>.

Funded by SCOAP³. SCOAP³ supports the goals of the International Year of Basic Sciences for Sustainable Development.

Appendix A: Efficiencies of the baseline H.E.S.S. cuts

We computed the background and gamma-ray efficiencies by running the H.E.S.S. analysis on the off run events and simulated gamma-rays with and without the baseline Boosted Decision Tree (BDT) cuts. The efficiency is then computed as the ratio of the events passing the BDT cut to the initial number of events. Note that this initial number comprises only events surviving the respective image amplitude threshold for each of the cut sets (60 p.e. for *standard* cuts and 200

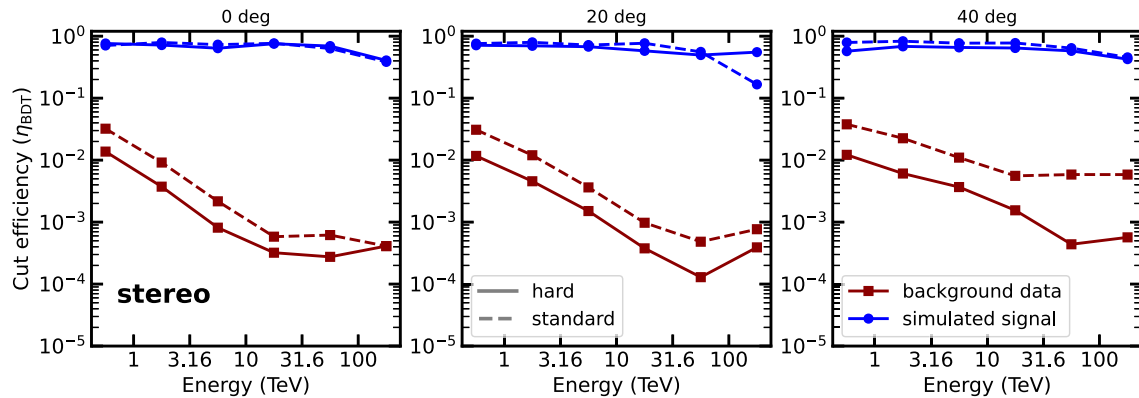


Fig. 6 Cut efficiencies of the *stereo* reconstruction for the *standard* and *hard* cuts

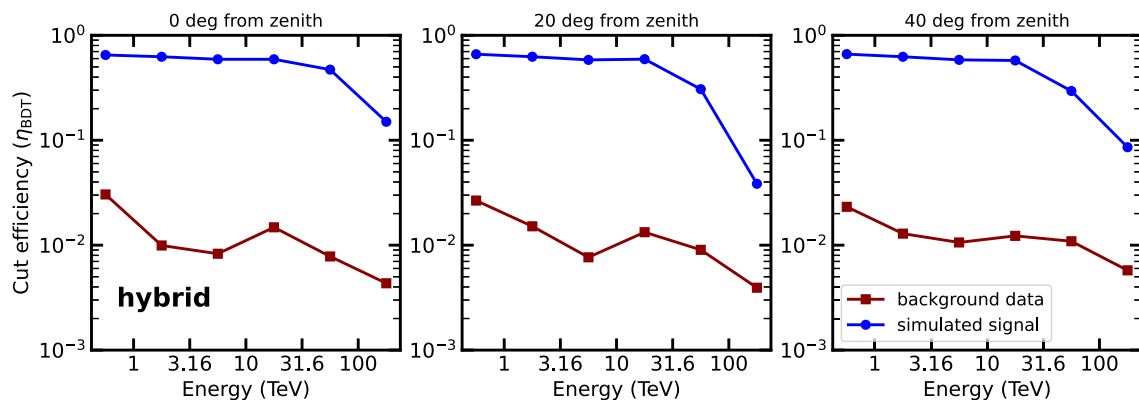


Fig. 7 Cut efficiencies of the *hybrid* reconstruction using the *standard-hybrid* cuts

p.e. for the *hard* cuts). The resulting efficiencies are shown for different energies and zenith ranges in Figs. 6 (*stereo* reconstruction) and 7 (*hybrid* reconstruction). Note that the cuts used in the *hybrid* case, so-called *standard-hybrid* cuts, are different from the *stereo* ones in terms of thresholds, but are optimized for the same science case: a Crab Nebula-like source.

References

1. W. Benbow, H. Collaboration, The H.E.S.S. standard analysis technique. In: Proc. Conf. Towards a Network of Atmospheric Cherenkov Detectors VII, Proc. Conf. Towards a Network of Atmospheric Cherenkov Detectors VII, vols. 163–172 (2005)
2. S. Ohm, C. van Eldik, K. Egberts, γ /hadron separation in very-high-energy γ -ray astronomy using a multivariate analysis method. *Astropart. Phys.* **31**(5), 383 (2009). <https://doi.org/10.1016/j.astropartphys.2009.04.001>
3. T.K. Gaisser, T. Stanev, F. Halzen et al., Gamma-ray astronomy above 50 TeV with muon-poor showers. *Phys. Rev. D* **43**(2), 314 (1991). <https://doi.org/10.1103/PhysRevD.43.314>
4. L. Olivera-Nieto, A.M.W. Mitchell, K. Bernlöhner et al., Muons as a tool for background rejection in imaging atmospheric Cherenkov telescope arrays. *Eur. Phys. J. C* **81**(12), 1101 (2021). <https://doi.org/10.1140/epjc/s10052-021-09869-0>
5. R. Mirzoyan, D. Sobczynska, E. Lorenz et al., Tagging single muons and other long-flying relativistic charged particles by ultra-fast timing in air Cherenkov telescopes. *Astropart. Phys.* **25**(5), 342 (2006). <https://doi.org/10.1016/j.astropartphys.2006.03.006>
6. M. de Naurois, H.E.S.S.-II—Gamma ray astronomy from 20 GeV to hundreds of TeV's. In: European Physical Journal Web of Conferences, European Physical Journal Web of Conferences, vol. 136, 03001 (2017). <https://doi.org/10.1051/epjconf/201713603001>
7. R. Parsons, J. Hinton, A Monte Carlo template based analysis for air-Cherenkov arrays. *Astropart. Phys.* **56**, 26 (2014). ISSN 0927-6505. <https://doi.org/10.1016/j.astropartphys.2014.03.002>
8. K. Bernlöhner, Simulation of imaging atmospheric Cherenkov telescopes with CORSIKA and sim_telarray. *Astropart. Phys.* **30**(3), 149 (2008). <https://doi.org/10.1016/j.astropartphys.2008.07.009>
9. D. Heck, J. Knapp, J.N. Capdevielle et al., CORSIKA: a Monte Carlo code to simulate extensive air showers. Forschungszentrum Karlsruhe GmbH (1998)
10. A. Abramowski, F. Aharonian, F. Ait Benkhali et al., Search for dark matter annihilation signatures in H.E.S.S. observations of dwarf spheroidal galaxies. *Phys. Rev. D* **90**, 112012 (2014). <https://doi.org/10.1103/PhysRevD.90.112012>
11. R.D. Parsons, H. Schoorlemmer, Systematic differences due to high energy hadronic interaction models in air shower simulations in the 100 GeV–100 TeV range. *Phys. Rev. D* **100**(2), 023010 (2019). <https://doi.org/10.1103/PhysRevD.100.023010>
12. Á. Pastor-Gutiérrez, H. Schoorlemmer, R.D. Parsons et al., Sub-TeV hadronic interaction model differences and their impact on air showers. *Eur. Phys. J. C* **81**(4), 369 (2021). <https://doi.org/10.1140/epjc/s10052-021-09160-2>

13. C. Deil, A. Donath, R. Terrier et al., `gammapy/gammapy: v.0.18.2` (2020). <https://doi.org/10.5281/zenodo.4701500>
14. L. Mohrmann, A. Specovius, D. Tiziani et al., Validation of open-source science tools and background model construction in γ -ray astronomy. *Astron. Astrophys.* **632**, A72 (2019). <https://doi.org/10.1051/0004-6361/201936452>
15. D. Berge, S. Funk, J. Hinton, Background modelling in very-high-energy γ -ray astronomy. *Astron. Astrophys.* **466**(3), 1219 (2007). <https://doi.org/10.1051/0004-6361:20066674>
16. F. Aharonian, A.G. Akhperjanian, A.R. Bazer-Bachi et al., Observations of the Crab nebula with HESS. *A&A* **457**(3), 899 (2006). <https://doi.org/10.1051/0004-6361:20065351>
17. M. Shayduk, C. Consortium, Optimized next-neighbour image cleaning method for cherenkov telescopes. In: International Cosmic Ray Conference, International Cosmic Ray Conference, vol. 33, 3000 (2013)
18. B. Bi, M. Barcelo, C. Bauer et al., Performance of the new FlashCam-based camera in the 28m telescope of H.E.S.S. In: 37th International Cosmic Ray Conference, 743 (2022). <https://doi.org/10.22323/1.395.0743>
19. C.R. Harris, K.J. Millman, S.J. van der Walt et al., Array programming with NumPy. *Nature* **585**, 357–362 (2020). <https://doi.org/10.1038/s41586-020-2649-2>
20. P. Virtanen, R. Gommers, T.E. Oliphant et al., SciPy 1.0: fundamental algorithms for scientific computing in Python. *Nat. Methods* **17**, 261 (2020). <https://doi.org/10.1038/s41592-019-0686-2>
21. W. McKinney et al., Data structures for statistical computing in python. In: Proceedings of the 9th Python in Science Conference, vol. 445, pp. 51–56, Austin (2010)
22. J.D. Hunter, Matplotlib: a 2D graphics environment. *Comput. Sci. Eng.* **9**(3), 90 (2007)
23. J. Pivarski, H. Schreiner, N. Smith et al., `scikit-hep/uproot4: 4.2.3` (2022). <https://doi.org/10.5281/zenodo.6540484>
24. K. Kosack, J. Watson, M. Nöthe et al., `cta-observatory/ctapipe: v0.11.0` (2021). <https://doi.org/10.5281/zenodo.4746317>

Chapter 5

Towards a Common Data Format in VHE Gamma-ray Astronomy

The future of VHE gamma-ray astronomy will see the field move away from the current paradigm of largely proprietary data into one in which data is routinely made publicly available. This change is being driven by the upcoming CTA (see Section 3.2.2), and it builds on the expertise developed by other experiments which adopted open data policies earlier.

CTA will be operated as an observatory, meaning that data will be made publicly available after a short proprietary period. The existence of publicly available data naturally requires the development of an analysis tool to allow any possible user to make use of this data. It was in this context that a number of open-source tools were developed, among them the *Gammapy* package, introduced in Section 3.5.1. *Gammapy* has been selected to be the base package for the CTA science tools¹.

In preparation for CTA, a data model for IACTs was developed (Contreras et al., 2015). A format specification building on this model was developed as an open-source community effort usually referred to as the *gamma-astro-data-format* (GADF, Nigro et al., 2021). This format was quickly tested by existing IACT experiments, such as MAGIC and H.E.S.S. (H.E.S.S. Collaboration, 2018). *Gammapy* and the other candidate packages to the CTA science tools were developed to expect input data and IRFs following the GADF specifications.

However, all of this development was exclusively focused on IACTs, as CTA will be an array of such telescopes. In this chapter we present an extension and validation of the use of these community-wide standards and tools to data from particle detector arrays such as the HAWC observatory or the SWGO.

In particular, we present the first production of HAWC event lists and IRFs that follow the GADF specifications, and use them to reproduce three published HAWC results. We also present, as a proof of concept, the first Crab Nebula spectrum derived jointly using data from the *Fermi*-LAT, four IACT arrays and the HAWC observatory.

The tools and methods described and validated in this chapter will be used in Chapter 8 to perform a joint analysis of the SS 433 region using data from H.E.S.S. and HAWC.

¹<https://www.cta-observatory.org/ctao-adopts-the-gammapy-software-package-for-science-analysis/>

Validation of standardized data formats and tools for ground-level particle-based gamma-ray observatories

A. Albert¹, R. Alfaro², J. C. Arteaga-Velázquez³, H. A. Ayala Solares⁴, R. Babu⁵, E. Belmont-Moreno², C. Brisbois⁶, K. S. Caballero-Mora⁷, T. Capistrán⁸, A. Carramiñana⁹, S. Casanova¹⁰, O. Chaparro-Amaro¹¹, U. Cotti³, J. Cotzomi¹², S. Coutiño de León¹³, E. De la Fuente¹⁴, R. Diaz Hernandez⁹, M. A. DuVernois¹³, M. Durocher¹, C. Espinoza², K. L. Fan⁶, M. Fernández Alonso⁴, N. Fraija⁸, J. A. García-González¹⁵, H. Goksu¹⁶, M. M. González⁸, J. A. Goodman⁶, J. P. Harding¹, J. Hinton¹⁶, D. Huang⁵, F. Hueyotl-Zahuantitla⁷, P. Hütemeyer⁵, A. Jardín-Blicq^{17,18,16}, V. Joshi^{19,*}, J. T. Linnemann²⁰, A. L. Longinotti⁸, G. Luis-Raya²¹, K. Malone²², V. Marandon¹⁶, O. Martínez¹², J. Martínez-Castro¹¹, J. A. Matthews²³, P. Miranda-Romagnoli²⁴, J. A. Morales-Soto³, E. Moreno¹², M. Mostafá⁴, A. Nayerhoda¹⁰, L. Nellen²⁵, M. U. Nisa²⁰, R. Noriega-Papaqui²⁴, L. Olivera-Nieto^{16,*}, E. G. Pérez-Pérez²¹, C. D. Rho²⁶, D. Rosa-González⁹, E. Ruiz-Velasco¹⁶, D. Salazar-Gallegos²⁰, F. Salesa Greus^{10,27}, A. Sandoval², H. Schoorlemmer^{16,28,*}, J. Serna-Franco², A. J. Smith⁶, Y. Son²⁶, R. W. Springer²⁹, K. Tollefson²⁰, I. Torres⁹, R. Torres-Escobedo³⁰, R. Turner⁵, F. Ureña-Mena⁹, L. Villaseñor¹², X. Wang⁵, I. J. Watson²⁶, E. Wilcox⁶, H. Zhou³⁰, C. de León³, A. Zepeda³¹ (HAWC Collaboration), A. Donath^{32,*}, and S. Funk¹⁹

(Affiliations can be found after the references)

Received 11 March 2022 / Accepted 24 June 2022

ABSTRACT

Context. Ground-based γ -ray astronomy is still a rather young field of research, with strong historical connections to particle physics. This is why most observations are conducted by experiments with proprietary data and analysis software, as is usual in the particle physics field. However, in recent years, this paradigm has been slowly shifting toward the development and use of open-source data formats and tools, driven by upcoming observatories such as the Cherenkov Telescope Array (CTA). In this context, a community-driven, shared data format (the *gamma-astro-data-format*, or GADF) and analysis tools such as *Gammapy* and *ctools* have been developed. So far, these efforts have been led by the Imaging Atmospheric Cherenkov Telescope community, leaving out other types of ground-based γ -ray instruments.

Aims. We aim to show that the data from ground particle arrays, such as the High-Altitude Water Cherenkov (HAWC) observatory, are also compatible with the GADF and can thus be fully analyzed using the related tools, in this case, *Gammapy*.

Methods. We reproduced several published HAWC results using *Gammapy* and data products compliant with GADF standard. We also illustrate the capabilities of the shared format and tools by producing a joint fit of the Crab spectrum including data from six different γ -ray experiments.

Results. We find excellent agreement with the reference results, a powerful confirmation of both the published results and the tools involved.

Conclusions. The data from particle detector arrays such as the HAWC observatory can be adapted to the GADF and thus analyzed with *Gammapy*. A common data format and shared analysis tools allow multi-instrument joint analysis and effective data sharing. To emphasize this, a sample of Crab nebula event lists is made public with this paper. Because of the complementary nature of pointing and wide-field instruments, this synergy will be distinctly beneficial for the joint scientific exploitation of future observatories such as the Southern Wide-field Gamma-ray Observatory and CTA.

Key words. methods: data analysis – gamma rays: general

1. Introduction

In preparation for the upcoming Cherenkov Telescope Array (CTA), the ground-based γ -ray astronomy community has made a joint effort to define standardized data formats and develop community-sourced tools aimed to facilitate access to the data by a wide audience. This requires the identification of a data-processing stage in which standardization between different instruments is possible. The primary source of background for any γ -ray observatory are events of hadronic origin usually referred to as cosmic rays. After reconstructing the events that

triggered the detector, a background rejection step is applied in which γ -ray-like events are selected. At this stage, denoted as Data Level 3 (DL3) in the CTA data model (Contreras et al. 2015), the structure of the data of all γ -ray observatories is essentially the same. The DL3 is thus defined to include the γ -like event lists and the corresponding instrument response functions (IRFs). This development and definition of a standard format for γ -ray astronomy has been a largely community-driven effort that is usually referred to as the *gamma-astro-data-format*, or GADF for short (Deil et al. 2017a). This format relies on file storage by the Flexible Image Transport System (FITS) format (Wells et al. 1981), which is widely used by the whole astronomical community. It builds on existing standards such as the one developed

* Corresponding author:
e-mail: laura.olivera-nieto@mpi-hd.mpg.de

by the FITS Working Group in the Office of Guest Investigators Program (OGIP) at NASA¹ and expands them to address the specific needs of the γ -ray community. The availability of such an open data format will not only help to prepare the operation of CTA as an open observatory, but also simplify the process for existing observatories and experiments to possibly publish and archive their data in an openly documented and maintained data format.

With similar motivation, a variety of open-source analysis tools has been developed. This signals a transition in a field that up until recently, and with the notable exception of the *Fermi* Large Area Telescope (LAT; Wood et al. 2017) or the INTEGRAL analysis tools², for instance, relied heavily on independent proprietary software developed for a specific observatory. These new open-source tools can be broadly classified into two classes. Some packages, such as the Multi-Mission Maximum Likelihood (3ML; Vianello et al. 2015), aim to bridge the gaps between different instruments by providing a common framework in which their respective proprietary tools interface, allowing joint, multiwavelength studies to be carried out. On the other hand, packages such as *Gammapy* (Deil et al. 2017b) and *ctools* (Knödlseder et al. 2016) aim to replace the existing frameworks altogether, and offer a single tool with which to carry out the analysis of data from multiple γ -ray observatories, individually or jointly. The latter requires GADF-conforming inputs, so that data from different observatories can be correctly read and analyzed by the same software.

There has been a number of studies that validated and highlighted the potential of the shared format and tools, focusing on either a single instrument (Mohrmann et al. 2019) or on multi-instrument analysis (Nigro et al. 2019). However, these efforts have largely been focused on Imaging Atmospheric Cherenkov Telescopes (IACTs), excluding the other type of ground-based γ -ray instrument: particle detector arrays such as the High-Altitude Water Cherenkov (HAWC) observatory. While initially the focus of the GADF and shared tools was on IACTs, given that CTA will be an array of such telescopes, the standard is in practice mostly compatible with the data from any other type of γ -ray instrument.

Because of the complementary nature of IACTs and particle detector arrays, including both in the conception and development of such tools can be very beneficial. Particle detector arrays continuously survey large fractions of the sky, but can do so with relatively low angular resolution (Abeysekara et al. 2019). IACTs, on the other hand, have to be pointed to the region of interest, and are limited by weather and dark time, but can achieve higher angular resolution. IACTs can achieve good performance at low energies, below 1 TeV, while particle detector arrays are able to reach higher energies, of above 100 TeV. Multi-instrument analysis thus becomes necessary to cover the entire TeV range. A common data format and analysis tools allow the combination of data from IACT and particle detector arrays without the need for proprietary analysis software. This is relevant for both the current wide-field particle detector arrays, such as HAWC and the Large High Altitude Air Shower Observatory (LHAASO; Aharonian et al. 2021), and for future arrays such as the Southern Wide-Field Gamma-ray Observatory (SWG0; Hinton 2021).

In this paper, we present the first full production of HAWC event lists and IRFs that follows the GADF specification. We

analyze it using *Gammapy* to reproduce a selection of published HAWC results. To do this, we start by building a background model that takes the produced event lists as input. Thereafter, we check the consistency of low-level data products such as the number of events and maps by comparing them with published examples. Furthermore, we reproduce three published HAWC results, each for a different source class by using *Gammapy*. Last, as a proof of concept, we perform a joint fit using data of the Crab nebula from six different γ -ray observatories using *Gammapy*.

2. HAWC observatory

The High Altitude Water Cherenkov (HAWC) γ -ray observatory is situated on the flanks of the Sierra Negra at 18°59′41″N, 97°18′30.6″W in Mexico. It detects cosmic rays and γ -rays in the energy range from a few hundreds of GeV to more than a hundred TeV with a wide field of view (FoV) of ~ 2 sr. HAWC has been fully operational with 300 Water Cherenkov Detectors (WCDs) since March 2015. In each such WCD of 4.5 m height and 7.3 m diameter, four photomultiplier tubes (PMTs) are submerged in 200 m³ of purified water. The modular structure of HAWC WCDs allows optically isolating the detected Cherenkov light (300–500 nm) signal produced by the secondary particles such as e^\pm , γ , and μ^\pm , while traveling through the water volume. It also facilitates the identification of the local variations in the observed lateral distribution of detected showers, which in turn greatly helps performing γ -hadron separation.

The standard HAWC analysis procedure begins with the production of the instrument response functions (IRFs), which characterize the performance of the instrument. For this, air shower and detector simulations are generated using CORSIKA (Heck et al. 1998) and a dedicated package based on GEANT4 (v4.10.00, Agostinelli et al. 2003) named HAWCSim, respectively. These simulations are ran through the reconstruction procedure to obtain the two histograms that describe the detector response: the angular resolution and energy dispersion, the latter not normalized so that it also contains the effective area information. These quantities are usually stored in a ROOT (Brun & Rademakers 1997) file. The reconstructed data are first binned depending on the fraction of the available PMTs triggered by the air shower, a quantity referred to here as f_{Hit} . This results in a total of nine f_{Hit} bins, referred to with integer numbers between 1 and 9, as described in Abeysekara et al. (2017b). The value of f_{Hit} is only weakly correlated with energy. In order to estimate the energy on an event-by-event basis, more advanced algorithms have been developed. The ground-parameter (GP) algorithm is based on the charge density deposited at the ground by the shower. The neural network (NN) algorithm estimates energies with an artificial neural network that takes as input several quantities computed during the event reconstruction. A detailed overview of both algorithms can be found in Abeysekara et al. (2019). All results shown in this paper correspond to energies estimated using the GP method, but that is only for simplicity, as it is also possible to use the NN estimator results instead.

Energy bins are usually defined beforehand, with 12 reconstructed energy bins, each spanning a quarter decade in $\log_{10}(E/\text{TeV})$. Energy bins are labeled alphabetically with increasing energy, as shown in Table 1. The combination of both binning schemes leads to a total of 108 2D f_{Hit} /energy bins (Abeysekara et al. 2019), identified by the combination of the f_{Hit} number and the energy letter. For each bin, the γ -hadron separation cuts are optimized independently and applied

¹ https://heasarc.gsfc.nasa.gov/docs/heasarc/ofwg/ofwg_intro.html

² <https://www.isdc.unige.ch/integral/analysis>

Table 1. Definition of the reconstructed energy bins. Each bin spans one quarter decade.

Bin	Low edge (TeV)	High edge (TeV)
a	0.316	0.562
b	0.562	1.00
c	1.00	1.78
d	1.78	3.16
e	3.16	5.62
f	5.62	10.0
g	10.0	17.8
h	17.8	31.6
i	31.6	56.2
j	56.2	100
k	100	177
l	177	316

Notes. The first two bins (a and b) are not used in the analysis as the estimate is highly biased.

to the reconstructed data. A detailed description of the variables used for γ -hadron separation can be found in [Abeysekara et al. \(2017b\)](#).

DL3 products are currently not produced during the HAWC standard analysis procedure, and instead, the events are selected for γ -likeness and directly binned into a HEALPix ([Górski et al. 2005](#)) full-sky map. In this step, a pointing correction, usually referred to as alignment, is applied to the reconstructed data as described in [Abeysekara et al. \(2017b\)](#). During the same map-making procedure, a background and exposure map is computed as well ([Abeysekara et al. 2017b](#)). These maps and the detector response file are typically used within 3ML ([Vianello et al. 2015](#)) via the HAWC-specific plugin `hawc_ha1` ([Vianello et al. 2018](#)) to carry out γ -ray source analysis.

3. Gammapy

Gammapy is a community-developed Python package for γ -ray astronomy. It is built on the scientific Python standard packages *Numpy*, *Scipy*, and *Astropy* and implements data reduction and analysis methods for γ -ray astronomy. It will also be used as the base package for the science tools for the future CTA. *Gammapy* has already been successfully used and validated for analysis of IACT data from H.E.S.S. ([Mohrmann et al. 2019](#)) and has also been used to perform joint analyses of multiple IACTs with *Fermi*-LAT ([Nigro et al. 2019](#)). The standard analysis workflow of *Gammapy* begins at the level of selecting the DL3 data and time intervals based on Good Time Intervals (GTIs). In the next step, selected events are binned into multidimensional sky maps, such as the World Coordinate System (WCS) or HEALPix with an additional energy axis. The corresponding instrument response, including the residual hadronic background, is projected onto the same but possibly spatially coarser sky map. The binned data are bundled into a dataset, and together with a parametric model description, they can be used to model the data in a binned likelihood fit. Multiple datasets can be combined, and by sharing the same source model, they can be used to handle multiple event types or data from different instruments in a joint-likelihood fit. To fully support the analysis of HAWC data, we made one contribution to *Gammapy*. The HAWC point-spread function (PSF) is computed as a function of

reconstructed energy, as opposed to true energy, which is typical for IACTs. For this reason, we implemented the possibility to exchange the order of the application of the PSF and energy dispersion matrix (see Sect. 4.3). All of the other features are already compatible with standard analysis workflows used for ground-based wide-field instruments. This includes combined spectral and morphological modeling of γ -ray sources, computation of test-statistic (TS) maps, and estimation of flux points and light curves. All the results shown in this paper were produced using *Gammapy* version 0.18.2.

4. HAWC data and IRFs in the GADF

At the DL3 level, the GADF defines mandatory header keywords and columns, containing the basic information necessary for γ -ray data analysis, as well as optional entries that can be useful for specific instruments or observing strategies. The storage and distribution of γ -ray data as event lists together with some parameterization of the IRFs has been shown to be extremely successful by the *Fermi*-LAT observatory³. This format was extended to IACTs by the GADF initiative, and is extended in this work to particle detector arrays such as the HAWC Observatory.

4.1. Event lists

The DL3 stage refers to lists of reconstructed events that have been identified as γ -ray-like. Right after reconstruction, HAWC events are stored in event lists that mostly contain background events of a hadronic nature. The first step toward DL3 event lists is thus to bin them as described in Sect. 2 and apply the corresponding γ -hadron separation criteria in each bin to select γ -ray-like events. An additional alignment correction is applied to the direction of each event (see [Abeysekara et al. 2017b](#)), and the coordinates are transformed into the J2000 epoch. For each of the events, five basic quantities are required by the GADF: an event identification number, the two sky direction coordinates, the estimated energy, and the arrival time ([Deil et al. 2017a](#)). Event time-stamps are stored in GPS seconds after midnight January 6, 1980⁴, with the reference time provided in the FITS file header. Additionally, any other instrument-specific column can be added, such as the fraction of available triggered PMTs or the core location of the shower in the detector coordinates. Table 2 shows an example of such an event list. An integer indicating to which of the 108 2D bins each event belongs to is added as a column. This allows storing events from different bins in the same file without any loss of information.

4.2. GTIs and exposure calculation

The GTIs are defined as the time intervals during which the detector is stable and taking data. They are stored as a separate table within the same FITS file as the associated event list. They are used to compute the exposure time, which is crucial for measuring, for example, the γ -ray flux of astrophysical sources.

HAWC raw data are stored in files that span 125 s of data-taking. After the data are reconstructed, these intervals are checked for stability ([Abeysekara et al. 2019](#)); their duration becomes the minimum unit of time that can be described as

³ <https://fermi.gsfc.nasa.gov/cgi-bin/ssc/LAT/LATDataQuery.cgi>

⁴ https://gssc.esa.int/navipedia/index.php/Time_References_in_GNSS

Table 2. Simplified entries of an event list.

Event ID	RA (deg)	Dec (deg)	Energy (TeV)	Time (s)	Core X (m)	Core Y (m)	Bin ID
1	296.401	18.649	6.698	1132183230.200404	50.4	212.8	7f
2	305.046	27.225	7.063	1132183236.213954	-30.7	214.9	7f
3	16.556	14.990	7.709	1132183250.7916136	-37.1	214.9	6f

Notes. The real precision of the numbers has been reduced for formatting convenience. The Bin ID information is stored as an integer (e.g., bin 7f would correspond to number 77), with the bin name shown here only for convenience.

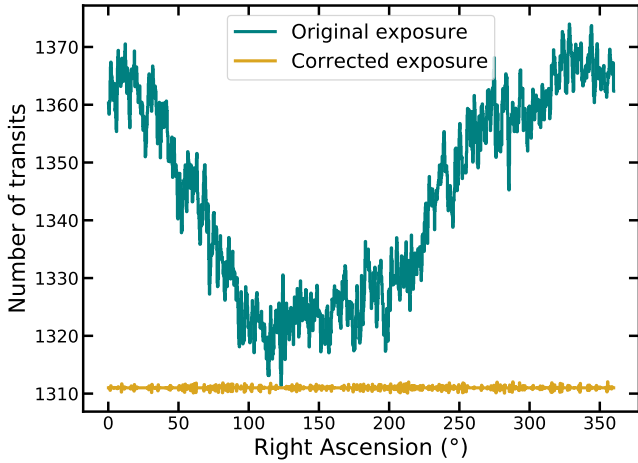


Fig. 1. Number of transits during which the detector was stable as a function of RA.

good. The GADF requires the GTI table to have two columns, one with the start of the interval (TSTART), and one with the end (TSTOP). For the DL3 production presented here, these time stamps are obtained from the reconstructed data files themselves. This is done by selecting the first and last event in a file before applying any γ -hadron separation or binning. Currently, the effect of trigger dead time, which is expected to be in the order of a few percent, is not taken into account when analyzing HAWC data. From these time intervals, the exposure map is constructed by considering which part of the sky is above the maximum zenith angle observation threshold as seen from the observatory during each interval.

Because of the continuous observations performed by HAWC, it is often useful to describe exposure in terms of a source transit above the detector, which is defined in [Abeysekara et al. \(2017a\)](#). The green curve in Fig. 1 shows the number of transits during which HAWC was stable and taking data between June 2015 and June 2019 as a function of right ascension (RA). Detector downtime can be caused by a variety of factors, ranging from hardware issues to meteorological conditions such as electric storms. As a result, these interruptions are not necessarily distributed uniformly over time; technical maintenance, for instance, is more likely during particular times of the day. This leads to the fluctuations in the exposure as a function of hour angle, or equivalently, RA, that is shown as the green curve in Fig. 1. These fluctuations are on the 3% level and are usually neglected in long-term source analysis. One of the advantages of the production of GTIs together with event lists is that this effect becomes easy to characterize and correct for.

The different data ranges defined by the GTIs can still be ranked by detector stability criteria, and those ranked lower are

iteratively removed, effectively shaving time off of the green curve in Fig. 1 until it becomes flat. The result is shown by the curve labeled “Corrected exposure” in Fig. 1. This allows accurately neglecting the RA dependence of the live time while still keeping a total data efficiency of more than 90%.

4.3. Instrument response

The IRFs describe the combined detection abilities and precision of an instrument data-taking and reconstruction procedure. Independent of the actual detection principle, the response of a γ -ray instrument can be described by a few key properties. The angular resolution of the experiment is the reconstruction accuracy of the direction of the incident γ -ray, and is described by the point-spread function (*PSF*). The energy dispersion (E_{disp}) is the reconstruction accuracy of the energy of each event. The detection probability of a γ -ray is given by the effective area (A_{eff}). Finally, the expected residual hadronic background by misclassified events (N_{B}) is described by the background model (see Sect. 5).

The current version of the GADF neglects the correlation between *PSF*, E_{disp} , and A_{eff} and considers them independent. This can be described by the following combined instrument response R :

$$R(\mathbf{x}, E|\mathbf{x}', E') = A_{\text{eff}}(\mathbf{x}', E') \cdot \text{PSF}(\mathbf{x}|\mathbf{x}', E) \cdot E_{\text{disp}}(E|\mathbf{x}', E'), \quad (1)$$

where \mathbf{x} and E represent the reconstructed position and energy, while \mathbf{x}' and E' are the corresponding unknown true quantities. The assumption of independence is mostly sufficient for the current generation of instruments, including HAWC. However, it will be readdressed for CTA and likely GADF in the future. As mentioned in Sect. 3, the HAWC PSF is currently provided in reconstructed energy, which introduces a dependence on the assumed spectral index of the modeled source. However, the data format also allows defining PSF in true energy as well, which allows the spectral reweighting of the PSF during model evaluation. Using this assumption, predicted counts N_{Pred} can be computed as

$$N(\mathbf{x}, E) = N_{\text{B}}(\mathbf{x}, E) + t_{\text{live}} \int_{\mathbf{x}'} d\mathbf{x}' \int_{E'} dE' R(\mathbf{x}, E|\mathbf{x}', E') \cdot \Phi(\mathbf{x}', E'), \quad (2)$$

where N_{B} is the expected residual hadronic background, t_{live} is the live time, R is the combined instrument response as defined in Eq. (1) and $\Phi(\mathbf{p}', E')$ the flux of the source model. One set of each IRF is produced per analysis bin because they are independent, resulting in a value of N_{Pred} per analysis bin. More details of the HAWC IRFs in the GADF can be found in [Olivera-Nieto et al. \(2021\)](#).

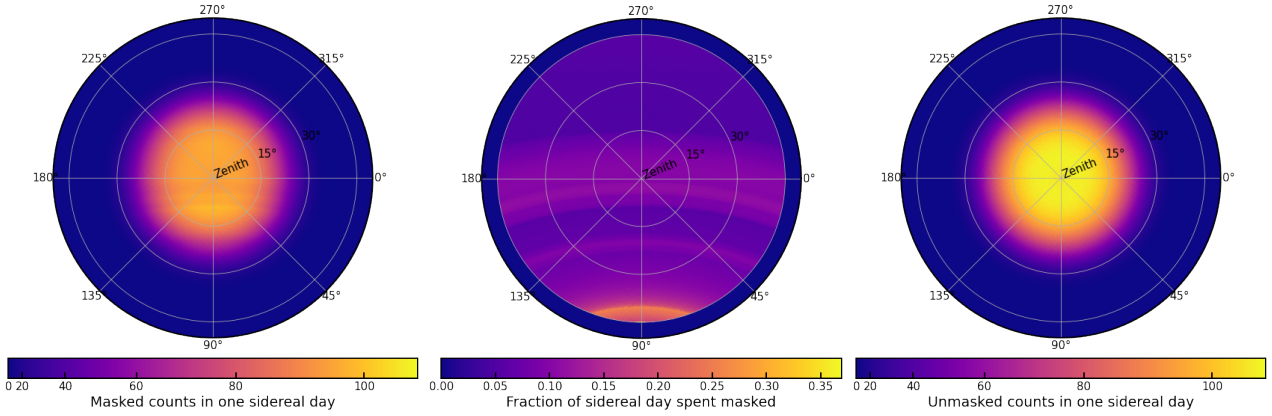


Fig. 2. Local coordinates view of the different quantities relevant to the background model construction. *Left:* masked spatial template for bin 1c, $\bar{B}_M(\theta, \phi)$. *Middle:* mask weights, $W_M(\theta, \phi)$, quantifying the fraction of the total time that a pixel is masked. *Right:* weighted (unmasked) spatial template for bin 1c, $\bar{B}(\theta, \phi)$.

5. Background modeling

5.1. Derivation of the background model

Background estimation in HAWC analysis is typically done using the so-called direct integration method (Abdo et al. 2012). This method deals with the expected dipole cosmic-ray anisotropy by splitting the data into time intervals (usually 2 h) and estimating the background in each of these intervals, which are then added up. This requires the input files to be provided chronologically sorted and is typically done in the same process as the γ -hadron separation and map-making. However, the production of γ -like event lists simplifies this process by allowing the use of the entire dataset at once with the slightly modified method described below. This has the advantage of significantly reducing the required computing time, given that the input events are already selected as γ -ray-like, as well as providing additional flexibility and modularity to the process. Removing the need for small sequential time intervals also leads to improved statistics at the highest energies.

At a given sidereal time, every day, the region of sky above the observatory is the same. The events in the event lists were selected using the GTIs described in Sect. 4.2, and split into 720 bins of sidereal time, τ . The duration of the bins is thus chosen to be 2 min of sidereal time, during which the sky above the observatory moves by 0.5° . This very fine binning is helpful to account for the dipole anisotropy. In each of these sidereal time bins, a sky map in local coordinates was filled using the selected events for each of the 2D analysis bins introduced in Sect. 2, which we refer to as $B_\tau(\theta, \phi)$, where θ and ϕ are the zenith and azimuth angles, respectively. We define a mask to exclude a band of $\pm 4^\circ$ around the Galactic plane, as well as other known bright γ -ray sources, as detailed in Table 3. We computed the mask in local coordinates for each of the defined sidereal time intervals, $M_\tau(\theta, \phi)$.

From these ingredients, we can construct the background model. First, we mask and add the maps in sidereal time to build a time-independent masked spatial template,

$$\bar{B}_M(\theta, \phi) = \sum_{\tau} M_\tau(\theta, \phi) \cdot B_\tau(\theta, \phi). \quad (3)$$

In order to correct for the presence of the mask, we integrate the mask in sidereal time to compute weights quantifying the fraction of a sidereal day that each spatial pixel spends inside of

Table 3. Mask components.

Component	Center (l°, b°)	Shape	Width/radius ($^\circ$)
Galactic Plane	(0, 0)	Band	8
Geminga	(195.14, 4.27)	Disk	10
Monogem	(201.11, 8.26)	Disk	10
Mrk421	(179.88, 65.01)	Disk	2
Mrk501	(63.60, 38.86)	Disk	2
Crab	(184.56, -5.78)	Disk	2

Notes. The center of the region is given in Galactic coordinates.

the mask,

$$W_M(\theta, \phi) = \left(\sum_{\tau} M_\tau(\theta, \phi) d\tau \right)^{-1}. \quad (4)$$

We can now recover the unmasked spatial templates,

$$\bar{B}(\theta, \phi) = W_M(\theta, \phi) \cdot \bar{B}_M(\theta, \phi). \quad (5)$$

An example of this process is shown in Fig. 2.

These spatial templates represent the time-independent spatial distribution of events in the HAWC sky for each of the 2D analysis bins. To account for temporal fluctuations in the event rate, we compute the event rate outside of the exclusion mask for the maps in sidereal time bins,

$$R(\tau) = \sum_{\theta, \phi} M_\tau(\theta, \phi) \cdot B_\tau(\theta, \phi), \quad (6)$$

and the event rate outside of the exclusion mask in the spatial template,

$$\bar{R}(\tau) = \sum_{\theta, \phi} M_\tau(\theta, \phi) \cdot \bar{B}(\theta, \phi). \quad (7)$$

We can now combine the time-independent spatial template $\bar{B}(\theta, \phi)$ for each analysis bin with the time-dependent rate as

$$B(\theta, \phi, \tau) = \bar{B}(\theta, \phi) \cdot \frac{R(\tau)}{\bar{R}(\tau)}. \quad (8)$$

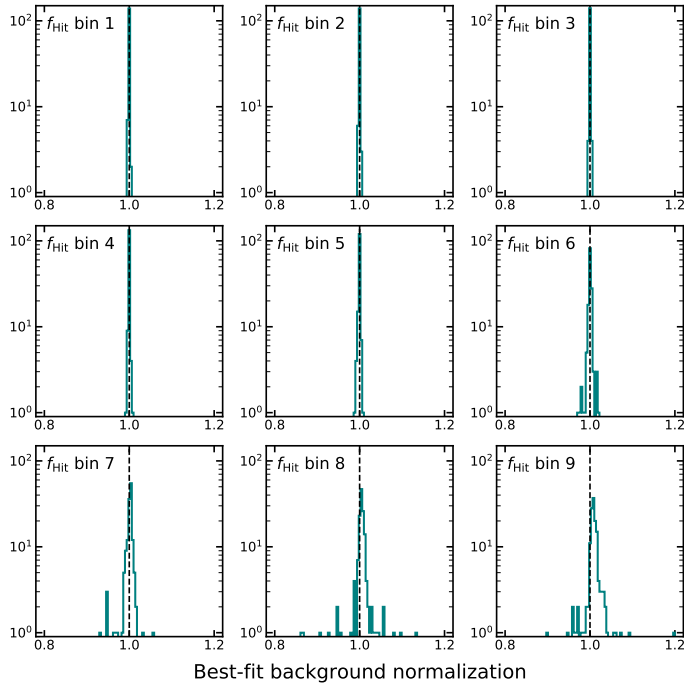


Fig. 3. Best-fit results for the background normalization of the tiles for each of the nine f_{Hit} bins.

This results in $B(\theta, \phi, \tau)$, the background map in local coordinates for each sidereal time interval, which takes into account the fluctuations in the event rate. Finally, in order to construct the desired map in sky coordinates, we project each of the local coordinate maps corresponding to a sidereal time τ into the corresponding sky coordinates and stack them together into one full-sky map. This process yields one such map per analysis bin. The different energy bins can be bundled together into groups of the same f_{Hit} bin, which results in a three-dimensional sky map that includes an energy axis for each of the f_{Hit} bins.

5.2. Checks of the background model

5.2.1. Background normalization

To validate the background model, we split the full-sky counts map into 192 tiles of equal solid angle, applying the same mask as was used for the background model creation. For the 148 tiles that are at least partially contained in the HAWC FoV, we then compared the background model to the observed counts outside of the mask, where no bright γ -ray sources are expected. To do this, we defined a background normalization parameter that multiplies the background model, and performed a fit. Figure 3 shows the histogram of the resulting best-fit background normalization for the tiles. The normalization distributions are centered around 1, as is expected for a well-normalized background model.

5.2.2. Full-sky significance map

Because particle detector arrays continuously survey large fractions of the sky, producing full-sky maps is critical for the science and diagnosis of the data products. An example of this are full-sky significance maps, which can also be used to identify new sources in the instrument FoV. Such a map has been shown repeatedly by the HAWC Collaboration, for example, in [Albert](#)

[et al. \(2020\)](#). Using the background map produced as described in Sect. 5.1 for 1311 transits and the corresponding count map produced with the event list, we can compute the significance map using *Gammapy*. We used this map to confirm the background model because we expect the significance to have no hotspots above 5σ and to be normally distributed outside of the mask described in Table 3. The general approach to this is again to divide the HEALPix-based all-sky data into smaller patches using tangential WCS projections, compute the maps, and reproject back to a HEALPix pixelization. One of the resulting maps, for f_{Hit} bin 4, is shown in Fig. 4. A histogram of the masked significance for all the other bins is shown in Fig. 5. As expected, there are no regions in the map with a significance above 5σ . The significance histograms for most bins follow a Gaussian distribution with a mean value of roughly zero and a width of unity, as expected from random fluctuations. The broader distribution in bin 1 is due to the imperfect characterization of the cosmic-ray anisotropy, which is most relevant in bins in which the background rate is higher, that is, low f_{Hit} bins. Additionally, all the pixels with a significance above 5σ in f_{Hit} bins 1 and 3 are located close to the edge of the HAWC FoV, indicating that they are likely the result of an edge effect of the map. The deviation from Gaussian behavior in bins 8 and 9 is explained by the relatively low number of events in these bins. Any source that is not covered by the mask is expected to contribute to the distributions shown in Fig. 5. However, following the construction of the mask, these sources would be faint, meaning that their individual contribution to each f_{Hit} bin is unlikely to cross the 5σ threshold.

6. Comparison of data products

In order to ensure that the event selection and alignment were performed correctly, we can compare the number of events classified into each bin. Because event lists were not previously produced in HAWC, we do this by comparing the number of counts in the standard maps to the number of events in the lists for the region defined by a radius of 3° around the Crab nebula. We make this comparison prior to the exposure flattening described in Sect. 4.2 in order to compare the same number of data. We expect the event lists to contain slightly more events than the maps because a few percent of the total events is rejected during the standard map-making process due to criteria on the gaps between the time-stamp of events required by the exposure calculation. This is no longer necessary when the exposure is computed by using GTIs, as described in Sect. 4.2. This effect is larger for bins with more events, such as low f_{Hit} bins. Figure 6 shows that the number of counts agrees well for all bins. The total difference is about the expected 1%.

In addition to the total number of events, it is important to also ensure that their spatial distribution follows the expectations. Figure 1 in [Abeysekara et al. \(2019\)](#) shows the excess map of the region around the Crab nebula above 1 TeV for 837.2 days. We reproduced this excess map for the same data range and present both maps together with the residual between them in Fig. 7. It is clear that the maps are strikingly similar.

7. Validation

To validate the production of the event lists and IRFs, we chose three sources representing three different analysis use cases: the Crab nebula (eHWC J0534+220) as the standard candle and Galactic point source, the extended source eHWC J1907+063, and the extragalactic variable source Mrk 421.

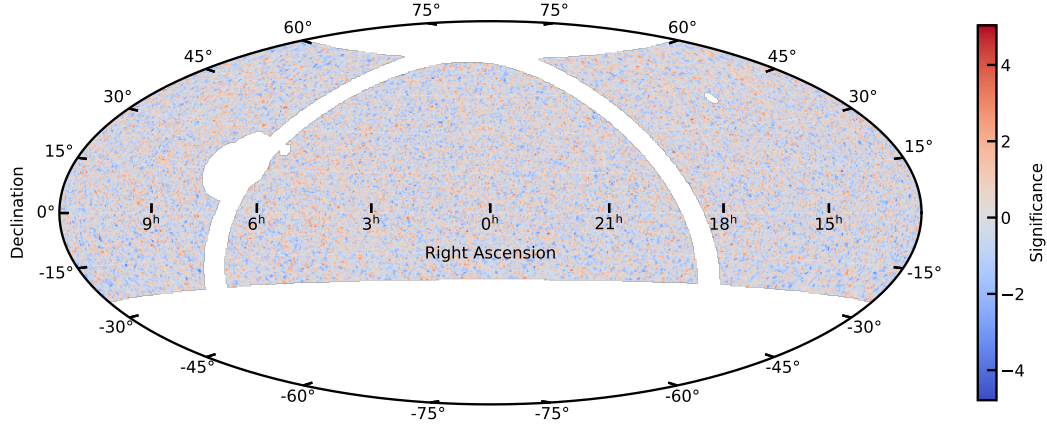


Fig. 4. Full-sky significance map for f_{Hit} bin 4 as computed with *Gammapy*. The map is masked using the mask described in Table 3.

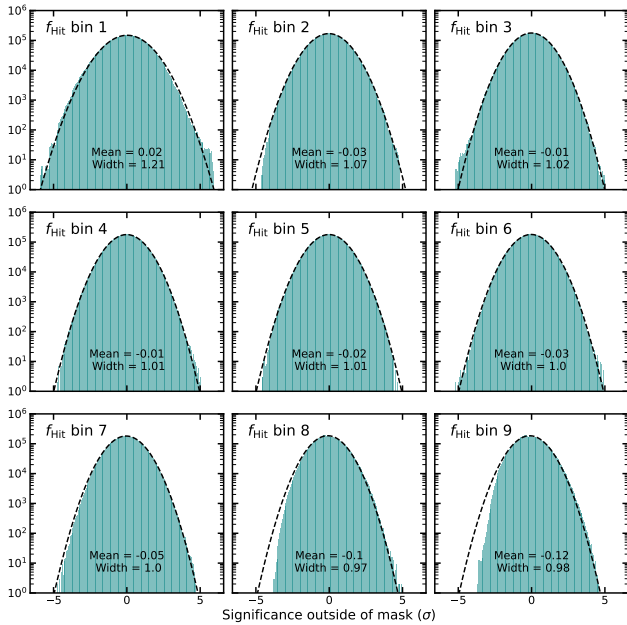


Fig. 5. Distribution of the significance values outside of the mask for all the f_{Hit} bins (green). A Gaussian function is fit to each of the histograms (dashed black line), and the best-fit mean and width are given in each panel.

For the two steady source analyses, we used the framework described previously, with the events and IRFs described in Sect. 4 and the background model described in Sect. 5. For the special case of Mrk 421, the background was estimated locally, as detailed in Sect. 7.3. Despite this difference, the workflow was very similar in all three cases. Events were selected from a $8^\circ \times 8^\circ$ region in the sky around the source position. For each of the f_{Hit} bins described in Sect. 2, a three-dimensional map was produced, with two spatial axes and a reconstructed energy axis, binned as also described in Sect. 2. The background map was interpolated to that same geometry, and so were the IRFs described in Sect. 4. As an additional check and because it is also possible within *Gammapy*, the analyses in Sects. 7.1 and 7.2 were also carried out using the existing HAWC counts and direct integration background maps.

The data and IRFs were bundled into a *Gammapy* dataset (see Sect. 3), one for each f_{Hit} bin. Then, the relevant model was attached to the datasets, and a joint-likelihood fit was performed

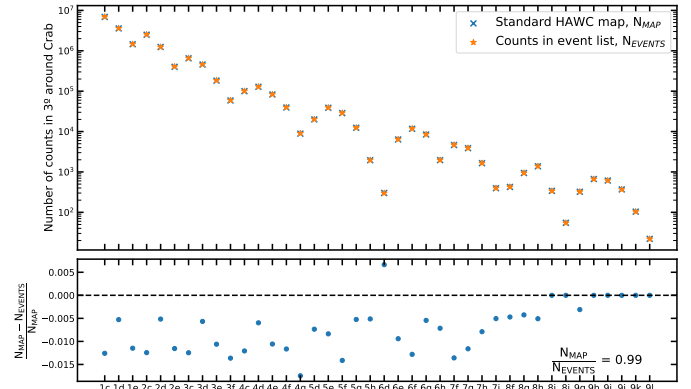


Fig. 6. Comparison of the number of events in a region of 3° radius around the Crab nebula in the standard HAWC map and in the event lists for each of the analysis bins. The selected 2D bins shown here are those that are used in Sect. 7.1 and follow the selection procedure described in [Abeysekara et al. \(2019\)](#).

to all nine datasets together. The only difference in the case of Mrk 421 is that this same procedure was carried out for each of the selected time intervals to build the light curve.

We do not expect to exactly reproduce the reference best-fit values for several reasons. First, some of the validation analyses shown here make use of a different background model than the reference (see Sect. 5). Second, as mentioned in Sect. 4.2, the exposure for the reference analyses is assumed to be flat. This introduces an error in the flux of up to a few percent that is not present in the validation analysis. Finally, the data reduction process described in Sect. 3 includes the projection into a sky-map and interpolation of the IRFs to a coordinate grid centered on the source position. This is not done in the reference analysis, which uses the IRF value that corresponds to the nearest declination node, spaced by 5° . This can result in differences for the best-fit parameters, especially for sources located between declination nodes for which the IRFs evolve rapidly in the spatial dimension. All error values shown throughout this section are statistical only.

7.1. Point source: Crab nebula

As one of the brightest sources in the γ -ray sky, the Crab nebula is used as the standard candle for calibration and reference analysis. Due to its declination, it transits over the HAWC sky

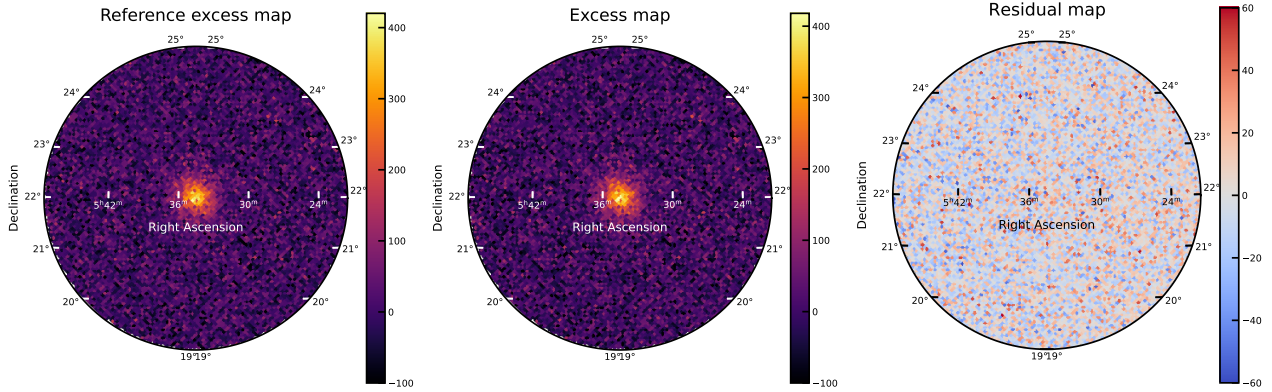


Fig. 7. Comparison of excess counts maps of the Crab nebula region. *Left:* crab excess counts map above 1 TeV as computed from the standard HAWC pipeline. *Middle:* Crab excess counts map above 1 TeV as computed from the DL3 data products. *Right:* residual map resulting from subtracting the reference map from the map derived from the DL3 data products.

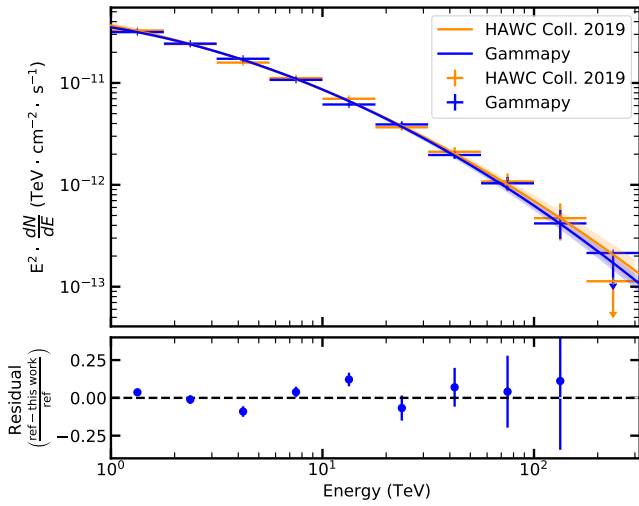


Fig. 8. Best-fit Crab spectrum obtained with *Gammapy* compared with *Abeysekara et al. (2019)* for the GP energy estimator. The bottom panel shows the comparison between the flux points computed in this work and those reported in the reference.

passing very close to the zenith. HAWC is able to detect (with a significance of roughly 5σ) the Crab nebula every day, that is, in the span of one transit.

We fit a point source and assumed a log-parabolic shape of the spectrum,

$$\frac{dN}{dE} = \phi_0 (E/E_0)^{-\alpha - \beta \ln(E/E_0)}, \quad (9)$$

where E_0 is the only fixed parameter with a value of 7 TeV. We compared against *Abeysekara et al. (2019)*. Figure 8 shows the spectrum obtained with *Gammapy* and the exported data, compared against the reference analysis. The two results agree excellently.

The resulting best-fit parameters are shown in Table 4 as “From events”, together with those from *Abeysekara et al. (2019)*. Additionally, we repeated the exercise, but instead of using the exported data, we used the same standard HAWC counts and background map as were used in *Abeysekara et al. (2019)*. The results of this fit are also shown in Table 4 as “From map”.

Table 4. Maximum likelihood fit results for the Crab nebula.

	ϕ_0 ($10^{-13} \text{ TeV}^{-1} \text{ cm}^2 \text{ s}^{-1}$)	α	β
From events	2.39 ± 0.04	2.79 ± 0.02	0.113 ± 0.007
Reference	2.35 ± 0.04	2.79 ± 0.02	0.10 ± 0.01
From map	2.35 ± 0.05	2.79 ± 0.02	0.12 ± 0.01

Notes. The fit result obtained using the DL3 products is given in the row labeled “From events”. The fit result obtained using the standard HAWC map products is given in the “From map” row. The values in the “reference” column are taken from *Abeysekara et al. (2019)*.

7.2. Extended source: eHWC J1907+063

Abeysekara et al. (2020) reported the detection by HAWC of several sources emitting above 56 and 100 TeV. One of those detected above 100 TeV is eHWC J1907+063. It is found in the vicinity of MGRO J1908+063. The 1σ extension of the emission is reported to be 0.67° over the entire energy range with a Gaussian assumption. The best-fit spectrum is modeled as a log-parabola (see Eq. (9)), with the pivot energy E_0 fixed at 10 TeV. We fit a combined spatial and spectral model made with the same assumptions as described above. Both components were fitted at the same time, including the source extension and position. The best-fit parameters are presented in Table 5. Figure 9 shows the spectrum of eHWC J1907+063 compared against the reference analysis. The agreement is clearly excellent. Figure 10 shows the resulting best-fit spatial model compared to the result in *Abeysekara et al. (2020)*. When the errors detailed in Table 5 are taken into account, the agreement is very good.

Additionally, we repeated the exercise, but instead of using the DL3 products, we used the same standard HAWC counts and background map as were used in *Abeysekara et al. (2020)*. The results of this fit are also shown in Table 5 as “From map”.

7.3. Time domain: Mrk 421

Markarian (Mrk) 421 is a BL Lac object that has been extensively observed in the γ -ray band (*Albert et al. 2022*). Its emission is known to be variable on timescales of hours or less. *Abeysekara et al. (2017a)* presented the HAWC light curve of Mrk 421, spanning over 17 months between November 2014 and April 2016. This work was carried out before the energy estimator techniques

Table 5. Maximum likelihood fit results for eHWC J1907+063.

	RA (°)	Dec (°)	Extension (1σ) (°)	ϕ_0 ($10^{-13} \text{ TeV}^{-1} \text{ cm}^2 \text{ s}^{-1}$)	α	β
From events	286.94 ± 0.02	6.35 ± 0.02	0.69 ± 0.03	0.94 ± 0.06	2.46 ± 0.03	0.11 ± 0.01
Reference	286.91 ± 0.10	6.32 ± 0.09	0.67 ± 0.03	0.95 ± 0.05	2.46 ± 0.03	0.11 ± 0.02
From map	286.96 ± 0.03	6.36 ± 0.03	0.68 ± 0.03	0.94 ± 0.06	2.45 ± 0.04	0.12 ± 0.02

Notes. The position in [Abeysekara et al. \(2020\)](#) is determined above 56 TeV, which leads to higher statistical errors due to the lower number of events. The fit result obtained using the DL3 products is given in the row labeled “From events”. The fit result obtained using the standard HAWC map products is given in the “From map” row. The values in the “reference” column are taken from [Abeysekara et al. \(2020\)](#).

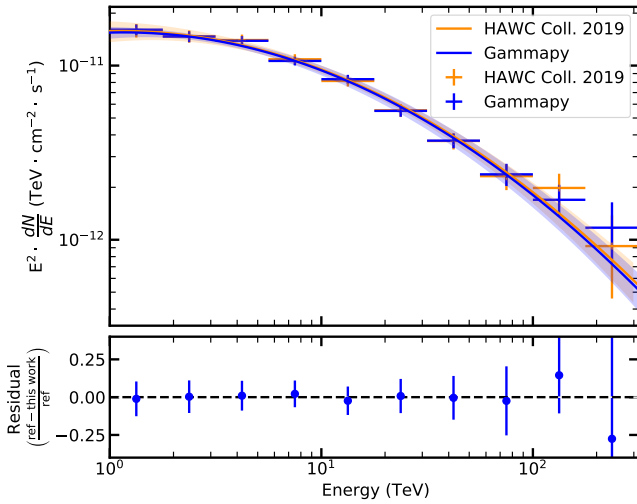


Fig. 9. Best-fit spectrum of eHWC J1907+063 obtained with *Gammapy* compared with [Abeysekara et al. \(2020\)](#). The bottom panel shows the comparison between the flux points computed in this work and those reported in the reference.

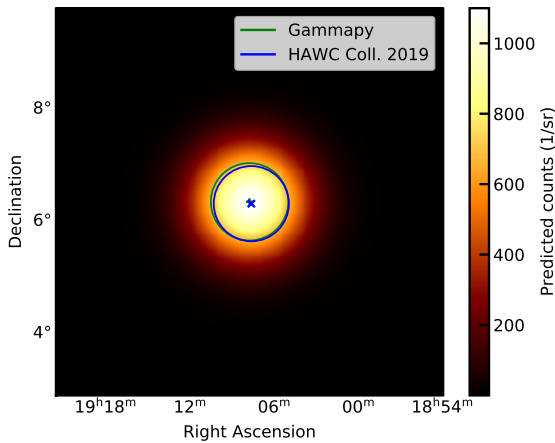


Fig. 10. Spatial model of eHWC J1907+063 as obtained with *Gammapy*. The green star and circle represent the best-fit position and the 68% containment region, respectively. The blue cross and circle are the reference values from [Abeysekara et al. \(2020\)](#) for each quantity.

described in [Abeysekara et al. \(2019\)](#) were implemented, which means that the energy of individual events could not be obtained. This leads to a different data selection and binning based only on f_{Hit} , like the one described in [Abeysekara et al. \(2017b\)](#). Consequently, there is no such thing as an energy dispersion matrix for each of the f_{Hit} bins. In order to deal with this, we

Table 6. Maximum likelihood fit results for Mrk 421.

	ϕ_0 ($10^{-11} \text{ TeV}^{-1} \text{ cm}^2 \text{ s}^{-1}$)	Γ	E_C (TeV)
This work	2.67 ± 0.16	2.20 ± 0.09	5.2 ± 2.6
Reference	2.82 ± 0.19	2.21 ± 0.14	5.4 ± 1.1

introduced an assumed energy axis with a single bin for each f_{Hit} bin dataset. This workaround allowed us to use the *Gammapy* framework in the same way as the previous two cases. The data selection and time binning were performed in a similar way as in [Abeysekara et al. \(2017a\)](#). Each event was associated with a sidereal day, starting at midnight local sidereal time at the HAWC site. The current HAWC detector stability criteria for data selection were applied, noting that these are slightly stricter than those used by [Abeysekara et al. \(2017a\)](#). For each of the sidereal days, the fraction of a Mrk 421 transit that is included in the data was computed by integrating the curve shown in Fig. 1 of [Abeysekara et al. \(2017a\)](#). Sidereal days for which this fraction is lower than 0.5 were removed from the selection. The result is a total of 463 transits, slightly fewer than the 471 included in [Abeysekara et al. \(2017a\)](#) due to the stricter data selection cuts. For each of these transits, the background was estimated locally. This was done by masking the expected source location and computing the number of counts outside the mask in overlapping declination bands, which takes into account the varying instrument response with declination. Because Mrk 421 is seen by HAWC as an isolated point source, this approximation suffices. Finally, counts and background maps were bundled with the PSF and effective area, the latter corrected for the transit fraction.

A point source spatial model was used with the position fixed to $(166.11^\circ, 38.21^\circ)$ in equatorial coordinates, as was done in [Abeysekara et al. \(2017a\)](#) and [Lauer \(2017\)](#). The spectrum of Mrk 421 was modeled by a power law with normalization ϕ_0 at $E_0 = 1$ TeV, photon index Γ , and an exponential cut-off E_C ,

$$\frac{dN}{dE} = \phi_0 \left(\frac{E}{E_0} \right)^{-\Gamma} \exp\left(-\frac{E}{E_C} \right). \quad (10)$$

The best-fit spectrum was first obtained for the entire data range. The resulting parameters are presented in Table 6 together with those reported in [Abeysekara et al. \(2017a\)](#). In order to ensure a stable fit, a minimum value for $E_C = 0.1$ TeV was imposed because of the high correlation between Γ and E_C .

When the values of $E_C = 5$ TeV and $\Gamma = 2.2$ were fixed, the normalization was set free and was fit for each of the transits. The resulting spectra were integrated above 2 TeV to match the result of [Abeysekara et al. \(2017a\)](#). Figure 11 shows the light curve

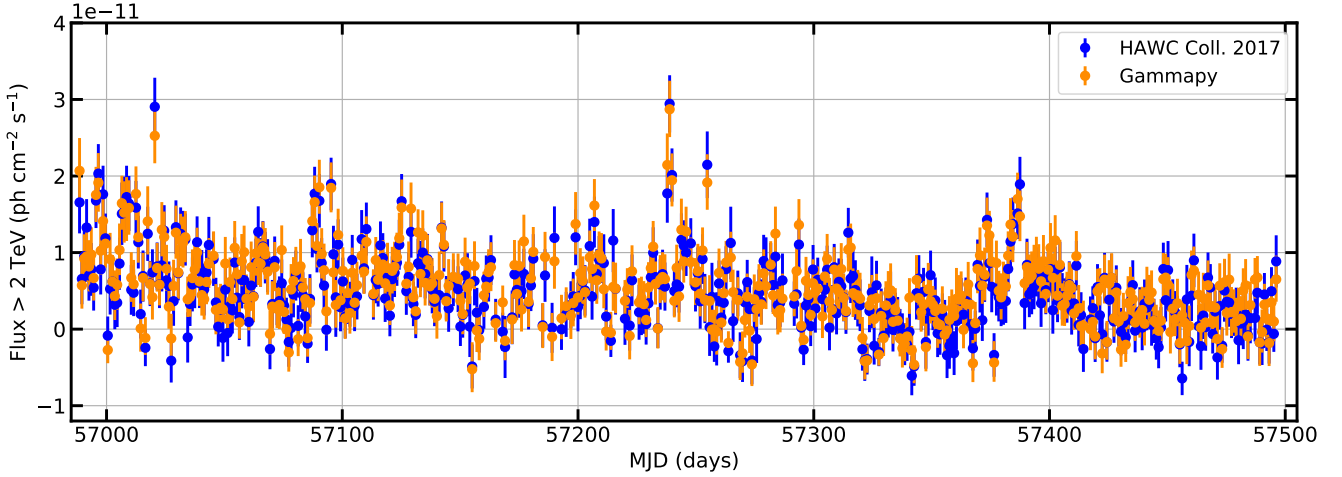


Fig. 11. Light curve of Mrk 421 computed with *Gammapy* (orange points) compared to the reference in [Abeysekara et al. \(2017a\)](#) (blue points).

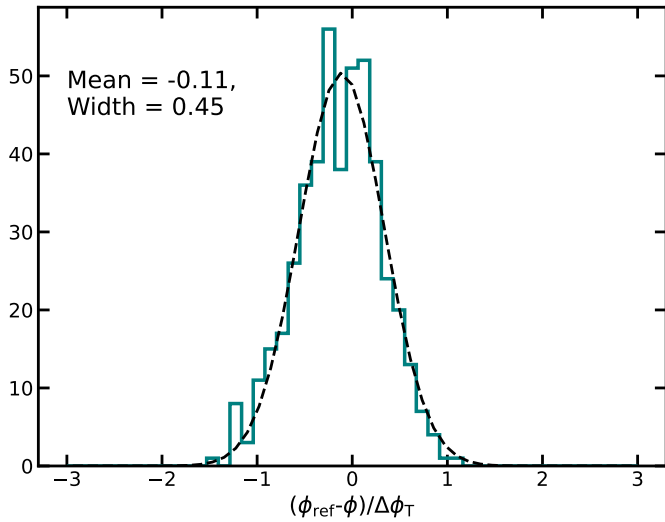


Fig. 12. Distribution of the difference between the reference light-curve values (ϕ_{ref}) and those obtained with *Gammapy* (ϕ) as a fraction of the combined error $\Delta\phi_{\text{T}} = \sqrt{\Delta\phi_{\text{ref}}^2 + \Delta\phi^2}$. A Gaussian fit is indicated with the dashed black line.

obtained with *Gammapy* together with the light curve from the reference analysis ([Abeysekara et al. 2017a](#)). The agreement is good, given the differences in data selection. The overall trend is clearly reproduced and the majority of points are compatible within errors. Figure 12 shows the distribution of the differences between the reference light-curve points and those obtained with *Gammapy* as a fraction of the statistical error. The large majority of values clearly lies within the 1σ region; the total is contained in the 2σ region.

8. Proof of concept: Joint fit

[Nigro et al. \(2019\)](#) presented the first fully reproducible measurement of the Crab nebula spectrum using public data from many different instruments. The analysis was carried out in *Gammapy*, and emphasizes the power of a shared and open analysis tool. Similar to [Nigro et al. \(2019\)](#), the goal of this study is not to reach any scientific conclusion regarding the Crab nebula. For this reason, we selected a small range of HAWC data, spanning only one

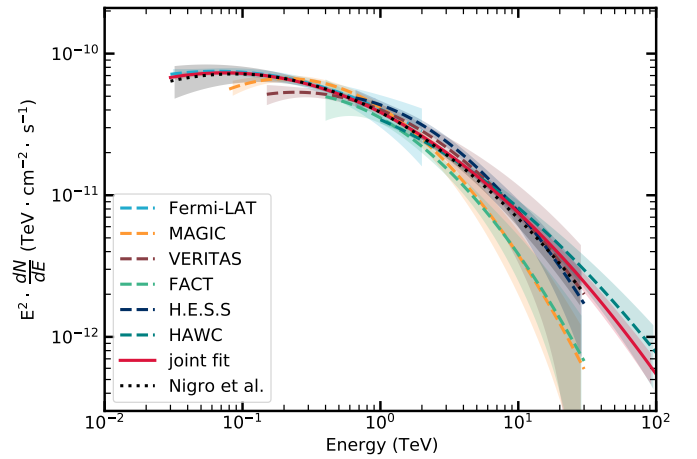


Fig. 13. Crab nebula spectral energy distribution for individual instrument fits and from the joint fit. Single-instrument results are represented with dashed lines, and the fit of all the datasets together, labeled as joint, is represented as a thick solid red line. The joint fit result from [Nigro et al. \(2019\)](#) is represented with a dotted black line.

month in time, and included it in the joint fit from [Nigro et al. \(2019\)](#). This was easily done due to the fully reproducible nature of that work. A log-parabola (see Eq. (9)) spectral shape with fixed $E_0 = 1$ TeV was assumed for all the instruments. Performing the individual instrument data reductions and joint fits was straightforward after the data and IRFs were stored according to the GADF. Figure 13 shows the result of this joint fit.

The spectrum of the Crab nebula might not be best described by the same spectral shape in all the different energy ranges, which could lead to differences in the best-fit parameters from the different experiments. However, this choice was made for simplicity, as the goal was not to reach any scientific conclusion regarding the Crab nebula, but rather show a proof of concept for this multi-instrument analysis. The joint fit shown in Fig. 13 is indeed not noteworthy for the resulting spectral shape, but for the fact that a multi-instrument fit was performed using data from six different γ -ray instruments, including one satellite (*Fermi-LAT*), four IACTs, and one particle detector array (HAWC) natively within the same tool.

The HAWC event lists and IRFs used in this section have been made publicly available on the HAWC Observatory

website⁵. This data release is the first to include HAWC data at the event list level. The data being public makes the result shown in Fig. 13 fully reproducible, as an extension of Nigro et al. (2019).

9. Conclusions and outlook

We have presented the first full production of HAWC data and IRFs that follows the community-shared specifications of the GADF. Data in this format allow reusing existing high-level analysis tools such as *Gammapy* for the analysis of HAWC data. We validated this approach by reproducing several published HAWC results and found excellent agreement. We additionally reproduced the analysis using the maps that are typically produced by the HAWC Collaboration directly into *Gammapy*, which also yielded a very good agreement.

This cross-check does not only validate the analysis tools, it also provides a valuable cross-check of the corresponding HAWC results. The published results have been reproduced with high precision with a different analysis tool, which is a powerful, non-trivial check.

The lifetime of observatories is finite, and one of the concerns at the end of the operation is to ensure that the archival data are available and easy to use both for future studies and to reproduce previous results. In this regard, having data in a format that is shared across the community and that can be analyzed with a general-use tool is a key advantage. The evolution of the GADF will be driven by the requirements imposed by current and future observatories, which will require data and IRFs to be described in increasingly realistic and complex ways. This will directly benefit the current generation of instruments, which will be able to ensure that their legacy data are properly used and interpreted.

The joint Crab nebula fit presented in Sect. 8 highlights the potential of this approach to perform multi-instrument analyses, spanning energy ranges much wider than those of a single instrument. This in turn can lead to synergies, bringing the IACT and particle detector array communities together. Future and current detectors, such as SWGO and LHAASO, will operate at the same time as CTA, and thus would benefit most from the ability to share data and analysis tools. A shared analysis tool translates into a much larger developer and user base than any of the other collaboration-specific tools individually. This increases the complexity of features that can be implemented and maintained, benefiting all the instruments involved.

The work presented here is a proof of concept of what a particle detector array data analysis chain would look like when the shared format and tools are used. The very few limitations encountered arise because the initial development was led by the IACT community. However, these are minimal, and furthermore, expected to be resolved by future improvements, for example, with the expansion of the GADF standard for sky maps, which are tremendously useful given the high event rates recorded by particle detector arrays. This development should be made taking existing standards into account when possible, and would allow data products to be efficiently distributed in map form as well.

The GADF and science tools are constantly evolving to meet the needs of the community. Future particle detector arrays, such as SWGO, will be able to and should partake in this effort by ensuring that the format remains compatible with this detector class, while taking advantage of all the benefits it has to offer.

Acknowledgements. This work made use of *numpy* (Harris et al. 2020), *scipy* (Virtanen et al. 2020), *matplotlib* (Hunter 2007) and *astropy* (Astropy Collaboration 2013). We acknowledge the support from: the US National Science Foundation (NSF); the US Department of Energy Office of High-Energy Physics; the Laboratory Directed Research and Development (LDRD) program of Los Alamos National Laboratory; Consejo Nacional de Ciencia y Tecnología (CONACyT), México, grants 271051, 232656, 260378, 179588, 254964, 258865, 243290, 132197, A1-S-46288, A1-S-22784, cátedras 873, 1563, 341, 323, Red HAWC, México; DGAPA-UNAM grants IG101320, IN111716-3, IN111419, IA102019, IN110621, IN110521; VIEP-BUAP; PIFI 2012, 2013, PRO-FOCIE 2014, 2015; the University of Wisconsin Alumni Research Foundation; the Institute of Geophysics, Planetary Physics, and Signatures at Los Alamos National Laboratory; Polish Science Centre grant, DEC-2017/27/B/ST9/02272; Coordinación de la Investigación Científica de la Universidad Michoacana; Royal Society – Newton Advanced Fellowship 180385; Generalitat Valenciana, grant CIDEGENT/2018/034; Chulalongkorn University’s CUniverse (CUAASC) grant; Coordinación General Académica e Innovación (CGAI-UdeG), PRODEP-SEP UDG-CA-499; Institute of Cosmic Ray Research (ICRR), University of Tokyo. We also acknowledge the significant contributions over many years of Stefan Westerhoff, Gaurang Yodh and Arnulfo Zepeda Dominguez, all deceased members of the HAWC collaboration. Thanks to Scott Delay, Luciano Díaz and Eduardo Murrieta for technical support.

References

- Abdo, A. A., Allen, B. T., Atkins, R., et al. 2012, *ApJ*, 750, 63
- Abeyskara, A. U., Albert, A., Alfaro, R., et al. 2017a, *ApJ*, 841, 100
- Abeyskara, A. U., Albert, A., Alfaro, R., et al. 2017b, *ApJ*, 843, 39
- Abeyskara, A. U., Albert, A., Alfaro, R., et al. 2019, *ApJ*, 881, 134
- Abeyskara, A. U., Albert, A., Alfaro, R., et al. 2020, *Phys. Rev. Lett.*, 124, 021102
- Agostinelli, S. et al. 2003, *Nucl. Instrum. Methods*, A506, 250
- Aharonian, F., An, Q., Axikegu, et al. 2021, *Chin. Phys. C*, 45, 025002
- Albert, A., Alfaro, R., Alvarez, C., et al. 2020, *ApJ*, 905, 76
- Albert, A., Alfaro, R., Alvarez, C., et al. 2022, *ApJ*, 929, 125
- Astropy Collaboration (Robitaille, T. P., et al.) 2013, *A&A*, 558, A33
- Brun, R., & Rademakers, F. 1997, *Nucl. Instrum. Methods Phys. Res. A*, 389, 81
- Contreras, J. L., Satalecka, K., Bernlör, K., et al. 2015, in *International Cosmic Ray Conference*, Vol. 34, 960
- Deil, C., Boisson, C., Kosack, K., et al. 2017a, in 6th International Symposium on High Energy Gamma-Ray Astronomy, *American Institute of Physics Conference Series*, 1792, 070006
- Deil, C., Zanin, R., Lefaucheur, J., et al. 2017b, in *International Cosmic Ray Conference*, 301, 766
- Górski, K. M., Hivon, E., Banday, A. J., et al. 2005, *ApJ*, 622, 759
- Harris, C. R., Millman, K. J., van der Walt, S. J., et al. 2020, *Nature*, 585, 357
- Heck, D., Knapp, J., Capdevielle, J. N., Schatz, G., & Thouw, T. 1998, *CORSIKA: a Monte Carlo code to simulate extensive air showers*
- Hinton, J. 2021, *PoS, ICRC2021*, 023
- Hunter, J. D. 2007, *Comput. Sci. Eng.*, 9, 90
- Knödseder, J., Mayer, M., Deil, C., et al. 2016, *A&A*, 593, A1
- Lauer, R. J. 2017, HAWC internal documentation pages for Abeyskara et al
- Mohrmann, L., Specovius, A., Tiziani, D., et al. 2019, *A&A*, 632, A72
- Nigro, C., Deil, C., Zanin, R., et al. 2019, *A&A*, 625, A10
- Olivera-Nieto, L., Joshi, V., Schoorlemmer, H., et al. 2021, *PoS, ICRC2021*, 727
- Vianello, G., Lauer, R. J., Younk, P., et al. 2015, arXiv e-prints, [arXiv:1507.08343]
- Vianello, G., Riviere, C., Brisbois, C., Fleischhack, H., & Burgess, J. M. 2018, HAWC Accelerated Likelihood – python-only framework for HAWC data analysis
- Virtanen, P., Gommers, R., Oliphant, T. E., et al. 2020, *Nat. Methods*, 17, 261
- Wells, D. C., Greisen, E. W., & Harten, R. H. 1981, *A&AS*, 44, 363
- Wood, M., Caputo, R., Charles, E., et al. 2017, in *International Cosmic Ray Conference*, 301, 35th International Cosmic Ray Conference (ICRC2017), 824

⁵ <https://data.hawc-observatory.org/>

- ⁵ Department of Physics, Michigan Technological University, Houghton, MI, USA
- ⁶ Department of Physics, University of Maryland, College Park, MD, USA
- ⁷ Universidad Autónoma de Chiapas, Tuxtla Gutiérrez, Chiapas, Mexico
- ⁸ Instituto de Astronomía, Universidad Nacional Autónoma de México, Ciudad de Mexico, Mexico
- ⁹ Instituto Nacional de Astrofísica, óptica y Electrónica, Puebla, Mexico
- ¹⁰ Institute of Nuclear Physics Polish Academy of Sciences, PL-31342 IFJ-PAN, Krakow, Poland
- ¹¹ Centro de Investigación en Computación, Instituto Politécnico Nacional, México City, Mexico
- ¹² Facultad de Ciencias Físico Matemáticas, Benemérita Universidad Autónoma de Puebla, Puebla, Mexico
- ¹³ Department of Physics, University of Wisconsin-Madison, Madison, WI, USA
- ¹⁴ Departamento de Física, Centro Universitario de Ciencias Exactas e Ingenierías, Universidad de Guadalajara, Guadalajara, Mexico
- ¹⁵ Tecnológico de Monterrey, Escuela de Ingeniería y Ciencias, Ave. Eugenio Garza Sada 2501, Monterrey, N.L., Mexico, 64849
- ¹⁶ Max-Planck Institute for Nuclear Physics, 69117 Heidelberg, Germany
- ¹⁷ Department of Physics, Faculty of Science, Chulalongkorn University, 254 Phayathai Road, Pathumwan, Bangkok 10330, Thailand
- ¹⁸ National Astronomical Research Institute of Thailand (Public Organization), Don Kaeo, MaeRim, Chiang Mai 50180, Thailand
- ¹⁹ Erlangen Centre for Astroparticle Physics, Friedrich-Alexander-Universität Erlangen-Nürnberg, Erlangen, Germany
- ²⁰ Department of Physics and Astronomy, Michigan State University, East Lansing, MI, USA
- ²¹ Universidad Politécnica de Pachuca, Pachuca, Hgo, Mexico
- ²² Space Science and Applications Group, Los Alamos National Laboratory, Los Alamos, NM, USA
- ²³ Dept of Physics and Astronomy, University of New Mexico, Albuquerque, NM, USA
- ²⁴ Universidad Autónoma del Estado de Hidalgo, Pachuca, Mexico
- ²⁵ Instituto de Ciencias Nucleares, Universidad Nacional Autónoma de México, Ciudad de México, Mexico
- ²⁶ University of Seoul, Seoul, Rep. of Korea
- ²⁷ Instituto de Física Corpuscular, CSIC, Universitat de València, E-46980, Paterna, Valencia, Spain
- ²⁸ Radboud Universiteit, Nijmegen, The Netherlands
- ²⁹ Department of Physics and Astronomy, University of Utah, Salt Lake City, UT, USA
- ³⁰ Tsung-Dao Lee Institute and School of Physics and Astronomy, Shanghai Jiao Tong University, Shanghai, PR China
- ³¹ Physics Department, Centro de Investigación y de Estudios Avanzados del IPN, Mexico City, DF, Mexico
- ³² Center for Astrophysics, Harvard and Smithsonian, Cambridge, MA, USA

Chapter 6

The H.E.S.S. view of SS 433

This chapter reports on dedicated H.E.S.S. observations of the SS 433 region resulting on the first detection of this system by an IACT array. The analysis presented here makes use of the new background rejection approach presented in Chapter 4. The better energy and angular resolution of H.E.S.S. compared to that of the HAWC observatory allows for a detailed study of the spectro-morphological properties of the emission from the outer jets of SS 433. This includes the discovery of striking energy-dependent morphology. The findings detailed here will be used in Chapter 7 to shed light on the SS 433 jet dynamics and particle acceleration sites.

As part of the standard H.E.S.S. analysis validation strategy, all the results shown here were reproduced by an independent analyzer using an independent calibration and analysis chain.

6.1 H.E.S.S. Observations

The SS 433 region was first observed by H.E.S.S. as part of the Galactic plane survey (H.E.S.S. Collaboration et al., 2018), and later during two dedicated campaigns. The data taken in the first, in 2009-2011, were used by MAGIC and H.E.S.S. Collaborations et al., 2018 to derive upper limits as SS 433 was not detected (see Section 2.3.6). A second campaign, between 2018 and 2021 resulted in a total of around 150h of additional acceptance-corrected data. The combination of all observations amount to around 200h of acceptance-corrected data. This data can be split into different subsets depending on the hardware epoch and array configuration used:

- **H.E.S.S. I:** Data taken with CT1-4 prior to their upgrade in 2016, with a total of 277 runs. The majority of this data was taken in the context of the Galactic plane survey, and the exposure is concentrated in the upper part of the FoV, where the Galactic plane is. A small number of these observation runs were taken after the construction of CT5 in 2012, but the largest telescope was never used during these observation runs, and instead was usually pointing at a different target in *mono* mode.
- **H.E.S.S. IU:** Data taken with CT1-4 after the 2016 upgrade of their cameras without including CT5 in the observation, with a total of 91 runs.

- **H.E.S.S. IU+CT5:** Data taken with CT1-4 after the 2016 upgrade of their cameras that include CT5 in the observation. This data set has a total of 318 runs. All of these runs were taken after the upgrade of the CT5 camera in 2019. Only 8 runs were taken with the previous camera, a number too low to assess any possible systematic issues due to the hardware differences. For this reason, the presence of CT5 in those 8 runs was ignored and they are classified in the above category instead.

Figure 6.1 shows the acceptance-corrected observation exposure maps for each of these eras and the combined total. The pointing positions for the observations in the H.E.S.S. IU and H.E.S.S. IU+CT5 data sets were chosen to make up for the fact that most of the exposure in the existing H.E.S.S. I observations was concentrated on the top part of the FoV.

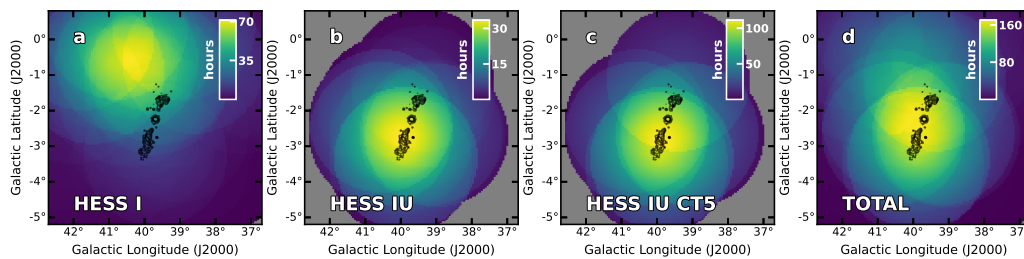


FIGURE 6.1: **Acceptance-corrected exposure.** The color scale indicates the amount of observation time corrected for the radial dependence of the system acceptance. The figure shows this quantity for the H.E.S.S. I (a), H.E.S.S. IU (b), H.E.S.S. IU+CT5 (c) and total (d) data sets. Sky regions with no observation time are depicted in gray. The black contours outline the X-ray emission from the jets (Brinkmann et al., 1996; Safi-Harb and Ögelman, 1997) as a visual reference.

A summary of the properties of each data set can be found in Table 6.1.

data set	exposure (h)	mean zenith (deg)	start date (DD/MM/YY)	end date (DD/MM/YY)	CT5 present
H.E.S.S. I	71.1	38.8	03/06/2005	20/08/2013	no
H.E.S.S. IU	33.5	44.2	29/08/2018	03/11/2021	no
H.E.S.S. IU+CT5	111.1	48.9	19/06/2020	05/11/2021	yes

TABLE 6.1: **The different data sets.** Values of the exposure, mean zenith, and starting dates for each of the used data set. The exposure quoted corresponds to the maximum in the acceptance-corrected value.

6.2 Analysis Configuration and Data Reduction

The data were reduced as detailed in Section 3.3 using only CT1-4 images as input to the ImPACT reconstruction algorithm (see Section 3.3.3) and the *hard* gamma-hadron separation cuts (see Section 3.3.4). At this stage the data has been reduced to a list of gamma-ray-like events, one per run, and their corresponding IRFs.

In order to achieve better performance at the highest energies, an extra step of background rejection is applied to the H.E.S.S. IU+CT5 data set with the Algorithm for Background Rejection using Image Residuals (ABRIR) introduced in Chapter 4. In this step, the calibrated and cleaned image of the CT5 telescope (which was not used in the prior event reconstruction) is compared against the ImpACT template prediction (which was obtained using only CT1-4 data) in order to accept or reject the event. Details on the algorithm, its motivation and performance are given in Chapter 4. Note that the effective areas are corrected to account for the gamma-ray efficiency of the ABRIR cut.

The resulting event lists and corrected IRFs are then further reduced using *Gammapy* (see Section 3.5.1). For each run, the events are binned into a three-dimensional WCS sky-map with an energy axis. The spatial dimensions of the map are 6° by 6° centered on the position of SS 433 with square spatial bins of 0.01° width. The energy axis has 22 logarithmically spaced bins between 0.63 TeV and 100 TeV. Only events falling within 2° radius from the pointing position of each run are considered in order to avoid the systematic issues associated with large-offset events. A *safe* energy range is defined by requiring the energy bias (see Section 3.3.5) to be smaller than 10% (Aharonian et al., 2006). This requirement excludes the energy bin between 0.63 and 0.8 TeV in all observations, so it is not considered further. The resulting counts map is shown in Figure 6.2.

An exclusion mask is defined to cover the known and expected sources in the region. It is made up of:

- A band of 2° height centered in the Galactic plane.
- A circle of radius 1.33° centered in the Galactic coordinate $l = 40.45^\circ$, $b = -0.8^\circ$ to cover the nearby extended source MGRO J1908+06.
- A circle of radius 0.57° centered in the Galactic coordinate $l = 40.0^\circ$, $b = -2.66^\circ$ to cover the eastern jet.
- A circle of radius 0.57° centered in the Galactic coordinate $l = 39.75^\circ$, $b = -1.95^\circ$ to cover the western jet.

For each run the prediction of the associated background model IRF is matched to the measured counts outside of this exclusion region in that same run using the FoV background method (see Section 3.3.6). This method results in a run-wise correction of the background model normalization and spectral shape to better match the data. The resulting expected background from each individual run is combined to form a background map for the entire data set. The run-wise count maps are also combined to the full counts map for the entirety of the observations. The resulting background map is shown in Figure 6.2.

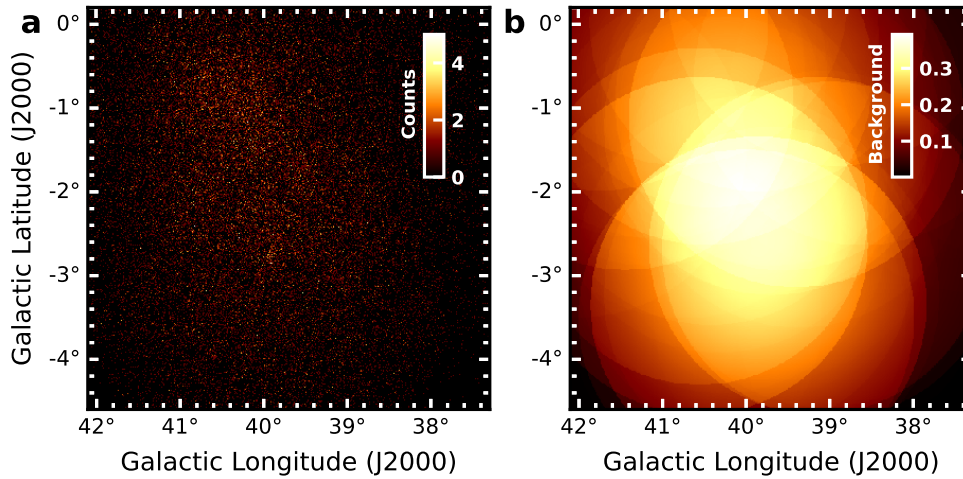


FIGURE 6.2: **Total counts and background map.** **a:** Total measured counts in the FoV for the entire data set. As can be seen, due to the very low flux of VHE sources, the number of measured counts is relatively low. In order to identify structures, smoothing is usually applied. **b:** Map of predicted background counts for the entire FoV derived using the combination of the IRF background model and the FoV background method.

The remaining IRFs are projected into the sky run-wise and combined for the entire data set using the exposure to weigh the PSF and energy dispersion appropriately. The resulting maps and IRFs are bundled into a *Gammapy* `MapDataset`¹ which will be the input to all the remaining procedures detailed in the following sections. All the significance maps shown in this chapter were derived without a source model assumption, i.e. the "based on excess" case introduced in Section 3.5.2 using a correlation radius of 0.1° , a value motivated by the scale of the H.E.S.S. PSF (see Figure 3.12).

6.3 Modeling MGRO J1908+06

The brightest gamma-ray source in the FoV is HESS J1908+063, which is robustly associated with MGRO J1908+06² (Abdo et al., 2007; Aharonian et al., 2009). It has a large extension and is detected with significance above 10σ . The MGRO J1908+06 region has been reported by both HAWC and LHAASO to be a significant source of gamma-rays well above 100 TeV (Abeysekara et al., 2020; Cao et al., 2021). It remains extended even at the highest energies. The origin of the emission is unclear and has been tentatively associated with the nearby pulsar PSR J1907+0602, although other explanations cannot be ruled out (Albert et al., 2022a; Abdalla et al., 2022). As a consequence, the distance of MGRO J1908+06 to Earth is unknown, although usually the distance to the pulsar of 2.37 kpc is assumed. This places MGRO J1908+06 and SS 433 at very different locations in the Galaxy. However, when integrating over the

¹<https://docs.gammapy.org/1.0/api/gammapy.datasets.MapDataset.html#gammapy.datasets.MapDataset>

²Through this chapter, we will refer to HESS J1908+063 as MGRO J1908+06 for consistency with Section 2.3.6 and Chapter 8.

	ϕ_0 ($10^{-11} \text{ TeV}^{-1} \cdot \text{cm}^{-2} \cdot \text{s}^{-1}$)	Γ	β
spectral	$1.28 \pm 0.07_{\text{stat.}} \pm 0.28_{\text{syst.}}$	$1.98 \pm 0.06_{\text{stat.}} \pm 0.10_{\text{syst.}}$	$0.15 \pm 0.02_{\text{stat.}} \pm 0.03_{\text{syst.}}$
	l (deg)	b (deg)	σ (deg)
spatial	$40.48 \pm 0.02_{\text{stat.}} \pm 0.03_{\text{syst.}}$	$-0.69 \pm 0.03_{\text{stat.}} \pm 0.01_{\text{syst.}}$	$0.61 \pm 0.02_{\text{stat.}} \pm 0.03_{\text{syst.}}$

TABLE 6.2: **Results of the spectro-morphological fit to MGRO J1908+06.** Best-fitting photon spectral and spatial parameters from the fit to the H.E.S.S. data. ϕ_0 is the amplitude at the reference energy $E_0 = 1 \text{ TeV}$. Γ is the spectral index and β the curvature parameter (see Equation 3.16). The best-fit position in Galactic coordinates are given by l and b . The 1σ radius of the Gaussian model is given by σ .

line of sight, and due to the extended nature of MGRO J1908+06, their emission is located less than 2° away from each other.

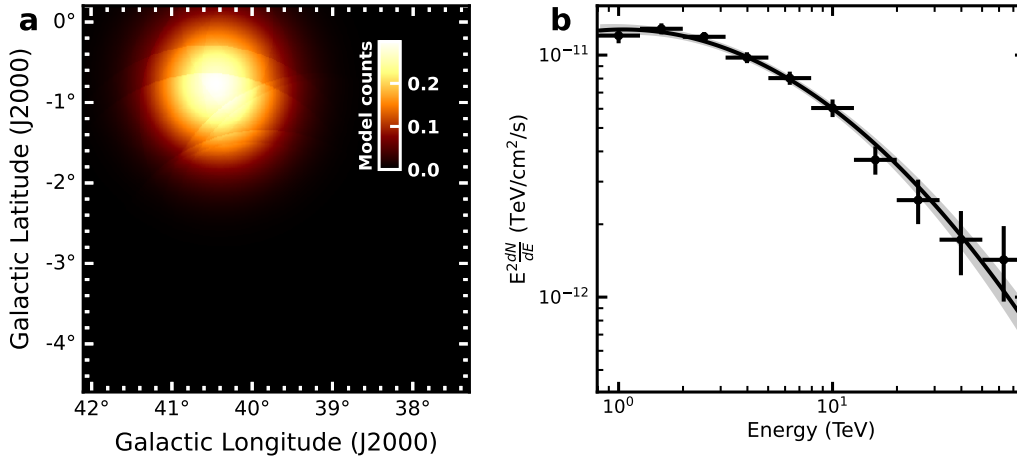


FIGURE 6.3: **Characterization of MGRO J1908+06.** **a:** predicted counts from the best-fit Gaussian spatial model of MGRO J1908+06. **b:** Best-fit spectral model with flux points for MGRO J1908+06. Errors shown here are statistical only.

Understanding the MGRO J1908+06 region is thus necessary to accurately characterize the gamma-ray emission from the jets of SS 433 and assess any possible contamination into the jet emission. We do this using the spectro-morphological modeling approach introduced in Section 3.5.5. We model MGRO J1908+06 using a combined spatial Gaussian model (described by Equation 3.18 with $e = 0$ and $\chi = 0.5$) and log-parabola spectral shape (see Equation 3.16). The presence of curvature in the spectrum is preferred to a simpler power-law (see Equation 3.14) by 6.4σ . This description agrees with existing dedicated studies of the gamma-ray emission of MGRO J1908+06 (Albert et al., 2022a; Abdalla et al., 2022). The resulting best-fit spectral and spatial model can be seen in Figure 6.3.

In order to assess the quality of the fit, we can compute significance maps before and after subtracting the MGRO J1908+06 component. This is shown in Figure 6.4, which shows the significance map of the entire FoV. Even after subtracting the MGRO J1908+06 model, the outer jets of SS 433 are clearly detected above 5σ .

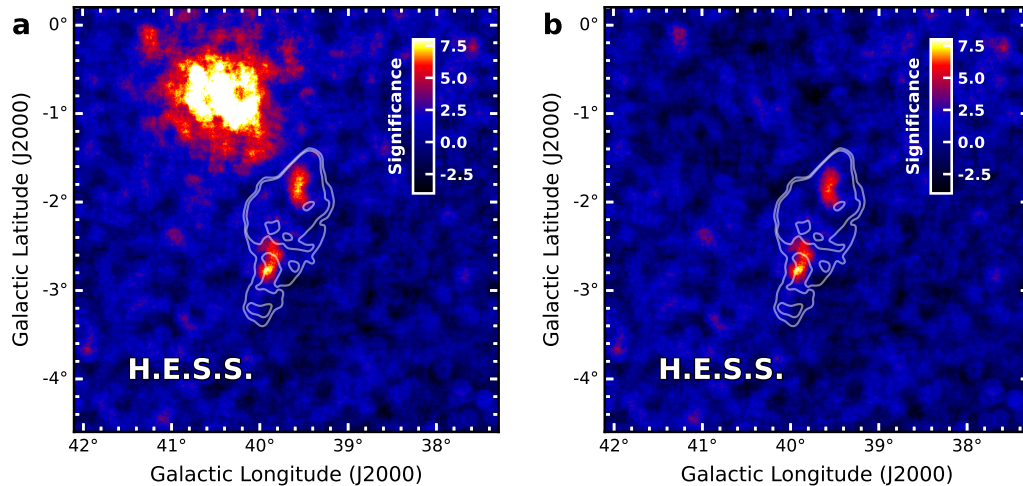


FIGURE 6.4: **Significance map before and after modeling and subtracting MGRO J1908+06.** The figure shows the statistical significance of the gamma-ray excess measured in the full FoV before (a) and after (b) fitting and subtracting the emission from the nearby extended source MGRO J1908+06. The solid white contours show the radio emission from the surrounding nebula W50 measured by the Effelsberg telescope (Reich et al., 1984, 1990; Furst et al., 1990).

6.4 Detection of SS 433

The H.E.S.S. observations reveal two elongated structures coincident with the X-ray emission of the outer jets, as can be seen in Figure 6.5. This finding agrees with the results by the HAWC observatory (Abeysekara et al., 2018). Additionally, the better angular and energy resolution of H.E.S.S. allows for a more detailed study of the properties of the gamma-ray emission than it was possible with the HAWC observations. This is obvious when comparing Figure 6.5 with the equivalent HAWC significance map in Figure 2.12. As can be seen in Figure 6.5, the jets are detected with a statistical significance of 7.8σ and 6.8σ for the eastern and western sides respectively, so well above the 5σ threshold.

The gamma-ray emission traces remarkably closely the X-ray emission of the outer jets, supporting its interpretation as non-thermal emission. However, the comparatively smooth gamma-ray surface brightness relative to the knotty X-ray features in both jets indicates that the latter is a consequence of inhomogeneities in the magnetic field and not in the underlying electron distribution. This is particularly obvious in the case of the *e2* region, marked in Figure 6.5, which is almost 5 times brighter in X-ray than its surroundings, whereas no such distinct feature is seen in the gamma-ray emission.

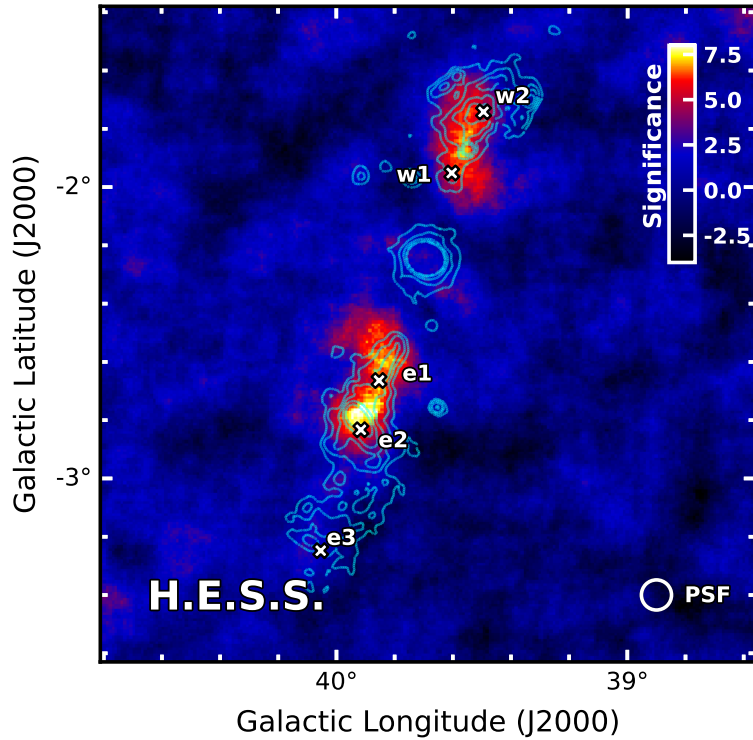


FIGURE 6.5: **Significance map of the SS 433 region.** The figure shows the statistical significance of the gamma-ray excess measured in the SS 433 region after the fitting and subtraction of the emission from the nearby extended source MGRO J1908+06. The solid cyan contours show the X-ray emission measured by the ROSAT satellite (Brinkmann et al., 1996; Safi-Harb and Ögelman, 1997). The locations of the X-ray regions $w1$, $w2$, $e1$, $e2$ and $e3$ are marked with white crosses. The 68% containment region of the PSF is denoted with a white circle.

No TeV emission is significantly detected from the central source (see Section 6.9) or from the eastern termination region ($e3$). This is in accordance with X-ray observations, which have previously suggested that the X-ray emission from this region has a thermal origin (e.g Brinkmann et al., 1996; Brinkmann et al., 2007; Safi-Harb et al., 2022).

6.5 Morphology of the Jets

The spatial properties of the jets are described using increasingly complex models until no longer preferred ($> 3\sigma$) by the data. An extended description using a symmetric Gaussian (described by Equation 3.18 with $e = 0$ and $\chi = 0.5$) is preferred over a point-source spatial model by 7.8σ and 4.7σ for the eastern and western excess respectively. The use of an additional parameter allowing the presence of ellipticity ($e \neq 0$) is preferred again by 5.8σ and 3.5σ compared to the symmetric case for the eastern and western excess respectively when freezing the angle to that of the SS 433 X-ray jets ($\theta = -19^\circ$). When allowing the angle to vary we obtain $\theta = -16.2 \pm 3.5^\circ$ for the eastern excess, preferred by 0.74σ and $\theta = -7.1 \pm 5.4^\circ$ for the western excess,

preferred by 1.9σ . As neither is significant, we keep the angle frozen to that of the jets. The parameters of the resulting best-fit elongated Gaussian model for each jet are presented in Table 6.3. Figure 6.6 shows the resulting spatial model and residual significance map when including the western jet (top panels) and the eastern jet (bottom panels). As can be seen in the figure, once MGRO J1908+06 and both jets are included there are no more significant hotspots in the FoV.

	l (deg)	b (deg)	σ_{maj} (deg) (pc)	σ_{min} (deg) (pc)	θ (deg)
east	$39.88 \pm 0.02_{\text{stat.}}$	$-2.69 \pm 0.03_{\text{stat.}}$	$0.21 \pm 0.04_{\text{stat.}}$ $20.1 \pm 3.8_{\text{stat.}}$	$0.04 \pm 0.02_{\text{stat.}}$ $3.8 \pm 1.9_{\text{stat.}}$	-19
west	$39.56 \pm 0.01_{\text{stat.}}$	$-1.85 \pm 0.03_{\text{stat.}}$	$0.13 \pm 0.03_{\text{stat.}}$ $12.5 \pm 2.9_{\text{stat.}}$	$0.05 \pm 0.02_{\text{stat.}}$ $4.8 \pm 1.9_{\text{stat.}}$	-19

TABLE 6.3: **Results of the elongated Gaussian fits to the morphology.** Best-fitting spatial parameters from the fit of an elongated Gaussian model. The center position in Galactic coordinates is given by l and b . The major and minor axis 1σ radius is given by σ_{maj} and σ_{min} respectively, with the corresponding physical size calculated for a distance of 5.5kpc (Blundell and Bowler, 2004). The angle with respect to the constant Galactic longitude axis θ is frozen in the fit.

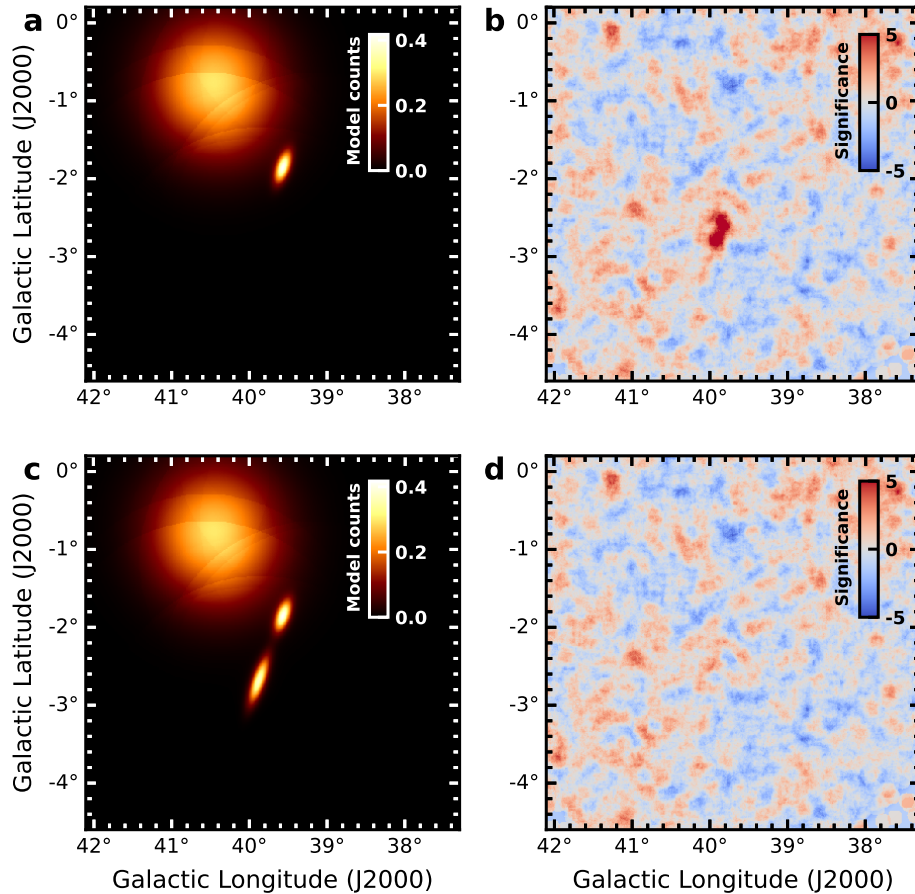


FIGURE 6.6: **Spatial modeling of the jets.** The top two panels show the prediction of the best-fit model that includes the MGRO J1908+06 component (see Figures 6.3 and 6.4) and the western jet (a) as well as the significance map after subtracting these two components (b). The bottom two panels have the same structure but with the complete model that includes also the eastern jet (c). There are no remaining significant hotspots in the residual significance map (d), which means the region is well modeled.

6.6 Energy-Dependent Morphology

The whole energy range is split into three smaller bins ($0.8 - 2.5$, $2.5 - 10$ and > 10 TeV), chosen so that the statistics in each of them are roughly comparable. We then compute significance maps in the same manner as above for each of the energy bins. The resulting maps, which reveal the presence of striking energy-dependent morphology can be seen in Figure 6.7. Gamma-ray excesses are detected along both jets in all energy bins with significance values (from low to high energy) of 4.4σ , 7.6σ , 5.9σ for the eastern jet, and 4.7σ , 5.6σ and 6.6σ for the western jet. The location of the most energetic gamma-rays is restricted to the base of the X-ray jets for both the eastern and western outer jets. Lower energy gamma-rays reach peak surface brightness instead at locations further along each of the jets.

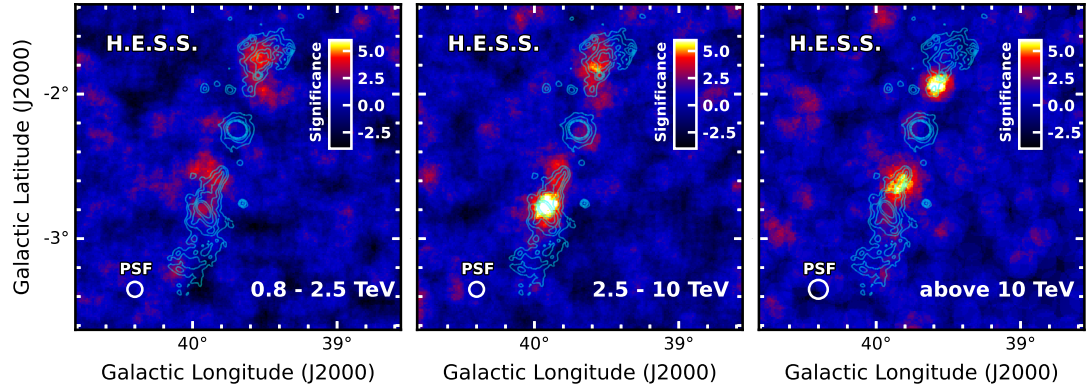


FIGURE 6.7: **Energy-dependent morphology.** The figure shows the statistical significance of the gamma-ray excess measured in the SS 433 region after the fitting and subtraction of the emission from the nearby extended source MGRO J1908+06 for three different gamma-ray energy ranges. The solid cyan contours show the X-ray emission measured by the ROSAT satellite (Brinkmann et al., 1996; Safi-Harb and Ögelman, 1997). The 68% containment region of the PSF for each energy range is denoted with a white circle.

To ensure that the observed energy-dependent morphology is not an artifact of the choice of energy bins, the same maps were computed using 5 and 10 energy bins, as well as 3 bins with different edges. In all cases, the same trend in the position of the gamma-ray excesses was observed.

6.6.1 Verification of the PSF at High Zeniths and Offsets

As can be seen in Figure 3.8, the H.E.S.S. PSF worsens with increasing pointing zenith angles. On the other hand, the instrumental collection area is greater for showers with large incoming zenith angles because of geometrical effects. This translates to a dominant contribution to the exposure in the highest energy range from observation runs at relatively large zenith angles. For this reason, the PSF becomes dominated by the large zenith runs at high energies, which translates to a worsening PSF with energy. In order to be confident on the validity of the observed energy-dependent morphology, a study was performed using dedicated Crab Nebula observations at different zenith and offset ranges similar to those in the SS 433 data set. This was used to verify the PSF in the same energy ranges as used in Figure 6.7.

	offset 1.0° H.E.S.S. I	offset 1.5° H.E.S.S. I	offset 1.0° H.E.S.S. IU	offset 1.5° H.E.S.S. IU
zenith 50° - 55°	2	0	6	12
zenith 55° - 60°	1	1	4	6

TABLE 6.4: **Crab Nebula observation runs for the PSF check.** Number of runs in each era for the pointing zenith angle and offset from pointing position ranges considered.

Runs from both the H.E.S.S. I and the H.E.S.S. IU era are used for this check. Dedicated observations were performed in January 2022 in order to cover all the

required range of offsets and zenith angles. For the H.E.S.S. I era this is obviously not possible, so only existing runs could be used, meaning that the statistics are lower.

For each run, the corresponding energy-dependent PSF derived from MC simulations was extracted from the IRFs. This is done by interpolating the IRF table to the observation zenith angle of the run and extracting the value for the offset angle to the Crab Nebula of the run (see Section 3.3.5). The measured events from the run are then binned into a histogram of offset angle squared (θ^2) from the nominal position of the Crab Nebula. These type of distributions, known as *theta-squared plot*, are widely used in VHE astronomy. From the number of measured counts at large offsets, the background level is estimated, leading to a measurement of the excess counts as a function of radial offset. Since the Crab Nebula has a very small extension (H.E.S.S. Collaboration, 2020), this can be interpreted as a measurement of the PSF from data.

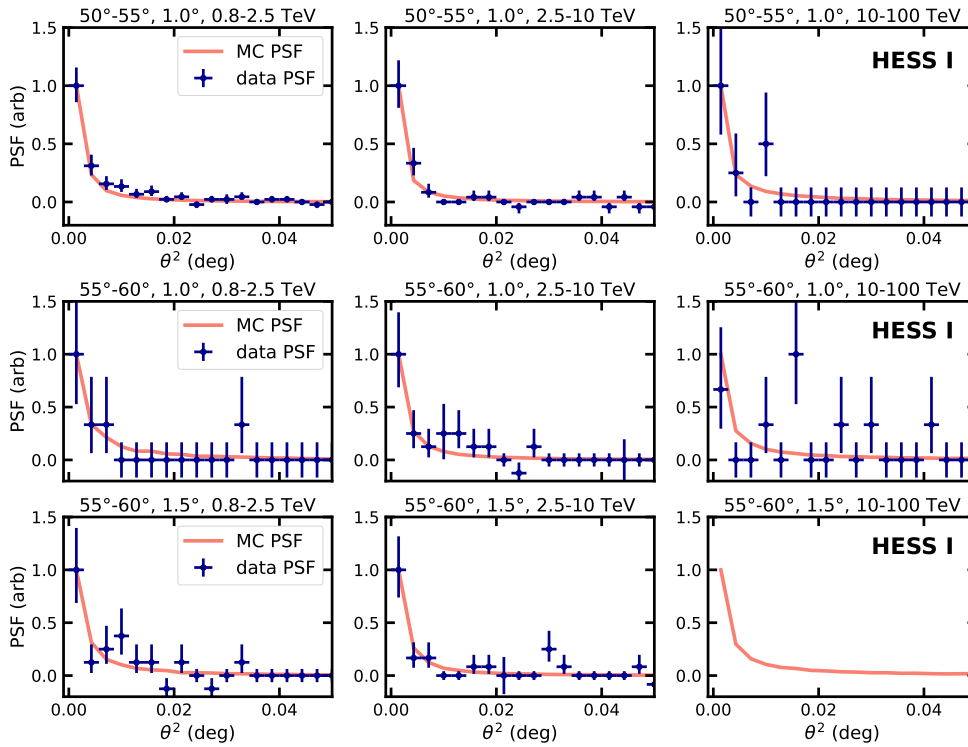


FIGURE 6.8: **PSF verification for the H.E.S.S. I era.** The title of each of the panels indicates the zenith range, the offset angle and the energy range. In each panel the PSF derived from gamma-ray simulations (MC PSF) is compared to the excess events measured from the Crab Nebula (data PSF) as a function of radial offset from its nominal position. Note that the number of runs in this data set is very low. The bottom right panel has no measured excess due to low statistics.

The shape of this excess is compared to the MC PSF, which is weighted by the Crab spectrum (assumed $E^{-2.6}$ Aharonian et al., 2006) in each of the selected energy ranges. The resulting data PSF and MC PSF are normalized and plotted together for each zenith, offset and energy combination. Both distributions are shown in Figure 6.8 for the H.E.S.S. I era and Figure 6.8 for the H.E.S.S. IU era. As can be seen, the

PSF derived from simulations describes the data reasonably well when the statistics allow for the comparison.

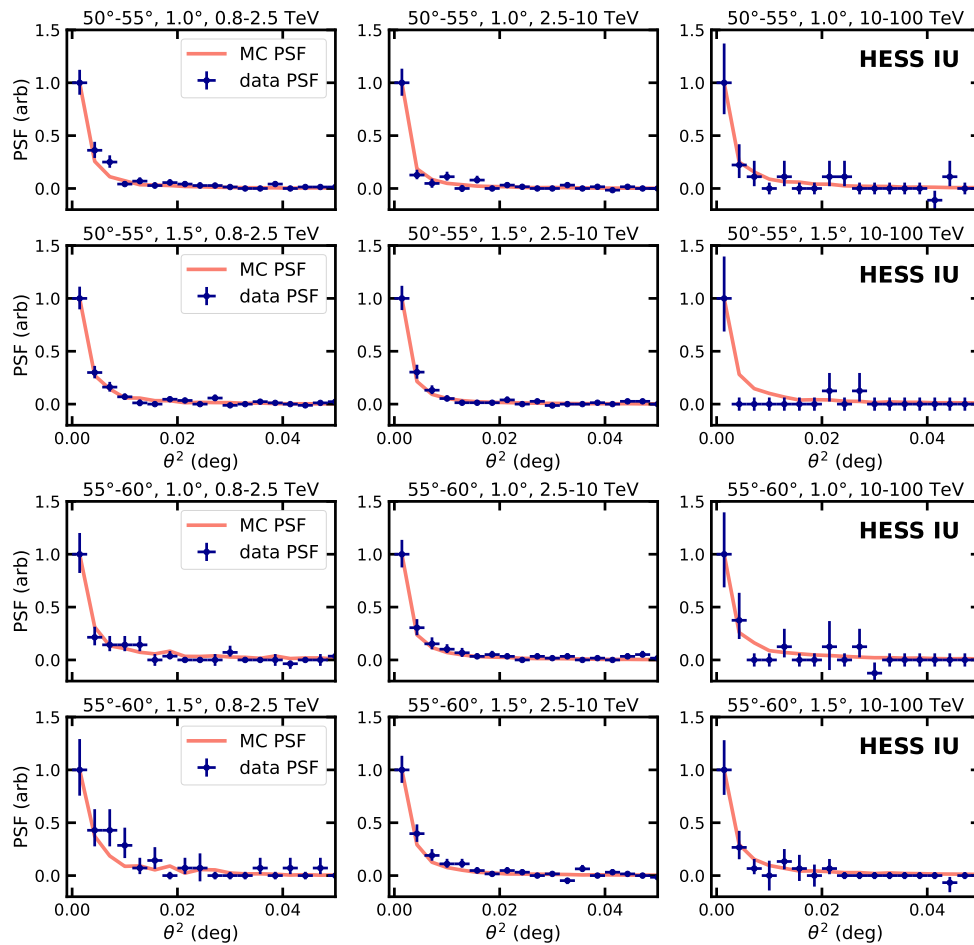


FIGURE 6.9: PSF verification for the H.E.S.S. IU era. The title of each of the panels indicates the zenith range, the offset angle and the energy range. In each panel the PSF derived from gamma-ray simulations (MC PSF) is compared to the excess events measured from the Crab Nebula (data PSF) as a function of radial offset from its nominal position.

6.6.2 3D Fits in Energy Bands

In the significance maps shown in Figure 6.7, a shift in the position of the gamma-ray excess can be seen as a function of energy. In order to assess the significance of this shift, we fit the morphology of the measured gamma-ray excess separately in each band, and compare the resulting best-fit positions. For simplicity, and due to the reduced statistics when splitting the data set into ranges, we fit a symmetric Gaussian in all cases, with the spectral parameters frozen to those from the best-fit to the full energy range. The same exercise was done with the spectral parameters free, which did not result in significant differences.

The resulting best-fit positions in Galactic coordinates for each of the jets in all three energy ranges can be seen in Figure 6.10. Note that in the lowest energy range,

neither jet is detected above 5σ , which is why the measurements in this range are represented with a transparent point.

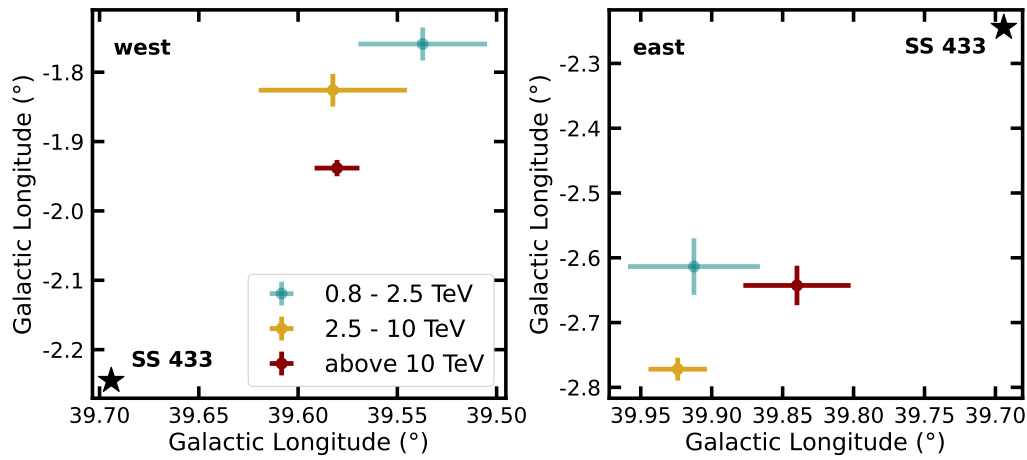


FIGURE 6.10: **Best-fit positions in different energy bands.** The best-fit position resulting from the 3D modeling of the gamma-ray excess in each of the energy bands. The left panel corresponds to the western jet and the right panel to the eastern. The position of SS 433 is indicated in both for reference with a black star.

The shift between the position of the middle and high energy ranges is at the level of 4.3 and 3σ for the eastern and western jet respectively. Another interesting quantity are the distances, both angular and physical between the centroid of the emission at each energy range and the location of the central binary, shown in Figure 6.11.

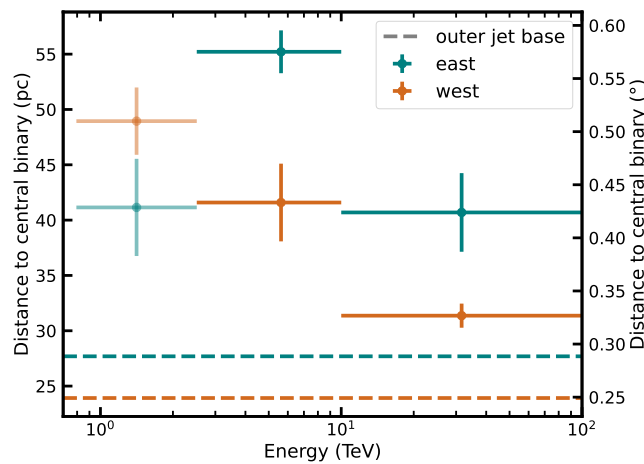


FIGURE 6.11: **Distance to the central binary in energy bands.** Distance between the best-fit position resulting from the 3D modeling of the gamma-ray excess in each of the energy bands and the central binary for the eastern (green) and western (orange) jets. The location of the base of the outer jets is marked with a dashed line for each side. The distances in pc is calculated assuming a distance of 5.5 kpc to the system.

6.6.3 Flux Profiles

Another way to visualize the energy-dependent morphology are spatial flux profiles along the jets in the different energy bands. This is done using the *Gammapy* FluxProfileEstimator³ method. We define an axis going through both jets and the central binary as the line between the Galactic coordinates (40.246°, -3.695°) and (39.340°, -1.295°). We then define a rectangular box of width 0.7° along this axis, and split it into 19 perpendicular boxes of height 0.14°. The height of the boxes is chosen as a compromise between maintaining sufficient statistics in each slice and sufficiently sampling the spatial shape of the gamma-ray emission, taking into account the size of the H.E.S.S. PSF. In each of these boxes the excess counts are computed and the integrated flux is fitted assuming a power-law spectral shape with index 2.3, the mean of the measured index of the eastern and western jets. The resulting flux profiles are shown in Figure 6.12.

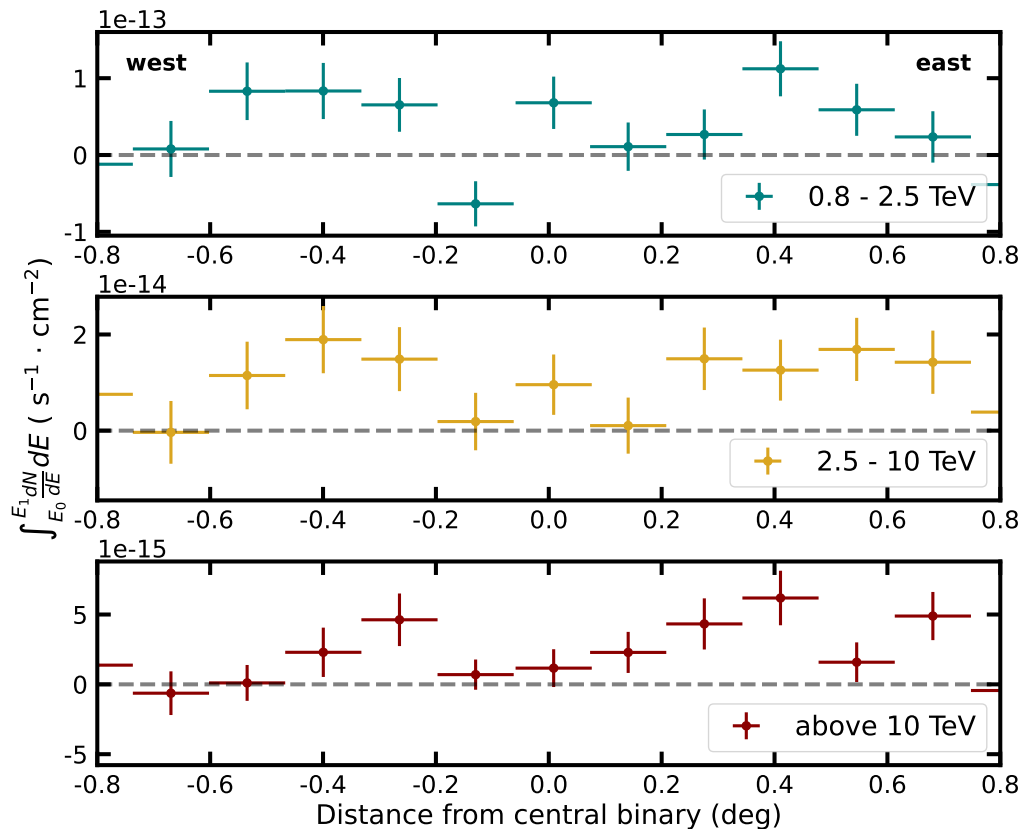


FIGURE 6.12: **Flux profiles of the jets.** Measured flux in spatial bins alongside the axis joining both jets through the central binary for three different energy bands. A gray dashed line is drawn at zero for reference.

³<https://docs.gammapy.org/1.0/api/gammapy.estimators.FluxProfileEstimator.html#gammapy.estimators.FluxProfileEstimator>

6.7 Spectra of the Jets

Because of the strong energy-dependent morphology, the assumption of a Gaussian spatial model for the jets across all energies can introduce inaccuracies in the associated spectral model when fitting both components together. For this reason, we measure the spectra of the jets without assuming a spatial model by extracting the spectral information in the 1D approach inside two elliptical regions large enough to completely contain the entirety of the gamma-ray excess in each jet. We do this after subtracting the 3D model for MGRO J1908+06. For both jets the spectral component is best described by a power-law (see Equation 3.14), with no significant preference for curvature (1.5σ and 0.7σ for east and west) or an exponential cutoff (1.3σ and 0.15σ) found. The resulting best-fit parameters are listed in Table 6.5. The best-fit models and flux points for each of the jets are shown in Figure 6.13. As can be seen, there are some differences between the spectra of the two jets but they are still compatible within errors (which include systematic uncertainties, see Section 6.10). The flux at 20 TeV measured by HAWC for each of the jets is also shown in Figure 6.13. For both jets, this value is in agreement with the measured H.E.S.S. flux.

	ϕ_0 ($10^{-13} \text{ TeV}^{-1} \cdot \text{cm}^{-2} \cdot \text{s}^{-1}$)	E_0 (TeV)	Γ
east	$2.30 \pm 0.58_{\text{stat.}} \pm 0.32_{\text{syst.}}$	1	$2.19 \pm 0.12_{\text{stat.}} \pm 0.12_{\text{syst.}}$
west	$2.83 \pm 0.70_{\text{stat.}} \pm 0.39_{\text{syst.}}$	1	$2.40 \pm 0.15_{\text{stat.}} \pm 0.13_{\text{syst.}}$

TABLE 6.5: **Results of the power-law fits to the spectra of the jets.** Best-fitting photon spectral parameters from the fit to the H.E.S.S. data with a power-law model. E_0 is the reference energy, ϕ_0 is the amplitude at the reference energy and Γ is the index.

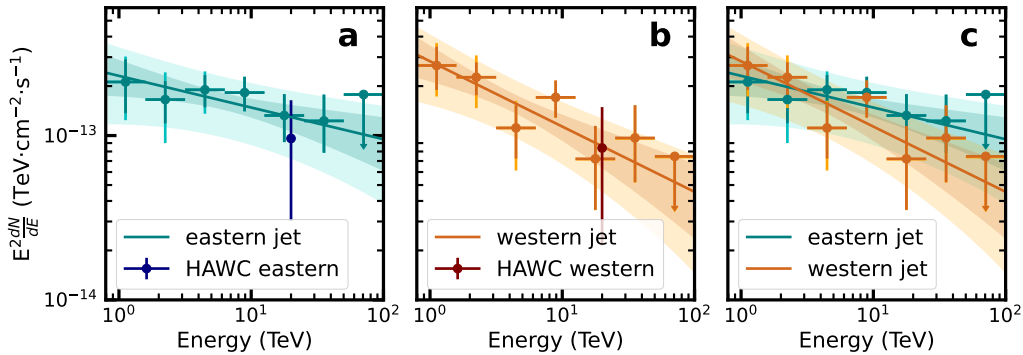


FIGURE 6.13: **Spectra of the jets.** Resulting best-fit spectral model from the 1D spectral extraction of the eastern (a) and western (b) jets. The dark shaded areas and flux points represent the statistical errors only, whereas the lighter colors include the systematic uncertainties. The flux measured by HAWC for each jet is shown as well (Abeysekera et al., 2018). The spectra from both jets is shown in panel c for easy comparison.

6.8 Search for Periodic Variability

Motivated by the discovery of a pulsating GeV source Fermi J1913+0515 in the vicinity of SS 433 displaying a period consistent with that of the jet precession period (Li et al., 2020, see Section 2.3.6) we search for periodic variability across the system. In order to not bias the periodicity search to one specific location, we simply assign to each of the observation runs a phase according to the jet precession period. We adopted a value of this period of 162.250 days and starting time T_0 as JD 2443508.4098, following Li et al., 2020. We then split the observations into 8 groups of phase and repeated the data reduction process for each data set. No significant emission was found in the vicinity of Fermi J1913+0515 in any of the phase bins, even when further splitting the data into the same three energy bands as in Figure 6.7. In order to increase the statistics, we also combine these eight data sets further into four and two bins of phase, which lead to the same non-detection for all energy ranges. No significant phase trend is found for any other part of the system in any of the data sets or data ranges either. Figure 6.14 shows the significance maps for the entire energy range when splitting the data set into two bins of phase.

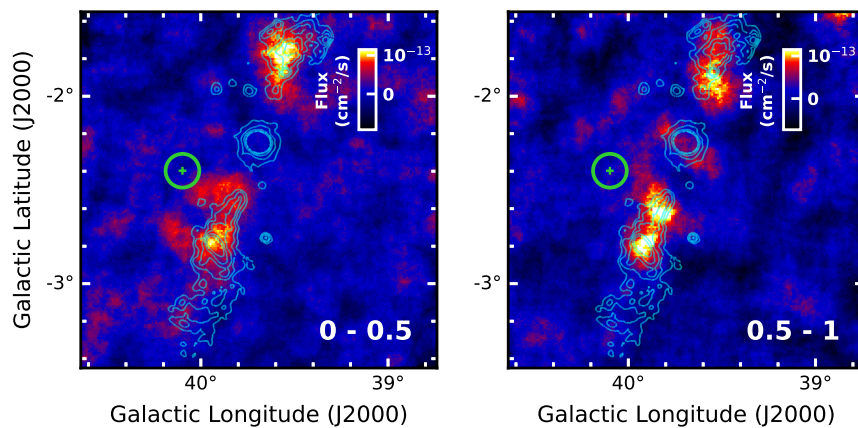


FIGURE 6.14: **Flux maps for different phase bins.** Integrated flux maps after the subtraction of the emission from MGRO J1908+06 in two bins of the jet precession phase indicated in the bottom right. The location of Fermi J1913+0515 is marked with a green circle and cross. The blue contours show the X-ray emission measured by the ROSAT satellite (Brinkmann et al., 1996; Safi-Harb and Ögelman, 1997).

6.9 The Central Source

No VHE emission is detected from the region where the central binary is located. This points to a thermal nature of the bright X-ray emission originating in this region, as it was previously suggested (e.g. Brinkmann et al., 1996; Safi-Harb and Ögelman, 1997). We derive spectral upper limits assuming a spectral index of 2.7, as it was done for previously reported limits (MAGIC and H.E.S.S. Collaborations et al., 2018). The limits derived, which are shown in Figure 6.15 are around an order of magnitude more constraining than previous ones, and extend to higher energies.

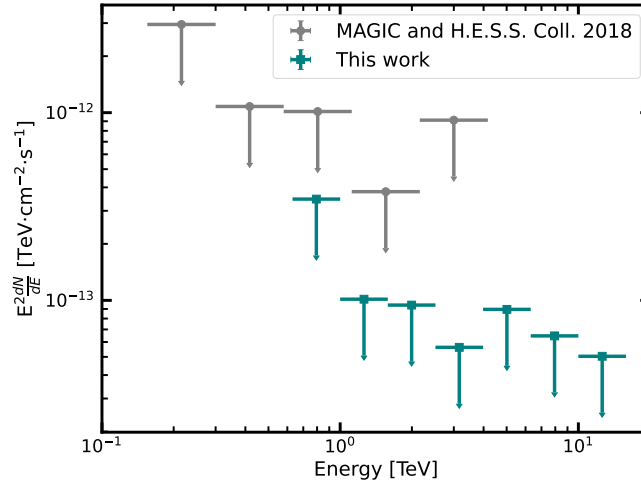


FIGURE 6.15: **Central source upper limits.** Spectral upper limits from the core region. The previously most constraining limits from MAGIC and H.E.S.S. Collaborations et al., 2018 are shown in gray.

6.10 Systematic Uncertainties

6.10.1 Systematic uncertainties introduced by the background estimation

Systematic effects on the background were determined by measuring the significance distribution outside of the exclusion mask, shown in Figure 6.16. Although a width of 1 was expected, a width of 1.084 ± 0.005 was measured, which translates to a slight shift in the reported significance values. The corrected values when accounting for this effect are 7.2σ and 6.3σ for the eastern and western excess respectively.

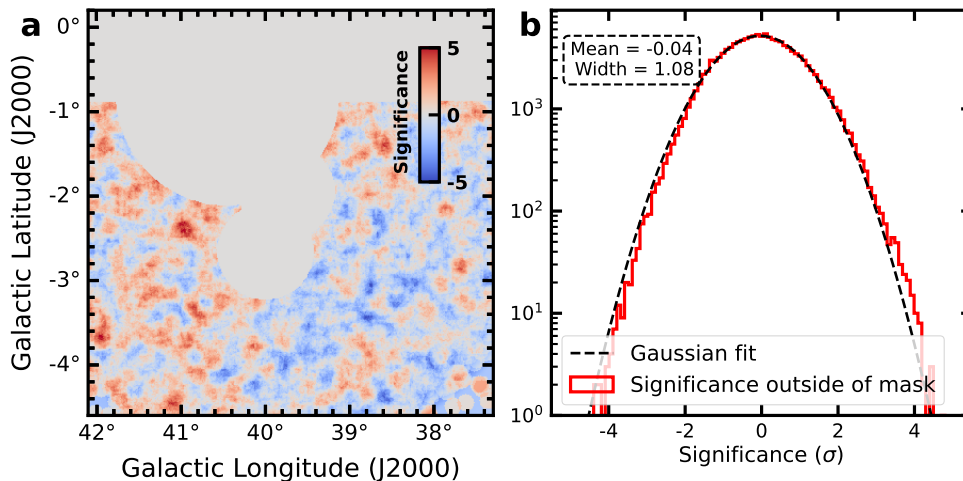


FIGURE 6.16: **Systematic uncertainties on the background.** **a:** Significance map multiplied by the exclusion mask defined to covering all expected sources. **b:** Distribution of the significance values outside of the exclusion mask (red line). A Gaussian function is fitted to the distribution (black line), with the resulting mean and width listed in the top left corner. The size of the deviation from the expected width of 1 is used to assess the impact of background systematic effects in the significance values.

In the case of the significance maps in energy bands shown in Figure 6.7, the same distribution is derived for each of the energy ranges. The resulting histograms can be seen in Figure 6.17, with widths of 1.033 ± 0.008 , 1.065 ± 0.008 and 1.011 ± 0.018 from low to high energy. The corrected significance values when accounting for this effect are 4.3σ , 7.2σ and 5.9σ for the eastern jet from low to high energy and 4.6σ , 5.3σ and 6.5σ for the western excess in the same order.

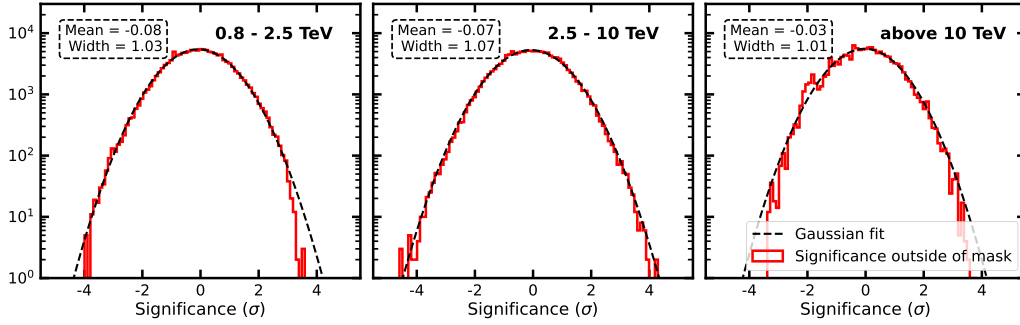


FIGURE 6.17: **Systematic uncertainties on the background for different energy bands.** Distribution of the significance values outside of an exclusion mask covering all expected sources (red line) for each of the used energy ranges. A Gaussian function is fitted each the distribution (black line), with the resulting mean and width listed in the top left corner of each panel. The size of the deviation from the expected width of 1 is used to assess the impact of background systematic effects in the significance values.

6.10.2 Systematic Uncertainties in Model Parameters

The systematic uncertainties quoted for the model parameters (see e.g. Table 6.5) are calculated with a MC-based approach, in which the IRFs are randomly varied in a number of ways that mimic possible inconsistencies in the way that the detector response is understood. The sizes of the variation of the parameters are chosen in such a way that the corresponding effects are of the right size given the degree of agreement between data and simulations in the H.E.S.S. analysis framework (Aharonian et al., 2006; Mohrmann et al., 2019).

- **Shift of the energy scale:** The energy axes of the effective area, energy dispersion and point-spread function are scaled by a factor f_E to simulate the effect of a wrongly calibrated energy reconstruction. This factor is sampled from a Gaussian distribution with mean 1 and width 0.1.
- **Modified background normalization:** The overall normalization of the background model is varied by a factor f_{BG} . This factor is sampled from a Gaussian distribution with mean 1 and width 0.01.
- **Modified background spectral tilt:** The spectral shape of the background model is modified by a factor $E^{\Gamma_{BG}}$. This index Γ_{BG} is sampled from a Gaussian distribution with mean 1 and width 0.02.

- **Presence of a background gradient:** A linear gradient is added over the FoV with amplitude A_{BG} and direction α_{BG} . The amplitude is sampled from a Gaussian distribution with mean 1 and width 0.01, whereas the angle is a uniform distribution between 0° and 360° .

For each realization of the sampling, the IRFs are modified and used to generate random pseudo-data sets based on the composite global best-fit model. These pseudo-data sets are identical to the real one but instead of measured counts, the predicted counts from the combination of the source models and background are used. They are then re-fitted using the original, unmodified IRFs. This process is repeated 2500 times. The obtained spread in the fitted parameters then reflects their combined statistical and systematic uncertainty.

This procedure is applied to both the full 3D analysis as well as to the spectral-only fits. Similarly, the systematic errors for flux points are derived by calculating flux-points from the pseudo-data sets. The resulting systematic uncertainty is of the same magnitude as the statistical one at the lowest energies considered here, and quickly becomes negligible at higher energies.

In order to assess the contamination of MGRO J1908+06 into the western jet region, the MGRO J1908+06 model is not included when performing half of the spectral fits of the western jet. This represents the most extreme case of poor modeling of MGRO J1908+06: when the source is not modeled at all. The resulting effect to the best-fit parameters and flux points in the western jet region is included in the quoted values of systematic errors.

For certain fitted parameters, such as the eccentricity and width of the elongated Gaussian components used to model the jets (see Table 6.3), the distribution was not broadened by the systematic effects considered here. This is also the case for the best-fit Galactic coordinates of the jet models. However, we note that these parameters may be affected by other systematic effects neglected in the MC approach. In particular, the source positions are subject to the systematic uncertainty of the pointing position of the H.E.S.S. telescopes, which is of the order of $10'' - 20''$ (Gillesen, 2004).

6.11 Summary and Outlook

In this chapter, we have presented H.E.S.S. observations of SS 433 which have resulted in the first detection of this system by an IACT array, following the first detection by HAWC. Below we summarize the main results of this analysis:

- **Spatially resolved emission from the jets.** The H.E.S.S. PSF allows for a first-ever measurement of the extension and approximate shape of the TeV emission from the jet lobes.

- **Spectra of the jets measured out to 50 TeV.** The flux level is found to be in agreement with previously reported values from HAWC. No significant evidence for a cutoff in the spectrum is found in either of the jets, meaning that their spectra likely extend to higher energies. An extension to the measured spectra above 100 TeV might then be possible via deep exposures with, e.g. the HAWC outrigger array, the LHAASO experiment or the upcoming CTA observatory.
- **Presence of energy-dependent morphology.** This is the first-ever observation of energy-dependent morphology in the gamma-ray emission of a jetted source. The location of the TeV emission sites is seemingly moving outwards in the jets with decreasing energy. This has many implications for the dynamics and particle acceleration in the jets, which will be discussed in the next chapter.
- **Non-detection of time variations.** No significant time-dependence of the emission is found across the system, including the region of Fermi J1913+0515.
- **Non-detection of emission from central source.** Confirming the picture that most of the X-ray emission in that region is of thermal nature. Upper limits are derived, which are almost an order of magnitude more constraining than the previously published values.

The implications of the H.E.S.S. observations for our understanding of the particle acceleration in the SS 433 system and the dynamics of the jets are discussed in detail in Chapter 7.

Chapter 7

Acceleration Sites and Dynamics in the SS 433 Jets

This chapter frames the TeV view of SS 433 detailed in Chapter 6 into the broader context of the non-thermal emission and dynamics of the SS 433 jets and their environments. The observation of energy-dependent morphology in the TeV emission of the outer jets allows the identification of their base as the site where electrons are accelerated to very-high energies, most likely by a shock. The measured flux of each jet across the EM spectrum is modeled by a combination of the synchrotron and IC radiation produced by the accelerated electrons, which results in an estimate of the average magnetic field values. The energy-dependent morphology is then explained as a combination of the particle cooling times and the advection flow of the jet, which constrains the jet dynamics and, in particular, results in an estimate of the velocity of the outer jets at their base.

7.1 Acceleration Sites in the SS 433 Jets

The absence of correlation between the gamma-ray emission, especially at the highest energies, and the presence of relatively dense target material needed for pp interactions (see Section 2.3.3) allows us to conclude that the bulk of the gamma-ray emission is most likely due to relativistic electrons. Additionally, the fact that energy-dependent morphology is observed indicates that the velocity of the outer jets cannot have a constant value as high as $0.26c$, as in that case adiabatic losses, the loss timescale of which is energy independent (see Section 1.5.2), would dominate.

The dominant energy loss mechanisms for high energy electrons are then synchrotron and IC cooling (see Section 1.5.1). From equations 1.28 and 1.35, we concluded that for these processes, the most energetic particles have the shortest cooling timescales. This fast cooling limits the distance around the acceleration site within which the highest energy electrons can radiate as they stream away, either by diffusive or advective transport. Most attempts to model the TeV emission from the jets of SS 433 have posited that particles are being accelerated to VHE energies in the bright X-ray knots (see Section 2.4.2). However, the H.E.S.S. observations detailed in Chapter 6, and in particular Figure 6.7, reveal that the highest energy gamma-ray are

observed only close to the base of the outer jets. This means that the acceleration of the highest energy electrons is occurring not in the X-ray knots, but slightly closer to the central binary.

In fact, recent X-ray observations (Safi-Harb et al., 2022; Kayama et al., 2022) reveal a sharp brightness transition at that location in the base of the outer jets. This is consistent with the presence of a shock, which would then be responsible for the acceleration of the particles that cause the TeV and X-ray emission (see Section 1.4).

Despite numerous theoretical and numerical studies on the SS 433 jets and their interplay with W50 (see Section 2.4), the fact that this surface, at around 25 pc from the central binary, would host a shock discontinuity has never been predicted. In fact, there are no observational indications beyond the reappearance of the jets themselves that attach physical significance to this location. The three-phase shell structure suggested by Konigl, 1983 would provide an explanation for such a feature, although it would require an alternative explanation for the origin of W50 than the commonly accepted SNR scenario. This picture would require this shock to be moving very slowly, in order to have not advanced a large distance during the lifetime of the electrons responsible for the TeV emission (see Section 7.3.1).

7.2 Multi-Wavelength SED

From Figures 1.6 and 1.7 it can be inferred that the same population of electrons will emit radiation at photon energies ranging between the radio and X-ray regime via synchrotron radiation and at gamma-ray energies via IC. Thus, in order to estimate the value of the ambient magnetic field, the gamma-ray data alone is not sufficient, and multi-wavelength information is needed to cover the synchrotron regime. We build the multi-wavelength spectral description of the jets of SS 433 by combining the H.E.S.S. spectra shown in Figure 6.13 with publicly available or published radio, X-ray and GeV data.

7.2.1 Radio Data

The outer jets have not been detected in the radio band, a range in which the shell of W50 is instead a bright source (see Section 2.3.1). We use public data from the 11 cm Effelsberg radio telescope survey (Reich et al., 1984, 1990; Furst et al., 1990) to obtain the total flux inside the same region as where the gamma-ray spectra was extracted. This provides an upper limit to the radio flux coming from the jets, as they must at least be fainter than W50.

7.2.2 X-ray Data

We use publicly available data from the XMM (Brinkmann et al., 2007) and Chandra (Kayama et al., 2022) satellites for the eastern and western jet respectively. The

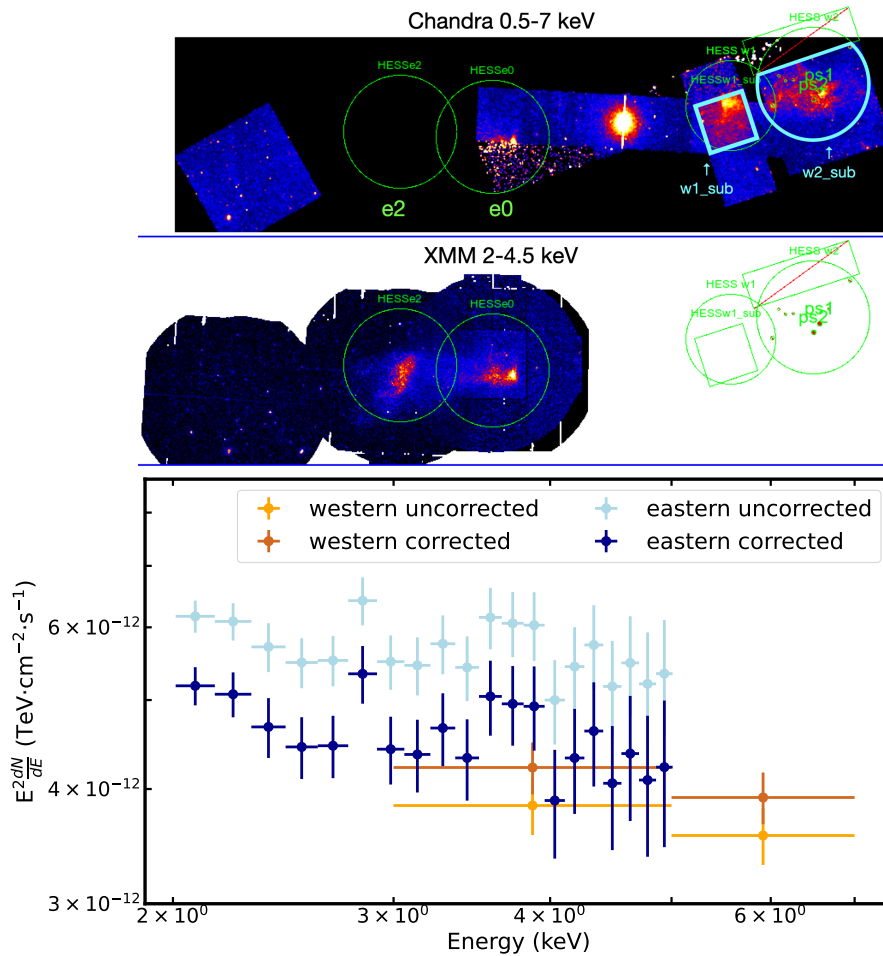
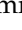
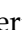


FIGURE 7.1: X-ray flux maps and spectra. *Top*: Chandra (top) and XMM (bottom) flux maps of the SS 433 regions. The spectral extraction regions are marked in green for the eastern case and blue for the western case. Image and data analysis by Naomi Tsuji  *Bottom*: Resulting flux points for each of the jets, before and after the correction described in the text was applied.

X-ray flux points are extracted from the same spatial regions used for the TeV measurements. The resulting flux maps and flux points are shown in Figure 7.1. Only data above 2 keV is used in the fit to minimize the contribution of thermal X-ray emission and the effect of absorption by the interstellar medium. The X-ray data analysis was performed by Naomi Tsuji . Two corrections were applied to the resulting flux points:

- **Western jet:** The observations with Chandra have a relatively small FoV (see Figure 7.1), which means that the region covered is not exactly the same as that of the TeV flux points. In order to correct for the missing flux, we apply a correction factor of 10% derived using the surface brightness of the ROSAT image of the jets above 2 keV (Brinkmann et al., 2007).
- **Eastern jet:** The X-ray emission from the eastern jet includes that of the bright

lenticular region usually labeled as $e2$. Due to the absence of a comparable brightness increase in the highest energy gamma-rays at that location, we conclude that this is due to a local enhancement of the magnetic field. Since we are interested in the average magnetic field of the jets, we subtract the spectrum of this region as measured by Safi-Harb et al., 2022.

Note that after these corrections are applied, the flux level and spectral behavior of the overall X-ray emission from each jet are consistent with one another. This, together with the similarities between the gamma-ray spectra of both jets (see Figure 6.13) indicates that the electron populations responsible for the emission of the jets cannot be significantly different between the western and eastern sides.

7.2.3 GeV Data

We use the results from the most recent study using Fermi-LAT data of the SS 433 region (Fang et al., 2020). In this work, the presence of a sub-threshold ($\sim 4\sigma$) excess nearby the large scale western jet is reported. They produce upper limits for both the western and eastern side, which are used here to constrain the broadband model in the GeV range.

7.3 Broadband Model

We model the broadband spectral distribution of the jets as a whole by a combination of synchrotron and IC emission (see Section 1.5.1). We do this using the GAMERA code (Hahn, 2015; Hahn et al., 2022) introduced in Section 1.5.1.

We assume accelerated electrons are injected constantly over a time $t_{\text{age}}=10,000$ yr (see Section 7.3.1) with a spectral shape described using a power-law with index Γ_e with a spectral cutoff at energy $E_{c,e}$ (see Equation 3.15). The injected electrons lose energy due to synchrotron losses in ambient magnetic field B and IC scattering of soft ambient photons. Both the magnetic field and the energy density of target soft photons are assumed to be constant within each jet. We use the combination of an axisymmetric Galactic model for the energy densities of the diffuse interstellar radiation field (Popescu et al., 2017) and the CMB as the target radiation fields. We assume a distance of 5.5 kpc, and extract the ambient photons at the location of each of the jet lobes. Figure 7.2 shows the energy density of ambient photons for each jet and at the central binary position for reference. The resulting radiation fields for both jets are relatively similar, with differences on the order of 20% at the largest. The effect of varying the distance from Earth is also shown in the figure. For a reasonable range of distances, this effect is also small, well within 10% for most energies.

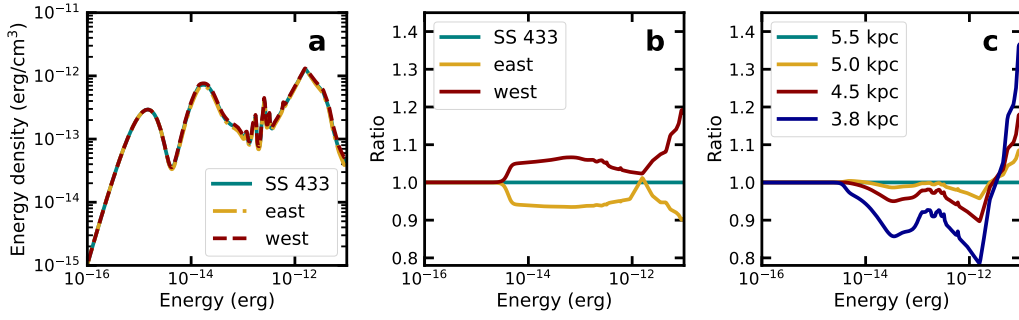


FIGURE 7.2: **Ambient radiation fields.** **a:** Energy density of the ambient radiation fields at the location of SS 433 (teal), the east (yellow) and the west (red) jets assuming a distance of 5.5 kpc to Earth. **b:** Energy densities shown in panel **a** divided by the value for SS 433 in order to highlight the differences between the two jets. **c:** Energy densities at the SS 433 position for different values of the distance to Earth divided by the curve assuming 5.5 kpc.

The amount of power injected per second is parameterized as a fraction α of the jet kinetic power, taken to be 10^{39} erg/s. We assume that the injected electron spectrum has the same parameters (Γ_e , α and $E_{c,e}$) for both of the jets, but we allow the ambient magnetic field to differ between the two jets. We fix $\Gamma_e = 2$, motivated by the measurement of a hard index (~ 1.5) in the X-ray spectra at the base of both the western (Kayama et al., 2022) and eastern (Safi-Harb et al., 2022) outer jets.

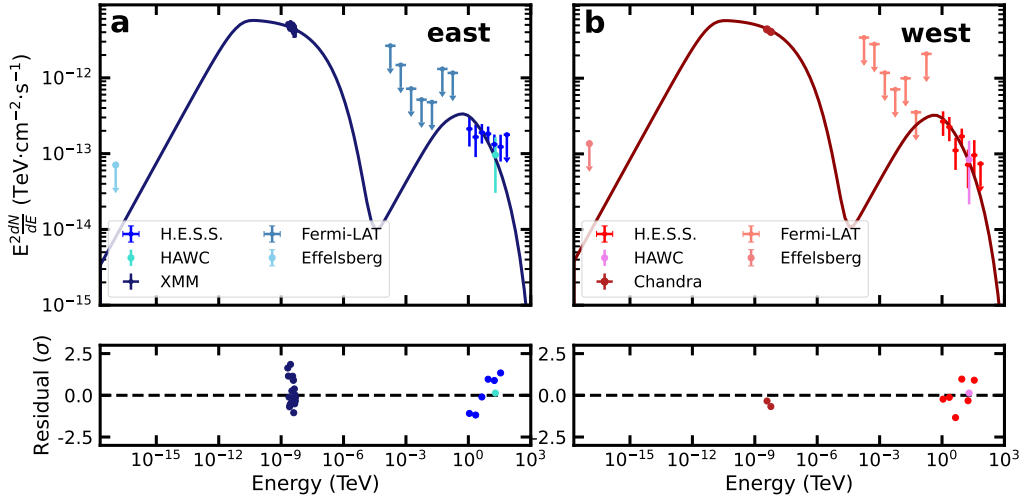


FIGURE 7.3: **Multi-wavelength spectral energy distribution (SED) of the jets.** Multi-wavelength SED of both the eastern (**a**) and western (**b**) outer jets. The low energy component is due to synchrotron emission (see Section 1.5.1), while high energy photons are produced due to IC radiation (see Section 1.5.1). The best-fit model for each of the jets is shown with a solid line. The bottom panels show the residuals for the east (**c**) and west (**d**) case.

We fit the models using a maximum likelihood approach to the H.E.S.S. and X-ray data of the jets, with the GeV and radio observations as upper limits. The resulting best-fit values of the parameters are presented in Table 7.1. The value of $E_{c,e}$ is not

constrained towards higher energies, but must be greater than 200 TeV (68% C.L.). The amount of power required to reproduce the observed emission is around 0.13% of the jet kinetic power of 10^{39} ergs/s. The best-fit magnetic field values are found to be 19 and 21 μG for the eastern and western jet respectively, in agreement with estimates derived from X-ray observations (Safi-Harb et al., 2022; Kayama et al., 2022). The resulting broadband spectral model is shown in Figure 7.3 for both jets.

	east	west	shared	fixed
Γ_e	2	2	yes	yes
$E_{c,e}$ (TeV)	630_{-430}^{+9370}		yes	no
α	$(1.29 \pm 0.03) \cdot 10^{-3}$		yes	no
B (μG)	19 ± 3	21 ± 2	no	no

TABLE 7.1: **Model parameters.** Best-fit values of the injected electron spectral parameters and ambient magnetic field. The errors correspond to statistical uncertainty. Whether a parameter was fitted simultaneously for both jets is indicated by the column "shared".

7.3.1 Age of the Jets

The combination of the injected index required by the X-ray data, the Fermi-LAT upper limits and the steepness of the H.E.S.S. spectra translate to bounds on the age of the observed jets, which should be older than 1,000 years, but younger than 30,000, with an age of around 10,000 yr yielding the best agreement with the observations. This result is consistent with previous theoretical and numerical studies, which placed the age of the jets in the 10,000-30,000 yr bracket (e.g. Goodall et al., 2011a; Bowler and Keppens, 2018).

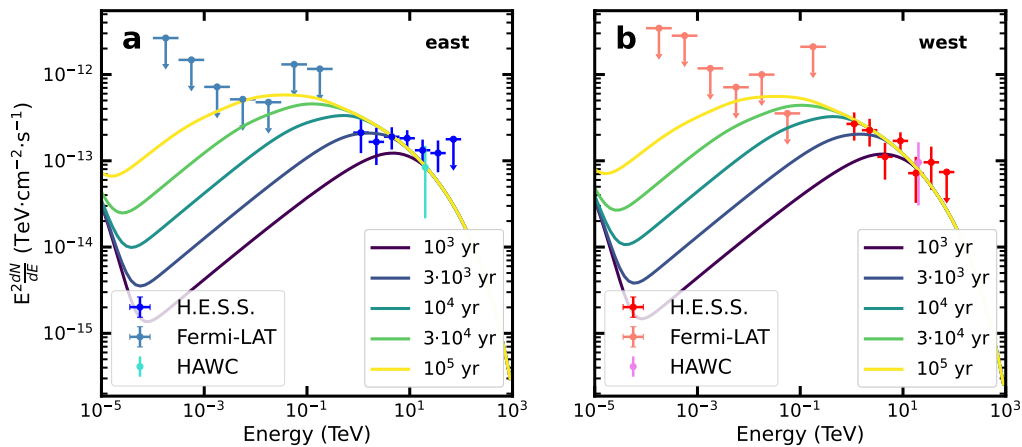


FIGURE 7.4: **Model dependency on total age.** Gamma-ray emission predicted by the model as a function of the total system age compared to the H.E.S.S. and HAWC flux points and Fermi-LAT upper limits.

Note that an age older than 30,000 would also be incompatible with the radio upper limit described in Section 7.2.

7.4 SS 433 as a Cosmic-Ray Source

Given the upper limit on the age of the electrons of $t = 30,000$ years and taking the value of the average Galactic diffusion coefficient to be $D_{\text{gal}} = 10^{28} \left(\frac{E}{1\text{GeV}}\right)^{1/3} \text{ cm}^2 \text{ s}^{-1}$ (Strong et al., 2007), we can estimate the distance that cosmic rays would have covered since escaping from the source as $r = \sqrt{4D_{\text{gal}}t}$. For proton energies of 1 PeV, this results in ≈ 0.6 kpc, which is much lower than the lowest estimate for the distance to SS 433 of 3.8 kpc (Arnason et al., 2021). For cosmic rays from the system to have reached Earth by today, the age would need to be more than 40 times older, which is incompatible with the radio and GeV measurements, as well with the estimates of the age of W50 (e.g. Goodall et al., 2011a; Bowler and Kepkens, 2018), or the Galactic diffuse coefficient be significantly smaller above energies of 100 TeV. This means that even if protons are accelerated in the jets of SS 433, they are not expected to contribute to the cosmic-ray flux measured on Earth.

7.5 Particle Transport in the Jets of SS 433

The observed energy-dependent position of the gamma-ray emission in the jets of SS 433 can then be interpreted as a consequence of the combination of particle cooling timescales and advection with the jet flow, and thus can be used to constrain the internal dynamics of the outer jets.

7.5.1 A Model for Particle Transport and Cooling

We model this process by implementing a one-dimensional Monte Carlo simulation which uses GAMERA to calculate the radiation and cooling of particles as they are transported due to both advective and diffusive flows. The simulation is run from $t = 0$ to $t = t_{\text{age}}$. At each time-step t_{step} , electrons are injected at the position $z = 0$ with a spectral shape described by a power-law with a spectral cutoff. Particles then suffer radiative losses due to the magnetic field and soft radiation field, which are assumed to be spatially constant, which leads to a change in the electron spectrum at each t_{step} . Particles are shifted in the z direction by the combination of two effects:

- **Diffusion:** implemented as a random Gaussian smearing with scale $\sqrt{2Dt_{\text{step}}}$ where $D = D_{100} \left(\frac{E}{100\text{TeV}}\right)^{1/3}$ is the diffusion coefficient.
- **Advection:** in a flow described by a spatially-dependent velocity $v(z)$. Note that whereas diffusion happens in both increasing and decreasing z directions, advection only happens in one direction, given by the sign of $v(z)$.

When t reaches t_{age} the result is a two-dimensional distribution of the number of electrons as a function of their energy and position along the z direction. Electron packets that were injected earlier on the simulation time have suffered more cooling and are also further away from the injection location than freshly injected ones.

Using the electron distribution as input, we use GAMERA again to derive the radiation spectrum, which depends on photon energy and position along the z direction. This allows to construct a prediction of the observed flux for any chosen energy range as a function of distance to the injection position.

7.5.2 Application to SS 433

We apply this model to the case of the jets of SS 433, aiming to reproduce the measured flux profiles shown in Figure 6.12. We use the best-fit injected electron spectrum parameters and magnetic field presented in Table 7.1, as well as the ambient radiation fields shown in Figure 7.2. We consider different values of the magnetic field and also different radiation fields for each jet. However, these differences are rather minor, leading to very similar conditions for both jets. We use a total $t_{\text{age}}=10,000$ yr and a $t_{\text{step}}=4$ yr, chosen to be smaller than the shortest particle cooling timescale (see below).

Relevant Timescales

The resulting particle cooling timescales (see Equations 1.28 and 1.35) for both the eastern and western jet are shown in Figure 7.5. The relatively high values of B derived from the multi-wavelength fit result in the cooling being dominated by synchrotron emission for all electron energies. The fact that this is the main channel of energy loss can also be inferred from the difference in flux between the synchrotron and IC components of the spectra shown in Figure 7.3.

We derive the acceleration timescale assuming shock acceleration (see Equation 1.21) and parameterize the efficiency of this acceleration using a parameter η (see Equation 1.22). The resulting acceleration times for several values of η are shown as dotted lines in Figure 7.3. The energy at which the total cooling timescale crosses the acceleration time represents the maximum achievable electron energy.

The fit to the multi-wavelength data (see Table 7.1) resulted on a best-fit value for the energy cutoff of the electron spectrum of 600 TeV or higher. This range is marked with the gray shaded area in Figure 7.5, and implies values of $\eta > 0.1$.

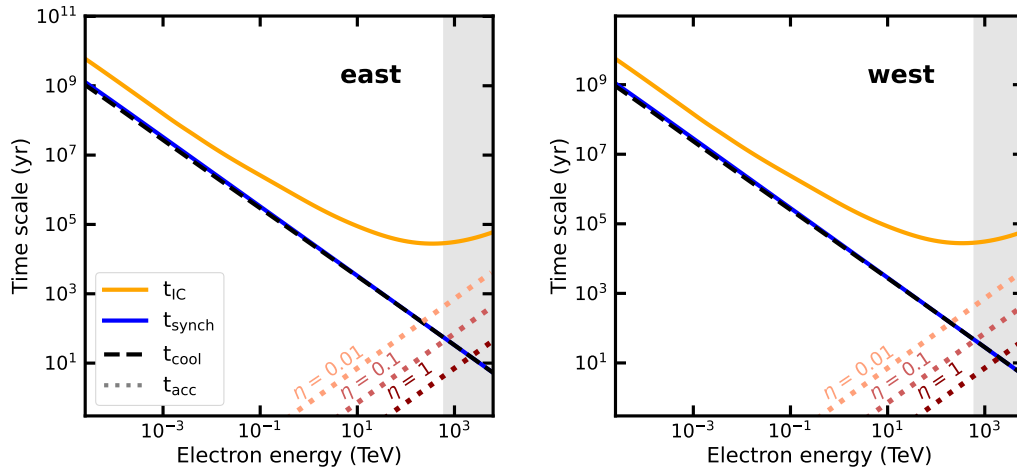


FIGURE 7.5: **Cooling and acceleration timescales.** Cooling timescale as a function of electron energy for due to IC (yellow), synchrotron (blue) and total (black dashed) for the eastern (left) and western (right) jets. Dotted lines display the acceleration timescales for different values of η . The electron energy range allowed by the data for the cutoff energy of the electron spectrum is indicated with a gray band.

From Electron Energies to Gamma-Ray Energies

We can determine which electron energies contribute to the three different energy ranges considered in Figures 6.7 and 6.12 given the dominant radiative losses. This is shown in Figure 7.6. As can be seen in the figure, photons above 10 TeV are produced in the most part by electrons with energies above 50 TeV. These electrons will cool on timescales of around 400 yr. From the energy-dependent morphology revealed by the TeV emission, we can infer that these electrons do not make it further than ~ 15 pc from the acceleration site. That places a back-of-the-envelope upper limit on the jet flow of around $0.1c$. Similarly, the fact that lower-energy electrons were carried by the jet flow before they had time to radiate the bulk of their energy away and produce photons in the 2.5-10 TeV range, can be used to place a lower limit on the jet velocity. We can combine these constraints by fitting the result from the model to the TeV data in order to obtain a measurement of the jet velocity at the base of the outer jets.

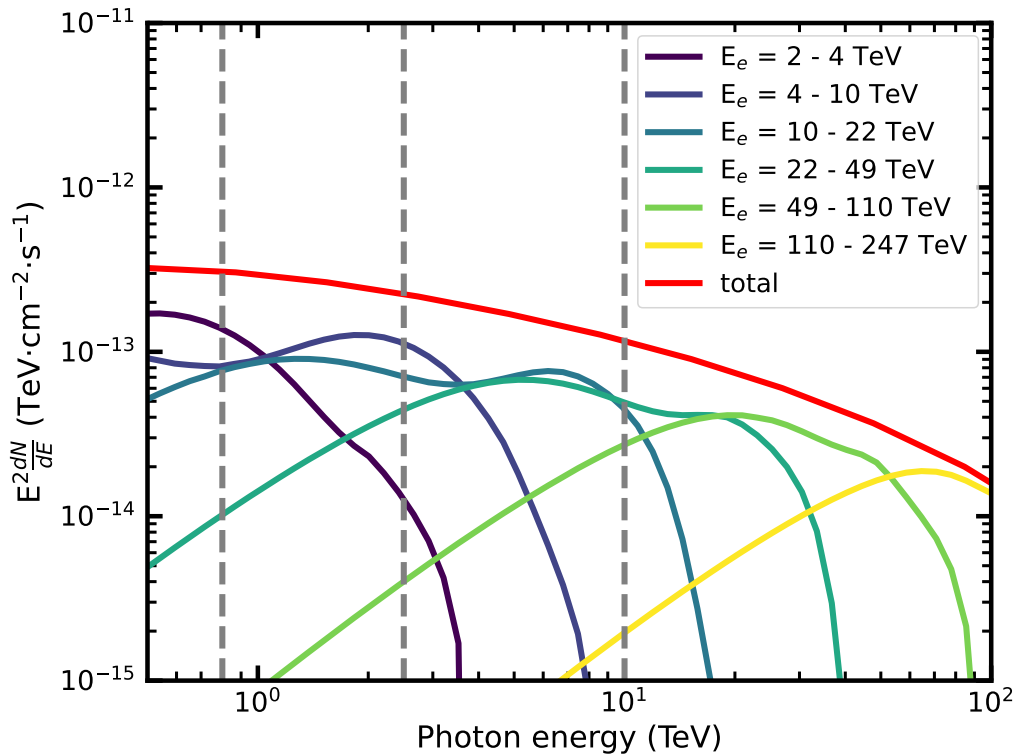


FIGURE 7.6: **Electron energy contributions.** Contribution of different electron energy ranges to the total predicted gamma-ray flux by the model. The three gamma-ray energy bands are marked with gray dashed lines.

In this application, the coordinate z corresponds to the distance from the base of the outer jets, located at around 25 pc from the core in each side. The jet base, so $z = 0$, will also be the site where particles are injected in each time-step, as motivated in Section 7.1.

7.6 Revealing the Jet Dynamics

From long baseline radio observations (Goodall et al., 2011b; Sakemi et al., 2021), it is known that the jets have decelerated significantly by the time they reach the edge of the W50 shell. However, details on how this deceleration happens are largely unclear. The H.E.S.S. results can be used to shed light on the jet dynamics, using the relative positions of the gamma-ray excesses at different energies.

We parameterize the velocity in the outer jets as $v_{\text{jet}}(z) = v_0 \cdot \Lambda(z)$, where v_0 is the velocity at their base. The factor $\Lambda(z)$ represents the shape of the velocity profile along the jet axis. We compare two different scenarios:

- **Constant velocity:** The flow of the jet has constant velocity along the z direction, so $\Lambda(z)=1$. Note that this scenario is difficult to reconcile with the observed opening angle of the jet in the X-ray images. In this case, adiabatic losses need to be included in the model due to the change in jet density as it expands. This is done by adding an adiabatic cooling term (see Equation 1.44)

to the model described in Section 7.5. The cooling timescale is now a function of the position in the z direction, with particles cooling faster near the base of the jets than further out. Figure 7.7 shows the cooling and acceleration times at two z locations along the eastern jet including adiabatic losses for different values of the jet velocity. Note that $z = 0$ pc corresponds to the base of the outer jets, located approximately 25 pc away from the jet launch site.

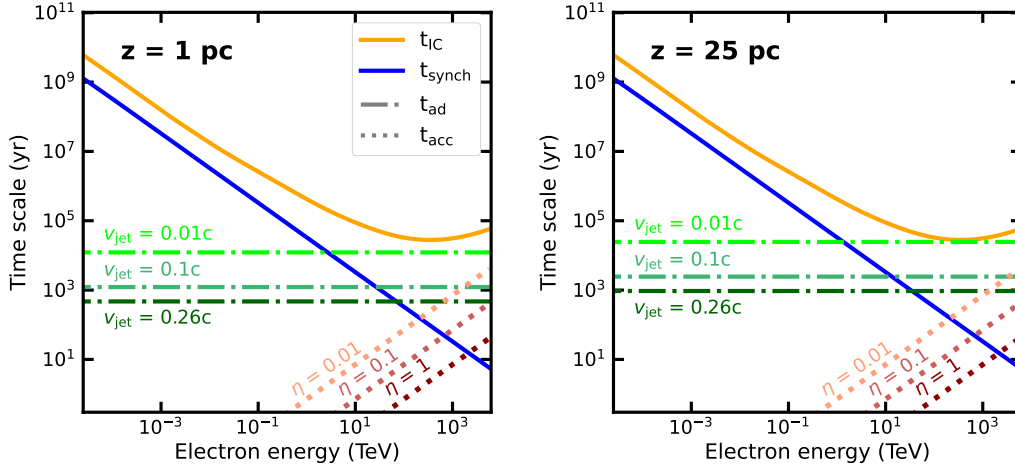


FIGURE 7.7: **Cooling and acceleration times including adiabatic losses.** The lines represent the same quantities as in Figure 7.7 for the eastern case with the addition of the adiabatic loss timescale for different values of the jet velocity. The left panel corresponds to a location 1 pc away from the base of the outer jets, whereas the right panel shows the timescales for a location further out, a total of ~ 50 pc from the central binary system.

- Smooth deceleration:** We use the only publicly available X-ray image of both jets by the ROSAT satellite (Brinkmann et al., 1996; Safi-Harb and Ögelman, 1997) and the fact that the opening angle of a jet is inversely proportional to its Mach number $M = v_{jet}/c_s$. We assume the jet axis to be perpendicular to the line of sight, not far from the true angle $\phi \approx 80^\circ$ (Roberts et al., 2010). The opening angle of the jet can then be estimated as a function of distance to its base in an axis that joins both jets via the central binary. We then take the inverse square to motivate the shape of the velocity profile $\Lambda(z)$. The resulting velocity profile is shown in Figure 7.8, smoothed with the H.E.S.S. PSF. Variations of this profile on scales smaller than the H.E.S.S. resolution will not affect the result. Note that the eastern and western jets are expanding into slightly different ambient conditions, as the Galactic plane lies a few degrees away from the western jet. This is usually invoked to explain the different jet length from each side, as well as the faster deceleration on the western side (e.g. Goodall et al., 2011a). This deceleration profile assumes that the density of the jet remains constant, which means that there are no adiabatic losses (see Equation 1.41). This assumption is consistent with the presence of a shock at the base of the outer jets, as the post-shock flow would then be incompressible.

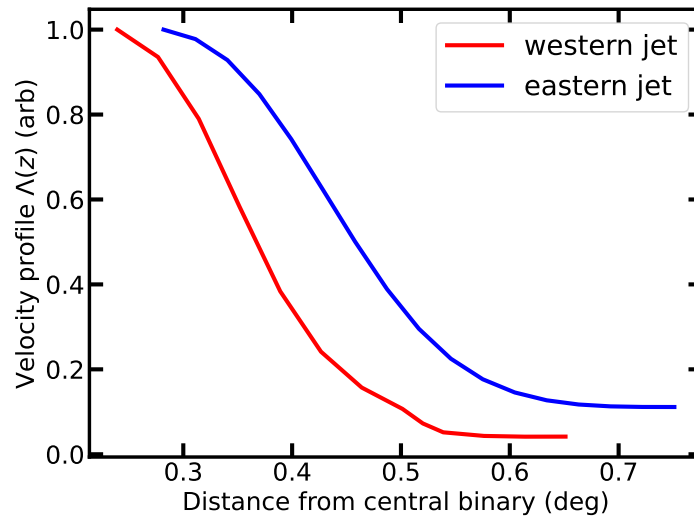


FIGURE 7.8: **Deceleration profiles.** Shape of the deceleration profile $\Lambda(z)$ derived as described in the text for the western (red line) and eastern (blue line) jets.

With the framework and parameters described above, the only two remaining quantities that need to be determined are the values of the velocity at the base of the outer jets, v_0 and the diffusion coefficient D_{100} . We assume both values to be the same for both of the jets. We fit the prediction of the model to the gamma-ray profiles shown in Figure 6.12 for both values of $\Lambda(z)$ using a maximum likelihood approach.

7.6.1 Favoring Deceleration

The likelihood profiles for the v_0 parameter for the constant velocity case and the case assuming deceleration are shown in Figure 7.9. As can be seen, the deceleration is weakly preferred by the data, with a difference of TS of around 4. However, note that the best-fit velocity resulting in the case where the velocity is kept constant of $v_0 = 0.045 \pm 0.01c$ is twice the value of the upper limit set by the long baseline radio observations of $0.023c$ (Goodall et al., 2011b; Sakemi et al., 2021). This means that the jets would need to decelerate rather abruptly in the region where no gamma-ray emission is detected.

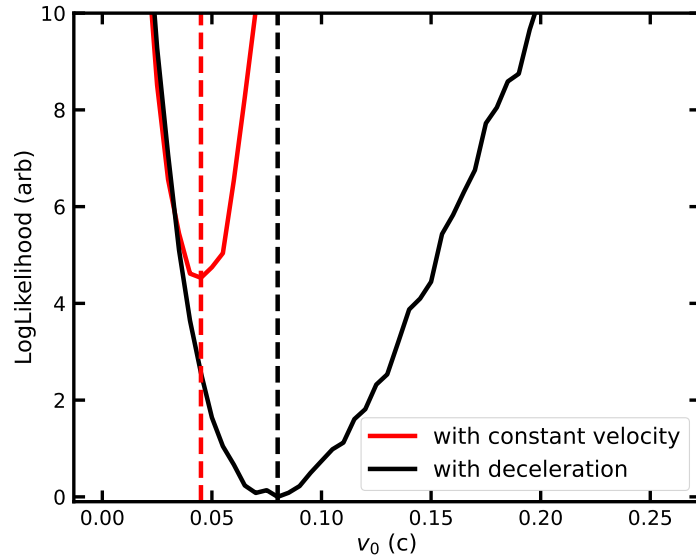


FIGURE 7.9: **Likelihood profiles of the velocity fit.** Resulting likelihood profiles from the fit assuming a constant velocity profile (red) and the deceleration profile shown in Figure 7.8. The value of v_0 at which the curve has its minimum is the preferred one. The width of the parabola reflects the statistical uncertainty on this value.

Given that it is weakly preferred by the data and it presents a more physical picture, we favor the scenario in which the jets decelerate smoothly. Note that this is naturally connected to the observed increase of the spread in the X-ray images of the jets.

7.6.2 Estimate of the Jet Velocity Assuming Deceleration

Setting $\Lambda(z)$ to the profiles shown in Figure 7.8, we find the best values for the velocity at the base of the jets and the diffusion coefficient. The best-fit value of the diffusion coefficient is $D_{100} = (2.3 \pm 1.4) \cdot 10^{28} \text{ cm}^2 \text{ s}^{-1}$. This is around an order of magnitude lower than the average Galactic diffusion coefficient (Strong et al., 2007), and an order of magnitude higher than the diffusion coefficient measured by the HAWC observatory around Galactic pulsars (Abeysekara et al., 2017). That the diffusion coefficient is smaller than the Galactic average is justified, since the magnetic field is stronger than the Galactic average and the jet is turbulent.

For a magnetic field $B = 20 \mu\text{G}$, the value of the Bohm diffusion coefficient at 100 TeV is $D_B = 1.7 \cdot 10^{26} \text{ cm}^2 \text{ s}^{-1}$ (see Equation 1.22). The best-fit value for the diffusion coefficient is thus found to be around a hundred times larger than the Bohm diffusion coefficient, meaning $\eta > 0.01$. This lower bound on η is compatible with the one found by comparing the cutoff electron energy with the intersection of the cooling and acceleration timescales (see Section 7.5.2, in particular Figure 7.5).

The best-fit value of the velocity is found to be $v_0 = 0.08 \pm 0.03_{\text{stat}} \pm 0.01_{\text{syst}} c$. The systematic errors are derived from the choice of parameters for the injected electron spectrum (see Section 7.6.3). The spatial profiles resulting from these parameters are shown in Figure 7.10, together with the TeV data presented in Section 6.6.3.

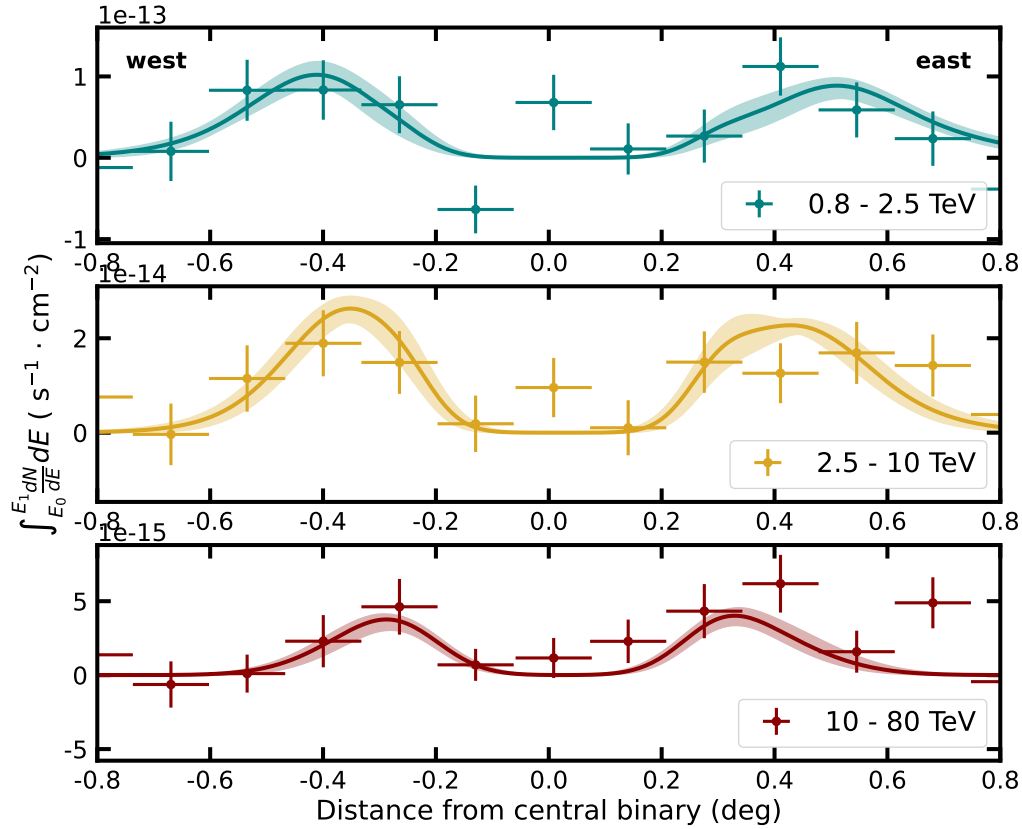


FIGURE 7.10: **Gamma-ray profiles along the jet including the best-fit model prediction.** The data points represent the measured flux in spatial bins alongside the axis joining both jets through the central binary for three different energy bands. The lines correspond to the prediction of the 1D Monte Carlo model for the best fit values of the starting velocity, diffusion coefficient and injected electron spectrum parameters. The shaded areas represent the combined statistical error of all the best-fit parameters.

The inferred velocity at the base of the outer jets is a fraction $v_{\text{jet}}/v_0 = 0.31 \pm 0.12_{\text{stat}} \pm 0.04_{\text{syst}}$ of the value of the jet velocity at launch. This value is compatible with the post-shock conditions of a mildly sub-relativistic shock (e.g. Landau and Lifshitz, 1987; Kirk and Duffy, 1999). This finding supports the picture in which a shock located at the base of the outer jets is responsible for the highly energetic electrons via relatively efficient ($\eta > 0.1$) particle acceleration. This shock scenario is also supported by the spatial coincidence between the position of the highest energy gamma-ray emission and the location of the recently reported sharp X-ray transitions (Safi-Harb et al., 2022; Kayama et al., 2022).

7.6.3 Impact of the Injected Spectrum on the Jet Velocity.

To assess the impact on the value of v_0 of the choice of injected electron spectrum parameters and magnetic field, we define a 2D grid with the values of Γ_e and $\log_{10}(E_{c,e})$ in steps of 0.05 for both parameters. Fixing the value of those parameters, we fit the remaining free parameters (magnetic field and normalization) to the multi-wavelength data shown in Figure 7.3. We select all the models defined by the interior of the 2σ likelihood surface in the Γ_e and $\log_{10}(E_{c,e})$ space. For each of these models, we find the best-fit value of v_0 by fitting the gamma-ray profiles shown in Figure 7.10 with the value diffusion coefficient fixed to the best-fit value. The left panel of Figure 7.11 shows the likelihood profiles for each of these models, with the overall best-fit model highlighted in red. Note that, unlike in the case of the best-fit model shown in Figure 7.3, the fit here is only performed to the H.E.S.S. data. That is why the overall best fit model is not the one that minimizes the likelihood. However, the overall best-fit model lies within 1σ of the actual minimum. The right panel of Figure 7.11 shows the distribution of the best-fit value of v_0 for the considered models. As can be seen, the statistical uncertainty band is wide enough to contain all the possible values of the velocity derived with different parameters.

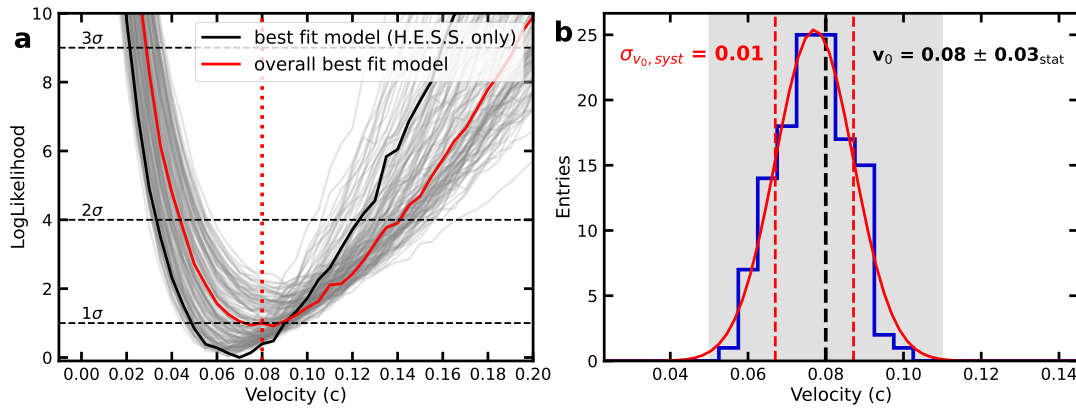


FIGURE 7.11: **Systematic uncertainties on the velocity estimation.**

a: Likelihood profiles of the velocity parameter for each of the considered combination of magnetic field and electron spectral parameters. The red solid line shows the overall best-fit model resulting from the fit to multi-wavelength data, whereas the black solid line shows the best-fit model when only H.E.S.S. data is considered. **b:** Distribution of the best-fit value of v_0 for all the considered values of magnetic field and electron spectral parameters. The black dashed line and grey band denote the best-fit value and statistical uncertainty of the velocity for the model selected using multi-wavelength data, also specified in the top right corner. The red line shows the fit of a Gaussian to the histogram, where the fitted width is indicated in the top left corner.

7.7 Summary and Outlook

This chapter presents an interpretation of the results presented in Chapter 6 by putting the TeV view of the system into the larger context of the non-thermal emission from the jets of SS 433 and their dynamics. The main conclusions are summarized below:

- **Identification of the acceleration sites.** In order to explain the observed energy-dependent morphology, the bulk of particle acceleration must be taking place at the base of the outer jets and not in the X-ray knots as previously thought (see Section 2.4.2).
- **Most of emission is of leptonic origin.** The absence of dense target material at the acceleration sites (see Section 2.3.3) and the observed energy morphology indicate that the bulk of the gamma-ray emission is produced by high energy electrons.
- **Absence of cutoff in the electron spectrum.** No statistically significant cutoff is found in the electron spectrum, with an upper bound placed at 600 TeV. In order to reach these energies, the acceleration needs to be relatively efficient ($\eta > 0.1$, see Equation 1.19). That the jets of SS 433 form a shock that accelerates particles with high efficiencies has far-reaching implications for extra-galactic jets such as those of radio galaxies, which are considered potential sources of the most energetic cosmic rays in the Universe.
- **Estimate of the magnetic field in the jets.** The value of the average magnetic field in the western and eastern jet is found to be 21 and 19 μG respectively, in accordance with previously derived values using only X-ray data. This relatively high value results in the main channel of energy loss being synchrotron radiation.
- **Weak preference for decelerating flow.** The presence of deceleration in the section of the jet that is a gamma-ray source is weakly preferred by the data. This is also supported by the observed spread of the jets and the fact that the resulting best-fit velocity assuming constant velocity is a factor of 2 higher than the upper limit set by long-baseline radio observations.
- **Estimate of the jet velocity.** Assuming a deceleration profile motivated by the observed lateral spread of the jets, we are able to estimate the velocity at the base of the outer jets to be $v_0 = 0.08 \pm 0.03_{\text{stat}} \pm 0.01_{\text{syst}} c$.
- **Evidence for shock acceleration.** The ratio between the jet velocity at launch of $0.26c$ and the estimate of the jet velocity at the base of the outer jets is consistent with a mildly sub-relativistic shock with compression ratio $0.31 \pm 0.12_{\text{stat}} \pm 0.04_{\text{syst}}$ located at the base of the outer jets. The discovery of a sharp discontinuity at that location via recent X-ray observations supports this picture. Note

that this shock would need to be quasi-stationary and not have moved much in the lifetime of the TeV-emitting electrons.

- **Similarities between the jets.** We find that the properties of the non-thermal emission from the jets of SS 433 can be described in a fully consistent way between the eastern and western jets by only taking into account the faster deceleration on the western side due to the vicinity of the Galactic plane, which results in a shorter jet on the western side. Even when the parameters of each jet are allowed to differ, the resulting values are consistent with one another, such as the values of the magnetic field.
- **Constraints on the age of the system.** The electrons responsible for the observed TeV emission need to be older than 1,000 years and younger than around 30,000. This places limits on the age of the system as well, and allow us to conclude that even if hadronic particles are being accelerated in the jets of SS 433, they would diffuse towards Earth too slowly to significantly contribute to the cosmic ray flux.

These results resolve some of the longstanding issues of the SS 433 jets but also create new questions. The surface located at ~ 25 pc from the core has been identified as the location of particle acceleration to very high energies, yet the reasons why that location is of special physical significance are not understood. Dedicated simulations of the jets of SS 433 and their interaction with the ambient medium that include not only the shell of W50 but perhaps a third phase due to e.g. a bubble created by the equatorial wind (see e.g. Konigl, 1983) might be able to shed light on this issue. Deep X-ray observations using an instrument with a wide FoV and high spatial resolution, such as the eROSITA satellite (Predehl et al., 2021), might be able to even image this bubble, were it to exist. Additionally, observations that extend the gamma-ray spectra of the jets to higher energies, such as those that will be probed by the CTA or the SWGO, would be able to further constrain the maximum energy at which particles are accelerated in the system, which has implications for the acceleration of cosmic rays in radio galaxies.

Chapter 8

Joint Analysis of SS 433 using H.E.S.S. and HAWC Data

The jets of SS 433 were first identified as sources of TeV gamma-rays by the HAWC observatory (henceforth referred to simply as HAWC) in 2018 (Abeysekara et al., 2018), as mentioned in Section 2.3.6. Because HAWC continuously surveys a large fraction of the sky (see Section 3.4.1), the amount of observation time of the SS 433 region by HAWC has almost doubled since its discovery. This chapter presents an updated analysis of the HAWC data of this region using the framework described and validated in Chapter 5, as well as a joint analysis of this and the H.E.S.S. data presented in Chapter 6. Note that this is the first joint analysis using H.E.S.S. and HAWC data besides the proof of concept shown in Chapter 5. This is made possible by the existence of a common data format and analysis tool. The results shown in this chapter are preliminary and will require further checks, including, most importantly, a careful determination of the systematic uncertainties.

8.1 Revisiting SS 433 with HAWC

The data presented here were taken between June 2015 and January 2021 and include, after data quality cuts (see Chapter 5), a total of 1894 transits of the SS 433 region across the sky above HAWC. For reference, the data used in the analysis that claimed the detection of SS 433 (see Section 2.3.6) included 1017 transits, ranging between November 2014 and December 2017. The reason why the current data selection starts at a later point in time is that this analysis makes use of the energy estimation techniques described in Section 3.4.1 and in Abeysekara et al., 2019. These algorithms are only validated for the time period starting when the array was fully built, which was in June 2015.

The use of the data set that has been reconstructed with an algorithm that includes energy estimation has the advantage that energies are measured on an event-by-event basis, which results in better energy resolution. In exchange, the data quality and background rejection cuts are slightly harder, leading to a reduced exposure when selecting the same time interval. In the analysis presented in this chapter, the *neural network* (NN) (see Abeysekara et al., 2019) energy estimator is used.

Another difference with respect to the already published analysis of the SS 433 region is that the pipeline employed to reconstruct the data has improved significantly since (Yun Carcamo et al., 2022), an upgrade that is referred to as *Pass 5*. This includes improvements to the energy reconstruction, the direction reconstruction and the background rejection. For these reasons, it is worth revisiting the SS 433 region using this expanded and improved data set.

8.1.1 Data Reduction

The data reduction, background modeling and high level analysis are carried out using *Gammapy* as described in Section 3.5 and extensively in Chapter 5. The whole-sky reconstructed data are stored in event lists (see Section 4 of Chapter 5), which are also used to build a background model (see Section 5 of Chapter 5). Events in a square of 6° by 6° centered on the position of SS 433 are selected and binned into a WCS sky-map with square spatial bins of 0.02° width. The energy axis has 12 logarithmically-spaced bins between 0.316 TeV and 316 TeV defined in Table 3.3.

Because of the relatively poor angular resolution and background rejection in the low f_{Hit} bins (see Table 3.2), the analysis presented here is restricted to f_{Hit} bins 3 and above as defined in the table, that is, only events that trigger more than $\sim 16\%$ of the array. Note that in the *Pass 5* reconstruction the f_{Hit} bin nomenclature has changed due to the addition of a new bin for events triggering less than 6% of the array, which shifts the identifiers by one. However, for consistency with Chapter 5, which used the *Pass 4* reconstruction, we will keep the old nomenclature and refer to Table 3.2 for clear definitions of the bin edges.

The product of the data reduction is, analogously to the H.E.S.S. analysis described in Chapter 6, a *Gammapy* MapDataset¹ that bundles the measured counts, expected background and IRFs. The main difference with respect to that analysis is that in this case, there is one such data set per f_{Hit} bin, that is, a total of seven.

These f_{Hit} data sets are independent and need to be fit jointly when constructing significance maps or performing the spectro-morphological (or "3D", see Section 3.5.5) analysis. All the significance maps shown in this chapter were derived with a model assumption (see Section 3.5.2), which is the combination of a point-source spatial model (see Equation 3.17) and a power-law spectral model (see Equation 3.14) with an index of 2.

8.1.2 Modeling MGRO J1908+06

As mentioned in Section 6.3, the nearby bright extended source MGRO J1908+06 needs to be carefully modeled in order to disentangle its contribution to the region of the jets of SS 433. For the first iteration, MGRO J1908+06 is modeled in the same

¹<https://docs.gammapy.org/1.0/api/gammapy.datasets.MapDataset.html#gammapy.datasets.MapDataset>

way as it was done in Section 6.3, assuming a Gaussian spatial shape and a log-parabola spectral distribution. However, as can be seen in Figure 8.1, the Gaussian spatial shape doesn't describe the morphology of the emission sufficiently well in this case. For this reason, we assume instead a generalized Gaussian function (i.e. Equation 3.18 with χ not fixed to 0.5) for the spatial distribution and repeat the fit. The result is shown in Figure 8.2. As can be seen, the description of the MGRO J1908+06 region has improved.

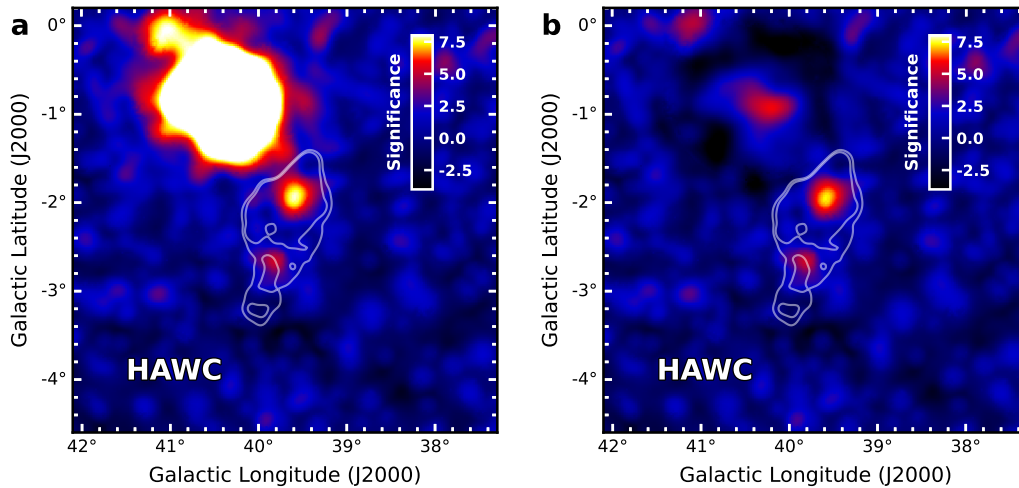


FIGURE 8.1: **Significance map before and after modeling and subtracting MGRO J1908+06 using HAWC data and a Gaussian spatial model.** The figure shows the statistical significance of the gamma-ray excess measured in the full FoV before (a) and after (b) fitting and subtracting the emission from the nearby source MGRO J1908+06 assuming a Gaussian spatial model. The solid white contours show the radio emission from the surrounding nebula W50 measured by the Effelsberg telescope (Reich et al., 1984, 1990; Furst et al., 1990).

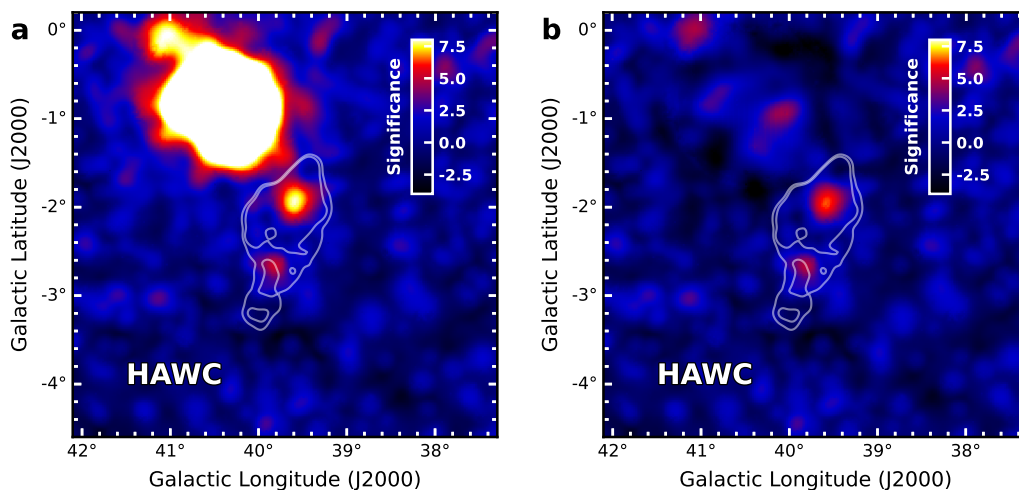


FIGURE 8.2: **Significance map before and after modeling and subtracting MGRO J1908+06 using HAWC data and a generalized Gaussian spatial model.** The figure shows the same quantities as Figure 8.1 but when modeling the spatial properties of MGRO J1908+06 using a generalized Gaussian model.

	ϕ_0 ($10^{-13} \text{ TeV}^{-1} \text{ cm}^{-2} \text{ s}^{-1}$)	Γ	β	
spectral	$2.17 \pm 0.07_{\text{stat.}}$	$2.29 \pm 0.02_{\text{stat.}}$	$0.15 \pm 0.01_{\text{stat.}}$	
	l (deg)	b (deg)	r_0 (deg)	χ
spatial	$40.40 \pm 0.02_{\text{stat.}}$	$-0.82 \pm 0.02_{\text{stat.}}$	$0.42 \pm 0.01_{\text{stat.}}$	$0.94 \pm 0.01_{\text{stat.}}$

TABLE 8.1: **Results of the spectro-morphological fit to MGRO J1908+06 using HAWC data.** Best-fitting photon spectral and spatial parameters from the fit to the HAWC data. ϕ_0 is the amplitude at the reference energy $E_0 = 7 \text{ TeV}$. Γ is the spectral index and β the curvature parameter (see Equation 3.16). The best-fit position in Galactic coordinates are given by l and b . r_0 and χ are the shape parameters of the generalized Gaussian (see Equation 3.18).

The parameters of the resulting best fit model can be found in Table 8.1. Note that the errors quoted are statistical only.

8.1.3 The SS 433 Region

The HAWC observations reveal two gamma-ray excesses structures consistent with the X-ray emission of the outer jets, as can be seen in Figure 8.3. The jets are detected with a statistical significance of 4.8σ and 6.5σ for the eastern and western sides respectively. The significance peaks around the location of the $w1$ and $e1$ regions.

This is consistent with the results reported in Abeysekara et al., 2018 (see Figure 2.12) for the western jet. However, the eastern excess has changed significantly with respect to the previous result. The significance has decreased, which can be explained in part by the differences between the data set used for the 2018 result and the one used here, but also the peak of the significance seems to have shifted away from the $e2$ region and closer to $e1$. This could be due to multiple possible factors, including statistical fluctuations or the combination of the energy-dependent morphology observed with the H.E.S.S. data set (see Section 6.6) and the different sensitivity as a function of energy of the analysis presented here with respect to the one from Abeysekara et al., 2018. A detailed comparison of the sensitivity of both analyses is thus needed to verify that the results are consistent with one another, which will be carried out as future work.

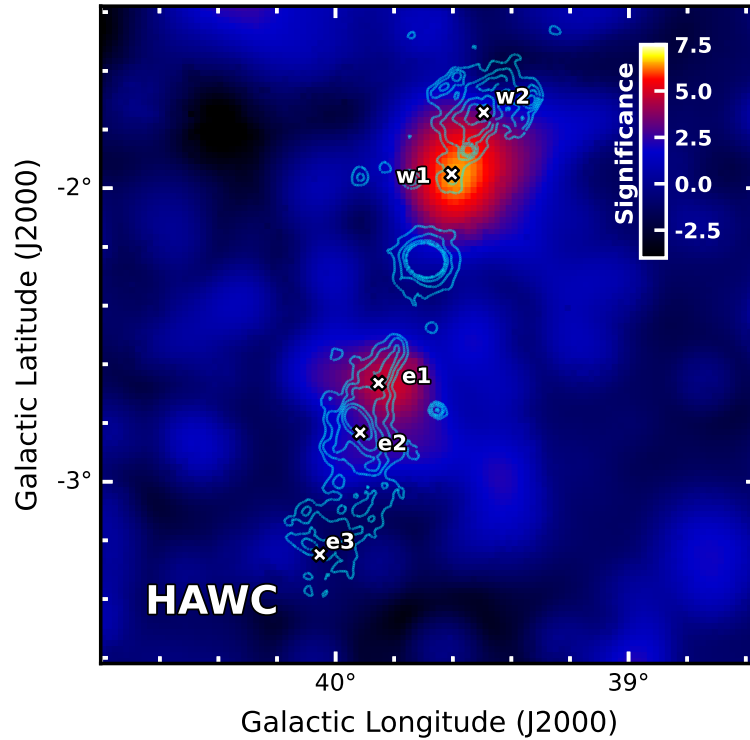


FIGURE 8.3: **Significance map of the SS 433 region using HAWC data.** The figure shows the statistical significance of the gamma-ray excess measured in the SS 433 region after the fitting and subtraction of the emission from the nearby extended source MGRO J1908+06. The solid cyan contours show the X-ray emission measured by the ROSAT satellite (Brinkmann et al., 1996; Safi-Harb and Ögelman, 1997). The locations of the X-ray regions $w1$, $w2$, $e1$, $e2$ and $e3$ are marked with white crosses.

We model the emission of the jets using two components with a combined point-source spatial model and a power-law spectral model. The best-fit spatial model and the residual significance after subtracting it can be seen in Figure 8.4. Given the angular resolution of HAWC, a simple point-like spatial model describes the data sufficiently well. The best fit positions for the eastern and western components are given in Table 8.2, together with the best-fit spectral parameters.

The presence of a cutoff in the spectrum (see Equation 3.15) is weakly favored by the data compared to the power-law assumption by 2.8σ and 1.9σ for the eastern and western jets respectively. A curved shape for the spectrum was also tested (see Equation 3.16), which is also weakly favored by the data compared to the power-law assumption by 2.5σ and 1.8σ for the eastern and western jets respectively. Given that none of these values reach the 3σ threshold, we keep the power-law description for simplicity.

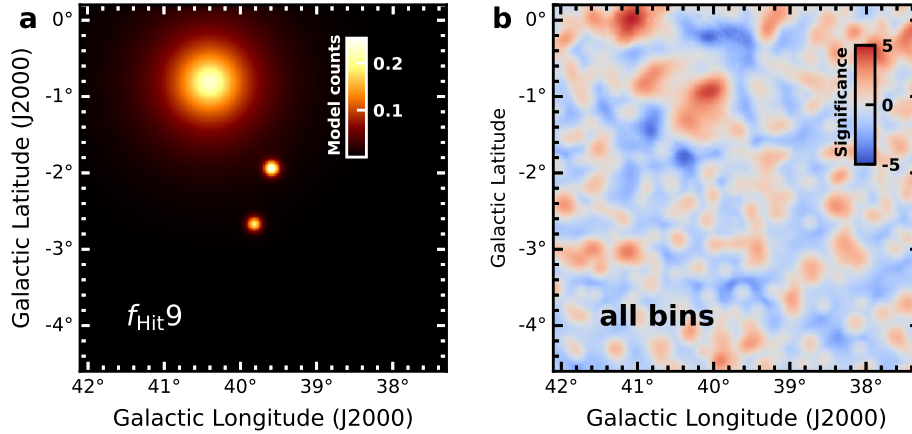


FIGURE 8.4: **Model and residual of the jets using HAWC data.** The figure shows the predicted counts in the highest f_{Hit} bin from the best-fit model that includes the MGRO J1908+06 component and the jets (a) as well as the significance map of the entire data set after subtracting these two components (b).

The resulting best-fit spectral models and flux points are shown in Figure 8.5 for both jets. Note that the measured flux at 20 TeV is in agreement with the previous value reported in Abeysekara et al., 2018. As it was the case for the H.E.S.S. view of the jets, spectral properties of the eastern and western jet are remarkably consistent with one another.

	l (deg)	b (deg)	ϕ_0 ($10^{-15} \text{ TeV}^{-1} \cdot \text{cm}^{-2} \cdot \text{s}^{-1}$)	E_0 (TeV)	Γ
east	$39.82 \pm 0.03_{\text{stat.}}$	$-2.67 \pm 0.03_{\text{stat.}}$	$3.72 \pm 0.43_{\text{stat.}}$	7	$2.51 \pm 0.07_{\text{stat.}}$
west	$39.59 \pm 0.03_{\text{stat.}}$	$-1.94 \pm 0.03_{\text{stat.}}$	$4.57 \pm 0.86_{\text{stat.}}$	7	$2.48 \pm 0.09_{\text{stat.}}$

TABLE 8.2: **Results of the spectro-morphological fits to the spectra of the jets using HAWC data.** The best-fit positions for the point-source models are given in Galactic coordinates (l, b). E_0 is the reference energy for the best-fit power-law, ϕ_0 is the amplitude at E_0 and Γ is the index.

The lowest energy bin at which a flux point is measured starts at 10 TeV for the eastern jet and ~ 6 TeV for the western jet. This means that most of the emission seen by HAWC is from energies above these values. Because of this, the fact that most of the emission in Figure 8.3 is observed to come from the locations *e1* and *w1* at the base of the jets is consistent with the picture of the energy-dependent locations revealed by the H.E.S.S. data (see Figure 6.7).

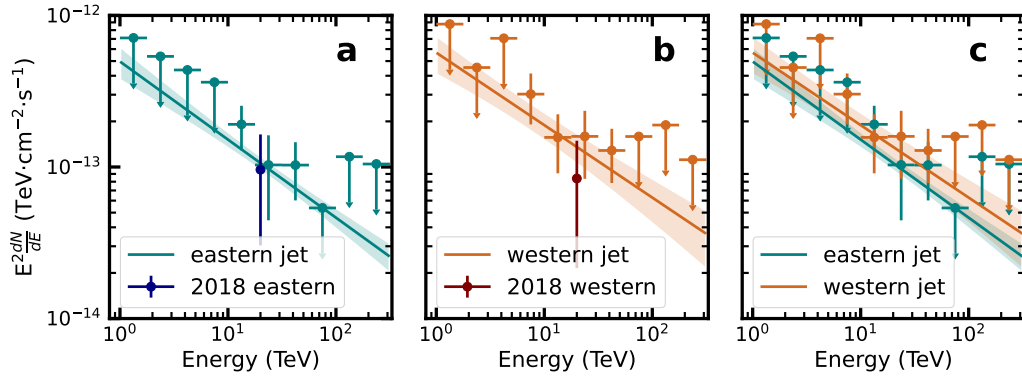


FIGURE 8.5: **HAWC spectra of the jets.** Best-fit spectral model from the 3D modeling of the eastern (a) and western (b) jets. The shaded areas and flux points include only statistical uncertainties. The previously measured flux is shown as well (Abeysekara et al., 2018). The spectra from both jets is shown in panel c for easy comparison.

Comparison with the H.E.S.S. Analysis

Figure 8.6 compares the spectra of the jets measured with HAWC to what was measured using H.E.S.S. data (see Figure 6.13). For the eastern jet, the best-fit index of the power-law differs significantly (see also Tables 8.4 and 8.2). This is likely heavily influenced by the very constraining upper limit at around 100 TeV. Further checks are needed in order to verify that the limit placed in that energy range is a robust estimate, given its difference with respect to the limit at that energy range in the western side. However, note that the flux points and upper limits of both jets are in remarkable agreement, especially taking into account that the HAWC results do not include systematic errors.

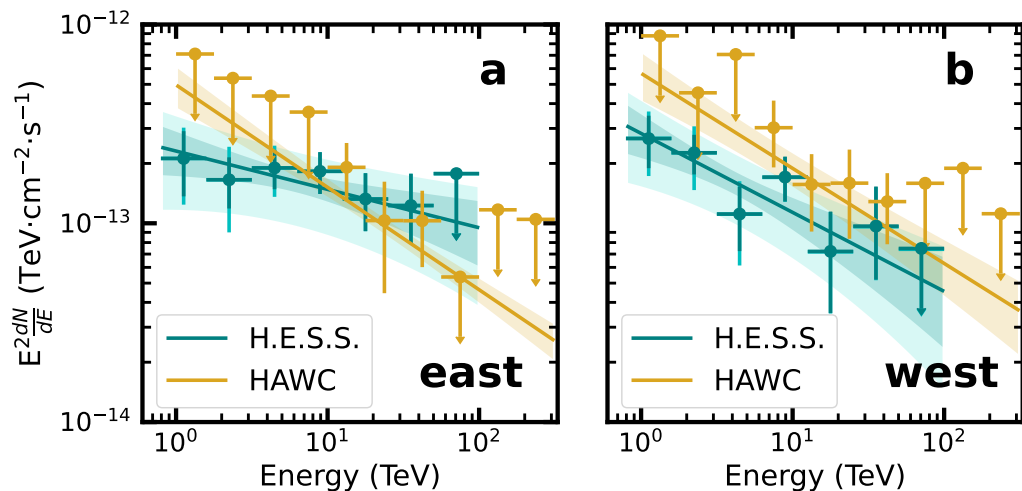


FIGURE 8.6: **H.E.S.S. and HAWC spectra of the jets.** Resulting best-fit spectral model from the 3D modeling of the eastern (a) and western (b) jets. Note that only the H.E.S.S. result includes systematic errors, shown with a lighter color band.

8.2 Joint Analysis using H.E.S.S. and HAWC Data

The existence of the analysis framework developed and presented in Chapter 5 enables the exporting of data from the HAWC observatory to the standard format, which can then be analyzed using *Gammapy*, as shown in the section above. At this stage, performing a joint fit with data from another gamma-ray instrument which also has been exported to the right format becomes a trivial task (see Section 8 of Chapter 5). Such a joint analysis, using the H.E.S.S. data introduced in Chapter 6 and the HAWC data described above, is presented in this section. Note that the results of this analysis are preliminary, and further studies are needed, in particular a careful estimate of systematic uncertainties. Despite this caveat, the results presented here, which constitute the first joint H.E.S.S. and HAWC analysis, are still of relevance, as they highlight the importance of the synergy between wide-field detectors and IACTs and the power of the existence of a shared data format and tools.

The reduction of the H.E.S.S. data used in this section was carried out exactly as described in Section 6.2, with the only difference that the spatial binning of the maps has been downsampled to square spatial bins of 0.02° width to match the HAWC data sets and the energy bins have been modified to be aligned with the HAWC energy bins (see Table 3.3).

8.2.1 Modeling MGRO J1908+06

We model MGRO J1908+06 assuming a generalized Gaussian spatial shape and a log-parabola spectral distribution. This model is fit jointly to both the H.E.S.S. data set and each of the HAWC data sets, each corresponding to one f_{Hit} bin. The resulting best-fit parameters are presented in Table 8.3. Note that the errors quoted are only statistical.

As in the previous section, we compute significance maps before and after subtracting the MGRO J1908+06 component in order to visually assess the quality of the fit. This is shown in Figure 8.7, which shows the significance map of the entire FoV. Even after subtracting the MGRO J1908+06 model, the outer jets of SS 433 are clearly detected.

Note that the MGRO J1908+06 region is still not perfectly modeled, with an excess of around 6σ remaining after subtracting the best-fit model. This means that the relatively simple spatial description used is not enough to characterize the emission of MGRO J1908+06 in the joint data set. Nevertheless, this excess is spatially distant from the jets and relatively weak, so for the remaining of this chapter, we neglect its contribution to the SS 433 region.

	ϕ_0 ($10^{-13} \text{ TeV}^{-1} \cdot \text{cm}^{-2} \cdot \text{s}^{-1}$)	Γ	β	
spectral	$1.97 \pm 0.06_{\text{stat.}}$	$2.37 \pm 0.02_{\text{stat.}}$	$0.95 \pm 0.01_{\text{stat.}}$	
	l (deg)	b (deg)	r_0 (deg)	χ
spatial	$40.44 \pm 0.01_{\text{stat.}}$	$-0.77 \pm 0.01_{\text{stat.}}$	$0.47 \pm 0.01_{\text{stat.}}$	$0.99 \pm 0.01_{\text{stat.}}$

TABLE 8.3: **Results of the spectro-morphological fit to MGRO J1908+06 using H.E.S.S. and HAWC data.** Best-fit photon spectral and spatial parameters from the joint fit to the H.E.S.S. and HAWC data. Quantities are equivalent to those shown in Table 8.1.

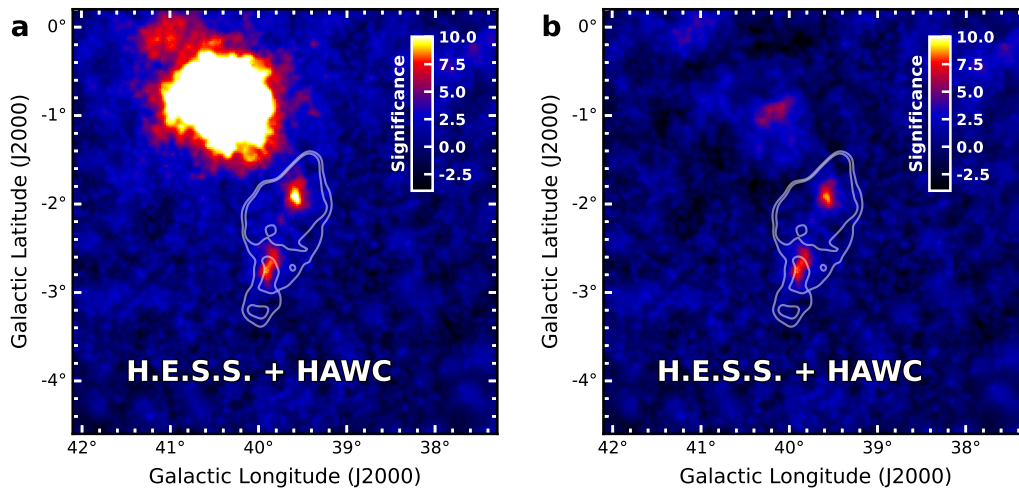


FIGURE 8.7: **Significance map before and after modeling and subtracting MGRO J1908+06 using H.E.S.S. and HAWC data.** The figure shows the same quantities as Figure 8.2 but for the joint analysis of H.E.S.S. and HAWC data.

8.2.2 The SS 433 Region

The joint analysis reveals two gamma-ray excesses structures consistent with the X-ray emission of the outer jets, as can be seen in Figure 8.8. The jets are detected with a statistical significance of 8.8σ and 8.3σ for the eastern and western sides respectively. The significance peaks around the location of the *w1* in the western side and between the *e1* and *e2* regions for the eastern side. This is consistent with what was observed in the separate analyses shown in Figures 6.5 and 8.3.

A detailed study of the relative contributions of each data set to the different energy ranges of the joint fit is needed in order to make a detailed interpretation of the morphology of the emission shown in the figure. However, given that the HAWC emission seemed to arise closer to the base of each jet (see Figure 8.3), and that the HAWC data set is most sensitive to energies above ~ 10 TeV (see Figure 8.5), the map shown in Figure 8.8 follows what would be expected given the H.E.S.S. result and the energy-dependent morphology found in the H.E.S.S. analysis.

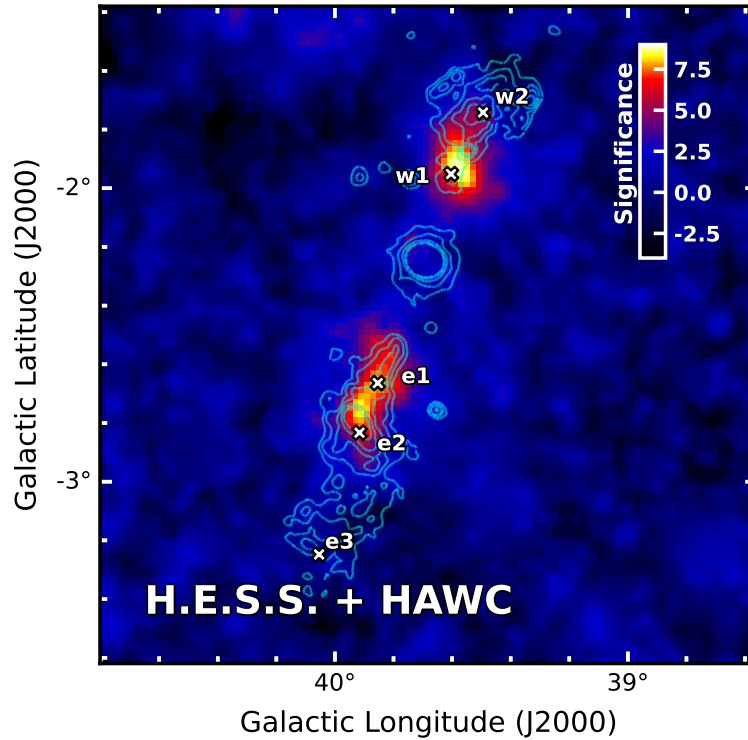


FIGURE 8.8: **Significance map of the SS 433 region using H.E.S.S. and HAWC data.** The figure shows the statistical significance of the gamma-ray excess measured in the SS 433 region after the fitting and subtraction of the emission from the nearby extended source MGRO J1908+06 in the joint analysis. The contours and markers are the same as in Figure 8.3.

We model the jets using a combined spectro-morphological model made up of a power-law for the spectral component and an elongated Gaussian with the angle fixed to that of the jets for the spatial model, following the result of the H.E.S.S. only analysis (see Section 6.5). The best-fit parameters for the spectral and spatial components are shown in Tables 8.4 and 8.5 respectively.

	ϕ_0 ($10^{-15} \text{ TeV}^{-1} \cdot \text{cm}^{-2} \cdot \text{s}^{-1}$)	E_0 (TeV)	Γ
east	$3.39 \pm 0.45_{\text{stat.}}$	7	$2.22 \pm 0.08_{\text{stat.}}$
west	$2.75 \pm 0.42_{\text{stat.}}$	7	$2.17 \pm 0.10_{\text{stat.}}$

TABLE 8.4: **Results of the power-law fits to the spectra of the jets using H.E.S.S. and HAWC data.** Best-fitting photon spectral parameters from the fit to the H.E.S.S. data with a power-law model. E_0 is the reference energy, ϕ_0 is the amplitude at the reference energy and Γ is the index.

The prediction of the best-fit model for the data set corresponding to the highest f_{Hit} bin is shown in Figure 8.9, together with the significance map computed jointly for both data sets after subtracting this model. As can be seen, besides the excess in the MGRO J1908+06 region mentioned above, there are no significant excesses,

	l (deg)	b (deg)	σ_{maj} (deg) (pc)	σ_{min} (deg) (pc)	θ (deg)
east	$39.87 \pm 0.01_{\text{stat.}}$	$-2.69 \pm 0.02_{\text{stat.}}$	$0.15 \pm 0.02_{\text{stat.}}$ $15.2 \pm 1.7_{\text{stat.}}$	$0.04 \pm 0.01_{\text{stat.}}$ $3.9 \pm 1.2_{\text{stat.}}$	-19
west	$39.57 \pm 0.01_{\text{stat.}}$	$-1.87 \pm 0.02_{\text{stat.}}$	$0.11 \pm 0.02_{\text{stat.}}$ $11.5 \pm 1.6_{\text{stat.}}$	$0.05 \pm 0.02_{\text{stat.}}$ $4.7 \pm 1.5_{\text{stat.}}$	-19

TABLE 8.5: **Results of the elongated Gaussian fits to the morphology of the jets using H.E.S.S. and HAWC data.** Best-fitting spatial parameters from the fit of an elongated Gaussian model. The center position in Galactic coordinates is given by l and b. The major and minor axis 1σ radius is given by σ_{maj} and σ_{min} respectively, with the corresponding physical size calculated for a distance of 5.5kpc (Blundell and Bowler, 2004). The angle with respect to the constant Galactic longitude axis θ is frozen in the fit.

meaning the models of the jets are adequate. The resulting best-fit parameters are compatible with those found with only H.E.S.S. data presented in Table 6.3.

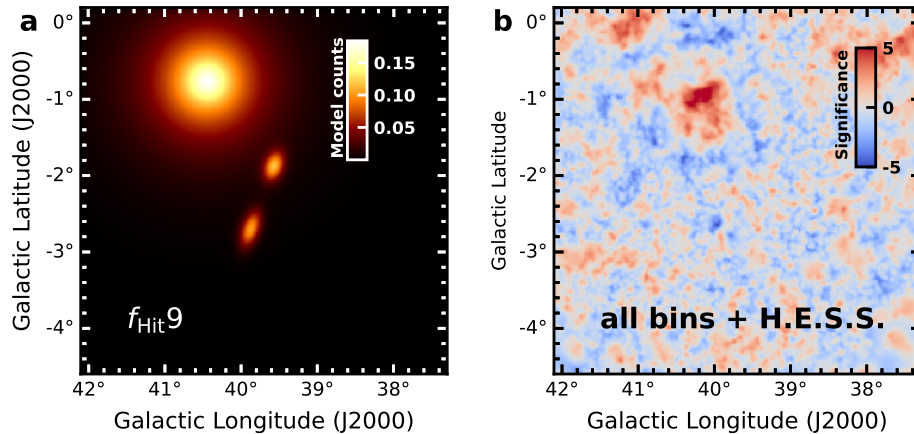


FIGURE 8.9: **Model and residual of the jets using H.E.S.S. and HAWC data.** The figure shows the predicted counts in the highest f_{Hit} bin HAWC from the best-fit model that includes the MGRO J1908+06 component and the jets (a) as well as the significance map of the joint data set after subtracting these two components (b).

The resulting joint spectral model is shown in Figure 8.10, together with the result of the individual analyses of the H.E.S.S. and HAWC data. As can be seen, the joint fit is compatible with both the individual analyses, with the exception of the very constraining HAWC upper limit at around 100 TeV mentioned above, a discrepancy which needs to be further studied. Similarly to the individual H.E.S.S. and HAWC results, the spectral properties of both jets are remarkably consistent with one another, especially considering that only the H.E.S.S. result includes systematic uncertainties.

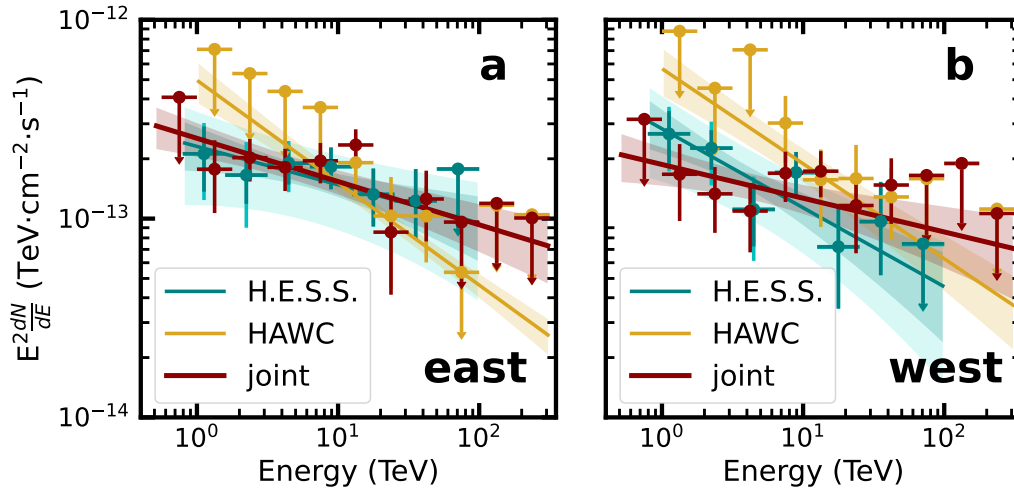


FIGURE 8.10: H.E.S.S., HAWC and joint spectra of the jets. Resulting best-fit spectral model from the 3D modeling of the eastern (a) and western (b) jets. Note that only the H.E.S.S. result includes systematic uncertainties, shown with a lighter color band.

For the fit presented here we have assumed a spectral power-law shape and not tested any other assumptions, such as the presence of curvature or a spectral cutoff. Due to its increased statistics and energy coverage, the combined analysis is more sensitive to the presence of spectral features. However, differences in the energy scale of the two instruments can also artificially introduce such features. For this reason, systematic checks need to be conducted beforehand in order to properly be able to assess the significance of any differences in spectral shape observed with respect to the single instrument analyses.

8.3 Summary and Outlook

This chapter presents an updated analysis of the HAWC data of the jets of SS 433, making use of improved reconstruction algorithms with respect to those employed in Abeysekara et al., 2018. This data set, reduced and analyzed using *Gammapy* via the framework presented in Chapter 5, was then analyzed jointly with the H.E.S.S. data presented in Chapter 6. These results are preliminary, and some more careful investigations, including in the characterization of MGRO J1908+06, are needed in order to present a complete picture of the region using this data set.

Despite these caveats, the results presented here show remarkable agreement with the study carried out using only H.E.S.S. data, and highlight the power of combined analyses between different instruments. Consistent spectra between the eastern and western jet is found in all three of the analyses. This supports the picture of the jets introduced in Chapter 7, with efficient particle acceleration occurring in a similar manner in both jets. Further improvements to the analyses presented here involve the testing of other spectral hypotheses, to identify or rule out the presence of curvature or a cutoff in the spectra.

Figure 8.11 shows the significance maps of the SS 433 region from the H.E.S.S., HAWC and joint data sets shown in Figures 6.5, 8.3 and 8.8 side-by-side using the same color map for easy comparison. As can be seen in the figure, the joint significance map resembles the H.E.S.S. map in terms of the shape of the gamma-ray excesses, but the position of the significance peaks has been shifted due to the contribution of the HAWC result.

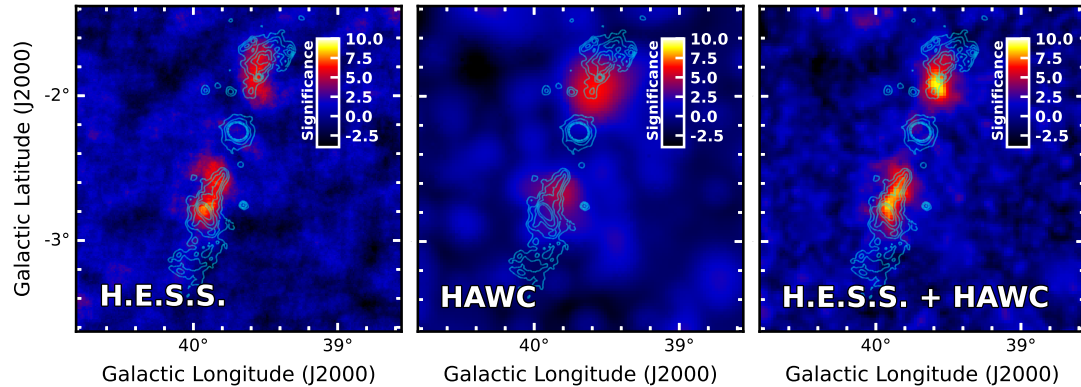


FIGURE 8.11: **H.E.S.S., HAWC and joint spectra of the jets.** Resulting best-fit spectral model from the 3D modeling of the eastern (a) and western (b) jets. Note that only the H.E.S.S. result includes systematic uncertainties, shown with a lighter color band.

Combining data from different instruments has a number of advantages, among them increased statistics and, in the case of H.E.S.S. and HAWC, the ability to cover a larger range of energies. This is made evident in Figure 8.10, which shows that the lower energy range of the spectrum is measured only by H.E.S.S., and the region above 100 TeV is covered only by HAWC. The joint analysis is thus able to probe the entire regime consistently, and provide a more complete picture of the physical properties of the emission. However, combining data sets with very different IRFs can lead also to an increase in the systematic uncertainties, which were not yet estimated for this analysis. A critical further step will then be a full estimation of the uncertainties associated with the joint analysis, using both simulations and real data from sources with well known spectra, such as the Crab Nebula.

Conclusions and Outlook

This thesis presents the most complete picture to date of the non-thermal gamma-ray emission from the jets of the microquasar SS 433. The main findings and conclusions are summarized below.

- Identifying the Cherenkov light produced by muons can improve the background rejection of IACTs arrays with at least one large telescope by more than one order of magnitude. A particular implementation of this finding is proposed here with an algorithm that flags any recorded light that doesn't belong to the main shower image, without identifying its origin. This approach yields a reduction of the background of a factor 3-4 above tens of TeV, and is used in the H.E.S.S. data analysis presented in this thesis.
- The outer jets of SS 433 are detected by the H.E.S.S. array, the first time for an array of IACTs. The energy and angular resolution of H.E.S.S. allow for a measurement of the spatial extension of the gamma-ray emission from the jets, as well as the measurement of the spectrum of each jet from below 1 TeV to several tens of TeV.
- The H.E.S.S. observations also reveal the presence of energy-dependent morphology, with the photons with energies > 10 TeV concentrating only close to the base of the outer jets. This observation allows to identify the nature of the particles responsible for the majority of the TeV emission as leptonic.
- Because of the energy-dependent morphology, the base of the outer jets is identified as the site of efficient particle acceleration to very high energies, with indications that a shock is present at that location.
- Modeling the energy dependent morphology as a combination of particle cooling times and advection motions in the jet flow, an estimate of the velocity at the base of the jets of $v_0 = 0.08 \pm 0.03_{\text{stat}} \pm 0.01_{\text{syst}} c$ can be derived. Comparing this velocity to that of the jets at launch of $0.26c$, yields results consistent with a mildly sub-relativistic shock with compression ratio $0.31 \pm 0.12_{\text{stat}} \pm 0.04_{\text{syst}}$.
- A clearer picture of the nature of the SS 433 outer jet thus emerges, with their sudden reappearance as bright X-ray emitters being due to the presence of a shock accelerating electrons up to very-high-energies at that location. The reasons why a shock would be present in that surface are however, not yet understood.

- The data from particle detector arrays such as the HAWC observatory can be adapted to formats developed originally for IACTs and thus analyzed using a shared tool such as *Gammapy*. A common data format and shared analysis tools allow multi-instrument joint analysis and effective data sharing. This is emphasized by the public release of a sample of HAWC event lists in this format from the Crab nebula region which was made public as part of the work presented in this thesis.
- HAWC has inferior angular resolution compared to H.E.S.S., but its sensitivity reaches energies higher than hundred TeV. Thus a joint analysis between both instruments provides coverage for the entire TeV energy range. Thanks to framework for the analysis of particle detector arrays presented and validated as part of this thesis, a joint analysis of the SS 433 region is possible.
- The SS 433 region is first revisited with the HAWC data only, making use of a longer exposure and improved reconstruction. The jets are detected above ~ 10 TeV, with the emission being consistent with the base of the outer jets as observed by H.E.S.S.. A preliminary joint analysis of the two data sets is finally presented, which allows the first measurement of the spectra of the jets of SS 433 ranging from below 1 TeV to several hundreds of TeV.

The observations presented here are able to shed light on many of the long-standing questions concerning the jets of SS 433, although many still remain, some of which might be answered by observations with future X-ray or gamma-ray experiments. The results presented here highlight the relevance of synergies between the different types of gamma-ray instruments, as well as the importance of gamma-ray observations to the understanding of non-thermal processes in astrophysical systems.

Bibliography

- Abdalla, H. et al. (2022). “Revisiting the PeVatron candidate MGRO J1908+06 with an updated H.E.S.S. analysis”. In: *37th International Cosmic Ray Conference. 12-23 July 2021. Berlin*. Ed. by Pos. Vol. ICRC2021. International Cosmic Ray Conference, p. 779.
- Abdo, A. A. et al. (2007). “TeV Gamma-Ray Sources from a Survey of the Galactic Plane with Milagro”. In: *ApJ* 664.2, pp. L91–L94. DOI: 10.1086/520717.
- Abdo, A. A. et al. (2009). “Fermi LAT Discovery of Extended Gamma-Ray Emission in the Direction of Supernova Remnant W51C”. In: *ApJ* 706.1, pp. L1–L6. DOI: 10.1088/0004-637X/706/1/L1.
- Abdo, A. A. et al. (2010). “Observation of Supernova Remnant IC 443 with the Fermi Large Area Telescope”. In: *ApJ* 712.1, pp. 459–468. DOI: 10.1088/0004-637X/712/1/459.
- Abdo, A. A. et al. (2012). “Observation and Spectral Measurements of the Crab Nebula with Milagro”. In: *ApJ* 750.1, 63, p. 63. DOI: 10.1088/0004-637X/750/1/63.
- Abell, G. O. and B. Margon (1979). “A kinematic model for SS433”. In: *Nature* 279.5715, pp. 701–703. DOI: 10.1038/279701a0.
- Abeysekara, A. U. et al. (2017). “Extended gamma-ray sources around pulsars constrain the origin of the positron flux at Earth”. In: *Science* 358.6365, pp. 911–914. DOI: 10.1126/science.aan4880.
- Abeysekara, A. U. et al. (2017). “Observation of the Crab Nebula with the HAWC Gamma-Ray Observatory”. In: *ApJ* 843.1, 39, p. 39. DOI: 10.3847/1538-4357/aa7555.
- Abeysekara, A. U. et al. (2018). “Very-high-energy particle acceleration powered by the jets of the microquasar SS 433”. In: *Nature* 562.7725, pp. 82–85. DOI: 10.1038/s41586-018-0565-5.
- Abeysekara, A. U. et al. (2019). “Measurement of the Crab Nebula Spectrum Past 100 TeV with HAWC”. In: *ApJ* 881.2, 134, p. 134. DOI: 10.3847/1538-4357/ab2f7d.
- Abeysekara, A. U. et al. (2020). “Multiple Galactic Sources with Emission Above 56 TeV Detected by HAWC”. In: *Phys. Rev. Lett.* 124.2, 021102, p. 021102. DOI: 10.1103/PhysRevLett.124.021102.
- Abramowski, A. et al. (2014). “Search for dark matter annihilation signatures in H.E.S.S. observations of dwarf spheroidal galaxies”. In: *Phys. Rev. D* 90 (11), p. 112012. DOI: 10.1103/PhysRevD.90.112012.
- Aharonian, F. et al. (2004). “Calibration of cameras of the H.E.S.S. detector”. In: *Astroparticle Physics* 22.2, pp. 109–125. DOI: 10.1016/j.astropartphys.2004.06.006.
- Aharonian, F. et al. (2005). “TeV gamma-ray observations of SS-433 and a survey of the surrounding field with the HEGRA IACT-System”. In: *A&A* 439.2, pp. 635–643. DOI: 10.1051/0004-6361:20042248.
- Aharonian, F. et al. (2006). “Observations of the Crab nebula with HESS”. In: *A&A* 457.3, pp. 899–915. DOI: 10.1051/0004-6361:20065351.
- Aharonian, F. et al. (2008). “Energy Spectrum of Cosmic-Ray Electrons at TeV Energies”. In: *Phys. Rev. Lett.* 101.26, 261104, p. 261104. DOI: 10.1103/PhysRevLett.101.261104.

- Aharonian, F. et al. (2009). "Detection of very high energy radiation from HESS J1908+063 confirms the Milagro unidentified source MGRO J1908+06". In: *A&A* 499.3, pp. 723–728. DOI: 10.1051/0004-6361/200811357.
- Aharonian, F. A. and A. M. Atoyan (1998). "Gamma rays from galactic sources with relativistic jets". In: *New A Rev.* 42.9-10, pp. 579–584. DOI: 10.1016/S1387-6473(98)00075-X.
- Aharonian, F. A. et al. (2000). "The Energy Spectrum of TEV Gamma Rays from the Crab Nebula as Measured by the HEGRA System of Imaging Air Cerenkov Telescopes". In: *ApJ* 539.1, pp. 317–324. DOI: 10.1086/309225.
- Aharonian, Felix A. (2004). *Very high energy cosmic gamma radiation : a crucial window on the extreme Universe*. DOI: 10.1142/4657.
- Akaike, H. (1973). "Information Theory and an Extension of the Maximum Likelihood Principle". In: *Proceedings of the 2nd International Symposium on Information Theory*. Ed. by F. Csaki B. N. Petrov, pp. 267–281.
- Albert, A. et al. (2022a). "HAWC Study of the Ultra-high-energy Spectrum of MGRO J1908+06". In: *ApJ* 928.2, 116, p. 116. DOI: 10.3847/1538-4357/ac56e5.
- Albert, A. et al. (2022b). "Validation of standardized data formats and tools for ground-level particle-based gamma-ray observatories". In: *A&A* 667, A36. DOI: 10.1051/0004-6361/202243527.
- Alves, E. P., J. Zrake, and F. Fiuza (2018). "Efficient Nonthermal Particle Acceleration by the Kink Instability in Relativistic Jets". In: *Phys. Rev. Lett.* 121.24, 245101, p. 245101. DOI: 10.1103/PhysRevLett.121.245101.
- Anderson, S. F., B. Margon, and S. A. Grandi (1983). "Precession instability in SS 433." In: *ApJ* 273, pp. 697–701. DOI: 10.1086/161404.
- Arnason, R. M. et al. (2021). "Distances to Galactic X-ray binaries with Gaia DR2". In: *MNRAS* 502.4, pp. 5455–5470. DOI: 10.1093/mnras/stab345.
- Ashton, T. et al. (2020). "A NECTAR-based upgrade for the Cherenkov cameras of the H.E.S.S. 12-meter telescopes". In: *Astroparticle Physics* 118, 102425, p. 102425. DOI: 10.1016/j.astropartphys.2019.102425.
- Astropy Collaboration et al. (2013). "Astropy: A community Python package for astronomy". In: *A&A* 558, A33, A33. DOI: 10.1051/0004-6361/201322068.
- Atwood, W. B. et al. (2009). "The Large Area Telescope on the Fermi Gamma-Ray Space Telescope Mission". In: *ApJ* 697.2, pp. 1071–1102. DOI: 10.1088/0004-637X/697/2/1071.
- Axford, W. I., E. Leer, and G. Skadron (1977). "The Acceleration of Cosmic Rays by Shock Waves". In: *International Cosmic Ray Conference*. Vol. 11. International Cosmic Ray Conference, p. 132.
- Baade, W. and R. Minkowski (1954). "Identification of the Radio Sources in Cassiopeia, Cygnus A, and Puppis A." In: *ApJ* 119, p. 206. DOI: 10.1086/145812.
- Balzer, A. et al. (2014). "The H.E.S.S. central data acquisition system". In: *Astroparticle Physics* 54, pp. 67–80. DOI: 10.1016/j.astropartphys.2013.11.007.
- Band, D. L. and M. A. Gordon (1989). "Millimeter-Wavelength Observations of SS 433 and Its Environs". In: *ApJ* 338, p. 945. DOI: 10.1086/167246.
- Band, David L. (1987). "IRAS observations of SS 433 and W 50." In: *PASP* 99, pp. 1269–1276. DOI: 10.1086/132113.
- (1989). "Comparison of Einstein and EXOSAT Observations of SS 433". In: *ApJ* 336, p. 937. DOI: 10.1086/167063.
- Barret, Didier, Christian Motch, and Peter Predehl (1998). "ROSAT and follow-up infrared observations of the X-ray burster KS 1731-260". In: *A&A* 329, pp. 965–970.

- Bell, A. R. (1978a). "The acceleration of cosmic rays in shock fronts - I." In: *MNRAS* 182, pp. 147–156. DOI: 10.1093/mnras/182.2.147.
- (1978b). "The acceleration of cosmic rays in shock fronts - II." In: *MNRAS* 182, pp. 443–455. DOI: 10.1093/mnras/182.3.443.
- (2013). "Cosmic ray acceleration". In: *Astroparticle Physics* 43, pp. 56–70. DOI: 10.1016/j.astropartphys.2012.05.022.
- Bell, A. R. et al. (2013). "Cosmic-ray acceleration and escape from supernova remnants". In: *MNRAS* 431.1, pp. 415–429. DOI: 10.1093/mnras/stt179.
- Bell, Anthony Raymond (2014). "Particle Acceleration by Shocks in Supernova Remnants". In: *Brazilian Journal of Physics* 44.5, pp. 415–425. DOI: 10.1007/s13538-014-0219-5.
- Bell, Michael R., David H. Roberts, and John F. C. Wardle (2011). "Structure and Magnetic Fields in the Precessing Jet System SS 433. III. Evolution of the Intrinsic Brightness of the Jets from a Deep Multi-epoch Very Large Array Campaign". In: *ApJ* 736.2, 118, p. 118. DOI: 10.1088/0004-637X/736/2/118.
- Berge, D., S. Funk, and J. Hinton (2007). "Background modelling in very-high-energy γ -ray astronomy". In: *Astronomy and Astrophysics* 466.3, pp. 1219–1229. DOI: 10.1051/0004-6361:20066674.
- Bethe, H. and W. Heitler (1934). "On the Stopping of Fast Particles and on the Creation of Positive Electrons". In: *Proceedings of the Royal Society of London Series A* 146.856, pp. 83–112. DOI: 10.1098/rspa.1934.0140.
- Bi, B. et al. (2022). "Performance of the new FlashCam-based camera in the 28m telescope of H.E.S.S." In: *37th International Cosmic Ray Conference. 12-23 July 2021. Berlin*, p. 743.
- Blandford, R. D. and J. P. Ostriker (1978). "Particle acceleration by astrophysical shocks." In: *ApJ* 221, pp. L29–L32. DOI: 10.1086/182658.
- Blandford, R. D. and D. G. Payne (1982). "Hydromagnetic flows from accretion disks and the production of radio jets." In: *MNRAS* 199, pp. 883–903. DOI: 10.1093/mnras/199.4.883.
- Blandford, R. D. and R. L. Znajek (1977). "Electromagnetic extraction of energy from Kerr black holes." In: *MNRAS* 179, pp. 433–456. DOI: 10.1093/mnras/179.3.433.
- Blandford, Roger and David Eichler (1987). "Particle acceleration at astrophysical shocks: A theory of cosmic ray origin". In: *Phys. Rep.* 154.1, pp. 1–75. DOI: 10.1016/0370-1573(87)90134-7.
- Blandford, Roger, David Meier, and Anthony Readhead (2019). "Relativistic Jets from Active Galactic Nuclei". In: *ARA&A* 57, pp. 467–509. DOI: 10.1146/annurev-astro-081817-051948.
- Blumenthal, George R. and Robert J. Gould (1970). "Bremsstrahlung, Synchrotron Radiation, and Compton Scattering of High-Energy Electrons Traversing Dilute Gases". In: *Reviews of Modern Physics* 42.2, pp. 237–271. DOI: 10.1103/RevModPhys.42.237.
- Blundell, K. M., M. G. Bowler, and L. Schmidtbreick (2007). "Fluctuations and symmetry in the speed and direction of the jets of SS 433 on different timescales". In: *A&A* 474.3, pp. 903–910. DOI: 10.1051/0004-6361:20077924.
- Blundell, Katherine M. and Michael G. Bowler (2004). "Symmetry in the Changing Jets of SS 433 and Its True Distance from Us". In: *ApJ* 616.2, pp. L159–L162. DOI: 10.1086/426542.
- Blundell, Katherine M., Michael G. Bowler, and Linda Schmidtbreick (2008). "SS 433: Observation of the Circumbinary Disk and Extraction of the System Mass". In: *ApJ* 678.1, p. L47. DOI: 10.1086/588027.
- Blundell, Katherine M. et al. (2001). "Images of an Equatorial Outflow in SS 433". In: *ApJ* 562.1, pp. L79–L82. DOI: 10.1086/324573.

- Bordas, P. et al. (2015). "Detection of Persistent Gamma-Ray Emission Toward SS433/W50". In: *ApJ* 807.1, L8, p. L8. DOI: 10.1088/2041-8205/807/1/L8.
- Bordas, Pol et al. (2017). "Gamma-ray emission towards SS433/W50". In: *6th International Symposium on High Energy Gamma-Ray Astronomy*. Vol. 1792. American Institute of Physics Conference Series, p. 040020. DOI: 10.1063/1.4968924.
- Boumis, P. et al. (2007). "Deep optical observations of the interaction of the SS 433 microquasar jet with the W50 radio continuum shell". In: *MNRAS* 381.1, pp. 308–318. DOI: 10.1111/j.1365-2966.2007.12276.x.
- Bowler, Michael G. and Rony Keppens (2018). "W 50 and SS 433". In: *A&A* 617, A29, A29. DOI: 10.1051/0004-6361/201732488.
- Brinkmann, W., B. Aschenbach, and N. Kawai (1996). "ROSAT observations of the W 50/SS 433 system." In: *A&A* 312, pp. 306–316.
- Brinkmann, W. et al. (1988). "The thermal evolution of the jets in SS 433." In: *A&A* 196, pp. 313–326.
- Brinkmann, W. et al. (1991). "The X-ray emission of SS 433." In: *A&A* 241, p. 112.
- Brinkmann, W. et al. (2007). "XMM-Newton observations of the eastern jet of SS 433". In: *A&A* 463.2, pp. 611–619. DOI: 10.1051/0004-6361:20065570.
- Calabretta, M. R. and E. W. Greisen (2002). "Representations of celestial coordinates in FITS". In: *A&A* 395, pp. 1077–1122. DOI: 10.1051/0004-6361:20021327.
- Camenzind, M. (1986). "Hydromagnetic flows from rapidly rotating compact objects. I - Cold relativistic flows from rapid rotators". In: *A&A* 162.1-2, pp. 32–44.
- (1987). "Hydromagnetic flows from rapidly rotating compact objects. II - The relativistic axisymmetric jet equilibrium". In: *A&A* 184.1-2, pp. 341–360.
- Cao, Zhen et al. (2021). "Ultrahigh-energy photons up to 1.4 petaelectronvolts from 12 γ -ray Galactic sources". In: *Nature*. ISSN: 1476-4687.
- Carilli, C. L. and P. D. Barthel (1996). "Cygnus A". In: *A&A Rev.* 7.1, pp. 1–54. DOI: 10.1007/s001590050001.
- Castellina, A. (2017). "Ground-based cosmic ray experiments: A review". In: *Nuovo Cim. C* 40.3. Ed. by M. Razzano, G. Spandre, and B. Patricelli, p. 143. DOI: 10.1393/ncc/i2017-17143-1.
- Cherepashchuk, A. M., K. A. Postnov, and A. A. Belinski (2019). "Mass ratio in SS433 revisited". In: *MNRAS* 485.2, pp. 2638–2641. DOI: 10.1093/mnras/stz610.
- Cherepashchuk, A. M. et al. (2021). "Discovery of orbital eccentricity and evidence for orbital period increase of SS433". In: *MNRAS* 507.1, pp. L19–L23. DOI: 10.1093/mnras/1/slab083.
- Chomiuk, Laura, Brian D. Metzger, and Ken J. Shen (2021). "New Insights into Classical Novae". In: *ARA&A* 59, pp. 391–444. DOI: 10.1146/annurev-astro-112420-114502.
- Ciatti, F., A. Mammano, and A. Vittone (1981). "A kinematical analysis of SS 433 after two observing seasons, 1978-79n." In: *A&A* 94, pp. 251–258.
- Clark, D. H. and P. Murdin (1978). "An unusual emission-line star/X-ray source radio star, possibly associated with an SNR." In: *Nature* 276, pp. 44–45. DOI: 10.1038/276044a0.
- Cohen, M. H. et al. (1971). "The Small-Scale Structure of Radio Galaxies and Quasi-Stellar Sources at 3.8 Centimeters". In: *ApJ* 170, p. 207. DOI: 10.1086/151204.
- Contreras, J. L. et al. (2015). "Data model issues in the Cherenkov Telescope Array project". In: *34th International Cosmic Ray Conference (ICRC2015)*. Vol. 34. International Cosmic Ray Conference, p. 960.
- Cramér, H. (1946). *Mathematical methods of statistics*. Princeton Univ. Press.

- CTA-Consortium (2019). *Science with the Cherenkov Telescope Array*. WORLD SCIENTIFIC.
DOI: 10.1142/10986.
- Curtis, H. D. (1918). "Descriptions of 762 Nebulae and Clusters Photographed with the Crossley Reflector". In: *Publications of Lick Observatory* 13, pp. 9–42.
- Davidson, K. and R. McCray (1980). "SS 433 as a prototype of astrophysical jets." In: *ApJ* 241, pp. 1082–1089. DOI: 10.1086/158423.
- Davies, John M. and Eugene S. Cotton (1957). "Design of the quartermaster solar furnace". In: *Solar Energy* 1.2-3, pp. 16–22. DOI: 10.1016/0038-092X(57)90116-0.
- De Naurois, Mathieu and Daniel Mazin (2015). "Ground-based detectors in very-high-energy gamma-ray astronomy". In: *Comptes Rendus Physique* 16.6-7, pp. 610–627. DOI: 10.1016/j.crhy.2015.08.011.
- Deil, C. et al. (2017). "Gammapy - A prototype for the CTA science tools". In: *35th International Cosmic Ray Conference (ICRC2017)*. Vol. 301. International Cosmic Ray Conference, p. 766.
- Dolan, J. F. et al. (1997). "SS 433 in the ultraviolet." In: *A&A* 327, pp. 648–655.
- Drury, L. Oc. (1983). "REVIEW ARTICLE: An introduction to the theory of diffusive shock acceleration of energetic particles in tenuous plasmas". In: *Reports on Progress in Physics* 46.8, pp. 973–1027. DOI: 10.1088/0034-4885/46/8/002.
- Drury, Luke O. 'C. (2012). "Origin of cosmic rays". In: *Astroparticle Physics* 39, pp. 52–60. DOI: 10.1016/j.astropartphys.2012.02.006.
- Dubner, G. M. et al. (1998). "A High-Resolution Radio Study of the W50-SS 433 System and the Surrounding Medium". In: *AJ* 116.4, pp. 1842–1855. DOI: 10.1086/300537.
- E.H.T. Collaboration et al. (2019). "First M87 Event Horizon Telescope Results. I. The Shadow of the Supermassive Black Hole". In: *ApJ* 875.1, L1, p. L1. DOI: 10.3847/2041-8213/ab0ec7.
- Eichler, D. (1983). "Focusing of high-mach number jets by an ambient medium." In: *ApJ* 272, pp. 48–53. DOI: 10.1086/161260.
- Eikenberry, S. S. et al. (2001). "Twenty Years of Timing SS 433". In: *ApJ* 561.2, pp. 1027–1033. DOI: 10.1086/323380.
- Elston, R. and S. Baum (1987). "High-Resolution Radio Observations of W50, the Remnant Associated with SS 433". In: *AJ* 94, p. 1633. DOI: 10.1086/114594.
- Fabian, A. C. and M. J. Rees (1979). "SS 433: a double jet in action?" In: *MNRAS* 187, 13P–16. DOI: 10.1093/mnras/187.1.13P.
- Fabrika, S. (2004). "The jets and supercritical accretion disk in SS433". In: *Astrophys. Space Phys. Res.* 12, pp. 1–152.
- Falle, S. A. E. G. (1991). "Self-similar jets." In: *MNRAS* 250, pp. 581–596. DOI: 10.1093/mnras/250.3.581.
- Fang, Ke, Eric Charles, and Roger D. Blandford (2020). "GeV-TeV Counterparts of SS 433/W50 from Fermi-LAT and HAWC Observations". In: *ApJ* 889.1, L5, p. L5. DOI: 10.3847/2041-8213/ab62b8.
- Farnes, J. S. et al. (2017). "Interacting large-scale magnetic fields and ionized gas in the W50/SS433 system". In: *MNRAS* 467.4, pp. 4777–4801. DOI: 10.1093/mnras/stx338.
- Fender, Rob (2006). "Jets from X-ray binaries". In: *Compact stellar X-ray sources*. Vol. 39, pp. 381–419.
- Fendt, C. and D. Elstner (2000). "Long-term evolution of a dipole type magnetosphere interacting with an accretion disk. II. Transition into a quasi-stationary spherically radial outflow". In: *A&A* 363, pp. 208–222.
- Fendt, Christian (2002). "Formation of Astrophysical Jets". Habilitationsschrift, Mathematisch-Naturwissenschaftlichen Fakultät der Universität Potsdam.

- Fendt, Christian and Detlef Elstner (1999). "Long-term evolution of a dipolar-type magnetosphere interacting with an accretion disk". In: *A&A* 349, pp. L61–L64.
- Fermi, Enrico (1949). "On the Origin of the Cosmic Radiation". In: *Physical Review* 75.8, pp. 1169–1174. DOI: 10.1103/PhysRev.75.1169.
- Frank, Juhan, Andrew King, and Derek J. Raine (2002). *Accretion Power in Astrophysics: Third Edition*.
- Furst, E. et al. (1990). "A radio continuum survey of the Galactic Plane at 11 cmwavelength. III. The area $76\text{deg} \leq L \leq 240\text{deg}$, $-5\text{deg} \leq B \leq 5\text{deg}$ ". In: *A&AS* 85, pp. 691–803.
- Gaisser, T. K. et al. (1991). "Gamma-ray astronomy above 50 TeV with muon-poor showers". In: *Physical Review D* 43.2, pp. 314–318. DOI: 10.1103/PhysRevD.43.314.
- Gaisser, Thomas K., Ralph Engel, and Elisa Resconi (2016). *Cosmic Rays and Particle Physics*.
- Gallo, Elena, Richard M. Plotkin, and Peter G. Jonker (2014). "V4641 Sgr: a candidate precessing microblazar". In: *MNRAS* 438.1, pp. L41–L45. DOI: 10.1093/mnrasl/slt152.
- Geldzahler, B. J., T. Pauls, and C. J. Salter (1980). "Continuum observations of the SNR W50 and G 74.9+1.2 at 2695 MHz." In: *A&A* 84, pp. 237–244.
- Gies, D. R., W. Huang, and M. V. McSwain (2002). "The Spectrum of the Mass Donor Star in SS 433". In: *ApJ* 578.1, pp. L67–L70. DOI: 10.1086/344436.
- Gillessen, Stefan (2004). "Sub-Bogenminuten-genaue Positionen von TeV-Quellen mit H.E.S.S." PhD thesis. Ruprecht-Karls-Universität Heidelberg.
- Goodall, Paul T., Fathallah Alouani-Bibi, and Katherine M. Blundell (2011a). "When microquasar jets and supernova collide: hydrodynamically simulating the SS 433-W 50 interaction". In: *MNRAS* 414.4, pp. 2838–2859. DOI: 10.1111/j.1365-2966.2011.18388.x.
- Goodall, Paul T., Katherine M. Blundell, and S. Jocelyn Bell Burnell (2011b). "Probing the history of SS 433's jet kinematics via decade-resolution radio observations of W 50". In: *MNRAS* 414.4, pp. 2828–2837. DOI: 10.1111/j.1365-2966.2011.18809.x.
- Górski, K. M. et al. (2005). "HEALPix: A Framework for High-Resolution Discretization and Fast Analysis of Data Distributed on the Sphere". In: *ApJ* 622, pp. 759–771. DOI: 10.1086/427976.
- Greisen, Kenneth (1966). "End to the Cosmic-Ray Spectrum?" In: *Phys. Rev. Lett.* 16 (17), pp. 748–750. DOI: 10.1103/PhysRevLett.16.748.
- Hahn, J. (2015). "GAMERA - a new modeling package for non-thermal spectral modeling". In: *34th International Cosmic Ray Conference (ICRC2015)*. Vol. 34. International Cosmic Ray Conference, p. 917.
- Hahn, Joachim, Carlo Romoli, and Mischa Breuhaus (2022). *GAMERA: Source modeling in gamma astronomy*. Astrophysics Source Code Library, record ascl:2203.007.
- Harris, Charles R. et al. (2020). "Array programming with NumPy". In: *Nature* 585, 357–362. DOI: 10.1038/s41586-020-2649-2.
- Hazard, C., M. B. Mackey, and A. J. Shimmins (1963). "Investigation of the Radio Source 3C 273 By The Method of Lunar Occultations". In: *Nature* 197.4872, pp. 1037–1039. DOI: 10.1038/1971037a0.
- Heck, D. et al. (1998). *CORSIKA: a Monte Carlo code to simulate extensive air showers*. Forschungszentrum Karlsruhe GmbH.
- Heitler, W. (1954). *Quantum theory of radiation*.
- Hess, Victor F. (1912). "Über Beobachtungen der durchdringenden Strahlung bei sieben Freiballonfahrten". In: *Phys. Z.* 13, pp. 1084–1091.
- H.E.S.S. Collaboration (2018). *H.E.S.S. first public test data release*. For terms of use, see README.txt and hess_dl3_dr1.pdf. DOI: 10.5281/zenodo.1421099.

- (2020). “Resolving the Crab pulsar wind nebula at teraelectronvolt energies”. In: *Nature Astronomy* 4, pp. 167–173. DOI: 10.1038/s41550-019-0910-0.
- H.E.S.S. Collaboration et al. (2018). “The H.E.S.S. Galactic plane survey”. In: *A&A* 612, A1, A1. DOI: 10.1051/0004-6361/201732098.
- Heuvel, E. P. J. van den (1981). “SS 433, X-ray binaries and stellar evolution”. In: *Vistas in Astronomy* 25.1, pp. 95–108. DOI: 10.1016/0083-6656(81)90050-7.
- Hillas, A. M. (1984). “The Origin of Ultra-High-Energy Cosmic Rays”. In: *ARA&A* 22, pp. 425–444. DOI: 10.1146/annurev.aa.22.090184.002233.
- (1985). “Cerenkov Light Images of EAS Produced by Primary Gamma Rays and by Nuclei”. In: *19th International Cosmic Ray Conference (ICRC19), Volume 3*. Vol. 3. International Cosmic Ray Conference, p. 445.
- Hillas, A.M. (2013). “Evolution of ground-based gamma-ray astronomy from the early days to the Cherenkov Telescope Arrays”. In: *Astroparticle Physics* 43, pp. 19–43. DOI: 10.1016/j.astropartphys.2012.06.002.
- Hillwig, T. C. and D. R. Gies (2008). “Spectroscopic Observations of the Mass Donor Star in SS 433”. In: *ApJ* 676.1, p. L37. DOI: 10.1086/587140.
- Hinton, J. and SWGO Collaboration (2022). “The Southern Wide-field Gamma-ray Observatory: Status and Prospects”. In: *37th International Cosmic Ray Conference. 12-23 July 2021. Berlin*, p. 23.
- Hjellming, R. M. and K. J. Johnston (1981). “An analysis of the proper motions of SS 433 radio jets.” In: *ApJ* 246, pp. L141–L145. DOI: 10.1086/183571.
- Hjellming, R. M. et al. (2000). “Light Curves and Radio Structure of the 1999 September Transient Event in V4641 Sagittarii (=XTE J1819-254=SAX J1819.3-2525)”. In: *ApJ* 544.2, pp. 977–992. DOI: 10.1086/317255.
- Holler, M. et al. (2015). “Observations of the Crab Nebula with H.E.S.S. phase II”. In: *34th International Cosmic Ray Conference (ICRC2015)*. Vol. 34. International Cosmic Ray Conference, p. 847.
- Hörandel, Jörg R. (2013). “Early Cosmic-Ray Work Published in German”. In: *AIP Conf. Proc.* 1516.1. Ed. by Jonathan F. Ormes, pp. 52–60. DOI: 10.1063/1.4792540.
- Hoshino, M. and Y. Lyubarsky (2012). “Relativistic Reconnection and Particle Acceleration”. In: *Space Sci. Rev.* 173.1-4, pp. 521–533. DOI: 10.1007/s11214-012-9931-z.
- Hughes, P. A. (1991). *Beams and Jets in Astrophysics*.
- Hunter, John D (2007). “Matplotlib: A 2D graphics environment”. In: *Computing in science & engineering* 9.3, pp. 90–95.
- Jansky, Karl G. (1933). “Radio Waves from Outside the Solar System”. In: *Nature* 132.3323, p. 66. DOI: 10.1038/132066a0.
- Jardin-Blicq, Armelle (2019). “The TeV gamma-ray emission of the Galactic Plane”. PhD thesis. University of Heidelberg.
- Jeffrey, Robert M. et al. (2016). “Fast launch speeds in radio flares, from a new determination of the intrinsic motions of SS 433’s jet bolides”. In: *MNRAS* 461.1, pp. 312–320. DOI: 10.1093/mnras/stw1322.
- Jennison, R. C. and M. K. Das Gupta (1953). “Fine Structure of the Extra-terrestrial Radio Source Cygnus I”. In: *Nature* 172.4387, pp. 996–997. DOI: 10.1038/172996a0.
- Jones, Frank C. (1968). “Calculated Spectrum of Inverse-Compton-Scattered Photons”. In: *Physical Review* 167.5, pp. 1159–1169. DOI: 10.1103/PhysRev.167.1159.
- Kafexhiu, Ervin et al. (2014). “Parametrization of gamma-ray production cross sections for p p interactions in a broad proton energy range from the kinematic threshold to PeV energies”. In: *Phys. Rev. D* 90.12, 123014, p. 123014. DOI: 10.1103/PhysRevD.90.123014.

- Kagan, D. et al. (2015). "Relativistic Magnetic Reconnection in Pair Plasmas and Its Astrophysical Applications". In: *Space Sci. Rev.* 191.1-4, pp. 545–573. DOI: 10.1007/s11214-014-0132-9.
- Kar, P. and VERITAS Collaboration (2017). "VERITAS Observations of High-Mass X-Ray Binary SS 433". In: *35th International Cosmic Ray Conference (ICRC2017)*. Vol. 301. International Cosmic Ray Conference, p. 713.
- Kayama, Kazuho et al. (2022). "Spatially resolved study of the SS 433/W50 west region with Chandra: X-ray structure and spectral variation of non-thermal emission". In: *arXiv e-prints*, arXiv:2207.05924, arXiv:2207.05924.
- Kelner, S. R., F. A. Aharonian, and V. V. Bugayov (2006). "Energy spectra of gamma rays, electrons, and neutrinos produced at proton-proton interactions in the very high energy regime". In: *Phys. Rev. D* 74.3, 034018, p. 034018. DOI: 10.1103/PhysRevD.74.034018.
- Kimura, Shigeo S., Kohta Murase, and Peter Mészáros (2020). "Deciphering the Origin of the GeV-TeV Gamma-Ray Emission from SS 433". In: *ApJ* 904.2, 188, p. 188. DOI: 10.3847/1538-4357/abbe00.
- Kirk, J. G. and P. Duffy (1999). "TOPICAL REVIEW: Particle acceleration and relativistic shocks". In: *Journal of Physics G Nuclear Physics* 25.8, R163–R194. DOI: 10.1088/0954-3899/25/8/201.
- Kirk, J. G. et al. (2000). "Particle Acceleration at Ultrarelativistic Shocks: An Eigenfunction Method". In: *ApJ* 542.1, pp. 235–242. DOI: 10.1086/309533.
- Klein, O. and T. Nishina (1929). "Über die Streuung von Strahlung durch freie Elektronen nach der neuen relativistischen Quantendynamik von Dirac". In: *Zeitschrift für Physik* 52.11-12, pp. 853–868. DOI: 10.1007/BF01366453.
- Koljonen, K. I. I. et al. (2018). "The hypersoft state of Cygnus X-3. A key to jet quenching in X-ray binaries?" In: *A&A* 612, A27, A27. DOI: 10.1051/0004-6361/201732284.
- Komissarov, Serguei and Oliver Porth (2021). "Numerical simulations of jets". In: *New A Rev.* 92, 101610, p. 101610. DOI: 10.1016/j.newar.2021.101610.
- Konigl, A. (1983). "W 50 - a stellar-wind bubble in a three-phase interstellar medium ?" In: *MNRAS* 205, pp. 471–485. DOI: 10.1093/mnras/205.2.471.
- Krymskii, G. F. (1977). "A regular mechanism for the acceleration of charged particles on the front of a shock wave". In: *Akademiia Nauk SSSR Doklady* 234, pp. 1306–1308.
- Kubota, K. et al. (2010). "Subaru And Gemini Observations Of SS 433: New Constraint On The Mass Of The Compact Object". In: *ApJ* 709.2, pp. 1374–1386. DOI: 10.1088/0004-637X/709/2/1374.
- Lagage, P. O. and C. J. Cesarsky (1983). "The maximum energy of cosmic rays accelerated by supernova shocks." In: *A&A* 125, pp. 249–257.
- Landau, L. D. and E. M. Lifshitz (1987). *Fluid Mechanics*.
- Li, Jian et al. (2020). "Gamma-ray heartbeat powered by the microquasar SS 433". In: *Nature Astronomy* 4, pp. 1177–1184. DOI: 10.1038/s41550-020-1164-6.
- Li, T. P. and Y. Q. Ma (1983). "Analysis methods for results in gamma-ray astronomy." In: *ApJ* 272, pp. 317–324. DOI: 10.1086/161295.
- Liska, M., A. Tchekhovskoy, and E. Quataert (2020). "Large-scale poloidal magnetic field dynamo leads to powerful jets in GRMHD simulations of black hole accretion with toroidal field". In: *MNRAS* 494.3, pp. 3656–3662. DOI: 10.1093/mnras/staa955.
- Liu, Qian-Cheng et al. (2020). "A Small-scale Investigation of Molecular Emission toward the Tip of the Western Lobe of W50/SS 433". In: *ApJ* 892.2, 143, p. 143. DOI: 10.3847/1538-4357/ab7a22.
- Longair, Malcolm S. (2011). *High Energy Astrophysics*.

- Lopez, J. A. (1997). "Jets and Brels in Planetary Nebulae (Invited Review)". In: *Planetary Nebulae*. Ed. by H. J. Habing and H. J. G. L. M. Lamers. Vol. 180, p. 197.
- MAGIC and H.E.S.S. Collaborations et al. (2018). "Constraints on particle acceleration in SS433/W50 from MAGIC and H.E.S.S. observations". In: *A&A* 612, A14, A14. DOI: 10.1051/0004-6361/201731169.
- Malkov, M. A. and L. O'C. Drury (2001). "Nonlinear theory of diffusive acceleration of particles by shock waves". In: *Reports on Progress in Physics* 64.4, pp. 429–481. DOI: 10.1088/0034-4885/64/4/201.
- Mannheim, K. and P. L. Biermann (1989). "Photomeson production in active galactic nuclei." In: *A&A* 221, pp. 211–220.
- Marandon, V., A. Jardin-Blicq, and H. Schoorlemmer (2019). "Latest news from the HAWC outrigger array". In: *36th International Cosmic Ray Conference (ICRC2019)*. Vol. 36. International Cosmic Ray Conference, p. 736.
- Marcowith, A. et al. (2016). "The microphysics of collisionless shock waves". In: *Reports on Progress in Physics* 79.4, 046901, p. 046901. DOI: 10.1088/0034-4885/79/4/046901.
- Margon, B. (1982). "Relativistic Jets in SS 433". In: *Science* 215.4530, pp. 247–252. DOI: 10.1126/science.215.4530.247.
- Margon, B. et al. (1979a). "Enormous periodic Doppler shifts in SS433." In: *ApJ* 233, pp. L63–L68. DOI: 10.1086/183077.
- Margon, B. et al. (1979b). "The bizarre spectrum of SS 433." In: *ApJ* 230, pp. L41–L45. DOI: 10.1086/182958.
- Margon, Bruce (1984). "Observations of SS 433". In: *ARA&A* 22, pp. 507–536. DOI: 10.1146/annurev.aa.22.090184.002451.
- Margon, Bruce and Scott F. Anderson (1989). "Ten Years of SS 433 Kinematics". In: *ApJ* 347, p. 448. DOI: 10.1086/168132.
- Marrocchesi, Pier Simone (2017). "Charged Cosmic Rays: a Review of Balloon and Space Borne Measurements". In: *arXiv e-prints*, arXiv:1704.00304, arXiv:1704.00304.
- Marshall, F. E. et al. (1978). "X-Ray Emission from SS 433". In: *IAU Circ.* 3314, p. 2.
- Martí, Josep et al. (2018). "The radio jets of SS 433 at millimetre wavelengths". In: *A&A* 619, A40, A40. DOI: 10.1051/0004-6361/201833733.
- Massaglia, S. et al. (2016). "Making Faranoff-Riley I radio sources. I. Numerical hydrodynamic 3D simulations of low-power jets". In: *A&A* 596, A12, A12. DOI: 10.1051/0004-6361/201629375.
- Massi, M. (2007). "Neutron stars in Microquasars". In: *WE-Heraeus Seminar on Neutron Stars and Pulsars 40 years after the Discovery*. Ed. by W. Becker and H. H. Huang, p. 185.
- Matthews, J. (2005). "A Heitler model of extensive air showers". In: *Astroparticle Physics* 22.5-6, pp. 387–397. DOI: 10.1016/j.astropartphys.2004.09.003.
- Matthews, James H., Anthony R. Bell, and Katherine M. Blundell (2020). "Particle acceleration in astrophysical jets". In: *New A Rev.* 89, 101543, p. 101543. DOI: 10.1016/j.newar.2020.101543.
- Melrose, D. B. (1980). *Plasma astrophysics: Nonthermal processes in diffuse magnetized plasmas. Volume 1 - The emission, absorption and transfer of waves in plasmas.*
- Migliari, Simone, Rob Fender, and Mariano Méndez (2002). "Iron Emission Lines from Extended X-ray Jets in SS 433: Reheating of Atomic Nuclei". In: *Science* 297.5587, pp. 1673–1676. DOI: 10.1126/science.1073660.
- Milgrom, M. (1979). "On the interpretation of the large variations in the line positions in SS433." In: *A&A* 76.1, pp. L3–L6.

- Mirabel, I. F. and L. F. Rodríguez (1994). “A superluminal source in the Galaxy”. In: *Nature* 371.6492, pp. 46–48. DOI: 10.1038/371046a0.
- (1999). “Sources of Relativistic Jets in the Galaxy”. In: *ARA&A* 37, pp. 409–443. DOI: 10.1146/annurev.astro.37.1.409.
- Mohrmann, L. et al. (2019). “Validation of open-source science tools and background model construction in γ -ray astronomy”. In: *A&A* 632, A72, A72. DOI: 10.1051/0004-6361/201936452.
- Monceau-Baroux, Rémi et al. (2015). “The SS433 jet from subparsec to parsec scales”. In: *A&A* 574, A143, A143. DOI: 10.1051/0004-6361/201425015.
- Monceau-Baroux, Remi et al. (2017). “The SS433 jet from subparsec to parsec scales (Corrigendum)”. In: *A&A* 607, C4, p. C4. DOI: 10.1051/0004-6361/201425015e.
- Mücke, A. et al. (2000). “Photomeson production in astrophysical sources”. In: *Nuclear Physics B Proceedings Supplements* 80, pp. 08/10.
- Nigro, C. et al. (2019). “Towards open and reproducible multi-instrument analysis in gamma-ray astronomy”. In: *A&A* 625, A10, A10. DOI: 10.1051/0004-6361/201834938.
- Nigro, Cosimo (2019). “Study of Persistent and Flaring Gamma-Ray Emission from Active Galactic Nuclei with the MAGIC Telescopes and Prospects for Future Open Data Formats in Gamma-Ray Astronomy”. PhD thesis. Humboldt-Universität zu Berlin.
- Nigro, Cosimo, Tarek Hassan, and Laura Olivera-Nieto (2021). “Evolution of Data Formats in Very-High-Energy Gamma-Ray Astronomy”. In: *Universe* 7.10, p. 374. DOI: 10.3390/universe7100374.
- Ohm, S., C. van Eldik, and K. Egberts (2009). “ γ /hadron separation in very-high-energy γ -ray astronomy using a multivariate analysis method”. In: *Astroparticle Physics* 31.5, pp. 383–391. DOI: 10.1016/j.astropartphys.2009.04.001.
- Ohmura, T. et al. (2021). “Continuous Jets and Backflow Models for the Formation of W50/SS 433 in Magnetohydrodynamics Simulations”. In: *ApJ* 910.2, 149, p. 149. DOI: 10.3847/1538-4357/abe5a1.
- Olivera-Nieto, L. et al. (2021). “Muons as a tool for background rejection in imaging atmospheric Cherenkov telescope arrays”. In: *The European Physical Journal C* 81.12. DOI: 10.1140/epjc/s10052-021-09869-0.
- Olivera-Nieto, L. et al. (2022). “Background rejection using image residuals from large telescopes in imaging atmospheric Cherenkov telescope arrays”. In: *The European Physical Journal C* 82.12. DOI: 10.1140/epjc/s10052-022-11067-5.
- Padovani, P. et al. (2017). “Active galactic nuclei: what’s in a name?” In: *A&A Rev.* 25.1, 2, p. 2. DOI: 10.1007/s00159-017-0102-9.
- Padovani, Paolo (2017). “On the two main classes of active galactic nuclei”. In: *Nature Astronomy* 1, 0194, p. 0194. DOI: 10.1038/s41550-017-0194.
- Panferov, Alexander A. (2017). “Jets of SS 433 on scales of dozens of parsecs”. In: *A&A* 599, A77, A77. DOI: 10.1051/0004-6361/201629256.
- Parsons, R. D. and H. Schoorlemmer (2019). “Systematic differences due to high energy hadronic interaction models in air shower simulations in the 100 GeV–100 TeV range”. In: *Phys. Rev. D* 100.2, 023010, p. 023010. DOI: 10.1103/PhysRevD.100.023010.
- Parsons, R.D. and J.A. Hinton (2014). “A Monte Carlo template based analysis for air-Cherenkov arrays”. In: *Astroparticle Physics* 56, pp. 26–34. ISSN: 0927-6505. DOI: <http://dx.doi.org/10.1016/j.astropartphys.2014.03.002>.
- Pastor-Gutiérrez, Á. et al. (2021). “Sub-TeV hadronic interaction model differences and their impact on air showers”. In: *European Physical Journal C* 81.4, 369, p. 369. DOI: 10.1140/epjc/s10052-021-09160-2.

- Peter, W. and D. Eichler (1993). "Hydrodynamic Collimation of Precessing Jets". In: *ApJ* 417, p. 170. DOI: 10.1086/173300.
- Picchi, Paolo et al. (2020). "An optical spectroscopic and polarimetric study of the micro-quasar binary system SS 433". In: *A&A* 640, A96, A96. DOI: 10.1051/0004-6361/202037960.
- Popescu, C. C. et al. (2017). "A radiation transfer model for the Milky Way: I. Radiation fields and application to high-energy astrophysics". In: *MNRAS* 470.3, pp. 2539–2558. DOI: 10.1093/mnras/stx1282.
- Porth, Oliver et al. (2019). "The Event Horizon General Relativistic Magnetohydrodynamic Code Comparison Project". In: *ApJS* 243.2, 26, p. 26. DOI: 10.3847/1538-4365/ab29fd.
- Predehl, P. et al. (2021). "The eROSITA X-ray telescope on SRG". In: *A&A* 647, A1, A1. DOI: 10.1051/0004-6361/202039313.
- Pudritz, R. E. and C. A. Norman (1983). "Centrifugally driven winds from contracting molecular disks". In: *ApJ* 274, pp. 677–697. DOI: 10.1086/161481.
- (1986). "Bipolar Hydromagnetic Winds from Disks around Protostellar Objects". In: *ApJ* 301, p. 571. DOI: 10.1086/163924.
- Rasul, Kajwan et al. (2019). "Gamma-rays from SS433: evidence for periodicity". In: *MNRAS* 485.2, pp. 2970–2975. DOI: 10.1093/mnras/stz559.
- Rees, M. J. (1966). "Appearance of Relativistically Expanding Radio Sources". In: *Nature* 211.5048, pp. 468–470. DOI: 10.1038/211468a0.
- (1967). "Studies in radio source structure-I. A relativistically expanding model for variable quasi-stellar radio sources". In: *MNRAS* 135, p. 345. DOI: 10.1093/mnras/135.4.345.
- Rees, Martin J. (1998). "Astrophysical Evidence for Black Holes". In: *Black Holes and Relativistic Stars*. Ed. by Robert M. Wald, p. 79.
- Reich, W. et al. (1984). "A radio continuum survey of the galactic plane at 11cm wavelength. I. The area $357.4 < \text{or} = L < \text{or} = 76$, $-1.5 < \text{or} = B < \text{or} = 1.5$." In: *A&AS* 58, pp. 197–248.
- Reich, W. et al. (1990). "A radio continuum survey of the Galactic Plane at 11 cm wavelength. II. The area $358\text{deg} \leq L \leq 76\text{deg}$, $-5\text{deg} \leq B \leq 5\text{deg}$ ". In: *A&AS* 85, pp. 633–690.
- Rieger, Frank M. and Peter Duffy (2004). "Shear Acceleration in Relativistic Astrophysical Jets". In: *ApJ* 617.1, pp. 155–161. DOI: 10.1086/425167.
- Roberts, David H. et al. (2008). "Structure and Magnetic Fields in the Precessing Jet System SS 433. I. Multifrequency Imaging from 1998". In: *ApJ* 676.1, pp. 584–593. DOI: 10.1086/527544.
- Roberts, David H. et al. (2010). "Structure and Magnetic Fields in the Precessing Jet System SS 433. II. Intrinsic Brightness of the Jets". In: *ApJ* 719.2, pp. 1918–1925. DOI: 10.1088/0004-637X/719/2/1918.
- Robinson, E. L. (1976). "The structure of cataclysmic variables." In: *ARA&A* 14, pp. 119–142. DOI: 10.1146/annurev.aa.14.090176.001003.
- Rosado, M. et al. (2021). "Kinematics of the western filament of W50". In: *MNRAS* 506.3, pp. 4263–4274. DOI: 10.1093/mnras/stab1890.
- Rossi, Bruno and Kenneth Greisen (1941). "Cosmic-Ray Theory". In: *Reviews of Modern Physics* 13.4, pp. 240–309. DOI: 10.1103/RevModPhys.13.240.
- Ruiz Velasco, Edna L. (2021). "Search and first detection of very-high-energy photons in gamma-raybursts: an analysis with HAWC and H.E.S.S." PhD thesis. University of Heidelberg.
- Rybicki, George B. and Alan P. Lightman (1986). *Radiative Processes in Astrophysics*.
- Safi-Harb, Samar and Hakki Ögelman (1997). "ROSAT and ASCA Observations of W50 Associated with the Peculiar Source SS 433". In: *ApJ* 483.2, pp. 868–881. DOI: 10.1086/304274.

- Safi-Harb, Samar et al. (2022). "Hard X-Ray Emission from the Eastern Jet of SS 433 Powering the W50 "Manatee" Nebula: Evidence for Particle Reacceleration". In: *ApJ* 935.2, 163, p. 163. DOI: 10.3847/1538-4357/ac7c05.
- Sakemi, Haruka et al. (2021). "Energy estimation of high-energy particles associated with the SS 433/W 50 system through radio observation at 1.4 GHz". In: *PASJ* 73.3, pp. 530–544. DOI: 10.1093/pasj/psab018.
- Salpeter, E. E. (1964). "Accretion of Interstellar Matter by Massive Objects." In: *ApJ* 140, pp. 796–800. DOI: 10.1086/147973.
- Sams, Bruce J., Andreas Eckart, and Rashid Sunyaev (1996). "Near-infrared jets in the Galactic microquasar GRS1915+105". In: *Nature* 382.6586, pp. 47–49. DOI: 10.1038/382047a0.
- Schmidt, M. (1963). "3C 273 : A Star-Like Object with Large Red-Shift". In: *Nature* 197.4872, p. 1040. DOI: 10.1038/1971040a0.
- Schwartz, R. D. (1983). "Herbig-haro objects." In: *ARA&A* 21, pp. 209–237. DOI: 10.1146/annurev.aa.21.090183.001233.
- Seifina, Elena and Lev Titarchuk (2010). "On the Nature of the Compact Object in SS 433: Observational Evidence of X-ray Photon Index Saturation". In: *ApJ* 722.1, pp. 586–604. DOI: 10.1088/0004-637X/722/1/586.
- Seward, F. et al. (1980). "Diffuse X-ray emission from the jets of SS433". In: *Nature* 287.5785, pp. 806–808. DOI: 10.1038/287806a0.
- Shakura, N. I. and R. A. Sunyaev (1973). "Black holes in binary systems. Observational appearance." In: *A&A* 24, pp. 337–355.
- Shkovskii, I. S. (1981). "Mass loss by SS 433, and its effect on the X-ray and radio emission." In: *Soviet Ast.* 25, pp. 315–319.
- Sikora, Marek and Mitchell C. Begelman (2013). "Magnetic Flux Paradigm for Radio Loudness of Active Galactic Nuclei". In: *ApJ* 764.2, L24, p. L24. DOI: 10.1088/2041-8205/764/2/L24.
- Sirca, Simon (2016). *Probability for Physicists*. DOI: 10.1007/978-3-319-31611-6.
- Spencer, R. E. (1979). "A radio jet in SS433". In: *Nature* 282.5738, pp. 483–484. DOI: 10.1038/282483a0.
- Stephenson, C. B. and N. Sanduleak (1977). "New H-alpha emission stars in the Milky Way." In: *ApJS* 33, pp. 459–469. DOI: 10.1086/190437.
- Strong, Andrew W., Igor V. Moskalenko, and Vladimir S. Ptuskin (2007). "Cosmic-Ray Propagation and Interactions in the Galaxy". In: *Annual Review of Nuclear and Particle Science* 57.1, pp. 285–327. DOI: 10.1146/annurev.nucl.57.090506.123011.
- Su, Yang et al. (2018). "The Large-scale Interstellar Medium of SS 433/W50 Revisited". In: *ApJ* 863.1, 103, p. 103. DOI: 10.3847/1538-4357/aad04e.
- Sudoh, Takahiro, Yoshiyuki Inoue, and Dmitry Khangulyan (2020). "Multiwavelength Emission from Galactic Jets: The Case of the Microquasar SS433". In: *ApJ* 889.2, 146, p. 146. DOI: 10.3847/1538-4357/ab6442.
- Sun, Xiao-Na et al. (2019). "Tentative evidence of spatially extended GeV emission from SS433/W50". In: *A&A* 626, A113, A113. DOI: 10.1051/0004-6361/201935621.
- Tavani, M. et al. (2008). "The AGILE space mission". In: *Nuclear Instruments and Methods in Physics Research A* 588.1-2, pp. 52–62. DOI: 10.1016/j.nima.2008.01.023.
- Urry, C. Megan and Paolo Padovani (1995). "Unified Schemes for Radio-Loud Active Galactic Nuclei". In: *PASP* 107, p. 803. DOI: 10.1086/133630.
- Velázquez, P. F. and A. C. Raga (2000). "A numerical simulation of the W 50-SS 433 system". In: *A&A* 362, pp. 780–785.

- Velusamy, T. and M. R. Kundu (1974). "Observations of intensity and linear polarization in supernova remnants at 11 cm wavelength." In: *A&A* 32, pp. 375–390.
- Verbunt, Frank (1993). "Origin and Evolution of X-Ray Binaries and Binary Radio Pulsars". In: *Annual Review of Astronomy and Astrophysics* 31.1, pp. 93–127. DOI: 10.1146/annurev.aa.31.090193.000521.
- Vermeulen, R. C. et al. (1993a). "A series of VLBI images of SS 433 during the outbursts." In: *A&A* 270, pp. 177–188.
- Vermeulen, R. C. et al. (1993b). "Daily spectra of radio flares from SS 433 in may/june 1987." In: *A&A* 270, pp. 189–199.
- Vermeulen, R. C. et al. (1993c). "Monitoring of very rapid changes in the optical spectrum of SS 433 in may/june 1987." In: *A&A* 270, pp. 204–222.
- Vieu, Thibault and Brian Reville (2022). "Massive star cluster origin for the galactic cosmic ray population at very-high energies". In: *arXiv e-prints*, arXiv:2211.11625, arXiv:2211.11625.
- Virtanen, Pauli et al. (2020). "SciPy 1.0: Fundamental Algorithms for Scientific Computing in Python". In: *Nature Methods* 17, pp. 261–272. DOI: 10.1038/s41592-019-0686-2.
- Waisberg, Idel et al. (2019a). "Collimated radiation in SS 433. Constraints from spatially resolved optical jets and Cloudy modeling of the optical bullets". In: *A&A* 624, A127, A127. DOI: 10.1051/0004-6361/201834747.
- Waisberg, Idel et al. (2019b). "Super-Keplerian equatorial outflows in SS 433. Centrifugal ejection of the circumbinary disk". In: *A&A* 623, A47, A47. DOI: 10.1051/0004-6361/201834746.
- Walter, M. and A. W. Wolfendale (2012). "Early history of cosmic particle physics". In: *Eur. Phys. J. H* 37, pp. 323–358. DOI: 10.1140/epjh/e2012-30020-1.
- Watson, M. G. et al. (1983). "The X-ray lobes of SS 433." In: *ApJ* 273, pp. 688–696. DOI: 10.1086/161403.
- Watson, M. G. et al. (1986). "Doppler-shifted X-ray line emission from SS 433." In: *MNRAS* 222, pp. 261–271. DOI: 10.1093/mnras/222.2.261.
- Weekes, T. C. (1988). "Very high energy gamma-ray astronomy." In: *Phys. Rep.* 160.1, pp. 1–121. DOI: 10.1016/0370-1573(88)90177-9.
- Weekes, T. C. et al. (1989). "Observation of TeV Gamma Rays from the Crab Nebula Using the Atmospheric Cerenkov Imaging Technique". In: *ApJ* 342, p. 379. DOI: 10.1086/167599.
- Xing, Yi et al. (2019). "Fermi Observation of the Jets of the Microquasar SS 433". In: *ApJ* 872.1, 25, p. 25. DOI: 10.3847/1538-4357/aafc60.
- Yamamoto, Hiroaki et al. (2022). "Physical properties of the molecular cloud, N4, in SS 433: Evidence for an interaction of molecular cloud with the jet from SS 433". In: *PASJ* 74.3, pp. 493–509. DOI: 10.1093/pasj/psac012.
- Young, David S. de (2002). *The physics of extragalactic radio sources*.
- Yun Carcamo, Sohyoun, Andrew Smith, and HAWC Team (2022). "Performance of HAWC with the improved reconstruction algorithm". In: *APS April Meeting Abstracts*. Vol. 2022. APS Meeting Abstracts, S17.060.
- Zacks, S. (1975). *The theory of statistical inference*. Ed. by Wiley. Wiley.
- Zatsepin, G. T. and V. A. Kuz'min (1966). "Upper Limit of the Spectrum of Cosmic Rays". In: *Soviet Journal of Experimental and Theoretical Physics Letters* 4, p. 78.
- Zavala, Jesús et al. (2008). "Three-dimensional hydrodynamical simulations of the large-scale structure of W50-SS433". In: *MNRAS* 387.2, pp. 839–844. DOI: 10.1111/j.1365-2966.2008.13281.x.
- Zel'dovich, Ya. B. and I. D. Novikov (1965). "Mass of Quasi-Stellar Objects". In: *Soviet Physics Doklady* 9, p. 834.

Bibliography of L. Olivera-Nieto

Publications

I am listed as an author on a total of 37 publications, see <https://orcid.org/0000-0002-9105-0518> for a full list. Below is a selection of publications in which I am either a corresponding author or made large contributions to.

- **Olivera-Nieto, L**, et al. (2021). "Muons as a tool for background rejection in imaging atmospheric Cherenkov telescope arrays". *The European Physical Journal C* 81.12.
- Nigro, Cosimo, Tarek Hassan, and **Laura Olivera-Nieto** (2021). "Evolution of Data Formats in Very-High-Energy Gamma-Ray Astronomy". *Universe* 7.10, p. 374
- Albert, A.,..., **Olivera-Nieto, L**, et al. (2022). "Validation of standardized data formats and tools for ground-level particle-based gamma-ray observatories". *Astronomy and Astrophysics* 667, A36.
- **Olivera-Nieto, L**, et al. (2022). "Background rejection using image residuals from large telescopes in imaging atmospheric Cherenkov telescope arrays". Accepted for publication in the *European Physical Journal C*.

In preparation

- H.E.S.S. Collaboration, ..., **Olivera-Nieto, L**, et al. "SS 433 large-scale jet dynamics revealed". *Prepared for submission* to *Science*.
- *Gammapy* Collaboration, ..., **Olivera-Nieto, L**, et al. "*Gammapy*: A Python package for gamma-ray astronomy". *Prepared for submission* to *Astronomy and Astrophysics*.


Conference proceedings

- **Olivera-Nieto, L**, et al. "Muons as a tool for background rejection in imaging atmospheric Cherenkov telescope arrays". 37th International Cosmic Ray Conference, July 2021, id.727
- **Olivera-Nieto, L**, for the HAWC Collaboration. "Standardized formats for gamma-ray analysis applied to HAWC observatory data". 37th International Cosmic Ray Conference, July 2021, id.754

Conference contributions





- **Olivera-Nieto, L.** "Muons as a tool for background rejection in Imaging Atmospheric Cherenkov Telescope arrays". Spring meeting of the Deutsche Physikalische Gesellschaft, March 2022.
- **Olivera-Nieto, L.** "The jets of SS 433 as seen by H.E.S.S. ". 7th Heidelberg International Symposium on High-Energy Gamma-Ray Astronomy, Barcelona July 2022.
- **Olivera-Nieto, L.** "Highlights from Gamma Ray Atmospheric Cherenkov Telescopes". *Invited talk*. XVIII Vulcano Workshop on Frontier Objects in Astrophysics and Particle Physics, Vulcano Island November 2022.


List of Figures


- 1.1 **The jets of Cygnus A.** 5 GHz frequency image of the jets of Cygnus A made with data from the VLA. The jets extend out to kpc distances from the core. Figure from Carilli and Barthel (1996). 6
- 1.2 **The cosmic ray energy spectrum measured by several experiments.** The measured fluxes of electrons, gamma-rays and neutrinos are also shown. The spectral features described in the text are marked, as well as the particle rates expected for different level of flux. Figure by Carmelo Evoli, <https://doi.org/10.5281/zenodo.4396125>. 10
- 1.3 **The Hillas condition.** Size and magnetic field strength of possible sites of particle acceleration. The diagonal represents the boundary below which objects can't accelerate protons to 10^{20} eV. Figure from Hillas (1984). 13
- 1.4 **Schematic depiction of second-order Fermi acceleration.** A particle with energy E_1 enters a magnetized cloud, which results in it undergoing several scatterings until it leaves, with a new trajectory θ_2 and energy E_2 . Figure by Cosimo Nigro  (Nigro, 2019). 14
- 1.5 **Schematic depiction of shock acceleration.** Bulk velocities in the rest frame of the shock are shown with orange dashed lines, particle trajectories in red dashed lines and magnetic field lines as black arrows. Figure from Matthews et al. (2020). 16
- 1.6 **Synchrotron radiation from electrons. Left:** Spectrum of the electrons producing the radiation. The normalization is such that the total energy above 10 MeV is 10^{33} erg. **Right:** Resulting synchrotron radiation spectrum for different intensities of the magnetic field. Note that the quantity depicted is $E^2 \frac{dN}{dE}$ 21
- 1.7 **IC radiation from electrons. Left:** Energy density of the target blackbody photons for different temperatures. **Right:** Resulting IC radiation spectrum for the different target fields. The electron spectrum is the same as shown in Figure 1.6. 23
- 2.1 **The SS 433 system.** Schematic diagram showing the main components of the SS 433 system. Image credit: ESO. 28

- 2.2 **Interaction of the SS 433 jets with W50.** **a:** Radio image of W50 at 11 cm by the Effelsberg radio telescope (Reich et al., 1984, 1990; Furst et al., 1990) with X-ray contours overlaid in white. The X-ray regions defined by Safi-Harb and Ögelman (1997) are marked with crosses. The ones in the eastern jet have an *e* in their name, whereas the ones in the western jet have a *w*. **b:** X-ray image of SS 433 and the outer jets by the ROSAT satellite (Brinkmann et al., 1996; Safi-Harb and Ögelman, 1997) with radio contours overlaid in white. Figure adapted from Goodall et al. (2011a) using publicly available data. 29
- 2.3 **Radio images of the precessing jets.** **a:** Total intensity image at 4.85 GHz observed with the VLA. Overlaid is the projection on the sky of two oppositely directed jets with the inferred SS 433 parameters. **b:** Sobel-filtered version of the image shown in **a**. Figure from Blundell and Bowler (2004). 31
- 2.4 **Equatorial outflow from SS 433.** Total intensity image at 4.99 GHz of SS 433 on March 7th 1998, combining VLBA, MERLIN, and VLA data. Figure from Blundell et al. (2001). 32
- 2.5 **Time evolution of the radio filaments.** . Radio observations of W50 in 1984 (Elston and Baum, 1987) and 1996 (Dubner et al., 1998) with the radio filaments selected for the study of their proper motions highlighted. Figure adapted from Goodall et al. (2011b). 33
- 2.6 **H α spectra of SS 433 in two consecutive days.** Fragments of two spectra of SS 433. Figure from Vermeulen et al. (1993c). 34
- 2.7 **Check of the kinematic model over twenty years.** Measured Doppler shifts, model prediction, and residuals as a function of precessional phase for the approaching (left panel) and receding (right panel) jets. Figures taken from Eikenberry et al. (2001). 35
- 2.8 **Optical-radio correlation of the W50 filaments** Combined image of the negative continuum-subtracted mosaic of W50 in the light of H α + [N II] and the radio emission at 1465 MHz (solid lines). The 1465 MHz (Dubner et al., 1998) radio contours scale linearly. Figure taken from Boumis et al. (2007). 36
- 2.9 **Composite color image of the SS 433/W50 complex.** Multi-wavelength image of the W50 nebula. Red: radio (Dubner et al., 1998); green: optical (Boumis et al., 2007); yellow: soft X-rays (0.5-1 keV); magenta: medium energy X-rays (1-2 keV); cyan: hard X-ray emission (2-12 keV). Figure from Safi-Harb et al. (2022). 37

- 2.10 **The *Fermi*-LAT view of SS 433.** *Fermi*-LAT map of the SS 433 region in the 0.1-300 GeV range during the off-peak phase of PSR J1907+0602. Background sources have been modeled and subtracted. The color scale shows the TS value, the square root of which gives an approximate detection significance. The X-ray and radio emission from the system is represented with blue and white contours respectively. Figure from Li et al. (2020), see also Fang et al. (2020). 39
- 2.11 **The pulsating excess Fermi J1913+0515.** **Top:** TS maps (see Section 3.5.2) of the SS 433 region in the 1-300 GeV band for the precessional phases 0.0-0.5 (left) and 0.5-1.0 (right). **Bottom:** Precessional phase light curve of Fermi J1913+0515 in the 1-300 GeV band for bin sizes of 0.5 (blue) and 0.25 (red). Figure from Li et al. (2020). 40
- 2.12 **Detection of TeV emission from the outer jets.** HAWC significance map of the SS 433 region showing the two significant hotspots. This map is computed after the fitting and subtraction of emission from the spatially extended source MGRO J1908+06. The jet regions e1, e2, e3, w1 and w2 defined using the X-ray data are indicated, as well as the location of the central binary. From Abeysekara et al. (2018). 41
- 2.13 **Modeling the nearby extended source MGRO J1908+06.** HAWC significance map of the entire SS 433 FoV including the region of MGRO J1908+06. The left panel shows the significance map without any modeling, whereas the right panel shows the residual from subtracting the best-fit model of MGRO J1908+06. The dashed square corresponds to the sky portion shown in Figure 2.12. From Abeysekara et al. (2018). 42
- 2.14 **Multi-wavelength SED of the eastern jet.** The data include radio, soft X-ray, hard X-ray and TeV gamma-ray upper limits, and HAWC measurements of e1. Figure from Abeysekara et al. (2018). 43
- 2.15 **Simulations of the interaction between a jet and a SNR shell.** The top panel shows the interaction of a non-precessing jet with a SNR shell, which results in a morphology consistent with the observed shape of W50 (purple outline). The bottom panel shows the interaction of a jet with the observed precession angle observed in the inner jets of SS 433 today and a SNR shell. As can be seen, the elongated shape of W50 is not reproduced. Figures adapted from Goodall et al. (2011a). 44


- 3.1 **EM shower.** Schematic illustration of the development of an EM shower in the Heitler model. In this sketch the primary particle is a gamma-ray of energy E_0 , which interacts with a nucleus in the atmosphere, after which a cascade develops. After each step of $d = \ln(2)\lambda_e$, the number of particles doubles, until the point where ionization losses become dominant. Image credit: Edna Ruiz Velasco  (Ruiz Velasco, 2021). 51
- 3.2 **Hadronic shower.** Schematic illustration of the development of an hadronic shower. The processes involved are more varied than in the EM case. Image credit: Edna Ruiz Velasco  (Ruiz Velasco, 2021). . . . 52
- 3.3 **Comparison between simulated EM and hadronic showers.** Green lines represent photon trajectories, blue represent electrons, light red muons and dark red protons. **Top:** Ten simulated showers initiated by a 300 GeV gamma-ray. **Bottom:** Ten simulated showers initiated by a proton of the same energy. Figure from De Naurois and Mazin (2015). 53
- 3.4 **Cherenkov radiation.** Sketch of the emission from a moving particle in a dielectric medium at different speeds. Image credit: Armelle Jardin-Blicq  (Jardin-Blicq, 2019). 54
- 3.5 **The IACT technique.** Illustration showing the basics of the IACT technique. A gamma-ray enters the atmosphere and initiates an EAS, which in turn produces a cone of blue Cherenkov light. Telescopes inside this light pool detect the light and image the EAS. An example shower image in an IACT camera can be seen in the bottom left of the figure. Image credit: Richard White . 55
- 3.6 **H.E.S.S..** Picture of the completed H.E.S.S. array in Namibia. Image credit: H.E.S.S. Collaboration. 56
- 3.7 **Hillas parameters.** Sketch illustrating the Hillas parameterization of the shower images. The shape recorded by the camera is approximated as an ellipse, with a certain width and length. The major axis of this ellipse indicates the direction of the incoming shower, which can be reconstructed with higher accuracy if the same shower is imaged by more than one telescopes as shown in the diagram. Figure from Aharonian et al. (2006). 59
- 3.8 **Performance of the ImPACT reconstruction.** Comparison of the energy bias (top left), energy resolution (top right), and angular resolution as a function of both energy (bottom left) and observation zenith angle (bottom left) for the reconstruction using just the Hillas parameters (black and blue lines) and the one using the ImPACT method (red lines). The ImPACT reconstruction outperforms the simpler methods in all cases. Adapted from Parsons and Hinton (2014). 60

- 3.9 **Distributions of the input parameters to the BDTs.** The figure shows the distribution of each of the parameters considered by the multivariate approach for simulated gamma-rays (black) and background from off-runs (red). The parameters shown, from top to bottom and left to right are: the Hillas width and length derived from gamma-ray simulations and averaged over telescopes (MRSW, MRSL), the Hillas width and length derived from background data and averaged over telescopes (MRSWO, MRSLO), the height of shower maximum (X_{\max}) and the spread in energy reconstruction averaged over the telescopes. Figure from Ohm et al. (2009) 61
- 3.10 **Effective area.** *Left:* Example effective area table for a H.E.S.S. observation at 45° zenith. *Right:* Effective area curves as a function of energy for some selected offsets. 63
- 3.11 **Energy dispersion matrix.** *Left:* Example energy dispersion matrix for a H.E.S.S. observation at 45° zenith. *Right:* Energy bias derived from the energy dispersion matrix. 64
- 3.12 **Point-spread function.** *Left:* Example PSF at a given energy and offset for a H.E.S.S. observation at 45° zenith. *Right:* 68% and 95% containment radius as a function of energy for offset 0.5° 64
- 3.13 **Background model.** *Left:* Example background model table for a H.E.S.S. observation at 45° zenith. *Right:* Background rates as a function of offset from the pointing position for several values of the energy. 65
- 3.14 **Ring and reflected background.** *Left:* Illustration of the ring method. The red rings illustrate the regions in which the background is estimated for two positions in the FoV. The ring size in each case is adaptively enlarged to ensure an adequate background estimate. The black circle represents a 2° FoV around the pointing position (black cross). *Right:* Illustration of reflected region background estimation method. The empty red circle represents the ON region, whereas the filled ones represent the OFF regions from which the background level is measured. Adapted from H.E.S.S. Collaboration et al. (2018). 67
- 3.15 **The HAWC observatory.** Picture of the completed HAWC array including the outrigger upgrade. Image credit: The HAWC Collaboration. 69
- 3.16 f_{Hit} **bins and event energy.** True energy distribution of photons from a simulated source with Crab Nebula-like spectrum and declination for the different f_{Hit} bins (indicated with \mathcal{B}), summed across a transit of the source. From Abeysekara et al. (2017). 71
- 3.17 **The case for a wide-field observatory in the Southern Hemisphere.** The HAWC full-sky significance map is shown together with the expected FoV of SWGO. Image credit: Richard White . 72

- 3.18 **Counts, background and significance maps.** *Left:* Counts sky-map of the Crab Nebula region. *Middle:* Expected background counts map. *Right:* Significance of the excess counts over the background of nearly isotropic cosmic rays. The top-hat filter with radius r_c used to smooth the counts and background maps is drawn in the image as a white circle. 75
- 3.19 **Excluded significance map.** *Left:* Significance map with the source region masked. As expected, no regions above and below 5σ are seen. *Right:* Histogram of the significance values outside of the mask (red) and a Gaussian fit (black). As expected, the mean and width of the Gaussian are roughly 0 and 1. This means the background was correctly estimated. 75
- 3.20 **1D spectral analysis.** *Left:* Measured excess counts in the extraction region (blue) compared to the predicted excess counts of the best fit model (orange). The residuals are shown in the bottom panel. *Right:* Best-fit power law model including statistical error bands. 77
- 3.21 **Significance map after source subtraction.** *Left:* Predicted model counts over the entire energy range for the best-fit 3D model. *Middle:* Significance map after the best fit model has been subtracted. *Right:* Histogram of the significance values of the entire map (red) and a Gaussian fit (black). As expected, the mean and width of the Gaussian are roughly 0 and 1. This means the source was correctly modeled. 78
- 3.22 **Comparison of 3D and 1D spectra.** Best-fit spectral model including statistical error bands for the 1D (teal) and 3D (yellow) analysis. 78
- 3.23 **Flux points and upper limits.** Flux points and upper limits from the Crab Nebula spectral measurement. 79
- 3.24 **Performance of current and future experiments.** *Top:* Estimated and projected sensitivity for current and future gamma-ray instruments. The dark blue curve represents the existing IACTs. The green and black lines show the sensitivity of HAWC and the LHAASO array respectively. The upcoming CTA south site is depicted by the light blue line, and the sensitivity of the SWGO is expected to lie between the solid and dashed orange lines. *Bottom:* Estimated and projected angular resolution for current and future gamma-ray instruments. The dark gray curve represents the existing IACTs, such as H.E.S.S.. The dark blue line shows the resolution of WCD arrays such as HAWC. The black line shows the angular resolution of the LHAASO. Values for the upcoming CTA are depicted by the light blue line, whereas the expected resolution of the SWGO is represented by the orange band. Figures by Jim Hinton . 80

- 6.1 **Acceptance-corrected exposure.** The color scale indicates the amount of observation time corrected for the radial dependence of the system acceptance. The figure shows this quantity for the H.E.S.S. I (**a**), H.E.S.S. IU (**b**), H.E.S.S. IU+CT5 (**c**) and total (**d**) data sets. Sky regions with no observation time are depicted in gray. The black contours outline the X-ray emission from the jets (Brinkmann et al., 1996; Safi-Harb and Ögelman, 1997) as a visual reference. 120
- 6.2 **Total counts and background map.** **a:** Total measured counts in the FoV for the entire data set. As can be seen, due to the very low flux of VHE sources, the number of measured counts is relatively low. In order to identify structures, smoothing is usually applied. **b:** Map of predicted background counts for the entire FoV derived using the combination of the IRF background model and the FoV background method. 122
- 6.3 **Characterization of MGRO J1908+06.** **a:** predicted counts from the best-fit Gaussian spatial model of MGRO J1908+06. **b:** Best-fit spectral model with flux points for MGRO J1908+06. Errors shown here are statistical only. 123
- 6.4 **Significance map before and after modeling and subtracting MGRO J1908+06.** The figure shows the statistical significance of the gamma-ray excess measured in the full FoV before (**a**) and after (**b**) fitting and subtracting the emission from the nearby extended source MGRO J1908+06. The solid white contours show the radio emission from the surrounding nebula W50 measured by the Effelsberg telescope (Reich et al., 1984, 1990; Furst et al., 1990). 124
- 6.5 **Significance map of the SS 433 region.** The figure shows the statistical significance of the gamma-ray excess measured in the SS 433 region after the fitting and subtraction of the emission from the nearby extended source MGRO J1908+06. The solid cyan contours show the X-ray emission measured by the ROSAT satellite (Brinkmann et al., 1996; Safi-Harb and Ögelman, 1997). The locations of the X-ray regions $w1$, $w2$, $e1$, $e2$ and $e3$ are marked with white crosses. The 68% containment region of the PSF is denoted with a white circle. 125
- 6.6 **Spatial modeling of the jets.** The top two panels show the prediction of the best-fit model that includes the MGRO J1908+06 component (see Figures 6.3 and 6.4) and the western jet (**a**) as well as the significance map after subtracting these two components (**b**). The bottom two panels have the same structure but with the complete model that includes also the eastern jet (**c**). There are no remaining significant hotspots in the residual significance map (**d**), which means the region is well modeled. 127

- 6.7 **Energy-dependent morphology.** The figure shows the statistical significance of the gamma-ray excess measured in the SS 433 region after the fitting and subtraction of the emission from the nearby extended source MGRO J1908+06 for three different gamma-ray energy ranges. The solid cyan contours show the X-ray emission measured by the ROSAT satellite (Brinkmann et al., 1996; Safi-Harb and Ögelman, 1997). The 68% containment region of the PSF for each energy range is denoted with a white circle. 128
- 6.8 **PSF verification for the H.E.S.S. I era.** The title of each of the panels indicates the zenith range, the offset angle and the energy range. In each panel the PSF derived from gamma-ray simulations (MC PSF) is compared to the excess events measured from the Crab Nebula (data PSF) as a function of radial offset from its nominal position. Note that the number of runs in this data set is very low. The bottom right panel has no measured excess due to low statistics. 129
- 6.9 **PSF verification for the H.E.S.S. IU era.** The title of each of the panels indicates the zenith range, the offset angle and the energy range. In each panel the PSF derived from gamma-ray simulations (MC PSF) is compared to the excess events measured from the Crab Nebula (data PSF) as a function of radial offset from its nominal position. 130
- 6.10 **Best-fit positions in different energy bands.** The best-fit position resulting from the 3D modeling of the gamma-ray excess in each of the energy bands. The left panel corresponds to the western jet and the right panel to the eastern. The position of SS 433 is indicated in both for reference with a black star. 131
- 6.11 **Distance to the central binary in energy bands.** Distance between the best-fit position resulting from the 3D modeling of the gamma-ray excess in each of the energy bands and the central binary for the eastern (green) and western (orange) jets. The location of the base of the outer jets is marked with a dashed line for each side. The distances in pc is calculated assuming a distance of 5.5 kpc to the system. 131
- 6.12 **Flux profiles of the jets.** Measured flux in spatial bins alongside the axis joining both jets through the central binary for three different energy bands. A gray dashed line is drawn at zero for reference. 132
- 6.13 **Spectra of the jets.** Resulting best-fit spectral model from the 1D spectral extraction of the eastern (a) and western (b) jets. The dark shaded areas and flux points represent the statistical errors only, whereas the lighter colors include the systematic uncertainties. The flux measured by HAWC for each jet is shown as well (Abeysekara et al., 2018). The spectra from both jets is shown in panel c for easy comparison. 133

- 6.14 **Flux maps for different phase bins.** Integrated flux maps after the subtraction of the emission from MGRO J1908+06 in two bins of the jet precession phase indicated in the bottom right. The location of Fermi J1913+0515 is marked with a green circle and cross. The blue contours show the X-ray emission measured by the ROSAT satellite (Brinkmann et al., 1996; Safi-Harb and Ögelman, 1997). 134
- 6.15 **Central source upper limits.** Spectral upper limits from the core region. The previously most constraining limits from MAGIC and H.E.S.S. Collaborations et al., 2018 are shown in gray. 135
- 6.16 **Systematic uncertainties on the background.** **a:** Significance map multiplied by the exclusion mask defined to covering all expected sources. **b:** Distribution of the significance values outside of the exclusion mask (red line). A Gaussian function is fitted to the distribution (black line), with the resulting mean and width listed in the top left corner. The size of the deviation from the expected width of 1 is used to assess the impact of background systematic effects in the significance values. 135
- 6.17 **Systematic uncertainties on the background for different energy bands.** Distribution of the significance values outside of an exclusion mask covering all expected sources (red line) for each of the used energy ranges. A Gaussian function is fitted each the distribution (black line), with the resulting mean and width listed in the top left corner of each panel. The size of the deviation from the expected width of 1 is used to assess the impact of background systematic effects in the significance values. 136
- 7.1 **X-ray flux maps and spectra.** *Top:* Chandra (top) and XMM (bottom) flux maps of the SS 433 regions. The spectral extraction regions are marked in green for the eastern case and blue for the western case. Image and data analysis by Naomi Tsuji  *Bottom:* Resulting flux points for each of the jets, before and after the correction described in the text was applied. 141
- 7.2 **Ambient radiation fields.** **a:** Energy density of the ambient radiation fields at the location of SS 433 (teal), the east (yellow) and the west (red) jets assuming a distance of 5.5 kpc to Earth.**b:** Energy densities shown in panel **a** divided by the value for SS 433 in order to highlight the differences between the two jets. **c:** Energy densities at the SS 433 position for different values of the distance to Earth divided by the curve assuming 5.5 kpc. 143

7.3	Multi-wavelength SED of the jets. Multi-wavelength SED of both the eastern (a) and western (b) outer jets. The low energy component is due to synchrotron emission (see Section 1.5.1), while high energy photons are produced due to IC radiation (see Section 1.5.1). The best-fit model for each of the jets is shown with a solid line. The bottom panels show the residuals for the east (c) and west (d) case.	143
7.4	Model dependency on total age. Gamma-ray emission predicted by the model as a function of the total system age compared to the H.E.S.S. and HAWC flux points and Fermi-LAT upper limits.	144
7.5	Cooling and acceleration timescales. Cooling timescale as a function of electron energy for due to IC (yellow), synchrotron (blue) and total (black dashed) for the eastern (left) and western (right) jets. Dotted lines display the acceleration timescales for different values of η . The electron energy range allowed by the data for the cutoff energy of the electron spectrum is indicated with a gray band.	147
7.6	Electron energy contributions. Contribution of different electron energy ranges to the total predicted gamma-ray flux by the model. The three gamma-ray energy bands are marked with gray dashed lines. . .	148
7.7	Cooling and acceleration times including adiabatic losses. The lines represent the same quantities as in Figure 7.7 for the eastern case with the addition of the adiabatic loss timescale for different values of the jet velocity. The left panel corresponds to a location 1 pc away from the base of the outer jets, whereas the right panel shows the timescales for a location further out, a total of ~ 50 pc from the central binary system.	149
7.8	Deceleration profiles. Shape of the deceleration profile $\Lambda(z)$ derived as described in the text for the western (red line) and eastern (blue line) jets.	150
7.9	Likelihood profiles of the velocity fit. Resulting likelihood profiles from the fit assuming a constant velocity profile (red) and the deceleration profile shown in Figure 7.8. The value of v_0 at which the curve has its minimum is the preferred one. The width of the parabola reflects the statistical uncertainty on this value.	151
7.10	Gamma-ray profiles along the jet including the best-fit model prediction. The data points represent the measured flux in spatial bins alongside the axis joining both jets through the central binary for three different energy bands. The lines correspond to the prediction of the 1D Monte Carlo model for the best fit values of the starting velocity, diffusion coefficient and injected electron spectrum parameters. The shaded areas represent the combined statistical error of all the best-fit parameters.	152

- 7.11 **Systematic uncertainties on the velocity estimation.** **a:** Likelihood profiles of the velocity parameter for each of the considered combination of magnetic field and electron spectral parameters. The red solid line shows the overall best-fit model resulting from the fit to multi-wavelength data, whereas the black solid line shows the best-fit model when only H.E.S.S. data is considered. **b:** Distribution of the best-fit value of v_0 for all the considered values of magnetic field and electron spectral parameters. The black dashed line and grey band denote the best-fit value and statistical uncertainty of the velocity for the model selected using multi-wavelength data, also specified in the top right corner. The red line shows the fit of a Gaussian to the histogram, where the fitted width is indicated in the top left corner. 153
- 8.1 **Significance map before and after modeling and subtracting MGRO J1908+06 using HAWC data and a Gaussian spatial model.** The figure shows the statistical significance of the gamma-ray excess measured in the full FoV before **(a)** and after **(b)** fitting and subtracting the emission from the nearby source MGRO J1908+06 assuming a Gaussian spatial model. The solid white contours show the radio emission from the surrounding nebula W50 measured by the Effelsberg telescope (Reich et al., 1984, 1990; Furst et al., 1990). 159
- 8.2 **Significance map before and after modeling and subtracting MGRO J1908+06 using HAWC data and a generalized Gaussian spatial model.** The figure shows the same quantities as Figure 8.1 but when modeling the spatial properties of MGRO J1908+06 using a generalized Gaussian model. 159
- 8.3 **Significance map of the SS 433 region using HAWC data.** The figure shows the statistical significance of the gamma-ray excess measured in the SS 433 region after the fitting and subtraction of the emission from the nearby extended source MGRO J1908+06. The solid cyan contours show the X-ray emission measured by the ROSAT satellite (Brinkmann et al., 1996; Safi-Harb and Ögelman, 1997). The locations of the X-ray regions $w1$, $w2$, $e1$, $e2$ and $e3$ are marked with white crosses. 161
- 8.4 **Model and residual of the jets using HAWC data.** The figure shows the predicted counts in the highest f_{Hit} bin from the best-fit model that includes the MGRO J1908+06 component and the jets **(a)** as well as the significance map of the entire data set after subtracting these two components **(b)**. 162

- 8.5 **HAWC spectra of the jets.** Best-fit spectral model from the 3D modeling of the eastern (a) and western (b) jets. The shaded areas and flux points include only statistical uncertainties. The previously measured flux is shown as well (Abeysekara et al., 2018). The spectra from both jets is shown in panel c for easy comparison. 163
- 8.6 **H.E.S.S. and HAWC spectra of the jets.** Resulting best-fit spectral model from the 3D modeling of the eastern (a) and western (b) jets. Note that only the H.E.S.S. result includes systematic errors, shown with a lighter color band. 163
- 8.7 **Significance map before and after modeling and subtracting MGRO J1908+06 using H.E.S.S. and HAWC data.** The figure shows the same quantities as Figure 8.2 but for the joint analysis of H.E.S.S. and HAWC data. 165
- 8.8 **Significance map of the SS 433 region using H.E.S.S. and HAWC data.** The figure shows the statistical significance of the gamma-ray excess measured in the SS 433 region after the fitting and subtraction of the emission from the nearby extended source MGRO J1908+06 in the joint analysis. The contours and markers are the same as in Figure 8.3. 166
- 8.9 **Model and residual of the jets using H.E.S.S. and HAWC data.** The figure shows the predicted counts in the highest f_{Hit} bin HAWC from the best-fit model that includes the MGRO J1908+06 component and the jets (a) as well as the significance map of the joint data set after subtracting these two components (b). 167
- 8.10 **H.E.S.S., HAWC and joint spectra of the jets.** Resulting best-fit spectral model from the 3D modeling of the eastern (a) and western (b) jets. Note that only the H.E.S.S. result includes systematic uncertainties, shown with a lighter color band. 168
- 8.11 **H.E.S.S., HAWC and joint spectra of the jets.** Resulting best-fit spectral model from the 3D modeling of the eastern (a) and western (b) jets. Note that only the H.E.S.S. result includes systematic uncertainties, shown with a lighter color band. 169

List of Tables

3.1	Selection cuts defining the <i>standard</i> and <i>hard</i> analysis cuts. Note that the total intensity cut is also to the input training data used to optimize the BDT algorithm weights used for the estimation of ζ	62
3.2	Event size (f_{Hit}) bins. Bins are defined from the fraction of PMTs triggered by each event.	70
3.3	The energy bins. Note that the first two bins are not used in the analysis as the estimate is highly biased.	70
6.1	The different data sets. Values of the exposure, mean zenith, and starting dates for each of the used data set. The exposure quoted corresponds to the maximum in the acceptance-corrected value.	120
6.2	Results of the spectro-morphological fit to MGRO J1908+06. Best-fitting photon spectral and spatial parameters from the fit to the H.E.S.S. data. ϕ_0 is the amplitude at the reference energy $E_0 = 1$ TeV. Γ is the spectral index and β the curvature parameter (see Equation 3.16). The best-fit position in Galactic coordinates are given by l and b . The 1σ radius of the Gaussian model is given by σ	123
6.3	Results of the elongated Gaussian fits to the morphology. Best-fitting spatial parameters from the fit of an elongated Gaussian model. The center position in Galactic coordinates is given by l and b . The major and minor axis 1σ radius is given by σ_{maj} and σ_{min} respectively, with the corresponding physical size calculated for a distance of 5.5kpc (Blundell and Bowler, 2004). The angle with respect to the constant Galactic longitude axis θ is frozen in the fit.	126
6.4	Crab Nebula observation runs for the PSF check. Number of runs in each era for the pointing zenith angle and offset from pointing position ranges considered.	128
6.5	Results of the power-law fits to the spectra of the jets. Best-fitting photon spectral parameters from the fit to the H.E.S.S. data with a power-law model. E_0 is the reference energy, ϕ_0 is the amplitude at the reference energy and Γ is the index.	133

7.1	Model parameters. Best-fit values of the injected electron spectral parameters and ambient magnetic field. The errors correspond to statistical uncertainty. Whether a parameter was fitted simultaneously for both jets is indicated by the column "shared".	144
8.1	Results of the spectro-morphological fit to MGRO J1908+06 using HAWC data. Best-fitting photon spectral and spatial parameters from the fit to the HAWC data. ϕ_0 is the amplitude at the reference energy $E_0 = 7$ TeV. Γ is the spectral index and β the curvature parameter (see Equation 3.16). The best-fit position in Galactic coordinates are given by l and b . r_0 and χ are the shape parameters of the generalized Gaussian (see Equation 3.18).	160
8.2	Results of the spectro-morphological fits to the spectra of the jets using HAWC data. The best-fit positions for the point-source models are given in Galactic coordinates (l , b). E_0 is the reference energy for the best-fit power-law, ϕ_0 is the amplitude at E_0 and Γ is the index. . .	162
8.3	Results of the spectro-morphological fit to MGRO J1908+06 using H.E.S.S. and HAWC data. Best-fit photon spectral and spatial parameters from the joint fit to the H.E.S.S. and HAWC data. Quantities are equivalent to those shown in Table 8.1.	165
8.4	Results of the power-law fits to the spectra of the jets using H.E.S.S. and HAWC data. Best-fitting photon spectral parameters from the fit to the H.E.S.S. data with a power-law model. E_0 is the reference energy, ϕ_0 is the amplitude at the reference energy and Γ is the index.	166
8.5	Results of the elongated Gaussian fits to the morphology of the jets using H.E.S.S. and HAWC data. Best-fitting spatial parameters from the fit of an elongated Gaussian model. The center position in Galactic coordinates is given by l and b . The major and minor axis 1σ radius is given by σ_{maj} and σ_{min} respectively, with the corresponding physical size calculated for a distance of 5.5kpc (Blundell and Bowler, 2004). The angle with respect to the constant Galactic longitude axis θ is frozen in the fit.	167

Acronyms

- ABRIR** Algorithm for Background Rejection using Image Residuals. 2, 3, 119, 200
- AGN** active galactic nuclei. 6–8, 23, 200
- ALMA** Atacama Large Millimeter Array. 31, 200
- BDT** Boosted Decision Tree. 61, 62, 191, 199, 200
- CMB** Cosmic Microwave Background. 11, 42, 140, 200
- CTA** Cherenkov Telescope Array. 56, 57, 73, 80, 81, 103, 136, 153, 192, 200
- DSA** diffusive shock acceleration. 15, 18, 200
- EAS** extensive air showers. 49, 50, 52, 54, 57–59, 71, 200
- EHT** Event Horizon Telescope. 200
- EM** electromagnetic. 9, 27, 46, 49–53, 83, 137, 190, 200
- ESO** European Southern Observatory. 28, 187, 200
- FoV** field of view. 41, 42, 56, 67, 68, 72, 74, 79, 117–120, 122, 124, 135, 139, 153, 157, 162, 189, 191, 193, 197, 200
- H.E.S.S.** High Energy Stereoscopic System. vii, ix, x, 1–3, 55–59, 61–65, 73, 74, 77–80, 83, 103, 117–122, 126–128, 130, 131, 134–138, 141, 142, 146, 147, 151, 155, 156, 158, 160–167, 169, 170, 185, 186, 190–194, 196–200
- HAWC** High Altitude Water Cherenkov. vii, ix, x, 1–3, 38, 40–43, 45–47, 68–70, 72, 73, 79, 80, 103, 117, 120, 122, 131, 135, 136, 142, 149, 155, 157–167, 170, 185, 189, 191, 192, 194, 196–198, 200
- HE** high-energy. 49, 200
- HEGRA** High Energy Gamma Ray Array. 55, 200
- IACT** Imaging Atmospheric Cherenkov Telescope. vii, ix, x, 54–57, 59, 63–65, 68, 72, 73, 79–81, 83, 103, 117, 135, 162, 169, 170, 190, 192, 200
- IC** inverse Compton. 21–23, 38, 137, 138, 140, 141, 144, 145, 187, 196, 200

- ImPACT** Image Pixel-wise fit for Atmospheric Cherenkov Telescopes. xiv, 59, 60, 118, 119, 190, 200
- IRF** instrument response function. 2, 63, 65, 73, 103, 118–120, 127, 134, 135, 156, 167, 193, 200
- LHAASO** Large High Altitude Air Shower Observatory. 68, 73, 80, 81, 83, 120, 136, 192, 200
- MAGIC** Major Atmospheric Gamma-ray Imaging Cherenkov. 40, 55, 103, 200
- MC** Monte Carlo. 59, 127, 128, 134, 135, 194, 200
- NSB** Night Sky Background. 58, 72, 200
- PMT** photomultiplier tube. 56, 58, 68–71, 199, 200
- PSF** Point-spread function. 64, 77, 120, 123, 126–128, 130, 135, 147, 191, 193, 194, 199, 200
- RM** rotation measure. 33, 200
- SED** spectral energy distribution. 42, 77, 141, 196, 200
- SMBH** supermassive black holes. 6–8, 200
- SNR** supernova remnant. 11, 30, 33, 43–45, 47, 138, 189, 200
- SWGO** Southern Wide-field Gamma-ray Observatory. 68, 72, 73, 80, 81, 103, 153, 191, 192, 200
- TS** test statistic. 39, 40, 74, 76, 148, 189, 200
- VERITAS** Very Energetic Radiation Imaging Telescope Array System. 40, 55, 200
- VHE** very-high-energy. 49, 55, 60, 68, 79, 83, 103, 120, 127, 132, 137, 193, 200
- VLA** Very Large Array. 5, 6, 30–32, 187, 188, 200
- VLBA** Very Long Baseline Array. 32, 188, 200
- WCD** water Cherenkov detector. 68, 80, 192, 200
- WCS** World Coordinate System. 73, 119, 156, 200



Image credit: National Radio Astronomy Observatory and Tracy Colson.